Enriching plasmon-enhanced Raman spectroscopy *via* electrochemistry and hybrid nanomaterials for trace chemical detection

Tabitha Jones

University College London

Department of Chemistry

2023

A thesis submitted in partial fulfilment of the requirements for the degree of Doctor of Engineering

Declaration

I, Tabitha Jones, confirm that the work presented in this thesis is my own. Where information has been derived from other sources, I confirm that this has been indicated in the thesis.

Abstract

Biomarker detection is critical for effective disease diagnosis and treatment. Surface-enhanced Raman spectroscopy (SERS) has been heralded as a technique capable of achieving rapid, low-cost healthcare sensing. However, improvements are needed to enable quantitative detection in complex media, such as bodily fluids. This work explores ways to enrich SERS using electrochemistry, machine learning and hybrid nanomaterials. Two different approaches are developed in this thesis: an electrochemical SERS (E-SERS) system based on silver nanoparticle electrodes and a hybrid semiconductor-plasmonic metal NP system.

The E-SERS system was used to detect two important biomarkers, uric acid (UA) and creatinine (CRN). Applying an external potential enhances the SERS signal and enables multiplexed detection of the two analytes. Machine learning approaches were applied to a large E-SERS dataset (>2,300 spectra) to achieve quantitative, multiplexed detection of UA and CRN. Finally, proof-of-concept experiments were performed in dilute synthetic urine to demonstrate the detection of clinically relevant concentrations of the analytes.

A hybrid SERS system was fabricated using tin dioxide coated silver nanoparticles (Ag@SnO_2 NPs). An unexpected, time-dependent increase in the SERS signal was observed when the Ag@SnO_2 NP substrates were irradiated with the Raman laser. The in-situ laser enhancement enabled lower concentrations (<1 μM) of analytes to be detected compared to unirradiated substrates. Potential applications of the Ag@SnO_2 NP system were demonstrated including the quantitative detection of uric acid, the indirect detection of the ketosis biomarker, 3-hydroxybutanoic acid, and the quantitative detection of ketamine in synthetic saliva.

Impact statement

Early diagnosis plays a critical role in the effective treatment of almost all diseases. Many of these illnesses can be identified by detecting specific molecules found in bodily fluids, such as urine or blood, called biomarkers. While effective sensors exist for certain conditions, for example COVID-19 lateral flow tests and electrochemical glucose sensors, these simple detection methods often do not have the required sensitivity or selectivity. They also typically only detect one analyte at a time. Bodily fluids contain a plethora of different biomarkers, which can be used to give a holistic understanding of a patient’s health. Therefore, the simultaneous measurement of different biomarkers, known as multiplexed detection, is extremely desirable. Advanced analytical methods, such as mass spectrometry or high-performance liquid chromatography, can achieve sensitive multiplexed detection, but they are time-consuming and require expensive, lab-based equipment. Thus, there is a need for sensitive, selective chemical sensors which can detect multiple biomarkers quickly and cheaply.

SERS is a technique which could achieve this goal due to its sensitivity, selectivity, and ease of use. However, multiplexed quantification can be difficult in complex media due to the competitive adsorption of analytes on the SERS substrate and the overlapping of characteristic peaks. This thesis develops ways to improve SERS using electrochemistry, machine learning, and hybrid nanomaterials and drive it towards clinical application.

Specifically, in Chapter 3, simple Ag NP electrodes are used to detect uric acid (UA) and creatinine (CRN) with electrochemical-SERS (E-SERS). UA is an indicator of preeclampsia, gout, and cardiovascular disease and CRN is used to assess kidney filtration function. Applying a potential to the SERS electrodes allows lower concentrations of the analytes to be detected compared to conventional SERS and enables multiplexed detection. Strategies to improve the reliability and robustness of the Ag NP electrodes are developed, which could benefit other researchers working in the field.

In Chapter 4, machine learning approaches are applied to a large UA/CRN dataset (>2,300 E-SERS spectra) to achieve quantitative, multiplexed detection of the analytes. Using ML-based concentration prediction reduces the need for time-consuming visual inspection of SERS spectra by trained operators, increasing the practicality of SERS as an analytical technique.

Chapter 5 focuses on a hybrid plasmonic metal-metal oxide system. This is an area of significant academic interest as these systems have recently been shown to boost SERS enhancements but are not yet fully understood. In-situ laser enhancement of the SERS signal is observed for tin dioxide-coated silver nanoparticles (Ag@SnO_2 NPs) substrates. This enhancement allows lower concentrations of target analytes, including UA, to be detected. The Ag@SnO_2 NP substrates are used to detect ketamine, an illicit drug responsible for drug-driving-related road traffic collisions. Quantitative detection in synthetic saliva is demonstrated and the limit of detection achieved (0.34 nM) offers a significant improvement over the current non-quantitative commercial lateral flow tests.

Publications

Published

- **Jones, T.** Fabrication of Nanostructured Electrodes for Electrochemical Surface-Enhanced Raman Spectroscopy (E-SERS): A Review. *Materials Science and Technology* **2023**, 1–15.

- **Jones, T.**; Davison, G.; Jeong, H.-H.; Lee, T.-C. Chapter 2. Engineered Gold Nanoparticles for Photothermal Applications. In Nanoscience & Nanotechnology Series; Ye, E., Li, Z., Eds.; Royal Society of Chemistry: Cambridge, 2022; pp 33–80.

- Davison, G.; **Jones, T**.; Liu, J.; Kim, J.; Yin, Y.; Kim, D.; Chio, W. K.; Parkin, I. P.; Jeong, H.; Lee, T. Computer-Aided Design and Analysis of Spectrally Aligned Hybrid Plasmonic Nanojunctions for SERS Detection of Nucleobases. *Adv Materials Technologies* **2023**, *8* (7), 2201400.

- Davison, G.; Yin, Y.; **Jones, T**.; Parkin, I. P.; Peveler, W. J.; Lee, T.-C. Multi-Mode Enhanced Raman Scattering Spectroscopy Using Aggregation-Free Hybrid Metal/Metal-Oxide Nanoparticles with Intrinsic Oxygen Vacancies. *J. Mater. Chem. C* **2023**,*11* (9), 3334–3341.

- Chio, W.-I. K.; Liu, J.; **Jones, T.**; Perumal, J.; Dinish, U. S.; Parkin, I. P.; Olivo, M.; Lee, T.-C. SERS Multiplexing of Methylxanthine Drug Isomers via Host–Guest Size Matching and Machine Learning. *J. Mater. Chem. C* **2021**, *9* (37), 12624–12632.

- Chio, W.-I. K.; Davison, G.; **Jones, T.**; Liu, J.; Parkin, I. P.; Lee, T.-C. Quantitative SERS Detection of Uric Acid via Formation of Precise Plasmonic Nanojunctions within Aggregates of Gold Nanoparticles and Cucurbit[n]Uril. *JoVE* **2020**, No. 164, 61682.

In preparation

- **Jones, T**.; Zhou, D.; Parkin, I. P.; Lee, T.-C. Multiplexed detection of uric acid and creatinine with electrochemical-SERS and machine learning, manuscript in preparation.

- **Jones, T**.; Wang, X.; Parkin, I. P.; Lee, T.-C. Triply enhanced hybrid SERS via extended utilisation of the Raman laser through the enrichment of oxygen vacancies in SnO_2, manuscript in preparation.

- To, K.; **Jones, T.**; Lee, T.-C.; Parkin, I. P. Detection of explosives using enhanced Raman spectroscopy approaches and machine learning, manuscript in preparation.

Acknowledgements

I would like to start by expressing my deep gratitude to my primary supervisor, Dr Tung Chun (John) Lee, for his continuous support and guidance. His passion and dedication towards research are truly inspiring and this thesis would not have been possible without him. My heartfelt thanks also go to my secondary supervisor, Professor Ivan Parkin, for his invaluable advice and encouragement throughout my EngD.

I am extremely grateful to the whole Nanomaterials Chemistry Lab for their support. Special mention must go to everyone in the LG6 office, particularly Gemma, Dan, Jia, Yidan, Alice, Andy, Deyue and Xiangyu, for their friendship. Our long chats made the hours waiting for experiments and the days when nothing worked so much brighter.

There are many people I would like to thank in the chemistry department. In particular, Dr Kersti Karu for her conscientious management of LG11; Dr Steve Firth, Dr Andy Steward and Dr Xueming Xia for their patient guidance on the SEM and TEM; and Dr Zhimei Du for her help through the CDT. I would also like to thank Dr Kevin To for his efforts in our collaborative project and for the many interesting discussions. I am very grateful to Camtech Innovations, particularly Dr Meng Han Kuok and Dr Daniel Kirilly, for sponsoring the EngD through the EPSRC M3S CDT and for their valuable insights.

Finally, I must thank all my friends and family for their unwavering love and support. I am especially indebted to those who made my time in London so much fun: thank you for all the laughs, long brunches, freezing lockdown walks, tag rugby matches and boozy dinners.

It is impossible to describe what my family means to me; I will be forever grateful for everything you do. Thank you, Blake, for your kindness, Dad for your wisdom and Mum for your strength. Together, you have taught me to “never never never give up”.

List of figures

List of appendix figures

List of tables

Acronyms

2,4-DNT	2,4-dinitrotoulene
3-HB	3-hydroxybutanoic acid
4-MBA	4-mercaptobenzoic acid
4-MPY	4-mercaptopyridine
ALS	asymmetric least squares
ANN	artificial neural network
APTES	3-aminopropyl)triethoxysilane
CE	chemical enhancement
CNN	convolution neural networks
CRN	Creatinine
CTAB	cetrimonium bromide
DPA	dipicolinic acid
E-SERS	electrochemical surface-enhanced Raman spectroscopy
EC	Electrochemical
ED	electrochemical deposition
EM	Electromagnetic
FON	film-over-nanosphere
FTO	fluorine doped tin oxide
HOMO	highest occupied molecular orbital
IR	Infrared
ITO	indium tin oxide
LC-MS	liquid chromatography – mass spectrometry
LoD	limit of detection
LSPR	local surface plasmon resonance
LUMO	lowest unoccupied molecular orbital
ML	machine learning
MLP	multilayer perceptrons
MV	methyl viologen
NF	Nanoflower
NP	Nanoparticle
NSL	nanosphere lithography
NSS	nanostructured substrates
NT	Nanotriangle
PCA	principal component analysis
Pdop	Polydopamine
PIERS	photo-induced enhanced Raman spectroscopy
PLS	polylactic acid
PLSR	partial least squares regression
R6G	rhodamine 6G
SEM	scanning electron microscopy

SERS	surface-enhanced Raman spectroscopy
SSV	sphere segment void
SU	synthetic urine
TEM	transmission electron microscopy
TEOS	tetraethyl orthosilicate
UA	uric acid
UV-vis	ultraviolet-visible
V_o	oxygen vacancies
XPS	x-ray photoelectron spectroscopy

Table of contents

Chapter 1 Introduction and literature review

N.B. Some sections of this chapter have been adapted from Jones, T. Fabrication of Nanostructured Electrodes for Electrochemical Surface-Enhanced Raman Spectroscopy (E-SERS): A Review. Materials Science and Technology 2023, 1–15.

1.1 Motivation

Early detection and diagnosis play a critical role in the effective management of almost all diseases.[1,2] This is exemplified by the NHS Long Term Plan's objective to diagnose 75% of individuals with cancer at stage 1 or 2 by 2028.[3] If this target is achieved, it would result in 55,000 more people surviving their cancer for at least five years after diagnosis each year.

Many illnesses can be identified by detecting specific molecules found in bodily fluids, such as blood, urine or saliva, called biomarkers.[4–6] They can include proteins, DNAs, RNAs, lipids and metabolites.[7–9] Examples include uric acid, which is a biomarker for preeclampsia in pregnant women[10–15], gout and cardiovascular disease[16–19], and 3-hydroxybutanoic acid, an indicator of diabetic ketoacidosis.[20]

Effective sensors do already exist for certain conditions, for example, COVID-19 lateral flow tests and electrochemical glucose sensors[21]. However, often the simpler, cheaper detection methods, such as colourimetric assays or lateral flow assays, do not have the required sensitivity or selectivity.[2,22,23] They also typically only detect one analyte at a time. Although this is acceptable in some scenarios, bodily fluids like urine contain a plethora of different biomarkers, which can all be used to give a holistic understanding of a patient's health. Therefore, the simultaneous measurement of different biomarkers, referred to as multiplexed detection, is extremely desirable.

Sensitive multiplexed detection of biomarkers is possible with advanced analytical methods, such as mass spectrometry and high-performance liquid chromatography, but these techniques are time-consuming and require expensive, specialist, lab-based equipment.[24–27] In light of this, there is a need for sensitive, selective chemical sensors which can detect multiple biomarkers quickly and cheaply.

SERS has been heralded as a technique which could overcome these limitations.[28] In SERS, the Raman signal of a molecule is significantly enhanced when it is adsorbed onto a nanostructured noble-metal surface, allowing analyte molecules to be identified by their vibrational fingerprints.[29,30] It is a promising technique due to its sensitivity, selectivity, and ease-of-use. Despite this, it is still yet to achieve clinical use.

Some of the current obstacles to widespread SERS adoption include difficulties detecting multiple analytes due to competitive adsorption of molecules and overlapping characteristic peaks; the need for trained operators to interpret the spectra; variability in the SERS substrates; and limited enhancement factors for simple, cost-effective SERS substrates made without specialist nanofabrication equipment. This thesis focuses on ways to overcome these issues using electrochemistry, hybrid nanomaterials, and machine learning.

1.2 Raman spectroscopy

Raman spectroscopy is an analytical technique used to determine the vibrational modes of a sample.[31] It can provide a “vibrational fingerprint” of a substance by detecting the small fraction of light (approximately 1 in 10^7 photons) which is inelastically scattered.[32] This inelastic scattering was first postulated by Smekal in 1923[33] and then observed experimentally in 1928 by Raman and Krishnan.[34,35]

During Raman spectroscopy, a monochromatic laser is used to irradiate a sample. When the laser is incident on a molecule, the oscillating electromagnetic field of a photon polarises the molecular electron cloud.[34] The energy of the photon is transferred to the molecule and a virtual energy state is formed. This virtual energy is not stable, and the photon is re-emitted almost immediately, as scattered light. In the vast majority of cases, the photon that is re-emitted has the same energy (and therefore wavelength) as the incident photon. This is called elastic or Rayleigh scattering (Figure 1.1).[31]

Raman scattering occurs when there is a difference between the energy of the incident and scattered radiation.[31] If the molecule gains energy from the photon during the scattering, then the scattered photon loses energy and its wavelength increases. This is called Stokes scattering. On the other hand, if the molecule relaxes back to a lower vibrational state than it had originally, the scattered photon will gain energy and its wavelength will decrease. This is called anti-Stokes scattering. Anti-Stokes scattering is less common than Stokes scattering, as it requires the molecule to be in a vibrationally excited state before the photon arrives. Consequently, Stokes scattering is normally used for Raman measurements. In Raman spectra, the intensity of photons detected is plotted as a function of Raman shift, which is the energy difference between the incident and Stokes scattered photons, given in wavenumber, $\tilde{v}$ (where $\tilde{v} = \frac{1}{\lambda}$ and $E = \frac{hc}{\lambda}$) (Figure 1.1).

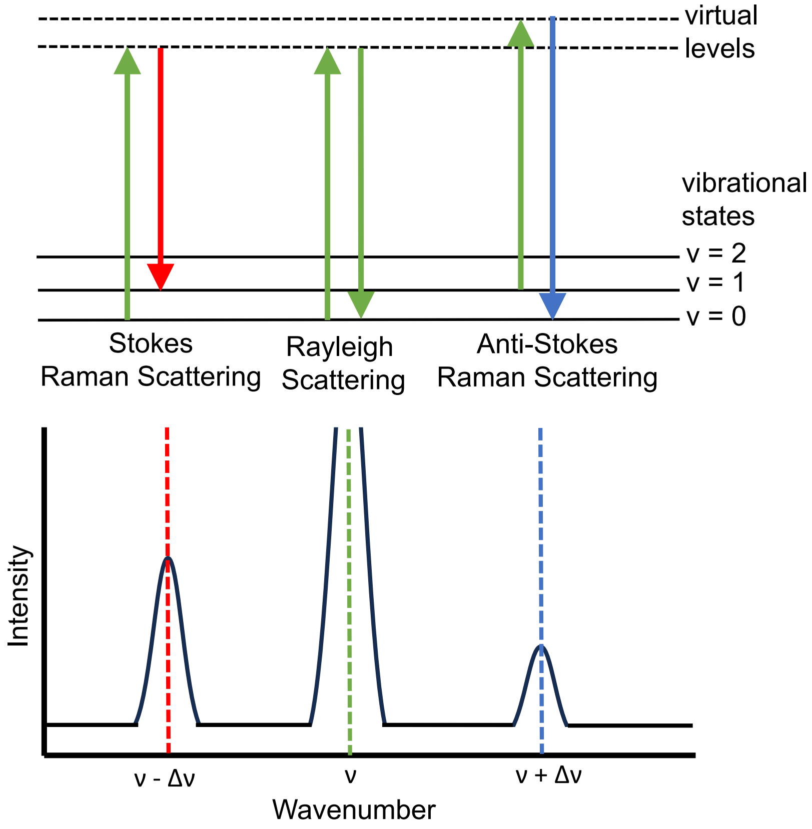

Figure 1.1: Illustration of the different types of light scattering. In Rayleigh scattering, the energy of the incident and the emitted photon is equal, resulting in no change in the photon wavelength. In Stokes Raman scattering, energy is transferred from the incident photon to the molecule, and in anti-Stokes Raman scattering, energy is transferred from the molecule to the emitted photon. This inelastic scattering causes a change in the photon wavelength, resulting in peaks in the Raman spectrum.

Not all vibrational modes can be observed using Raman spectroscopy. For a vibrational mode to be ‘Raman active”, the molecule must undergo a change in polarizability during the vibrational excitation. Polarizability is a measure of how easy it is to distort electrons from their original position. The polarizability of a molecule increases with increasing electron density and bond length and decreases with increasing bond strength.[31]

Infrared (IR) spectroscopy is a complementary technique to Raman spectroscopy. It also studies the interaction of radiation with molecular vibrations, but for a vibration to be IR active, there must be a change in the dipole moment.[36] Many molecules or vibrational modes which are IR inactive or weak will have intense Raman signals and vice versa, which is helpful for characterisation. The different vibrational modes for CO_2 are shown in Figure 1.2 along with whether they are Raman or IR active.[34]

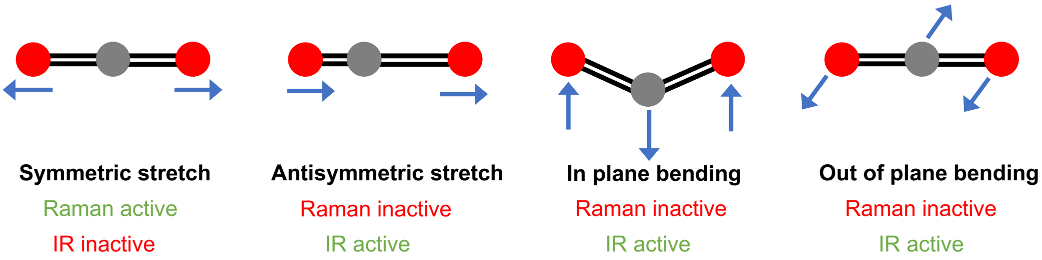

Figure 1.2: An illustration of the vibrational modes of CO_2. There are three infrared (IR) active modes (antisymmetric stretch, in plane bending and out of plan bending) and one Raman active mode (symmetric stretch).

Raman spectroscopy is a valuable technique and offers advantages such as minimal sample preparation, fast response, tolerance to water and the potential for portability. However, as the fraction of light that is inelastically scattered is very low, the signals are inherently weak, making the detection of low concentrations of analytes in dilute solutions difficult.

1.3 Surface-enhanced Raman spectroscopy

Surface-enhanced Raman Spectroscopy (SERS) is a type of Raman spectroscopy in which the signal is enhanced (by factors of up to 10^8) due to the adsorption of the target molecule onto a nanostructured metal surface.[28] SERS was discovered in 1974 by Fleischmann *et al*. when an unexpectedly large Raman signal was observed while studying pyridine on an electrochemically roughened silver electrode.[37] This was the start of a lengthy debate into the reason for the SERS enhancement which has only recently reached a good agreement among researchers. It is now understood to be a combination of an electromagnetic (EM) and a chemical enhancement.[28,38,39] The electromagnetic enhancement is the result of an increase in the local EM field at the surface of the metal caused by local surface plasmon resonance (LSPR).[28,39,40]

1.3.1 Local surface plasmon resonance

LSPR is the resonant oscillation of free electrons confined within a metal nanoparticle caused by light with a wavelength that is less than or equal to the diameter of the particle (Figure 1.3).[29,41]

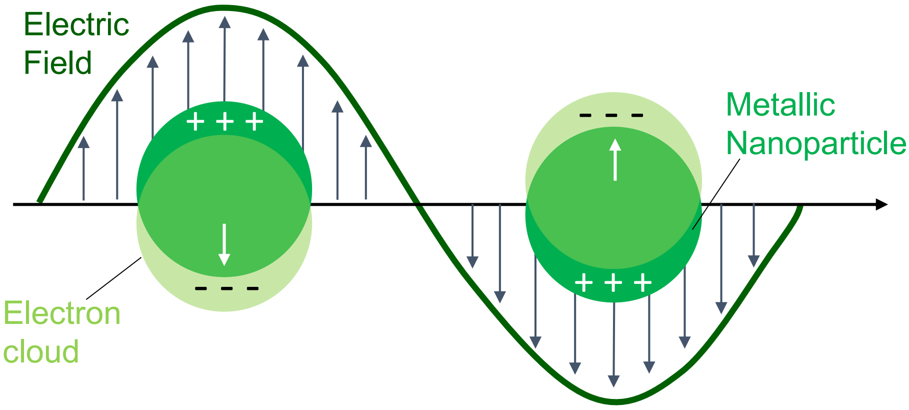

Figure 1.3: A schematic diagram illustrating local surface plasmon resonance (LSPR) in metallic nanoparticles caused by light with a wavelength less than or equal to the diameter of the particle.

Mie theory can be used to describe the scattering of electromagnetic radiation by spherical particles immersed in a continuous medium.[42] For a spherical particle which is much smaller than the wavelength of light, the polarizability (α) is given as:[43]

$$\alpha = a^3 \frac{\epsilon - \epsilon_m}{\epsilon + 2\epsilon_m} \qquad \text{Equation 1}$$

Where a is the radius of the sphere, ϵ is the dielectric constant of the metal sphere, and ϵ_m is the dielectric constant of the surrounding medium.

When light is incident on a spherical particle, it will either be scattered or absorbed. The absorption efficiency (Q_{abs}) can be written in terms of the extinction (Q_{ext}) and scattering (Q_{sca}) efficiencies as follows:

$$Q_{abs} = Q_{ext} - Q_{sca} \qquad \text{Equation 2}$$

Using the polarizability from equation 1, the Q_{ext} and Q_{sca} can be written as:[43]

$$Q_{ext} = 4xIm\left(\frac{\epsilon - \epsilon_m}{\epsilon + 2\epsilon_m}\right)$$ Equation 3

$$Q_{sca} = \frac{8}{3}x^4\left|\frac{\epsilon - \epsilon_m}{\epsilon + 2\epsilon_m}\right|^2$$ Equation 4

Where:

$$x = \frac{2\pi a\sqrt{\epsilon_m}}{\lambda}$$ Equation 5

It is important to note the a dependence of the extinction and scattering efficiencies; as the radius of a metal nanoparticle increases a higher proportion of the incident light will be scattered.[44] The presence of the dielectric constant of the surrounding medium in the expression also indicates that the extinction and scattering efficiencies will be affected if a nanoparticle is coated with a different material.

The wavelength dependence of the extinction and scattering efficiencies comes from the metal dielectric constant (ϵ) as this is strongly dependent on wavelength. The wavelength of the LSPR peak can be calculated by finding the point at which the denominator in equation 3 ($\epsilon + 2\epsilon_m$) vanishes. In a vacuum, this is when the real part of the metal dielectric constant is equal to -2. For particles that are not in a vacuum, plasmon resonance occurs when Re(ϵ/ϵ_m) = -2.

The real and imaginary parts of the silver dielectric constant are plotted against wavelength in Figure 1.4, along with the extinction efficiency for a 30 nm silver sphere.[43] Comparing these two plots, it is possible to confirm that the LSPR peak occurs when Re(ϵ/ϵ_m) = -2.

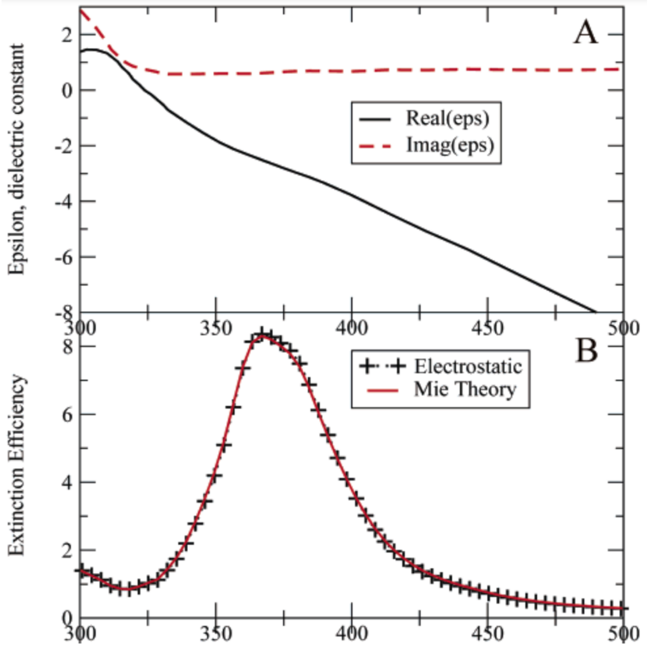

Figure 1.4: (a) The real and imaginary parts of the silver dielectric constant as a function of wavelength. (b) Extinction efficiency (the ratio of the extinction cross-section to the area of the sphere) of a silver sphere with a 30 nm radius as obtained from Mie Theory. Adapted from ref [43] *with permission. Copyright 2003 American Chemical Society.*

1.3.2 Electromagnetic Enhancement

The electromagnetic enhancement in SERS is the result of an increase in the local EM field at the surface of the metal caused by local surface plasmon resonance.[28,39,40] The LSPR in the nanoparticles amplifies the incident EM field. This enhancement of the EM field in SERS is described as:

$$G_{loc} = \left[\frac{E(\omega_{loc})}{E_0}\right]^2 \quad \text{Equation 6}$$

Where G_{Loc} is the enhancement factor of the EM field in SERS, $E(\omega_{loc})$ is the local EM field at the frequency of the incident light associated with the LSPR, and E_0 is the incident EM field at the same frequency.

As discussed in section 1.2, Raman spectroscopy depends on changes in the polarizability of molecules during vibrations. When a molecule is close to the surface of a metal nanoparticle, its Raman polarizability can be increased by one to three orders of magnitude compared to free molecules. Similarly, other sources of oscillation, such as the Raman dipole, can excite the LSPR. The mutual excitation of the Raman polarizability and the local EM field, mean that the EM field in SERS is enhanced by a factor of:[45]

$$G_R = \left[\frac{E(\omega_R)}{E_0}\right]^2 \qquad \text{Equation 7}$$

Where G_R is the enhancement factor of the EM field in SERS, $E(\omega_R)$ is the local EM field at the Raman frequency, and E_0 is the incident EM field at the frequency of the incident light.

For small Raman shifts, ω_{loc} can be considered roughly equal to ω_R so the overall enhancement of the EM field in SERS (G) can be defined as:[45]

$$G = G_{loc}G_R = \left[\frac{E(\omega_{loc})}{E_0}\right]^2 \left[\frac{E(\omega_R)}{E_0}\right]^2 = \left[\frac{E(\omega_R)}{E_0}\right]^4 \qquad \text{Equation 8}$$

This $|E(\omega_R)|^4$ relationship means that small changes in the local electric field have a substantial impact on the SERS signal.[46] The magnitude of the EM field depends on the size and shape of the nanoparticle (NP).[29] Very large enhancements, known as ‘hot spots’, can be formed between two NPs or in carefully designed nanostructures.[40,47–49] Single spherical particles do not exhibit particularly significant EFs (~10^3) but very large EFs (~10^5-10^8) are found at the junctions between two particles (Figure 1.5a). These enhancements decrease as the distance between the nanoparticles increases. The greatest EFs have been calculated to occur when the separation between NPs is 1 nm.[29,39,46,47] At this separation distance, the plasmons of the two NPs can strongly couple with each other, resulting in EFs as high as ~10^9-10^{12}.[45] Below 1 nm, quantum effects, such as electron tunnelling, are predicted to significantly reduce the field enhancement.[50]

As well as at gaps between nanoparticles, enhanced local electric fields are also found at sharp tips or edges of particles.[43] This is illustrated in Figure 1.5b and Figure 1.5c where the electromagnetic enhancement is calculated to be significantly higher at the points of a spheroidal Au nanorod than around a spherical Au NP. The maximum EM enhancement at the points of an ellipsoid have been shown to increase with aspect ratio.[51,52] This has led to extensive research into non-spherical NPs for SERS such as nanorods, nanocubes, nanotriangles, nanostars and nanoflowers.[28,38,53–55] Combining the enhancement from tips or edges with the 'hot spots' formed between particles can lead to enormous EM enhancements.[52]

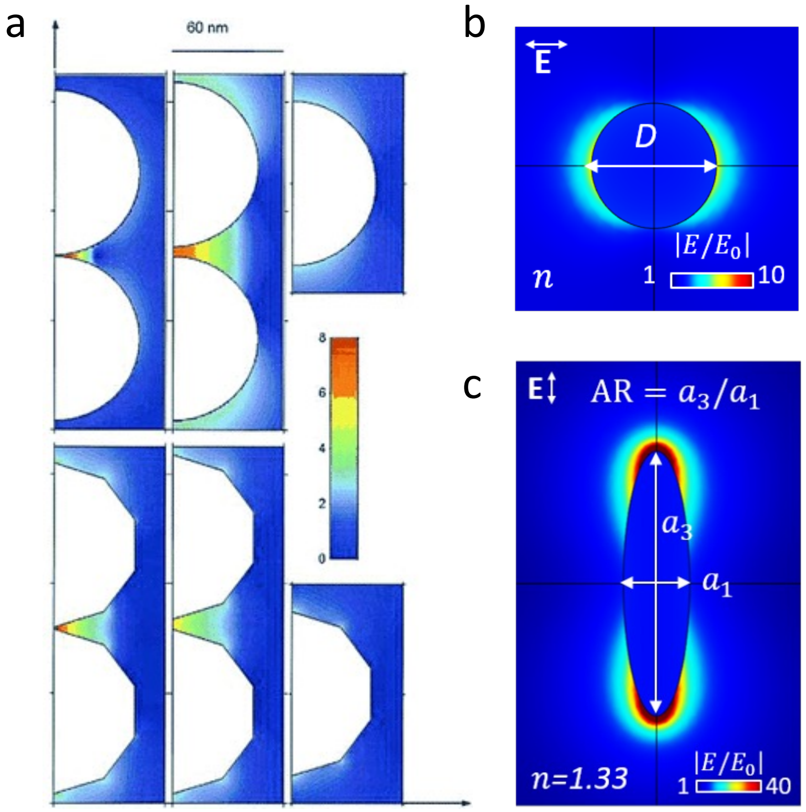

Figure 1.5: (a) The magnitude of the electromagnetic enhancement (colour-coded log scale) for dimers of silver nanoparticles (left and middle columns) compared with single isolated silver nanoparticles (right column). Reproduced from ref [47] with permission. Copyright 2000 American Chemical Society. (b) and (c) Electromagnetic enhancements for a (b) spherical and (c) spheroidal gold nanoparticle. Adapted from ref [51] with permission. Copyright 2022 Royal Society of Chemistry.

The EM enhancement is strongly dependent on the distance from the metal surface. The strength of the local electric field decreases with distance from the surface (r):

$$E(r) \propto (1+\frac{r}{a})^{-3} \qquad \text{Equation 9}$$

where a is the radius of the nanoparticle. Based on this, the SERS enhancement will scale with r roughly as:[56]

$$G \propto (1 + \frac{r}{a})^{-12} \qquad \text{Equation 10}$$

This highlights the importance of surface adsorption within SERS sensing.

1.3.3 Chemical enhancement

The chemical enhancement (CE) of the SERS signal is much less significant than the EM enhancement (~10^3 vs. ~10^5 – 10^{10}). However, it is still an important component of the enhancement and can explain shifts in the Raman peaks.[39] The CE originates from charge transfer or chemical complexation which can occur when the molecule adsorbs onto the metal nanostructure. Electrons can transfer between the Fermi level of the metal and the lowest unoccupied molecular orbital (LUMO) or highest occupied molecular orbital (HOMO) of the molecule.[45] These processes result in changes to the polarizability of the molecule which can shift or increase the Raman scattering signal.[28,39,40]

1.3.4 Hybrid plasmonic metal-semiconductor SERS

Although it is possible to observe SERS enhancements for dielectrics and semiconductors on their own, there has been significant interest in combining these materials with plasmonic metals to create hybrid SERS systems.[57,58] Combining semiconductors with plasmonic metals can enhance SERS by 10 - 10^3 times.[58] In a typical hybrid semiconductor/plasmonic metal SERS system, photoexcited electrons from LSPR in the plasmonic metal flow into the conduction band of the semiconductor which promotes subsequent semiconductor-to-molecule charge transfer and leads to CE enhancement of the SERS signal.[58] However, the charge transfer mechanism is highly dependent on the arrangement of the plasmonic metal and semiconductor, the band gap of the semiconductor and the work function of the plasmonic metal nanoparticle, therefore other charge transfer pathways are also possible.[57–59] Hybrid systems have the advantage of being able to customise the band gap, conduction and valence band edges, and refractive index of the semiconductor. This means that these properties can be adjusted to match the energy levels of target analytes, resulting in optimal SERS chemical enhancement, further boosting the SERS signal.

1.3.5 Photo-induced enhanced Raman spectroscopy

Photo-induced enhanced Raman spectroscopy (PIERS) is a recent development in hybrid SERS research, which combines metal oxide semiconductors and plasmonic nanoparticles to achieve significant Raman enhancements. It was first reported by the Parkin group in 2016.[60] In this work, Au or Ag NPs were drop-cast onto TiO_2 thin films and pre-irradiated with UV light. The hybrid semiconductor-metal substrates were then used to record Raman spectra of a range of analytes and larger signal enhancements (an order of magnitude) were observed compared to conventional SERS.[60]

The PIERS enhancement mechanism is explained through the formation of oxygen vacancies (Figure 1.6).[60,61] The UV irradiation of TiO_2 creates oxygen vacancies (V_o) and generates donor states below the conduction band. When the TiO_2 is illuminated with the Raman laser, electrons are excited from the donor states to the TiO_2 conduction band, and then transferred to the plasmonic metal. This electron injection shifts the Fermi level of the plasmonic metal to more negative values, increasing the probability of charge transfer to the adsorbed molecule and therefore, enhancing the Raman signal.

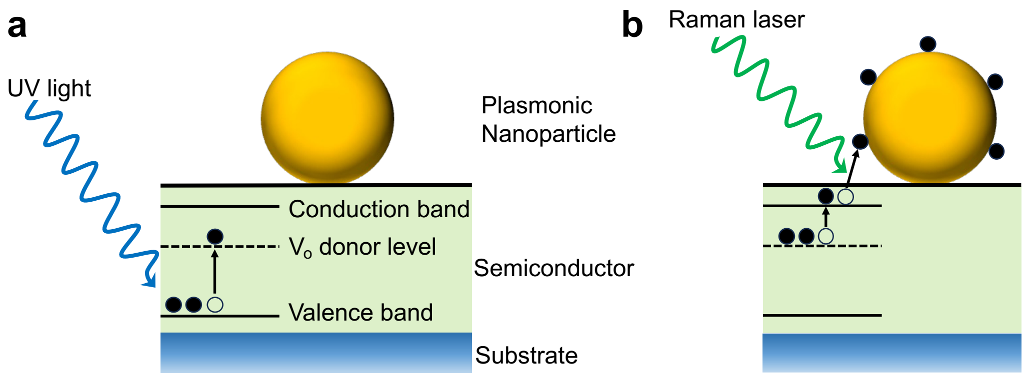

Figure 1.6: An illustration of the PIERS mechanism. (a) The ultraviolet light creates oxygen vacancy (V_o) donor levels in the semiconductor. (b) The Raman laser excites electrons from the donor level to the conduction band, where they can transfer to the plasmonic nanoparticle.

When PIERS measurements are performed with TiO_2, the signal intensity gradually decreases over time until the PIERS enhancement disappears around 60 minutes after the UV irradiation.[62] This is attributed to surface healing of the oxygen vacancies in the TiO_2 when exposed to air.

In addition to TiO_2, other substrates have been investigated including WO_3, ZnO, and $LiNbO_3$.[61–63] Different enhancements and healing rates are observed for the different materials depending on their surface vacancy formation energies.[62] Alternatives to the drop-casting method have also been reported including the thermal dewetting of Ag NPs on crystalline anodized TiO_2 nanotube arrays[64] and the co-deposition of Au NPs with TiO_2 to form embedded Au-TiO_2.[65] As PIERS research grows, the number of analytes investigated increases, with detection of explosives[60], pollutants[60,66], and biomarkers[60,67,68] being demonstrated so far.

PIERS relies on UV irradiation to generate additional oxygen vacancies in the metal oxide. Our group has recently demonstrated UV-irradiation-free PIERS-type enhancement by utilising SnO_2, which is intrinsically rich in oxygen vacancies.[69] Colloidal gold nanotriangles (Au NTs) were coated with SnO_2 and used for SERS. The strong signals were attributed to an electromagnetic enhancement from the anisotropic Au NTs, and a chemical enhancement resulting from the photo-induced charge transfer from the SnO_2 to the Au NTs, enabled by the presence of intrinsic oxygen vacancies in the SnO_2. The hybrid system achieved a limit of detection of 88 nM for an explosive marker (2,4-DNT) in water, exhibiting signals 16 times stronger than those of bare Au NTs, without UV-irradiation.

1.3.6 Plasmonic heating

Most discussion of local surface plasmon resonance (LSPR) focuses on the huge electromagnetic field enhancements observed at the surface of the nanostructure. This is the source of the SERS enhancement and has resulted in a range of other advances in biosensing, trace chemical detection and photovoltaics. However, the collective oscillation of electrons in LSPR also generates heat *via* Joule heating due to the increased frequency of collisions between the electrons and lattice atoms.[70] This is known as plasmonic or photothermal heating.

Traditionally, plasmonic heating has been seen as an undesirable phenomenon as energy dissipation as heat will weaken the optical signal. However, in the early 2000s, the field of thermoplasmonics started to grow quickly as researchers realised that the rapid and controlled generation of highly localised heat could be extremely useful.[70,71] One of the first prominent applications of plasmonic heating was plasmonic photothermal therapy, where Au NPs are used to destroy cancerous cells.[72–75] The Au NPs are delivered to the tumour site and irradiated with near-infrared light. The NPs absorb the light, convert it into heat *via* plasmonic heating, and consequently induce apoptosis of cancer cells while minimising damage to the surrounding healthy tissue. The temperature needed for full destruction of cancer cells *in vitro* can vary depending on the type of cell but is generally around 70 – 80 ^{o}C, which can be readily achieved *via* plasmonic heating.[51] Other key applications include photothermal-triggered drug and gene delivery[76–82], photoacoustic imaging[83–92], solar steam generation[93–96], nanofabrication[97–100], and catalysis[101–104].

1.3.7 Application of SERS in biosensing

SERS has been extensively studied for the detection of biomarkers and there are many comprehensive reviews of this area.[28,39,54,105] This review primarily focuses on electrochemical-SERS (section 1.4). However, the main approaches used in SERS biosensing are summarised here. Generally, the sensing methodologies can be separated into label-free and label-based approaches.

Label-free approaches detect the analyte directly when it is adsorbed onto the noble metal surface. It relies on the analyte being Raman active and is best suited to strong Raman scatterers, typically small molecules that often contain ring structures. The SERS substrates can be solid substrates (discussed further in section 1.4.2) or solution-based (i.e. colloidal plasmonic metal nanoparticles). Most research in this area focuses on the creation of “hot spots” and trapping the target analyte within these “hot spots” to achieve the largest SERS enhancements, enabling the detection of very low concentrations (<nM) of analytes. As discussed in section 1.3.2, “hot spots” are formed at sharp tips and edges of nanoparticles and in the “nanogaps” between particles. There has been extensive research into non-spherical NPs such as nanorods, nanotriangles and nanostars for SERS as well as ways to aggregate particles to form “hot spots”.[41,54,58,106–108]

A particularly successful aggregation approach uses cucurbit[*n*]urils to form precise nanogaps. Cucurbit[*n*]urils or CB[*n*]s are a family of barrel-shaped supramolecular host molecules, made up of *n* (where *n* = 5-8, 10) cyclically arranged glycouril units linked by methylene bridges.[109] CB[*n*]s are highly symmetric and rigid with a height of 0.9 nm.[109,110] The hydrophobic internal cavity of the barrel-shaped molecules can incorporate a wide variety of small molecules and can form host-guest complexes with very high binding affinities (up to $K_a = 15.3 \times 10^{15}\ M^{-1}$).[111–113] In 2010, Lee *et al*. showed that CB[5] could be used as a molecular linker for gold nanoparticles.[114] The carbonyl groups at the portals of the CB[5] molecule bind to the Au surface, resulting in aggregates with defined 0.9 nm gaps between the particles.[110,114,115] These precise nanojunctions result in large signal enhancements and the ability of CB[*n*]s to form host-guest complexes means that target analytes can be selectively positioned inside the SERS hot spot (Figure 1.7).[110,116] This approach has been used to sense a wide range of analytes, including neurotransmitters, nucleobases and creatinine.[48,49,110,117–124]

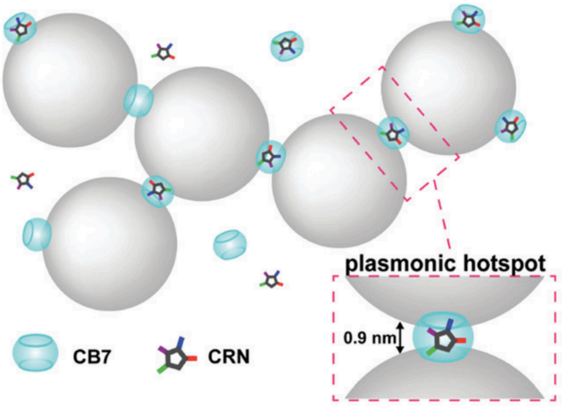

Figure 1.7: Schematic illustration of the precise nanojunctions created when CB[7] is used to aggregate Au NPs (not to scale). The target analyte, creatinine (CRN) in this case, is positioned inside the CB[7] cavity at the centre of the plasmonic hot spot. Adapted from ref [122] *under the terms of the CC BY 4.0 license.*

Label-free SERS sensors struggle to detect certain analytes such as weak Raman scatterers and large molecules, such as proteins. This is because they contain many bonds and therefore lots of different vibrational modes, which result in noisy SERS spectra that are difficult to interpret.[125] To overcome this issue, one approach is to use SERS tags.[28,126–129] In this method, instead of directly measuring the SERS signal of the analyte, a strong Raman scatterer (known as the Raman reporter) is used to indirectly detect the target analyte. SERS nanotags typically consist of a plasmonic nanoparticle, a Raman reporter molecule, and a target-specific ligand such as an antibody or oligonucleotide. The use of the target-specific ligand makes this approach extremely selective.

There are many different systems but essentially, the approach relies on the SERS signal of the Raman reporter increasing when the concentration of the target analyte increases. One method is the sandwich immunoassay.[128,130] In this technique, capture antibodies are immobilised on a surface which bind to the target analyte (an antigen in this case). Subsequently, SERS nanotags containing another antibody, a plasmonic nanoparticle, and a Raman reporter, also bind to a different site on the target analyte, forming a sandwich complex

(Figure 1.8). When the target analyte is present, the arrangement of plasmonic nanoparticles on the surface leads to the enhancement of the SERS signal of the Raman reporter molecule and consequently the detection of the target analyte. Recently, this approach has also been incorporated into lateral flow assays to increase their sensitivity and enable quantitative detection.[131–136]

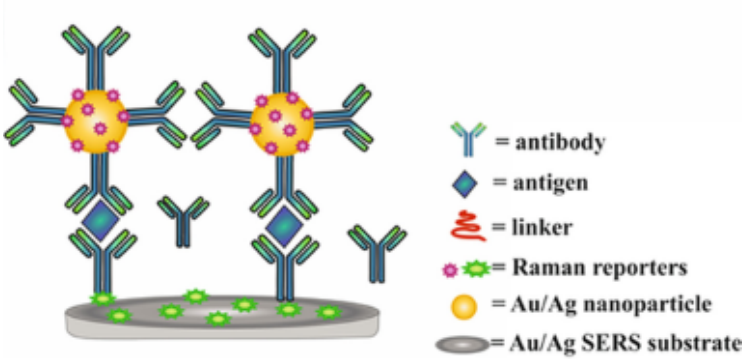

Figure 1.8: Schematic diagram showing the structure of a SERS sandwich immunoassay. Adapted from ref [130] under the terms of the CC BY 4.0 license.

1.4 Electrochemical surface-enhanced Raman spectroscopy

1.4.1 Principles of E-SERS

Electrochemical surface-enhanced Raman Spectroscopy (E-SERS) is a specific type of SERS which takes place within an electrochemical (EC) cell.[38,137] As with a conventional EC cell[138,139], the system contains a working, reference, and counter electrode and an electrolyte but in E-SERS, the working electrode is a nanostructured metal surface which can also be used for SERS measurements (Figure 1.9).[38,137] The counter electrode acts as a source/sink for the electrons involved in the reaction at the working electrode. The reference electrode is a half-cell with a known reduction potential that acts as the reference standard against which the potentials of the other electrodes in the cell can be measured. A potentiostat is used to control the potential of the working electrode.[38]

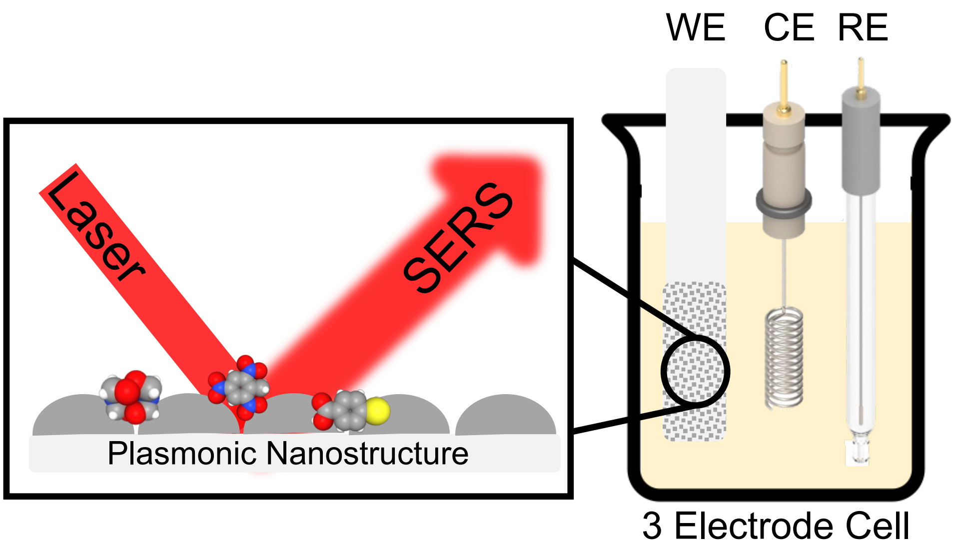

Figure 1.9: Schematic diagram of the E-SERS system. SERS spectra are recorded using a 3-electrode electrochemical cell containing a working (WE), reference (RE) and counter electrode (CE).

Initially, E-SERS was simply seen as a method of studying EC reactions in situ using Raman spectroscopy.[140] However, it was later found that applying a potential to the working electrode could actually enhance the SERS signal.[38,137] There are three main reasons for this enhancement.

The first relates to the electrochemical adsorption of analytes on the nanostructured surface. When a charged electrode is in contact with an electrolyte, an interfacial region, known as the EC double layer, will form between the surface and the bulk solution (Figure 1.10).[138] The nature of this double layer varies depending on the electrode potential. For example, if the electrode potential is more negative than the potential of zero charge, cations will be attracted to the surface and polar molecules such as water will interact with the electrode *via* their positively charged end.[38] The opposite is true for positive potentials. Consequently, the coverage, adsorption orientation and interaction strength of a target molecule at an electrode can be controlled using the potential.[38,141–143] This is significant because, as discussed in section 1.3, SERS is a surface-selective effect[40] and the magnitude of the SERS signal depends on the proximity of a molecule to the surface.[29] Therefore, increasing the adsorption of a target molecule on the surface will increase its SERS signal intensity.

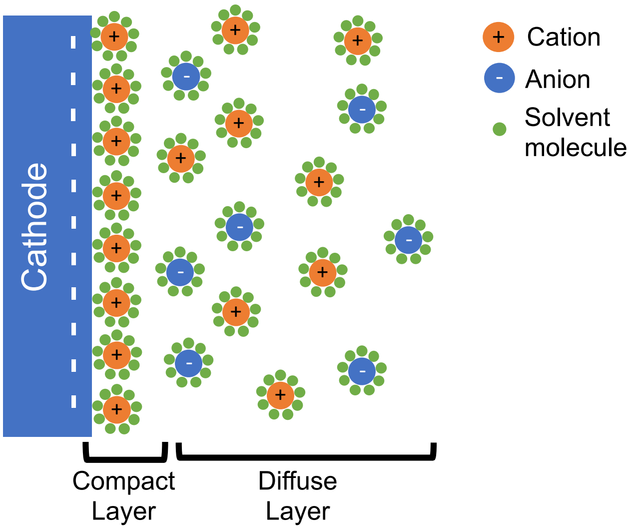

Figure 1.10: An illustration of an electrochemical double layer at a negatively charged surface. The cations and anions are represented with orange and blue spheres, respectively, and the green spheres represent the solvent molecules.

The second reason for the E-SERS enhancement relates to the electron density at the metal surface. Changing the potential of the electrode alters the surface charge density in the plasmonic nanostructure.[38] The surface charge density controls the frequency and amplitude of the surface plasmon resonance which, as discussed in section 1.3.2, is the reason for the electromagnetic SERS enhancement. When a negative potential is applied to the electrode, more electrons are injected into the SERS substrate, increasing the magnitude of the LSPR and consequently the magnitude of the SERS signal.

The third reason is linked to the Fermi level of the metal. The Fermi level determines the likelihood of photo-induced charge transfer between the electrode and the adsorbed molecules.[38] As discussed in section 1.3.3, charge transfer processes play an important part in the chemical enhancement of the SERS signal. Changing the potential of the electrode alters the Fermi level of the metal which can increase the probability of charge transfer between the electrode and the adsorbed molecules.[143,144] An increase in charge transfer processes can lead to an enhancement in the SERS signal.

The relative importance of these three phenomena depends on the system. The structure and composition of the electrode, the analyte, the electrolyte, and the environment all affect the E-SERS enhancement. Consequently, it can be difficult to establish the factors at play. Much of the research which has helped to illuminate this subject has been performed on very simple or well-studied analytes such as water and Rhodamine 6G.[145,146]

The interest in E-SERS is not simply due to the increased SERS signal. It is a powerful technique because it can be used to control which species adsorb onto the surface and how their SERS signal is enhanced. This could enable multiplexing through the detection of different molecules at different potentials. Therefore, enhancing the viability of using SERS to detect trace molecules in complex fluids.

1.4.2 Fabrication of E-SERS nanostructured electrodes

The nanostructured metal substrate is a critical part of the E-SERS system because it determines the magnitude of the Raman signal enhancement. Since the 1970s, there have been thousands of papers[147] on the fabrication of nanostructured substrates (NSS) for SERS which have been comprehensively reviewed.[28–30,40,148,149] On the other hand, NSS for E-SERS have been studied less extensively. The key requirements for E-SERS NSS are as follows:

- Plasmonic resonance in the visible/near-infrared range (~400–1000 nm).[29] Generally, this is the case when the real part of the dielectric function is negative (typically $-20 \leq \mathrm{Re}(\varepsilon) \leq -1$) and the imaginary part is small ($\mathrm{Im}(\varepsilon) \leq 5$).[29,30] Gold, silver and copper all fulfil these criteria.

- Electrochemical stability. This is why gold is a very popular NSS material.[30,40]

- Feature size that is less than ~100 nm.[29] Particularly large enhancement factors can be achieved when ‘hot spots’ are formed between two nanoparticles or at sharp edges or tips.[40]

- A regular structure that can be reproducibly fabricated to give consistent results.[40]

- Large surface area to allow many molecules to adsorb onto the surface at once.[29]

- Fast electron transfer kinetics.[139]

- Solid, conductive substrate to allow for incorporation into an electrochemical cell.

There are four main NSS fabrication methods which apply to E-SERS: electrochemical roughening, electrochemical deposition, nanosphere lithography and colloidal nanoparticle deposition. The following sections describe these fabrication methods and discuss their use in the literature. To quantify the performance of a substrate, the SERS enhancement factor or lowest concentration of an analyte detected is quoted. Although these are the typical metrics used to evaluate SERS nanostructures, they should be treated with caution.[29] The SERS enhancement factor is determined experimentally by measuring the intensity of the SERS signal for an absorbed molecule on the metal surface, relative to the intensity of the normal Raman signal of the same ‘free’ molecule in solution.[40] The two intensities must be normalised by the number of molecules either on the surface (SERS) or in the solution (conventional Raman).[40] Issues arise due to difficulties in calculating the number of molecules on the surface and the fact that some researchers calculate the enhancement factor based on signals produced at ‘hot spots’ on the metal surface rather than the average signal across the substrate.[29] This can make it difficult to compare work because papers often do not contain details of how the enhancement factor is calculated.

Comparing the lowest concentration of an analyte detected can also cause problems because some molecules are much better Raman scatterers than others.[29] For example, dye molecules such as rhodamine 6G, exhibit very large 'resonant Raman scattering', so being able to detect μM levels of these molecules is less significant than being able to detect the same concentrations of another non-resonant molecule. The most effective way to evaluate a novel nanostructured electrode is to perform SERS measurements for the new NSE and a traditional NSE in the same way, using the same analyte and equipment. This information is included if it is available in the articles being reviewed.

1.4.2.1 Electrochemically roughened electrodes

The first E-SERS measurements were performed using electrochemically roughened silver electrodes.[37] In this process, successive electrochemical oxidation and reduction cycles are used to create a nanostructured metal surface.[137,148] Initially, a positive potential is applied to the electrode to form soluble ions or an insoluble surface complex, then a negative potential is used to reduce these species, resulting in a randomly, roughened metal surface (Figure 1.11).[137] The established methods for electrochemically roughening gold, silver and platinum are described by Wu *et al*.[38] For gold electrodes, the procedure is as follows: First, the surface is cleaned electrochemically in 0.1 mol/L H_2SO_4 solution and rinsed with distilled water. The electrode is then placed in 0.1 mol/L KCl and held at -0.3V until the current is stable. Next, the potential is scanned to 1.2V at 1 V/s, set for 1.2 s to allow oxidation and then scanned back to -0.3V at 0.5 V/s and set for 30 s to allow reduction. The cycle is repeated for at least 15 minutes to produce a roughened surface.[38,150]

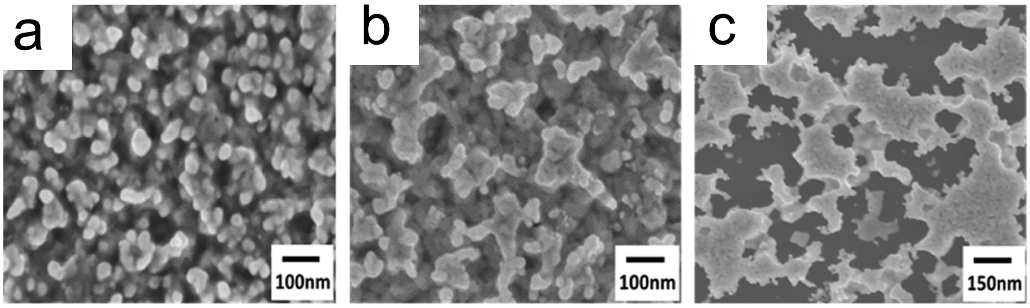

Figure 1.11: Scanning electron microscopy (SEM) images of electrochemically roughened Au films held at 1.2V in 0.1 M KCl for different numbers of cycles. (a) 3 cycles, (b) 5 cycles and (c) 12 cycles. Adapted from ref [151] with permission. Copyright 2020 Elsevier.

Despite their initial success, SERS research has moved away from electrochemically roughed electrodes since the early-2000s.[38] The structures are random and contain features from the angstrom to micron scale.[148] This means the SERS enhancement varies across the surface and between electrodes.[137] However, there are some recent examples of electrochemical roughening being used as a quick, easy, in-situ method of E-SERS substrate fabrication.[152–158] This approach is particularly suited to E-SERS because the same set-up can be used for surface preparation and analyte detection. In 2022, Moldovan *et al*. electrochemically roughened Au screen-printed electrodes and used them to quantitively detect the fungicide thiabendazole in spiked apple juice.[156]

1.4.2.2 Electrochemical deposition of plasmonic metal nanoparticles

Nanostructured electrodes can also be fabricated *via* electrochemical deposition (ED).[159–170] In this method, solid metal nanoparticles are deposited onto a working electrode from a solution of ions through the application of a negative potential.[171] The reduction of the metal ions can be represented by:

$$M^{z+}_{solution} + ze^{-} \rightarrow M_{(s)} \qquad \text{Equation 11}$$

Like electrochemical roughening, ED requires a three-electrode electrochemical cell and a potentiostat.[171] This makes it an attractive fabrication process for E-SERS because it uses much of the same equipment. It also has the potential to be quicker and easier than using colloidal nanoparticles because the NPs are deposited straight onto a rigid, conductive substrate, removing the need for drop-casting.

Dai and Compton first electrodeposited gold nanoparticles onto Indium Tin Oxide (ITO) in 2006.[167] They used 0.1 mM of $HAuCl_4$ in 0.5 M H_2SO_4 as their electrolyte and applied a potential step from +1.055V to -0.045V (vs. saturated calomel electrode) for a fixed time (15, 50, 150 or 300 s). Varying the experimental parameters revealed (unsurprisingly) that the particle size increased with $AuCl_4^-$ concentration and deposition time. They also found that for 0.1 mM $HAuCl_4$ applying 20 cycles of 15 s led to more monodisperse particles than a single potential step of 300 s (165 ± 30 nm vs. 154 ± 68 nm).[167]

Wang *et al*. refined Dai and Compton's method using a two-step approach (Figure 1.12).[160] First, they applied a potential step from +0.89V to -0.8V (vs. a saturated calomel electrode) to an ITO working electrode in a solution containing 0.1 mM $HAlCl_4$ and 0.1 M $NaClO_4$ for 10 s. This step triggers the formation of many small gold nanoparticles (mean diameter of 9 ± 2 nm). These NPs then act as seeds in the subsequent growth step due to the preferential reduction and deposition of $AuCl_4^-$ on existing gold particles. The NPs are grown in the same EC cell using cyclic voltammetry. The potential is scanned between +0.3V and -0.04V at 50 mV/s for a defined number of cycles. As the number of cycles increases, the size of the particles increases, and the density decreases. Importantly for SERS, the gap between the adjacent nanoparticles also decreases, resulting in the formation of 'hot spots'. 500 deposition cycles resulted in NPs with a mean diameter of 50 ± 9 nm and nanogap distances of less than 10 nm.[160] These particles are significantly smaller, more uniform and closer spaced than those made by Dai and Compton.[167] In some ways, electrochemical deposition can be seen as an extension of electrochemical roughening. The process and chemicals are slightly more complicated, but the nanostructures formed are significantly more uniform making it a very attractive fabrication method for E-SERS electrodes.

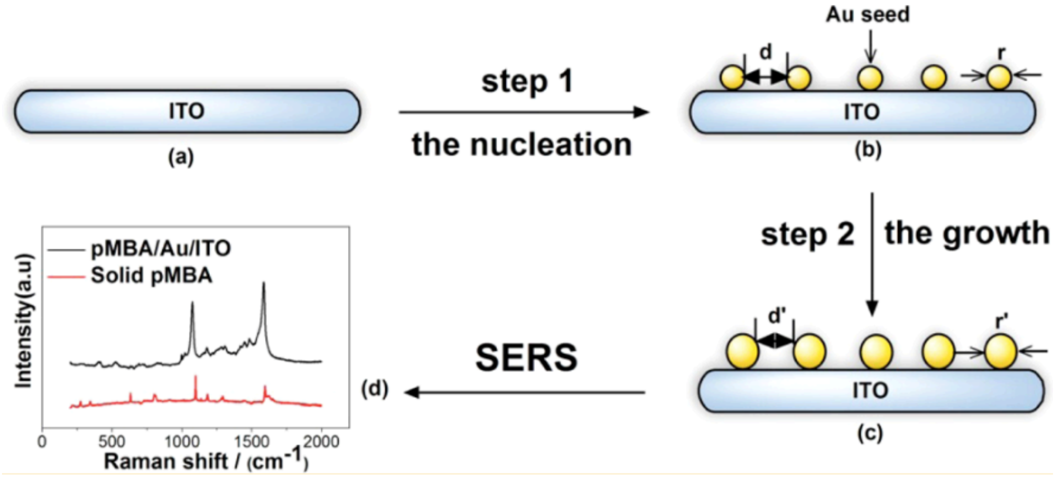

Figure 1.12: The two-step electrochemical deposition process used by Wang et al. to form gold nanoparticles on ITO. Reproduced from ref [160] with permission. Copyright 2013 American Chemical Society.

As discussed in section 1.3.2, anisotropic nanoparticles can display enhanced SERS signals due to 'hot spots' that form at edges or tips. The electrodeposited NPs discussed so far have all been spherical but there have been some attempts to ED non-spherical nanoparticles.[161,166,169,172–174] Flower-like nanostructures (Nanoflowers or NFs) can display high SERS enhancement factors due to the nanogaps that form between their 'petals'.[161]

Ye *et al*. electrodeposited gold NFs onto ITO from a solution of 2 mM $HAuCl_4$ and 0.1 M KNO_3 at a constant potential of -0.1V.[161] The ITO electrodes were coated with polydopamine (Pdop), a multifunctional biopolymer, which triggered the formation of Au NFs. The reason for the change in morphology is not completely clear but Ye *et al.* do show that the Pdop increases the nucleation rate of the gold nanoparticles.[161] They studied the SERS response of the nanostructures using Rhodamine 6G as a probe molecule and found that the Raman peaks were significantly larger for the nanoflowers than the nanoparticles.[161]

1.4.2.3 Nanostructured electrodes fabricated using template-based methods

As discussed in section 1.4.2.2, despite being able to regulate the size of electrochemically deposited nanoparticles, it is still difficult to control the spaces between them.[38] This leads to variation in the SERS enhancement because ‘hot spots’ formed at the gaps between NPs play a vital role in signal amplification.[40] Template-based methods can be used to create very ordered nanostructured electrodes with controlled inter-particle spacing.[38] The most popular template-based method in SERS research is nanosphere lithography (NSL) which was proposed by Hulteen and Van Duyne in 1995 (Figure 1.13).[175] First, monodisperse polystyrene or SiO_2 nanospheres with a chosen diameter are placed onto a substrate and allowed to self-assemble into a close-packed hexagonal array.[176,177] The substrate should be thoroughly cleaned, and, for E-SERS, it must also be conductive (e.g. ITO or metal coated glass).[38] Next, a thin layer (15 - 100 nm) of metal is deposited by physical vapour deposition on top of the spheres.[176] The nanospheres are then washed away leaving a uniform triangular nanoparticle array on the surface.

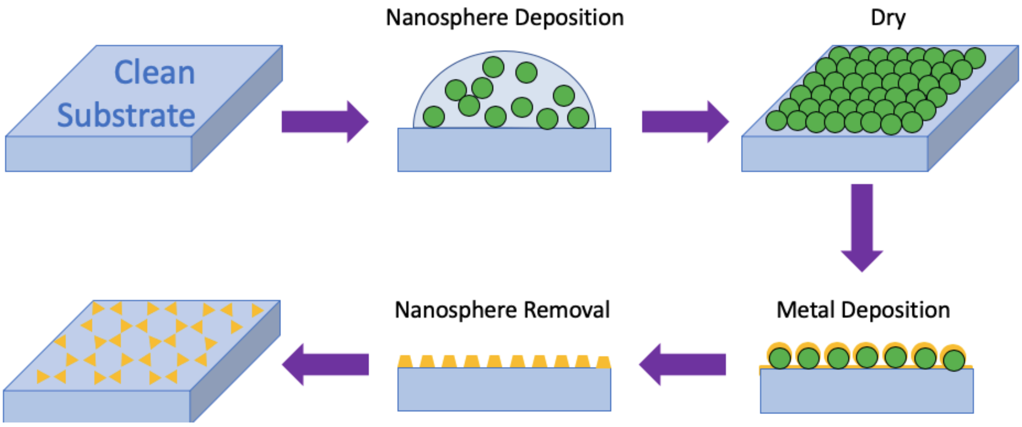

Figure 1.13: The nanosphere lithography fabrication process. Monodisperse nanospheres are deposited onto a substrate and allowed to self-assemble into a close-packed hexagonal array. Then, a thin layer of metal is deposited by physical vapour deposition on top of the spheres. The nanospheres are washed away leaving a uniform triangle nanoparticle array.

An alternative to using polystyrene or SiO_2 nanospheres as a template is nanoporous anodic aluminium oxide (AAO).[178,179] The low-cost electrochemical anodization of aluminium produces a self-organised alumina matrix with a close-packed array of hexagonally arranged cylindrical nanopores.[179] Depositing Au or Ag on top of the AAO results in a regular hexagonal nanostructure which can be used as an effective SERS substate.[178–181]

Van Duyne's group also developed another NSL method called 'film-over-nanosphere' (FON).[176,182–184] In this method, a thicker metal layer (~200 nm) is deposited on top of the polystyrene or SiO_2 nanospheres and, unlike traditional NSL, they are not removed. This results in a very uniform rough surface.[182] Zhang *et al*. used silver FON electrodes to perform E-SERS measurements of dipicolinic acid (DPA), an anthrax bacterial endospore marker.[184] They were able to detect 8 x 10^{-5} M of DPA in 5 minutes, which was a significant improvement on the results achieved using a traditional electrochemically roughened silver electrode.[184] In 2023, Falamas *et al*. successfully incorporated a AuFoN electrode into an E-SERS microfluidic device to detect the fungicide, thiabenzadole.[185]

Despite the many benefits of nanosphere lithography, the complexity of the process leads to several drawbacks. Physical vapour deposition requires expensive, specialist equipment and a significant amount of the deposited gold or silver is wasted when the nanospheres are washed away. The number of steps also makes the process quite time-consuming and costly.

In the early-2000s Bartlett and his colleagues developed a version of NSL which did not rely on expensive, specialist vapour deposition equipment.[186,187] The sphere segment void (SSV) method uses the same hexagonal arrangement of uniform nanospheres but instead of depositing a metal film on top of the spheres, the metal is electrodeposited onto the substrate between the nanospheres.[186,188] Removing the spheres results in a thin structured film containing a regular hexagonal array of uniform voids.[38,186] The size of the voids can be controlled by varying the thickness of the film. Figure 1.14 shows a copper/silver SSV surface fabricated using 1 μm diameter spheres.

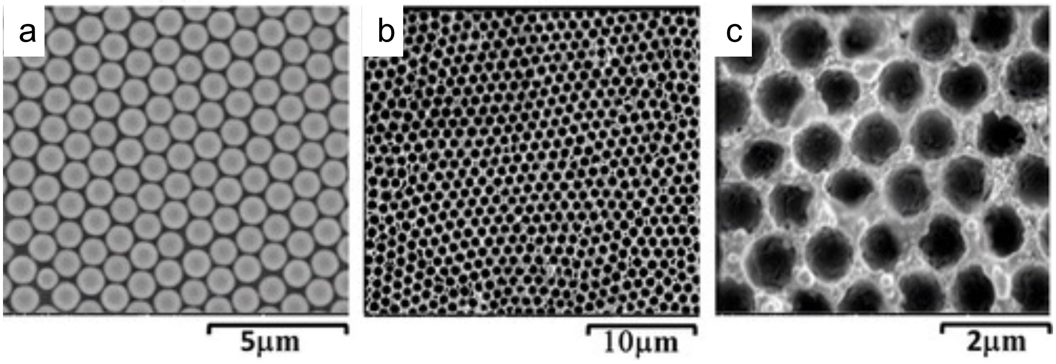

Figure 1.14: (a) SEM image of a polystyrene monolayer film used for the sphere segment void (SSV) method. (b) and (c) SEM images of the resulting Cu/Ag SSVs. Adapted from ref [189] with permission. Copyright 2019 American Chemical Society.

The sphere segment void method is an attractive electrode fabrication technique for E-SERS because it uses the same equipment needed for the electrochemical measurements. There have been a number of successful attempts to use SSV for E-SERS.[188,190–192] For example, Abdelsalam *et al.* fabricated SSV structured silver surfaces and used them to study the oxidation and reduction of a flavin analogue (isoalloxazine).[191] The SSV surfaces gave stable, reproducible surface enhancements at a range of electrode potentials and the spectra were sensitive to sub-femtomole quantities of immobilised flavin.[191] SSV is cheaper than conventional NSL because it does not require expensive vacuum chambers and less metal is wasted during fabrication. However, it is still a time-consuming multi-step process which could mean it is unsuitable for use in commercial sensors.

Electron beam lithography is another technique that can be used to create nanoparticles with precise sizes, shapes and spacings.[176,193] In this method, a substrate is coated with an electron sensitive polymer film (or resist) and then a focussed beam of electrons is used to draw custom shapes in the film.[194,195] The electron beam changes the solubility of the polymer allowing either the exposed or unexposed areas of the resist to be dissolved, resulting in a patterned mask. A metal film is then deposited on top of this mask and the polymer is washed away, leaving behind a nanostructured metal surface.[176,194] This method can create uniform nanostructures with dimensions below 10 nm but again, it is expensive and time-consuming.[194,196] The equipment required is even more expensive and specialist than that which is needed for NSL. As such, it is not practical to use this technique to fabricate low-cost substrates for healthcare applications, but it can be utilised in fundamental electrochemical research.[141,143,197]

1.4.2.4 Colloidal nanoparticles deposited on rigid substrates

Colloidal nanoparticles (NPs) synthesised *via* wet chemistry are a staple of SERS.[124,198–200] Gold NPs can be cheaply and reproducibly synthesised using techniques such as the Turkevich - Frens method.[198–200] In this method, tetracholoauric acid ($HAuCl_4$) is reduced by sodium citrate in water, with the citrate also acting as an electrostatic stabiliser.[198,199] By carefully controlling the nucleation and growth steps, nanoparticles with defined diameters between 10 – 200 nm ± 10% can be synthesised.[200]

Silver NPs can also be synthesised using a similar chemical reduction of silver nitrate ($AgNO_3$).[201] In this process, a reducing agent, such as trisodium citrate, sodium borohydride or ascorbic acid, provides electrons which reduce the silver ions (Ag^+) in the precursor to the metallic form (Ag^0).[202] Initially, there is rapid reduction which forms silver atoms, which immediately become dimers, trimers etc.[203] These initial clusters coalesce to form small particles (2-3 nm in radius). Then the reduction rate decreases, and the particles start to aggregate.[204] These particles then start to grow *via* Ostwald ripening, where larger particles grow at the expense of smaller ones.[205] This causes the average NP diameter to increase and the number of NPs to decrease. In citrate reduction, the final colloids are stabilised by the negatively charged citrate on the surface of the particles, which prevents them from aggregating. The colloidal Ag NP nucleation and growth steps are illustrated in Figure 1.15.

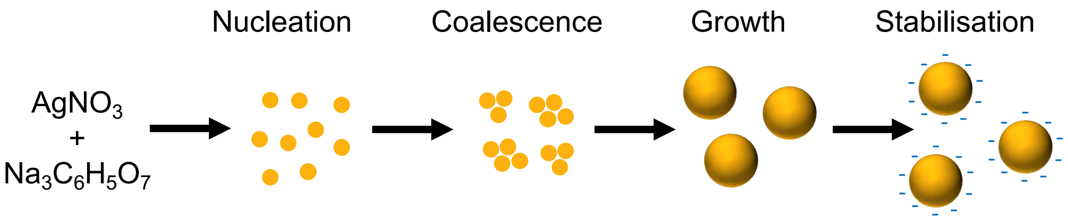

Figure 1.15: An illustration of the nucleation and growth steps in a citrate reduction synthesis of colloidal silver nanoparticles.

Colloidal NPs can be used in E-SERS by drop-casting or spin coating them onto a rigid conductive electrode (e.g. glassy carbon, ITO, or gold). Compared to electrochemically roughened electrodes, the surface features are much more uniform in size and the surface signal difference across the whole surface can be less than 10%.[38] This approach has been used successfully in a number of E-SERS sensors.[145,206–215]

The Brosseau group has pioneered the use of drop-cast colloidal NP substrates for E-SERS.[208,209,211–213,215–218] One of their early papers using this approach focused on the detection of uric acid in urine, an early indicator of preeclampsia in pregnant women.[208] They synthesised silver nanoparticles using a standard citrate reduction and then drop-cast them onto commercially available carbon screen printed electrodes. The electrode was placed into an electrochemical cell containing 1.0 mM of uric acid in urine simulant and the SERS signal was measured at potentials between 0 and -1V. The most intense uric acid peaks were observed at -0.8V vs. Ag/AgCl. At this potential, uric acid concentrations below 0.4 mM were easily identified.[208] Quantitative detection was not achieved in this work but two years later, they reported quantitative detection of uric acid at concentrations between 0.1 – 1 mM using a multi-layered Au/Ag nanoparticle electrode (Figure 1.16).[209] Although these detected concentrations are not particularly low compared to other SERS-based sensors, they are good enough to pass the threshold for a preeclampsia diagnostic test (0.4 mM of uric acid). This demonstrates that it is not always necessary to develop the most sensitive sensor possible but rather the most effective system for the application.

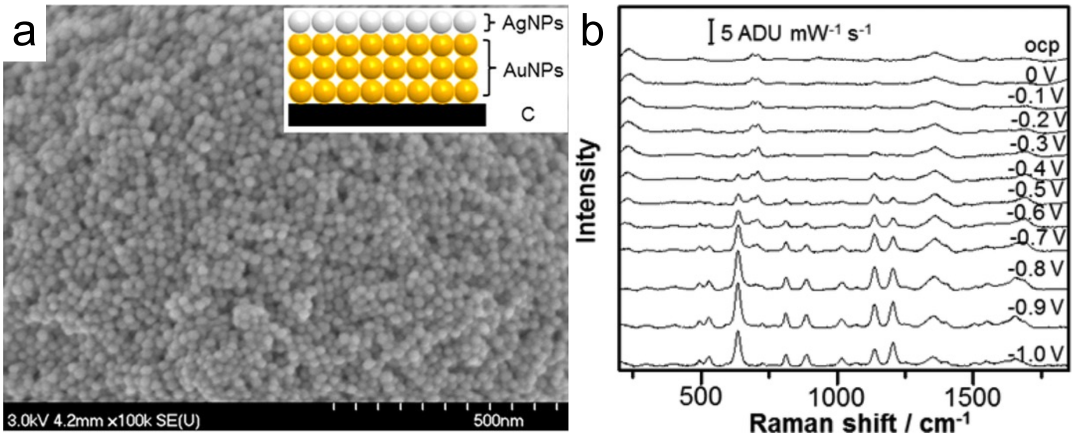

Figure 1.16: (a) SEM image of a multi-layered drop-cast Au/Ag nanoparticle electrode prepared on a screen-printed electrode by Zhao et al. Inset: schematic of the layered structure. (b) E-SERS spectra recorded using the multi-layer Au/Ag electrode for 0.5 mM uric acid in 0.1 M NaF supporting electrolyte. Adapted from ref [209] with permission. Copyright 2015 American Chemical Society.

Spherical NPs are highly reproducible and cost-effective but only have moderate signal enhancement due to their high symmetry.[28,51,219] More advanced NP shapes which amplify the Raman signal through hotspots at tips and edges are the focus of intense research.[28,40] There are now many papers and reviews which discuss different NPs for SERS including nanorods, nanocubes, nanostars and nanoflowers.[28,38,53–55,220] So far all of the published work on colloidal nanoparticles in E-SERS has used spherical NPs. However, given the attention anisotropic particles have received in SERS research, it seems likely that E-SERS will also start to investigate non-spherical NPs to enhance the Raman signal.

Core-shell nanoparticles have also attracted significant attention in SERS research.[221–224] Depending on the materials used, they can offer a range of benefits. For example, coating a plasmonic metal in a dielectric material can improve the stability and biocompatibility of the NPs[225,226] and coating an inexpensive carrier with a noble metal can reduce the cost of plasmonic NPs.[227] Core-shell nanoparticles are extremely versatile and changing the size, shape and components of the core and shell allows the properties of the NP to be tuned for a particular application.[221–223] Gold core – silver shell (Au@Ag) NPs are particularly interesting because they can exhibit larger SERS enhancements than monometallic Au or Ag NPs due to charge transfer processes which take place between the two metals.[209,228–232] Furthermore, coating Au NPs with Ag gives greater control of the size and shape of the NPs and can result in more uniform particles.[49,221,233,234] Au@Ag NPs have been used successfully for several SERS studies.[28,49,209,221,222,224,230–235] Work by Liu *et al*. demonstrated that the Raman enhancement of Au@Ag NPs to several sulphur-containing pesticides is ~2 orders of magnitude stronger than those of bare Au and Ag NPs.[230] Au@Ag NPs have not yet been used for E-SERS, but Zhao *et al.* have successfully used a multi-layered Au/Ag NP electrode to detect uric acid with E-SERS.[209]

The main problem with depositing colloidal nanoparticles on rigid substrates is the non-uniform distribution of the particles on the surface which limits the SERS enhancement.[38] Some methods have been developed to arrange the nanoparticles in a regular pattern.[28,236,237] Wang *et al.* produced highly ordered NP arrays with sub-10-nm gaps through the self-assembly of cetrimonium bromide (CTAB)-capped gold nanoparticles.[236] CTAB is a surfactant which forms a bilayer around the Au NP. This bilayer leads to a net positive charge on the NP surface which results in a repulsive force between the NPs that prevents aggregation. Empirical enhancement factors above 1×10^8 were observed for *p*-mercaptoaniline under near infrared (785 nm) excitation.[236] However, one of the issues with using CTAB-capped nanoparticles is that it is necessary to remove some of the surfactant molecules to allow the analyte of interest to reach the NP surface.[237] More recently, Smith and Lipkowski fabricated a reproducible 2D array of Au NPs by coating gold nanoparticles in SiO_2, arranging them on a gold substrate, dissolving the SiO_2 and then electrochemically cleaning the substrate.[237] This resulted in a monolayer of bare Au NPs with a regular spacing that was twice the SiO_2 shell thickness (4.2 ± 0.7 nm).[237]

1.4.2.5 Discussion of E-SERS nanostructured electrode fabrication methods

In section 1.4.2, the current most common E-SERS nanostructured electrode fabrication methods have been presented and discussed. The advantages and disadvantages of each method are summarised in Table 1.1. The assessment of these methods can be summarised very simply as: electrodes with large, repeatable SERS enhancements can be made but the processes are expensive, time-consuming and require specialist nanofabrication equipment; easier, quicker methods can also be used to create effective substrates, but they are much less uniform and reliable. Consequently, to determine the most effective fabrication method, one must consider the application. In the case of biomarker detection, the appropriate substrate depends on the molecule being detected and the concentrations present. If the biomarker is a very effective Raman scatterer or is present in high concentrations, an electrode with a lower SERS enhancement could still be part of a successful sensor. Conversely, if a biomarker is difficult to detect and only present at very low concentrations, large SERS signals are needed which would mean choosing a template-based fabrication method. It would also be necessary to consider the cost of the sensor in relation to its use case.

Table 1.1: Summary of the advantages and disadvantages of the different E-SERS electrode fabrication methods.

Method	**Advantages**	**Disadvantages**
Electrochemically roughening	- In-situ fabrication - Quick and simple - Cost-effective	- Irregular structure - Variable enhancement - Difficult to control
Electrochemical deposition	- In-situ fabrication - More control than electrochemical roughening - Cost-effective - No stabilizers on NP surface	- Harder to fabricate complex structures - Irregular spacing - Variable enhancement
Templated-based methods	- Regular structure - Control over shape and spacing - Reliable, large enhancements	- Requires specialist equipment - Multistep fabrication - Wasted material - Expensive
Colloidal nanoparticle deposition	- Quick and simple - Cost-effective - Well understood - Adaptable	- Irregular spacing - Variable enhancement - Stabilizers remain on NP surface

A key avenue for future research is to apply the most promising developments from SERS research to E-SERS electrode fabrication. The use of complex shaped nanostructures that have been engineered to maximise 'hot spots', such as nanotriangles, nanostars, and nanoflowers, have exhibited impressive enhancement factors in a range of SERS applications and employing these structures in E-SERS would likely offer improved detection limits.[28,38,53–55] Furthermore, in recent years, hybrid nanostructures which contain two or more different materials, such as core-shell nanoparticles, have received increased attention.[221–224] Depending on the materials used, they can offer a range of benefits. For example, coating a plasmonic metal in a dielectric material can improve the stability of the NPs[225,226] and coating an inexpensive carrier with a noble metal can reduce the cost of plasmonic NPs.[227] Additionally, certain hybrid particles, such as gold core-silver shell NPs and plasmonic metal-semiconductor NPs, can exhibit charge transfer between the two materials which can lead to boosted SERS enhancements.[49,209,228,230–232,60,57,69,238,229]

1.4.3 Analyte detection with E-SERS

Although E-SERS has not been studied as extensively as conventional SERS, the literature contains examples of it being used to identify a range of analytes. These include therapy drugs[183,213,217,239], biomarkers[153,188,191,208–210] and food contaminates[154,156,212]. Despite success detecting a variety of analytes, very few of these studies demonstrate quantitative detection. Reliable quantitative measurements rely on robust, repeatable nanostructured electrodes which can be difficult to fabricate. Issues also arise due to the complex nature of the E-SERS system, in particular, the important part surface adsorption plays in the detection of analytes. However, successful quantitative detection has been achieved. For example, Zaleski *et al.* reported the quantitative detection of dobutamine, a drug commonly administered after heart surgery, using an Au FON E-SERS substrate. They detected dobutamine at clinically relevant concentrations and pH range with a LoD of 300 nM and a linear range of 0.3 – 3000 μM. They also showed some preliminary results using a handheld Raman spectrometer in a clinical setting, although they did not demonstrate detection in synthetic or human bodily fluids. The E-SERS studies reported in the literature are summarised in Table 1.2 with details of the electrode fabrication method and, if quantitative analysis was performed, the limit of detection and detection range.

Table 1.2: Current state-of-the-art in E-SERS analyte detection reported in the literature.

Analyte	**Electrode fabrication method**	**Limit of Detection (μM)**	**Detection Range (μM)**	**Ref**
Thiabendazole (Fungicide)	Electrochemically roughened Au screen-printed electrodes	0.306	0.5 – 10	156
B vitamins	Electrochemically roughened Au screen-printed electrodes	-	-	154
Fentanyl	Electrochemically roughened Ag screen-printed electrodes	0.3	0.5 – 10	158
Atrazine (Herbicide)	Drop-cast colloidal Ag NPs	-	-	216
6-Thiouric acid (Therapeutic drug metabolite)	Drop-cast colloidal Ag NPs	-	-	217
Uric acid (Biomarker)	Drop-cast colloidal Ag NPs	-	-	208
Uric acid (Biomarker)	Drop-cast colloidal multilayer Au and Ag NPs	100	100 - 1000	209
Bacteria *(E. coli* K-12 and *B. megaterium)*	Drop-cast colloidal Ag NPs	-	-	211,240
Melamine (Milk contaminant)	Drop-cast colloidal Ag NPs	-	-	212
Polyphenolic dyes	Drop-cast colloidal Ag NPs	-	-	218
Levofloxacin (Antibiotic)	Ag NPs on cotton blend fabric	-	-	213
Aminoglutethimide (Therapeutic drug)	Ag NPs sputter coated onto screen printed electrodes	0.2	0.2 – 10	239
Uric acid (Biomarker)	Ag NPs sputter coated onto carbon	-	-	153

	and Au screen printed electrodes			
Dobutamine (Therapeutic drug)	Au ‘film over nanosphere’ electrodes	0.3	0.3 – 3000	241
Dipocolinic acid (Endospore marker)	Ag ‘film over nanosphere’ electrodes	-	-	184
Thiabenzadole (Fungicide)	Au ‘film over nanosphere’ electrodes	-	-	185
Amino acids (Tryptophan, Histidine, Phenylalanine, Serine, Alanine and Glycine)	Sphere segment void copper electrodes	-	-	188
Flavin	Sphere segment void silver electrodes	-	-	191
Uric acid	Polycarbonate nanocone array decorated with Au NPs	0.087	0.1 – 100	242

1.4.4 Other applications of E-SERS

E-SERS is not only an analytical sensing technique; but can also serve as a useful tool for characterisation.[243] It is particularly useful for studying electrocatalysis, an essential area in the transition towards renewable fuels. Electrocatalytic reactions take place right at the electrode surface and the intermediate species are usually present in monolayer or sub-monolayer amounts. This makes E-SERS, a technique which is highly surface selective and very sensitive, ideal for understanding these complex reactions. E-SERS studies have already contributed to the current understanding of the CO_2 reduction reaction.[243–248] It has been used to reveal the presence of dynamic CO intermediate during the electrochemical reduction of CO_2 on copper[248] and helped to understand the potential dependence of the local pH in a copper gas diffusion electrode undergoing CO_2 reduction.[246] In addition to the electrocatalysis studies, E-SERS has also been used to study lithium batteries and 2D materials.[249–252]

1.5 Advanced data analysis for SERS

SERS analysis normally relies on identifying a characteristic peak (or peaks) for a particular analyte, either through experimentation or modelling. To detect the analyte in an unknown sample, the SERS spectrum is studied to ascertain whether the characteristic peak is present. In conventional quantitative analysis, linear regression is then used to model the relationship between the concentration (or log(concentration)) of the analyte and the height of the characteristic peak. This can be effective when only one analyte is present. However, visual inspection becomes more difficult when studying a complex mixture that contains multiple analytes. The characteristic peak of one molecule can be obscured by a large peak of another and interactions between the analytes on the surface of the SERS substrate can also alter the signal.[253,254] Visual inspection can also be time consuming and relies on trained operators, which could limit the use of SERS in real world applications. Sophisticated data analysis techniques, often referred to as machine learning approaches, can be used to overcome these issues.

Machine learning (ML) for SERS analysis is growing rapidly[254–256] due to its ability to recognise subtle patterns in SERS datasets and identify the presence or concentration of analytes in unseen spectra. There are a wide range of different ML techniques, which can be described as either supervised (the input and output data is labelled) or unsupervised (the data is unlabelled or raw).[255] Supervised ML approaches are more commonly used to interpret SERS spectra.[254] The two techniques employed in this thesis, partial least squares regression (PLSR), and artificial neural networks (ANNs), are described below.

1.5.1 Partial least squares regression

Partial least squares regression (PLSR), also known as Projection of Latent Structures Regression, is a well-established multivariate regression technique related to principal component analysis (PCA).[257,258] It is a supervised machine learning approach which is particularly suited to noisy data that contains many collinear predictor variables and one or more response variables. This has led to its popularity in chemometrics, especially for quantitative spectral analysis.[257,259] In general terms, PLSR works by reducing the dimensionality of the predictor (X) variables by finding new latent variables which best describe the variation in the response (Y) variables.[258] The new variables are linear functions of those in the original dataset, with each variable successively increasing the total variance explained by the latent variables.

In PLSR, a dataset made up of *m* predictor variables, *p* response variables and *n* observations is split into a *m* x *n* **X** matrix and a *p* x *n* **Y** matrix (Figure 1.17).[258,259] In the case of the SERS data analysed in this thesis, there are *n* different spectra for solutions with known analyte concentrations. Each row of **X** contains the intensities of a SERS spectrum obtained at *m* different wavenumbers. **Y** contains the corresponding concentrations of the *p* analytes in each solution.[117,260]

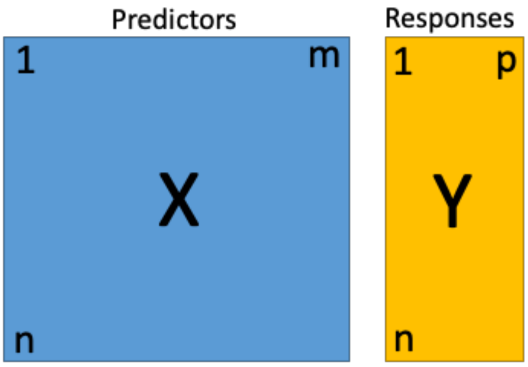

Figure 1.17: Illustration of the ***X*** *(predictor) and* ***Y*** *(response) matrices used in PLSR. m, p and n are the number of predictor variables, response variables and observations respectively.*

The **X** and **Y** matrices are decomposed according to:[257,258]

$$\boldsymbol{X} = \boldsymbol{T}\boldsymbol{P}^{\boldsymbol{t}} + \boldsymbol{E} \qquad \text{Equation 12}$$

$$\boldsymbol{Y} = \boldsymbol{U}\boldsymbol{Q}^{\boldsymbol{t}} + \boldsymbol{F} \qquad \text{Equation 13}$$

where $\mathbf{T}$ and $\mathbf{U}$ are the $\mathbf{X}$ and $\mathbf{Y}$ scores and $\mathbf{P}$ and $\mathbf{Q}$ are the $\mathbf{X}$ and $\mathbf{Y}$ loadings. $\mathbf{E}$ and $\mathbf{F}$ are the residuals. The decomposition is performed in a way that maximises the covariance of $\mathbf{T}$ and $\mathbf{U}$. The scores are related by:

$$\boldsymbol{U} = \boldsymbol{BT} \qquad \text{Equation 14}$$

where $\mathbf{B}$ is a matrix of the PLSR coefficients.

PLSR can also be explained graphically. Figure 1.18 shows a mean-centred dataset consisting of three predictor variables and three response variables (typically m >> p but this is difficult to visualise). Every observation is represented as one point in the X-space and another in the Y-space.[259,261]

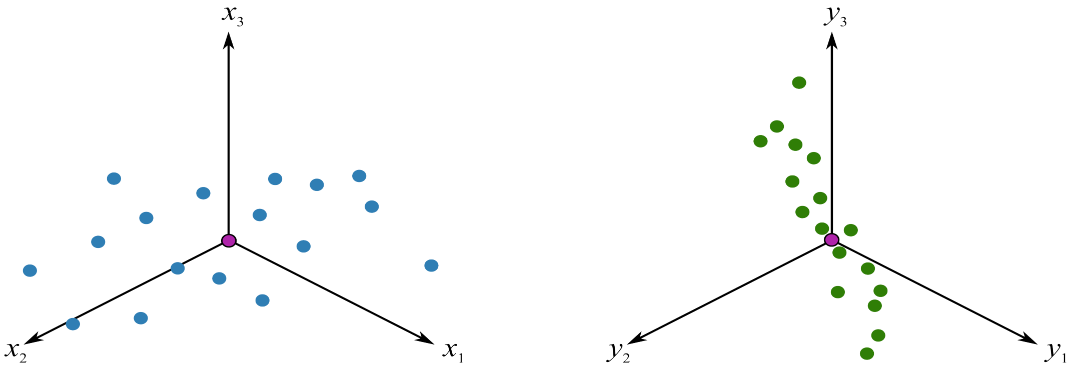

Figure 1.18: Example of a mean-centred dataset consisting of three predictor variables and three response variables. Image taken from ref [262] *under the terms of the CC BY 4.0 license.*

Latent variables, or principal components, are then found which best describe the variance in the dataset whilst also making sure there is a correlation between the X and Y components (Figure 1.19).[258,259,261] In the X-space, the second component is always orthogonal to the first, but this is not necessarily the case in the Y-space.[259] In this example, there are only two components and together they describe a plane. However, in cases where there are more predictor variables, more components may be necessary.

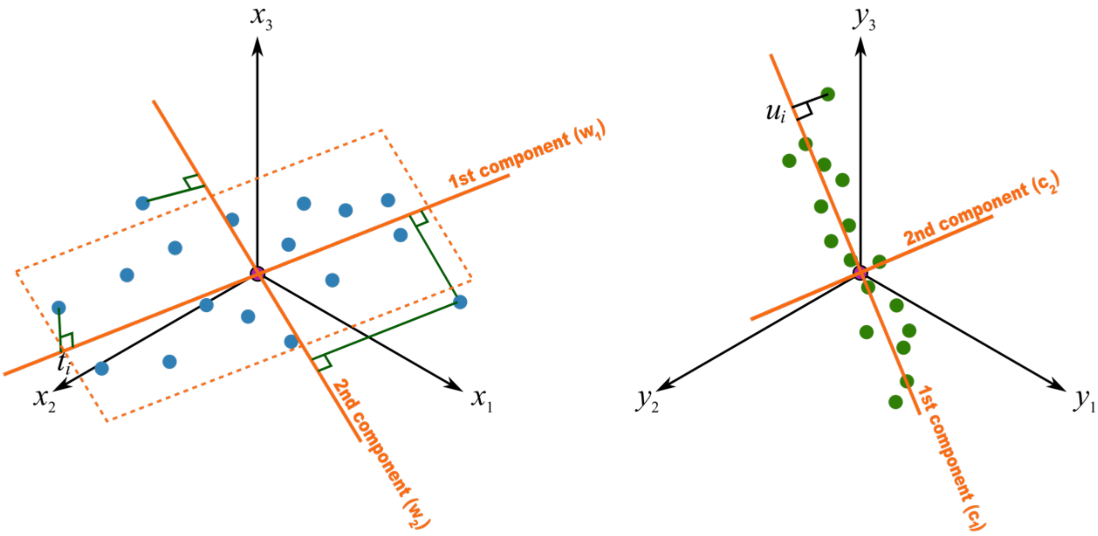

Figure 1.19: The first two PLS components projected in the X- and Y-spaces. Image taken from ref [262] under the terms of the CC BY 4.0 license.

Once the principal components have been found, PLSR can be used to predict the Y-values for a new set of X-values. This is achieved by simply converting the X-values into T-values, finding the corresponding U-values and then converting them into Y-values.[258,259]

1.5.2 Artificial neural networks

Artificial Neural Networks (ANNs) are computational systems inspired by the structure of biological brains.[263] Their ability to recognise patterns and classify data has led to their widespread use in recent years.[264] ANNs are made up of many connected nodes called artificial neurons (Figure 1.20).[260,263]

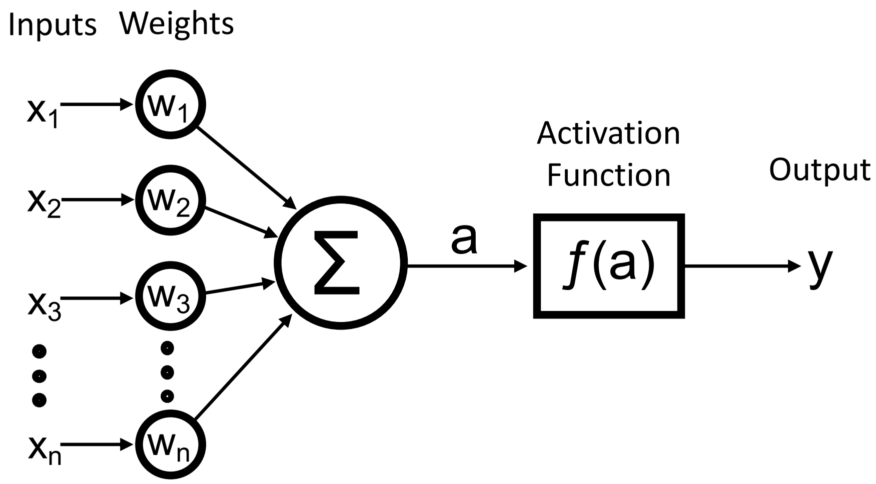

Figure 1.20: Basic structure of an artificial neuron. A weighted sum is calculated from all the inputs (x) and then a non-linear activation function is applied to the weighted sum to generate the output value (y).

As shown in Figure 1.20, an artificial neuron takes in multiple inputs and computes a single output value. First, a weighted sum (a) is calculated of all the inputs and then a non-linear activation function is applied to the weighted sum to generate the output value (y).[255,260] This can be expressed mathematically as:

$$a = \sum x_j w_j \qquad \text{Equation 15}$$

$$y = f(a) = f\left(\sum x_j w_j\right) \qquad \text{Equation 16}$$

Artificial neural networks are built by connecting these neurons into larger networks (Figure 1.21). Multilayer perceptrons (MLPs) are one of the simplest and most popular classes of feed-forward ANNs.[263] MLPs consist of at least three layers of nodes – an input layer, one or more hidden layers and an output layer.[117,263]

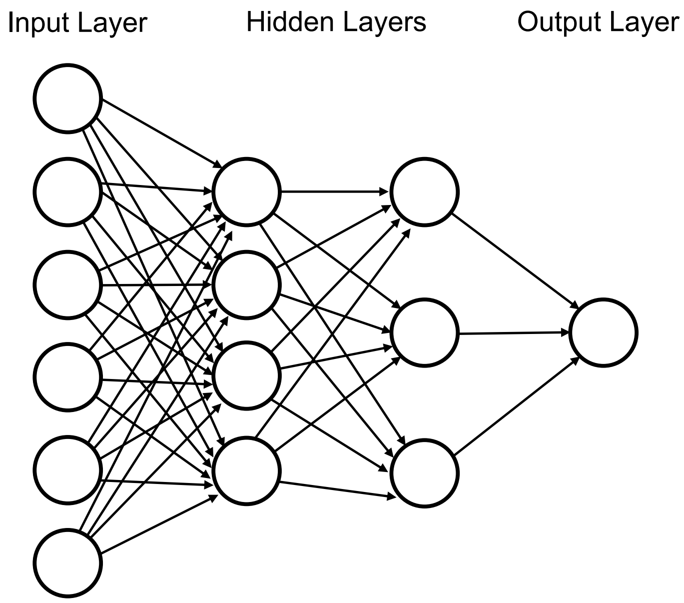

Figure 1.21: A schematic representation of a multilayer perceptron with two hidden layers.

Each circle in Figure 1.21 represents an artificial neuron and each line signifies a weight. Since multilayer perceptrons are fully connected, each node in one layer connects with every node in the following layer.[255] The power of ANNs comes from their ability to learn. Initially, the connections between nodes are assigned random weights.[117] When the network is presented with a training dataset, back-propagation is used to iteratively adjust the weights to reduce the difference between the output results and the actual results.[117,255,263] This process is repeated until the error is below an acceptable level. The resulting trained network can then be used to determine the output for a new unseen input dataset.

1.5.3 Application of machine learning in SERS analysis

The development of powerful and accessible machine learning libraries in recent years has enabled researchers to start utilizing ML techniques for SERS data analysis.[255]. In the relatively short time (< 15 years) since researchers started combining ML and SERS, there has been rapid progress and machine learning has now been used to classify or quantify biomarkers[49,117,265–267], bacteria[268,269], and food products[48,270–272]

In 2015, Kasera *et al.* used gold nanoparticles and CB[7] to record SERS spectra of solutions containing three different neurotransmitters: dopamine, epinephrine and serotonin.[117] The training dataset consisted of triplicate measurements of 30 different aqueous mixtures and the concentration of the analytes varied between 0.5 – 10 μM. They used a three-layer (one hidden layer) feed-forward ANN to detect the presence or absence of the neurotransmitters in the solutions. For 8 unseen samples (3 analytes x 8 samples = 24 predictions), 22 predictions were correct while 2 were false positives. PLSR was then used to predict the concentrations of the analytes present. The predicted concentrations were within ± 0.6 μM of the true concentrations of the analytes in the test dataset.[117]

Also in 2015, Alharbi *et al.* measured the SERS spectra of caffeine and its metabolites, theobromine and paraxanthine, on silver nanoparticles.[273] The solutions had analyte concentrations between 10^{-5} and 10^{-7} mol/dm^3 and an ANN with 1024 input nodes (the number of wavenumber shifts recorded), 20 nodes in a single hidden layer and 3 output nodes (the concentrations of the three analytes). The root mean square error of prediction was 1.32×10^{-6} mol/dm^3 for caffeine, 1.31×10^{-6} mol/dm^3 for theobromine and 1.06×10^{-6} mol/dm^3 for paraxanthine.[273] The same approach was also used by this group to successfully predict the concentrations of nicotine and its metabolites.[274]

After these early successes, recent work has employed more advanced ML algorithms such as convolution neural networks (CNNs) and very large datasets. Increasing the size of the training dataset significantly increases the robustness of ML models. In 2019, the Dionne group reported the use of a CNN to identify the antibiotic treatment needed for spectra of bacterial pathogens.[268] They constructed a reference dataset of 60,000 spectra from 30 bacterial and yeast isolates and 12,000 spectra from clinical patient isolates. The model was validated on clinical isolates from 50 patients and achieved a treatment identification accuracy of 99.7%.In 2022, Xie *et al.* classified serum exosomes for breast cancer diagnosis with an ANN trained on 8265 spectra from lab-derived samples.[265] A classification accuracy of 100% was achieved for the test dataset which contained spectra from patient-derived samples. This is a significant result as it shows how ML can enable the adoption of SERS in clinical settings.

1.6 Research hypotheses and objectives

This research aims to enrich SERS using electrochemistry, machine learning and hybrid nanomaterials, and exploit these enhancements to achieve quantitative detection of multiple trace analytes. Based on the literature review, the following research hypotheses and objectives were established:

- Robust, reliable substrates with significant SERS enhancements are essential for an effective E-SERS system. Given the intended application for these substrates, the fabrication method should also be simple and cost-effective. After studying the literature, drop-casting colloidal nanoparticles onto conductive glass electrodes was identified as one of the most promising approaches. This work aims to fabricate these substrates and determine their enhancement, robustness, and reliability. If issues are identified with the drop-cast NP electrodes, research will be undertaken to improve their performance and suitability for multiplexed quantitative detection.

- Extensive research has been conducted into the E-SERS nanostructured electrodes. However, it is equally important to look at ways to improve the E-SERS system as a whole to increase its sensitivity, selectivity, and reliability. This study aims to explore such improvements by investigating ways to mitigate reliability issues using internal standards.

- E-SERS research has demonstrated the improved sensing of a range of analytes but there are only a few published reports of quantitative detection and, to our knowledge, no examples of multiplexed detection. However, the selective enhancement offered by the applied potential means E-SERS is well-suited to this challenge. Therefore, a key aim of this work is to develop an E-SERS system for the reliable, quantitative, multiplexed detection of biomarkers.

- Quantitative, multiplexed detection with SERS remains a challenge due to the complex nature of the spectra, particularly the overlapping of peaks from different analytes, and the non-linear concentration-dependence of the signals due to the competitive adsorption of the analytes on the SERS substrate. Machine learning techniques can help identify subtle patterns in the spectra and enable the full utilisation of all the peaks. ML has been successfully used for SERS analysis but has yet to be applied to quantitative E-SERS. However, it is a promising approach as the applied potential offers an additional dimension for the ML analysis, enabling greater differentiation between the spectra recorded from complex multiplexed solutions. This work aims to apply machine learning approaches to E-SERS data to improve quantification, reliability, and interpretability.

- When considering the detection of biomarkers, it is important to test the performance of the sensing system in representative media as the plethora of analytes present in complex media can significantly dampen the SERS signal. Therefore, detection in synthetic bodily fluids will be investigated to assess the practicality of these techniques.

- Hybrid semiconductor-plasmonic metal nanostructures have exhibited significant SERS enhancement and recently, our group demonstrated PIERS-type enhancement without UV-activation using colloidal SnO_2-coated gold nanotriangles that are intrinsically rich in oxygen vacancies. Building on this work, solid electrodes will be fabricated using colloidal SnO_2-coated plasmonic NPs to see if similar enhancements can be observed in this format.

- There are still questions over the exact mechanisms behind the enhancements seen in some hybrid semiconductor-plasmonic metal nanostructures. Therefore, extensive characterisation of the SERS response of the drop-cast colloidal SnO_2-plasmonic metal NP substrates with be carried out to investigate this further.

- If significant enhancements are observed for the hybrid semiconductor-plasmonic metal NP system, attempts will be made to utilise this enhancement for the detection of lower concentrations of biomarkers and other trace analytes.

1.7 Thesis structure

This thesis documents my work developing E-SERS and hybrid SERS systems for the detection of biomarkers. Chapter 2 details the materials and methods used in this thesis. The protocols for the synthesis of a variety of colloidal nanoparticles are described, along with the method used to fabricate drop-cast SERS substrates. The characterisation techniques are then explained, followed by a detailed description of the E-SERS and SERS measurement procedures. Finally, the processes used for the SERS data analysis are detailed.

Chapter 3 describes the development of an E-SERS system for the detection of two important biomarkers, uric acid (UA) and creatinine (CRN). E-SERS substrates are fabricated by drop-casting Ag NPs onto conductive FTO-coated glass electrodes. These substrates are used to record E-SERS spectra of the target analyte and the way in which the applied potential enhances the Raman signal is studied. The robustness and reliability of the Ag NP electrodes are assessed, and strategies are developed to improve their performance. The quantitative detection of clinically relevant concentrations of UA and CRN is then demonstrated using the optimised E-SERS system.

Chapter 4 builds on the research detailed in Chapter 3 and uses the optimised E-SERS system for the quantitative, multiplexed detection of UA and CRN. A large E-SERS dataset (> 2300 E-SERS spectra) is recorded for solutions containing various concentrations of UA and CRN. Machine learning approaches are then applied to interpret the spectra and predict the analyte concentrations from unseen spectra. Finally, proof-of-concept experiments are performed in dilute synthetic urine to demonstrate the detection of clinically relevant concentrations of UA and CRN.

Chapter 5 focuses on a hybrid SERS system fabricated using tin dioxide coated silver nanoparticles (Ag@SnO_2 NPs). An unexpected, time-dependent increase in the SERS signal is observed when the Ag@SnO_2 NP substrates are irradiated with a 633 nm laser. This enhancement is characterised, and extensive testing is performed to determine the mechanism behind the enhancement. Potential applications of the Ag@SnO_2 NP system are then investigated. These include the quantitative detection of uric acid, the indirect detection of the ketosis biomarker, 3-hydroxybutanoic acid, and the quantitative detection of ketamine in synthetic saliva.

Finally, Chapter 6 summarizes the thesis, presents the key outcomes, and discusses potential future work. Additional experimental data is given in the Appendix.

Chapter 2 Materials and methods

2.1 Materials

Silver nitrate ($AgNO_3$), sodium citrate ($Na_3C_6H_5O_7$), uric acid ($C_5H_4N_4O_3$), creatinine ($C_4H_7N_3O$), (3-aminopropyl)triethoxysilane (APTES) ($C_9H_{23}NO_3Si$), urea (CH_4N_2O), potassium chloride (KCl), albumin from human serum, 4-mercaptobenzoic acid ($C_7H_6O_2S$), adenine ($C_5H_5N_5$), 2,4-dinitrotoluene ($C_7H_6N_2O_4$), 3-hydroxybutyric acid ($CH_3CH(OH)CH_2COOH$), ketamine hydrochloride ($C_{13}H_{17}Cl_2NO$), tetraethyl orthosilicate (TEOS) ($SiC_8H_{20}O_4$), acetic acid (CH_3COOH), calcium chloride ($CaCl_2$), citric acid ($C_6H_8O_7$), ethanol (C_2H_6O), and acetone (C_3H_6O) were all purchased from Sigma-Aldrich/Merck.

Sodium hydroxide (NaOH), ammonia solution (NH_4OH), and 4-mercaptopyridine (C_5H_5NS) were purchased from Fisher Scientific. Sodium fluoride (NaF) and rhodamine 6G ($C_{28}H_{31}N_2O_3Cl$) were purchased from ARCOS Organics. Sodium stannate trihydrate ($Na_2SnO_3{\cdot}3H_2O$), methyl viologen dichloride ($C_{12}H_{14}Cl_2N_2$), potassium dihydrogen phosphate (KH_2PO_4), and sodium chloride (NaCl) were purchased from Fluorochem, Aladdin, Alfa Aesar, and VWR Chemical respectively. The fluorine doped tin oxide (FTO) coated glass slides were purchased from Sigma-Aldrich. All chemicals were used as received, and Milli-Q water (18.2 MΩ at 25°C) was used in all experiments.

2.2 Nanoparticle synthesis

2.2.1 Synthesis of Ag NPs

To synthesise the silver nanoparticles, a standard citrate reduction was used following the Lee and Meisel method (Figure 2.1).[201] 36 mg of silver nitrate ($AgNO_3$) was dissolved in 200 ml H_2O and brought to the boil in a round-bottomed flask whilst stirring. Once boiling, 4 ml of a 1% sodium citrate ($Na_3C_6H_5O_7$) solution was added to the silver nitrate solution dropwise. Heating and stirring were maintained for an hour. A colour change from colourless to milky green/grey was observed which indicated successful nanoparticle formation. Once cool, the flask was wrapped in foil to prevent light degradation of the colloid solution.

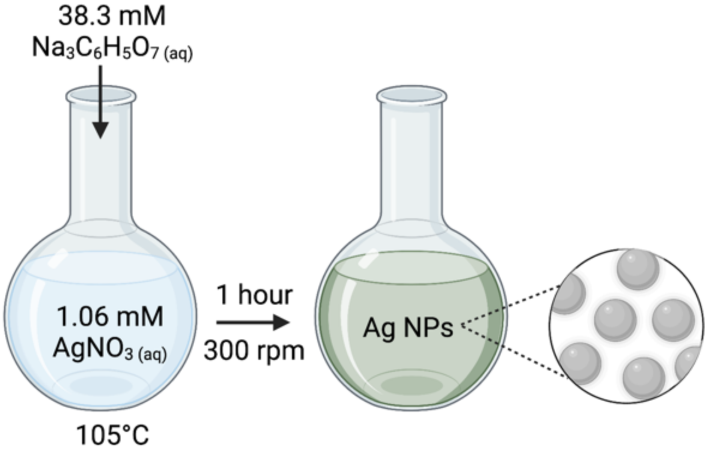

Figure 2.1: Illustration of the standard citrate reduction used to synthesise the Ag NPs using the Lee and Meisel method.[201] Created with BioRender.com.

2.2.2 Synthesis of Ag@SnO_2 NPs

Ag NPs were synthesised using the method described in section 2.2.1 and then coated with SnO_2 using a modified version of the precipitation method described by Oldfield *et al.* (Figure 2.2).[275] The pH of 10 ml of the as-prepared colloidal Ag NPs was adjusted to 10.5 by adding approximately 20 μL of 1 M sodium hydroxide (NaOH), monitored using a Mettler Toledo FiveEasy pH meter. 2 ml of 4 mM sodium stannate trihydrate ($Na_2SnO_3{\cdot}3H_2O$) was added at 20°C and the solution was mixed for 5 minutes in a thermomixer at 300 rpm and then heated to 60°C. The solution was held at this temperature under rapid mixing (800 rpm) for 1 hour. The coating process was repeated once more to form a thicker coating of SnO_2 (from ~5 nm to ~15 nm) using the as-synthesised single-coated NPs. The Ag@SnO_2 NPs were not purified further *via* repeat centrifugation and were used as-synthesised.

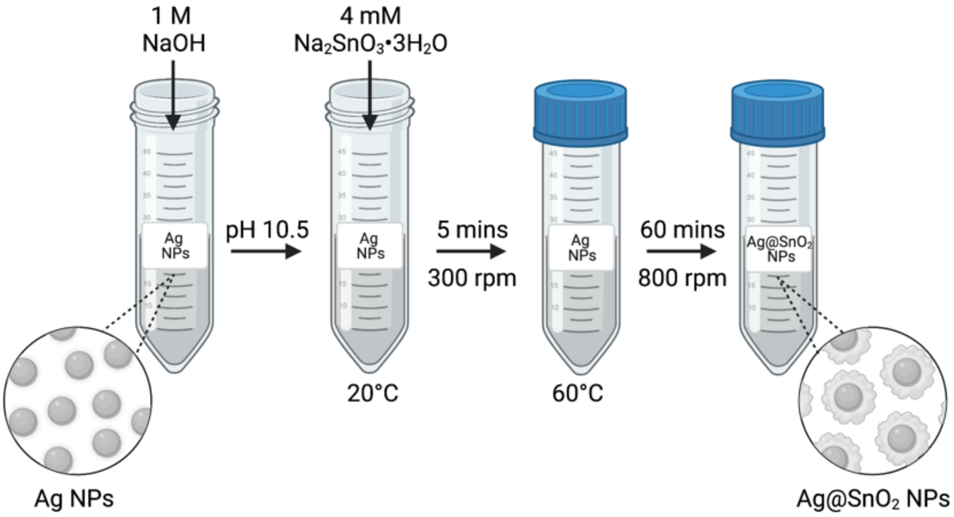

Figure 2.2: Illustration of the precipitation method used to synthesise the tin dioxide coated silver nanoparticles ($Ag@SnO_2$). Created with BioRender.com.

2.2.3 Synthesis of SnO_2 NPs

To synthesise the SnO_2 NPs, the pH of 10 ml of an aqueous 2 mM sodium citrate solution was adjusted to 10.5 by adding approximately 30 μL of 0.1 M sodium hydroxide (NaOH), monitored using a Mettler Toledo FiveEasy pH meter (Figure 2.3). 2 ml of 4 mM sodium stannate trihydrate ($Na_2SnO_3 \cdot 3H_2O$) was added at 20°C and the solution was mixed for 5 minutes in a thermomixer at 600 rpm and then heated to 60°C. The solution was held at this temperature under rapid mixing (800 rpm) for 1 hour. The solution was then left to cool to 20°C before adding another 2 ml of 4 mM sodium stannate and repeating the heating process.

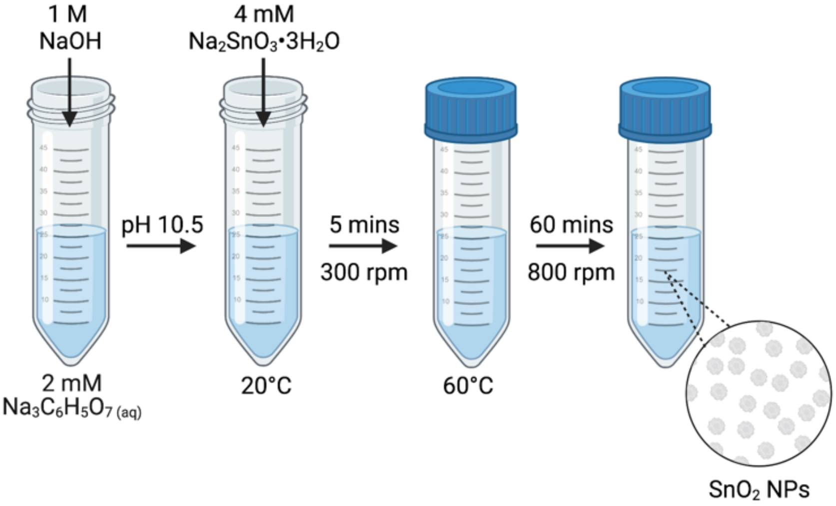

Figure 2.3: Illustration of the synthesis of SnO_2 NPs. Created with BioRender.com.

2.2.4 Synthesis of Ag@SiO_2 NPs

Ag NPs were synthesised using the method described in section 2.2.1 and then coated with SiO_2 using a modified version of the Stöber process described by Bai *et al.* (Figure 2.4).[276,277] 1.2 ml of the as-synthesized Ag NPs were mixed with 40 ml of absolute ethanol (C_2H_6O), 0.6 ml of 25 wt% ammonia hydroxide (NH_4OH) and 3.75 ml water (H_2O). 4 μL of tetraethylorthosilicate (TEOS) ($SiC_8H_{20}O_4$) was added to the solution, which was then stirred at room temperature for 12 hours. Multiple batches were prepared to produce the desired volume of NPs. The as-synthesised Ag@SiO_2 NPs were centrifuged at 12,000 rpm for 10 minutes, and the supernatant was removed and replaced with ethanol. The solution was then centrifuged again at 12,000 rpm for 10 minutes, but the supernatant was replaced with water. This was repeated once more before redispersing the NPs in water.

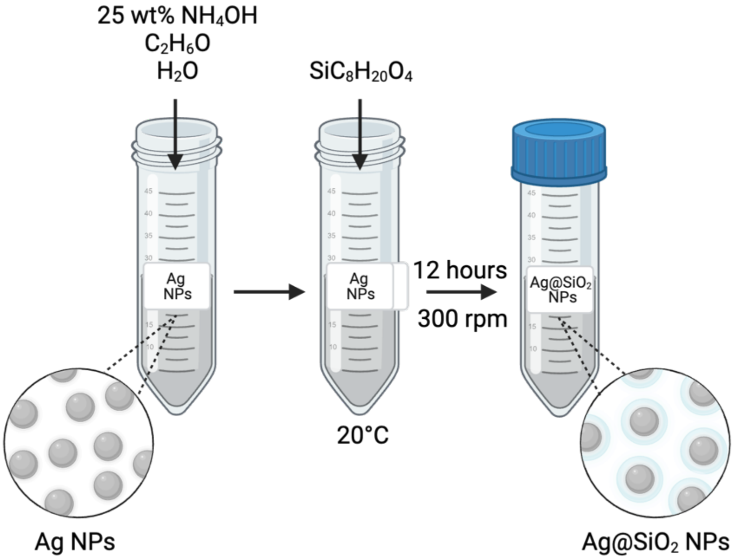

Figure 2.4: Illustration of the modified Stöber process used to coat the Ag NPs with SiO_2. Created with BioRender.com.

2.3 Fabrication of SERS substrates

2.3.1 Fabrication of drop-cast SERS substrates

To fabricate solid SERS substrates from NPs, colloidal NP solution was concentrated and then drop-cast onto glass slides (Figure 2.5). For the E-SERS experiments, conductive FTO-coated glass slides were used. FTO was chosen as it is electrochemically stable over the potential range of interest.[278] The transparency of FTO was thought to be necessary in initial designs of the E-SERS system, however in its current configuration a non-transparent substrate would also be effective. To make the drop-cast SERS substrates, 1 ml aliquots of the as-synthesised NP solution were added to 1.5 ml Eppendorf tubes and each tube was centrifuged at 3600 rpm for 15 minutes. The supernatant was then removed and discarded, and another aliquot of the colloidal solution was added. This was repeated 10 times. After the solution was centrifuged for the 10th time, almost all the supernatant was removed, leaving ~0.03 ml of concentrated NP solution. The concentrated NP solution was drop-cast onto a glass slide or APTES-coated FTO-coated glass electrode in three 10 μL aliquots. The substrate was then left to dry overnight prior to use.

In the case of the SnO_2 NP substrates, the same process was used, except the centrifugation speed was increased to 12,000 rpm to account for the smaller size of the SnO_2 NPs. For the Ag + SnO_2 substrates, 10 ml of Ag NP solution and 10 ml of SnO_2 NP solution were mixed and then all 20 ml of the mixture was centrifuged at the higher speed to fabricate the substrate.

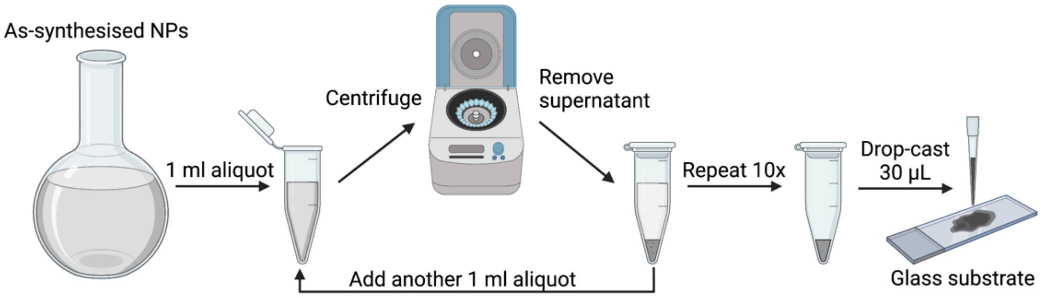

Figure 2.5: Schematic diagram showing the fabrication process of the drop-cast SERS substrates. Colloidal NPs are synthesised and then concentrated using centrifugation. The concentrated NP solution is drop-cast onto glass substrates. Created with BioRender.com.

2.3.2 Preparation of APTES-coated FTO-coated glass

To improve the adhesion of the NP film to the conductive glass electrodes for E-SERS, a (3-Aminopropyl)triethoxysilane (APTES) coating was applied to FTO-coated glass electoughed electrodes rodes. The FTO-coated glass electrodes were washed with soapy water and then ultrasonically cleaned for 20 minutes using ethanol, acetone, and Milli-Q water consecutively. The electrodes were then dried using a gentle stream of nitrogen gas. A 95% ethanol-5% water solution was prepared, and the pH was adjusted to 4.5 – 5.5 with approximately 10 μL 1 M acetic acid. APTES was added whilst stirring to give a 2% final concentration. The solution was then left for at least 5 minutes. The FTO-coated glass electrodes were dipped into the solution for 2 minutes and agitated gently. The electrodes were then dipped briefly in ethanol to remove excess APTES and left at room temperature overnight to cure the APTES layer.

2.4 Preparation of synthetic bodily fluids

2.4.1 Preparation of synthetic urine

Synthetic urine (SU) which did not contain uric acid or creatinine was prepared according to the literature with modifications.[279,280] For 200 ml of SU, 2 g of urea, 1.04 g of NaCl, 0.9 g of KCl, 0.96 g of NaH_2PO_4, 0.08 g of citric acid, and 10 mg of albumin were dissolved in 200 ml of deionized water.

2.4.2 Preparation of simulated salivary fluid

Simulated salivary fluid (also known as synthetic saliva) was prepared according to the literature with modifications.[281] For 200 ml of synthetic saliva, 325 mg of KH_2PO_4, 470 mg of NaCl and 33 mg of $CaCl_2$ were dissolved in 200 ml of water. The pH of the solution was then adjusted to 7.4 with 1M NaOH.

2.5 Characterisation methods

2.5.1 Ultraviolet-visible spectroscopy

Ultraviolet-visible (UV-vis) spectroscopy measures the amount of light absorbed by a sample at specific wavelengths in the UV and visible regions of the spectrum. Light is absorbed due to electrons in the sample being excited from the ground state to a higher energy state.[282] The amount of light which passes through the sample is detected and the absorbance at each wavelength is calculated and plotted. This technique can be used to determine the size, shape, composition, and LSPR of metal nanoparticles.[283]

The absorption spectrum for a plasmonic metal nanoparticle is typically a bell-shaped curve with a peak at the LSPR wavelength of the NP. The position of the peak can be used to determine the size of the nanoparticles through comparison with literature values or spectra from reference samples. The width of the peak can indicate the degree of polydispersity in a colloidal NP sample. NP aggregation can be identified through the observation of red-shifted and broadened peaks and sometimes an additional peak at higher wavelengths can appear.

In this work, UV-vis spectra were acquired using a DH-mini Ocean Optics light source and a Flame S UV-vis ES Ocean Optics spectrometer. Milli-Q water was used to store the reference and background spectra. The colloidal NP solutions were transferred into a 1 cm optical path length cuvette and placed in the spectrometer for measurement. A 10 ms integration time was used, with 300 scans to average, and a boxcar width of 3. The absorbance spectra were collected in a wavelength range of 180 - 880 nm.

2.5.2 Scanning electron microscopy

Scanning electron microscopy (SEM) is a type of electron microscopy where a focused beam of electrons is rastered across the surface of a material. The electrons interact with the atoms in the sample causing the emission of various electron and photons, including secondary electrons, backscattered electrons, and characteristic X-rays. Secondary electrons are low energy (<50 eV) electrons which are ejected from the atoms in the sample due to inelastic scattering from the primary electrons.[284] They can be detected to create a detailed topographic image of the surface and so are used in this work to study the morphology of the nanoparticle films.

Images of the NP films were obtained using a JEOL JSM 6701 FEG-SEM at an accelerating voltage of 10 kV. The samples were coated with gold for 10 seconds using an Agar sputter coater.

2.5.3 Transmission electron microscopy

Transmission electron microscopy (TEM) employs a similar principle to optical microscopy, except a beam of electrons is used instead of a beam of visible light.[285] The beam of electrons is generated by heating a filament with a high-voltage electrical current. It is then focussed and accelerated towards the sample using a series of lenses and apertures. When the beam reaches the sample, only the electrons that are not blocked by the sample pass through to the phosphor screen which is used to generate the image. The contrast in the image depends on the degree of electron transparency, with higher molecular weight atoms and areas of greater thickness absorbing or scattering more electrons and therefore, appearing darker.

In this work, images of the NPs were obtained using a JEOL JEM-2100 transmission electron microscope with an Orius SC200 1 camera at an accelerating voltage of 200 kV. A 5 μL droplet of the sample NP solution was drop-cast onto a C-coated 300-mesh Cu grid, air-dried and then imaged. Particle sizing was performed using ImageJ software.

2.5.4 X-ray photoelectron spectroscopy

X-ray photoelectron spectroscopy (XPS) is a technique used to study the surface composition of a material. It is based on the photoelectric effect. The sample is irradiated with X-ray photons with sufficient energy to eject core shell electrons from the atoms near the surface of the sample. The emitted electrons are collected, and their kinetic energy is detected. The kinetic energy of an emitted electron is approximately equal to the difference between the binding energy (energy needed to remove the electron from the atom) and the energy of the initial X-ray photon.[286] By studying the intensities of the different binding energies, it is possible to identify the elements present and their chemical states.

X-ray photoelectron spectroscopy (XPS) measurements were performed with a Thermo K-alpha spectrometer equipped with a monochromated Al K-Alpha X-ray source (1486.6 eV). The spot diameter was 400 μm and the optical camera was used to select the areas to analyse. A pass energy of 200 eV was used to record survey spectra between 0 – 1200 eV, and 50 eV was used to record the core level spectra. Sample charging was prevented using a dual beam flood gun. The binding energy scale was calibrated to the C 1s peak at 284.8 eV. CasaXPS software was used to analyse the data.[287]

2.5.5 Raman spectroscopy

Most of the Raman and SERS spectra were recorded using a 633 nm Ocean Optics QE Pro-Raman system with a 633 nm He-Ne laser (power ca. 22 mW).

Some measurements were also taken using a 785 nm Ocean Optics QE Pro-Raman system with a 785 nm diode laser (Coherent BT-785) (max. power of 500 mW). Both spectrometers have a 50 μm slit, a 1200 lines/mm grating and a 1044 x 64 element CCD array detector. The spectra resolution was 7 cm^{-1}. Both systems use an InPhotonics RPB Raman fibre optic probe (numerical aperture = 0.22, working distance = 7.5 mm). Laser power measurements were recorded at the end of the fibre optic probes. The spectra were obtained from 10 scans with an acquisition time of either 1s or 7s depending on the experiment. Asymmetric least squares (ALS) baseline correction (section 2.6.2.1) was used to remove the background noise in the SERS spectra.[288] The quoted peak heights are all relative to the baseline of the background subtracted spectra.

All the SERS and E-SERS experiments were performed in aqueous solutions inside a custom-built cell designed by Alvaro Castillo Bonillo, Dr Jia Liu, and Dr Tung Chun Lee. The cell shown in Figure 2.6 was 3D printed from polylactic acid (PLA). The lid contains two round holes for the reference and counter electrodes. The square-shaped hole is for the SERS substrate (working electrode) and the base contains a slot for it to sit in. The front of the cell is made of quartz glass and serves as an optical window which allows SERS spectra to be recorded whilst the NP substrates are submerged in the analyte solutions. During SERS measurements, the Raman probe was positioned so that it was flush with the quartz window and the entire cell was covered by a box to minimise background light contamination.

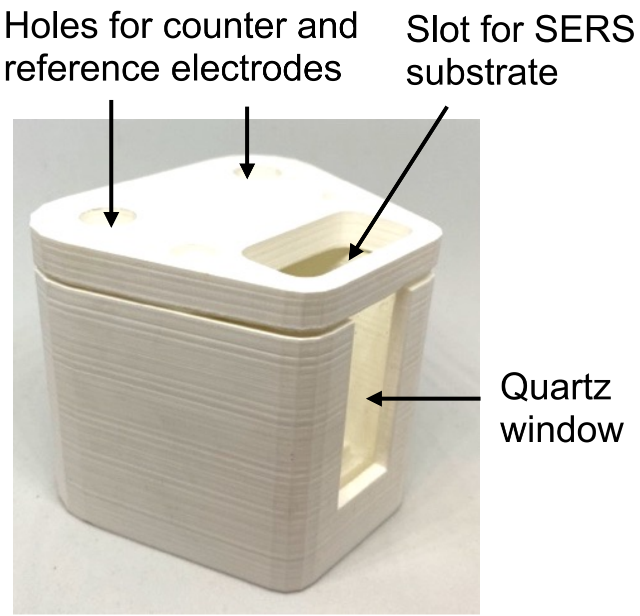

Figure 2.6: The custom-built PLA 3D printed cell used for SERS and E-SERS experiments.

To record a series of SERS spectra, the substrate was placed in the analyte solution and allowed to equilibrate for at least 15 minutes. The Raman probe was consistently positioned flush to the quartz window and spectra were recorded from a point on the NP film, which was chosen at random. However, in the final measurements described in section 5.6.3.3, the laser was positioned further away from the quartz window, in line with the edge of the front of the PLA cell. The OceanView software was set to continuously record spectra and then the laser was turned on. Neither the probe nor the substrate was moved whilst recording successive scans.

2.5.5.1 Electrochemical surface-enhanced Raman spectroscopy

To perform E-SERS, an electrochemical potential was applied to the SERS substrate using a Gamry Potentiostat Interface 1010E and a three-electrode electrochemical cell, which consisted of a leakless Ag/AgCl reference electrode, a platinum plate counter electrode, and the SERS substrate as the working electrode. 0.1 M $NaF_{(aq)}$ was used as the supporting electrolyte for all experiments. NaF was chosen as the supporting electrolyte as it has a high water solubility, (40.4 g/L at 25°C)[289], no significant Raman peaks in the wavenumber range of interest (500 – 1800 cm^{-1}), and is electrochemically stable over the potential range under investigation (-1V to 1V vs. Ag/AgCl).[208] The experimental set-up is shown in Figure 2.7.

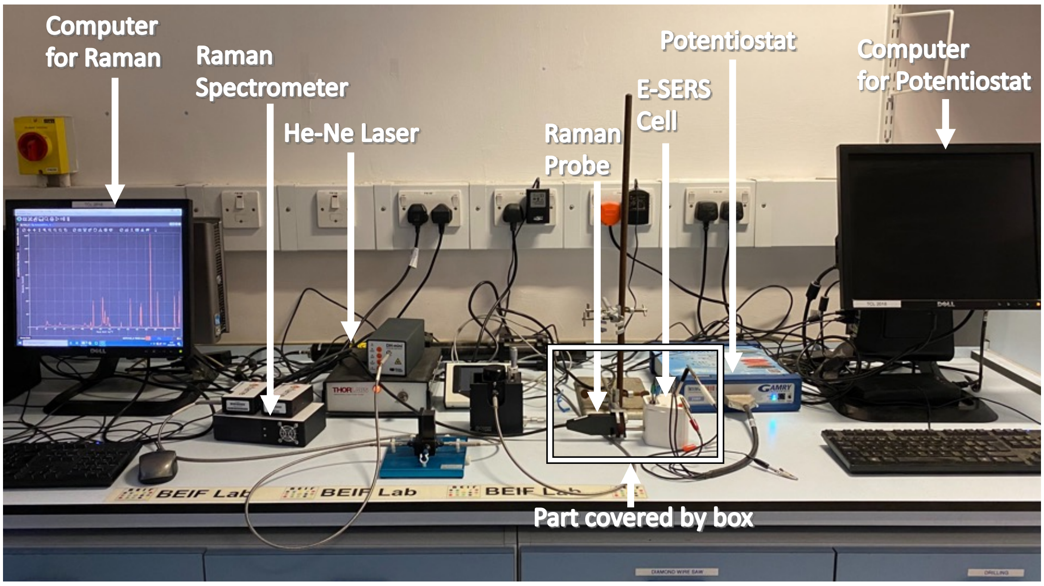

Figure 2.7: Photograph showing the experimental set-up for the E-SERS measurements including the Raman spectrometer and potentiostat.

During the E-SERS scans, the Gamry Framework Sequence Wizard was used to control the potential applied to the SERS substrate. The sequence wizard was programmed to perform successive chronoamperometry experiments, where the potential of the working electrode is stepped to a specific value (relative to the reference electrode) and the resulting current is recorded as a function of time. The potential is held for a defined amount of time to allow multiple SERS spectra to be recorded before the next potential is applied. During potential scans, the applied potential was held for 5 minutes at each potential. Spectra recorded in the first 75s were not included in the analysis to give the system time to equilibrate, this resulted in 3 spectra that were included in the analysis for each potential step. The spectra plotted in Chapter 3 and 4 of this thesis are the mean spectra of the 3 measurements and the magnitude of the error bars in the peak height plots is equal to the standard deviation of the peak height from the 3 spectra.

For some E-SERS experiments, spectra for multiple different analyte concentrations were recorded using the same electrode. To do this, a full E-

SERS scan was performed at the lowest analyte concentration and then stock solution of the analyte was added to the electrolyte to increase the overall concentration, whilst keeping the concentration of the supporting electrolyte and other molecules the same. The electrolyte was mixed well, and the electrode was left in the solution to equilibrate before performing the next E-SERS scan.

2.6 Data analysis and machine learning

2.6.1 Software

All the data analysis in this thesis was performed in Python (version 3.7.4). Several different libraries were used including pandas (data storage and manipulation)[290], NumPy (array and matrix processing)[291], scikit-learn (machine learning)[292] and Matplotlib (graph plotting)[293].

2.6.2 Pre-processing

2.6.2.1 Asymmetric least squares (ALS) baseline correction

Raw SERS spectra often have significant background noise that needs to be removed to determine the true heights of the peaks (Figure 2.8a). The most commonly used method, ALS baseline correction, was developed by Eilers in 2003.[288] This approach fits a smooth curve to the spectrum which is then removed to give a signal with a constant baseline. The algorithm aims to find the curve which best fits the data whilst also minimising the roughness.

This goal is represented by:[288]

$$Q = |y - z|^2 + \lambda|\boldsymbol{D}z|^2 \qquad \text{Equation 17}$$

Where Q is the value to be minimised, $|\mathrm{y} - \mathrm{z}|^2$ is the sum of squares of differences between the original spectrum (y) and the fitted curve (z), λ is a number chosen by the user which controls the roughness of z, and $|\mathbf{D}\mathrm{z}|^2$ is the sum of squares of differences between each z point (z_i) and the previous z point (z_{i-1}).

The partial derivative of Q with respect to z is calculated and set equal to zero to give the following equation:[288]

$$(\boldsymbol{I} + \lambda \boldsymbol{D}'\boldsymbol{D})z = y \qquad \text{Equation 18}$$

where $\mathbf{I}$ is the identity matrix. This equation is then solved to find the fitted curve, z. This process is repeated iteratively with a weighting of p applied to positive residuals (points where $y > z$) and $(1 - p)$ to negative residuals.

ALS baseline correction is not built-in to Python so a simple function was written and the parameters were optimised for the SERS dataset. An example of a trimmed ALS baseline corrected spectrum is shown in Figure 2.8b. All peak intensities were reported with respect to the background corrected baseline.

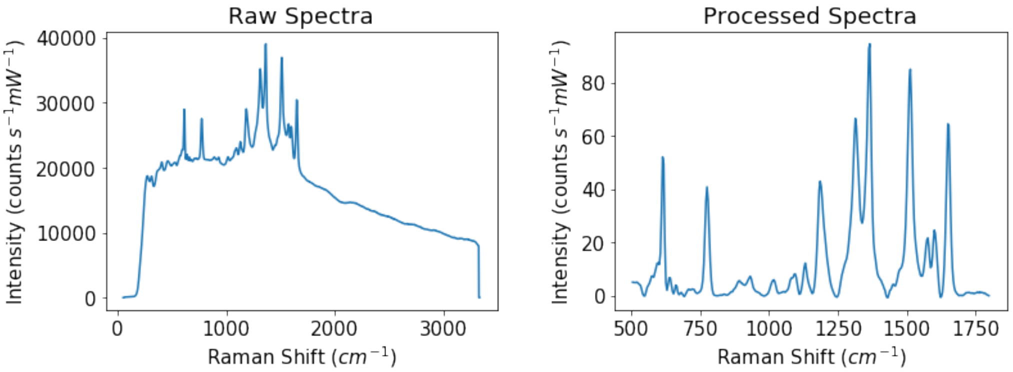

Figure 2.8: (a) An example of a raw SERS spectrum with significant background noise. (b) The same SERS spectrum after asymmetric least squares baseline correction where λ and p were 1 x 10^6 and 0.0001, respectively. The spectrum is also trimmed to the area of interest.

2.6.2.2 Pre-processing for machine learning

To pre-process the spectra for machine learning, they were first truncated to eliminate regions without significant Raman signals, removing measurements below 500 cm^{-1} and above 1800 cm^{-1}. After trimming the spectra, ALS baseline correction was applied.[288] Then, standard normal variate normalisation was performed to give each spectrum a mean intensity of 0 and a standard deviation of 1.[117,273] For the multilayer perceptron models, the analyte concentrations were also scaled *via* min-max normalization so that all of the values were transformed into the range [0,1].

2.6.3 Performance evaluation

2.6.3.1 R^2 calculation

To evaluate the performance of the machine learning models, the coefficient of determination, R^2, was calculated.[294] The R^2 describes how well a model fits a dataset. It is defined as the fraction of the variance in the response variables explained by the model, with a value of 1 indicating perfect agreement between the predicted and true values.[294] R^2 is calculated using the following equation:

$$R^2 = 1 - \frac{\sum_i (y_i - f_i)^2}{\sum_i (y_i - \bar{y})^2} \qquad \text{Equation 19}$$

where, for this work, y_i is the true concentration, f_i is the predicted concentration and $\bar{y}$ is the mean of the true concentrations.

2.6.3.2 Training and test datasets

The aim in supervised machine learning is to create a model from a labelled dataset that can correctly interpret new unseen, unlabelled measurements. The best way to assess a model is to randomly split the data into two separate datasets – one for training and the other for testing. Typically, the training dataset will contain 70 – 80% of the observations and the other 20 – 30% will be in the test dataset. In this work, the training/test split was 80:20. The training dataset can also be further split to produce a validation set which can be used to optimise the hyperparameters of a model. For this method of evaluation to work, a lot of data is required. There needs to be enough data in the training set to build an effective model whilst also having a test dataset that is large enough to reliably assess its performance.[295] If there is not plenty of data, the success of the model will vary significantly depending on which observations are in each dataset. *K*-fold cross-validation can be used to optimise hyperparameters for smaller datasets.

2.6.3.3 K-fold cross-validation

In *K*-fold cross-validation, a dataset is randomly divided in *K* groups, or folds, of approximately equal size (Figure 2.9).[295] The first fold is treated as the test set and the remaining $K - 1$ folds are used to train the model.[296] The model is then evaluated using the held-out fold and a performance metric, such as the R^2, is calculated and recorded. This process is repeated *K* times, and each time a different group of observations is used as the test set. This procedure results in *K* values of the performance metric, which are then averaged to give an overall assessment of the model.[295] In this work, $K = 5$ was used to evaluate the different parameters during the hyperparameter optimisation.

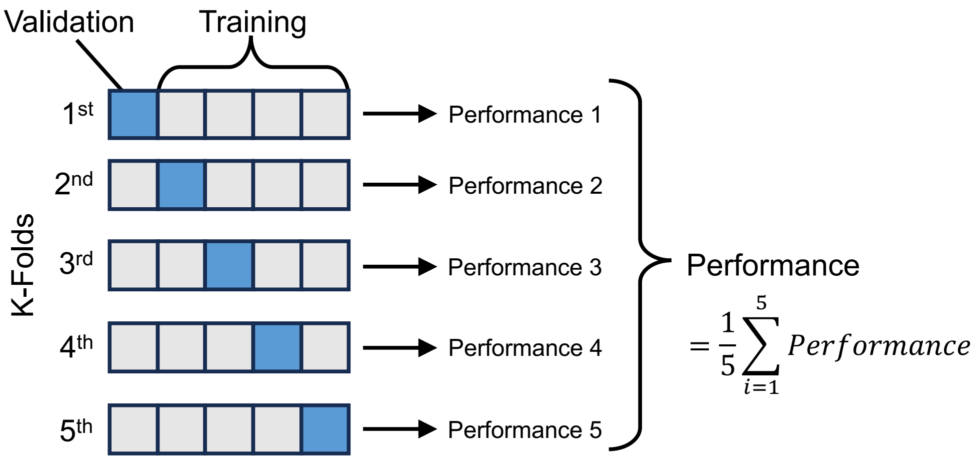

Figure 2.9: Illustration of K-fold cross-validation with 5 folds.

Chapter 3 Development of an E-SERS system for the detection of uric acid and creatinine

3.1 Motivation

This work aims to develop an E-SERS system that can detect multiple biomarkers in complex bodily fluids. Urine is particularly valuable for clinical diagnostics as it is readily available, easy to collect and contains a multitude of components which can be used to assess a patient's health.[297] Two particular biomarkers of interest found in urine are uric acid (UA) and creatinine (CRN).

Uric acid ($C_5H_4N_4O_3$) is the end product of purine metabolism, and in normal circumstances, urinary UA excretion ranges from 250 to 750 mg per 24 hours.[298] Elevated uric acid levels are indicative of several conditions including gout, cardiovascular disease and renal diseases.[16–19] Increased UA levels have also been linked to preeclampsia, a hypertension disorder that affects pregnant women and is the primary cause of maternal mortality worldwide.[10–15,299] Urinary uric acid concentrations of approximately 0.4 mM were found to be indicative of patients experiencing hypertension and proteinuria and concentrations above 0.4 mM were associated with severe preeclampsia.[300] Current uric acid detection methods include colourimetric enzymatic assays, high-performance liquid chromatography and capillary electrophoresis, which are expensive, time-consuming and require sophisticated sample preparation.[124,208,209,301] As such, there is a need for sensitive, selective sensors which can detect uric acid quickly and cheaply.

Creatinine ($C_4H_7N_3O$) is the end product of muscle metabolism and has typical urinary excretion rates of 0.7 to 2.4 g per 24 hours.[122,302,303] It is an important indicator of kidney filtration function in renal clearance tests.[122,302] The standard technique for creatinine quantification is based on the Jaffe reaction, where picric acid reacts with CRN under alkaline conditions to form a reddish-orange coloured complex.[304] However, this reaction is not specific to creatinine as the coloured complex also forms with other biomarkers.[305] Other clinical methods include high-performance liquid chromatography, isotope dilution mass spectrometry, capillary electrophoresis and enzymatic methods.[306–309] However, as with the uric acid detection methods, they are either expensive, time-consuming or lack sensitivity. Therefore, there is still a need for easy-to-use, cost-effective creatinine sensors.

On top of the demand for effective uric acid and creatinine sensors, there is a desire for systems which allow multiplexed detection, where multiple analytes are detected simultaneously. The complex nature of urine means that this is typically only achieved using specialised and expensive lab-based equipment such as Liquid Chromatography-Mass Spectrometry and High-performance Liquid Chromatography.[27] Detecting multiple analytes at once using more accessible techniques could enable quicker and cheaper diagnostics.

E-SERS holds significant promise for the multiplexed detection of biomarkers due to its potential to enhance both the sensitivity and selectivity of SERS. By adjusting the applied potential, it is possible to control the molecules adsorbed on the SERS substrate, enabling modulation of the SERS spectrum and selective enhancement of specific peaks (Figure 3.1). However, to achieve reliable multiplexed detection of UA and CRN using E-SERS, there are several hurdles to cross and questions that need to be answered.

The first step is to fabricate robust, reliable E-SERS substrates with significant SERS enhancements. Given the intended application for these substrates, the fabrication method must also be simple and cost-effective. After studying the literature, drop-casting colloidal nanoparticles onto conductive glass electrodes was identified as one of the most promising approaches (section 1.4.2.4). Work by the Brosseau group has shown that drop-cast Ag NPs can make effective E-SERS substrates.[208,209] An aim of this work is to fabricate these substrates and determine their robustness and reliability. If issues are identified with the drop-cast Ag NP electrodes, research will be undertaken to improve their performance and suitability for multiplexed quantitative detection.

Uric acid has been sensed before using colloidal Ag NPs for E-SERS[208,209], but this work aims to detect lower concentrations (<0.1 mM) than those previously studied. Creatinine has not been studied previously using E-SERS but it is SERS active[122,302,310,311] and an important biomarker.[122,302] Based on the current understanding of the relationship between applied potential and SERS, it is expected that the creatinine SERS signal will be enhanced in E-SERS. Studying how the spectrum changes will help to understand the reasons for the E-SERS enhancement in this system and the creatinine adsorption behaviour.

Research has been published demonstrating E-SERS detection of a variety of analytes (section 1.4.3). However, very few of these studies have demonstrated quantitative[209,241] or multiplexed detection. The ability to measure multiple analytes at once is key for enabling quicker and cheaper diagnostics from complex bodily fluids.[312] Therefore, this work aims to use E-SERS to achieve quantitative, multiplexed detection of uric acid and creatinine.

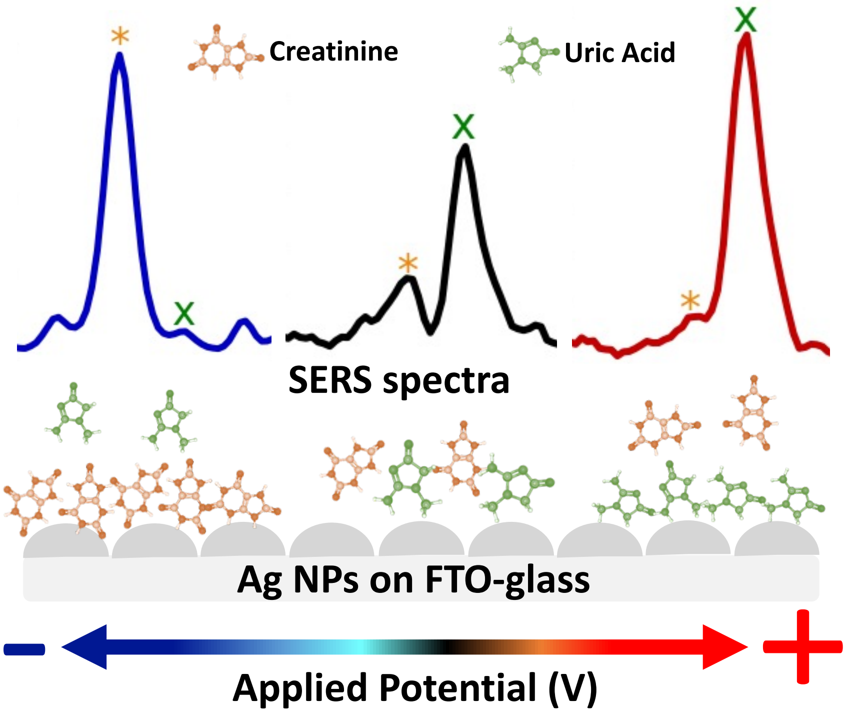

Figure 3.1: Diagram illustrating the principle of multiplexed analyte detection with E-SERS. By adjusting the applied potential, it is possible to control the molecules adsorbed on the SERS substrate, enabling modulation of the SERS spectrum and selective enhancement of specific peaks.

3.2 Characterisation

3.2.1 Nanoparticle characterisation

Ag NPs were synthesised *via* a standard citrate reduction based on the Lee and Meisel method.[201] The as-synthesised colloidal Ag NPs had a milky green/grey colour (Figure 3.2 inset). The UV-visible (UV-vis) spectrum of the Ag NPs showed a LSPR peak at ca. 434 nm (Figure 3.2). According to Paramelle *et al.*, this would correspond to Ag NPs of approximately 62 nm in diameter for spherical monodisperse particles.[313] However, the broad nature of the UV-vis peak indicates that the nanoparticles are not monodisperse.

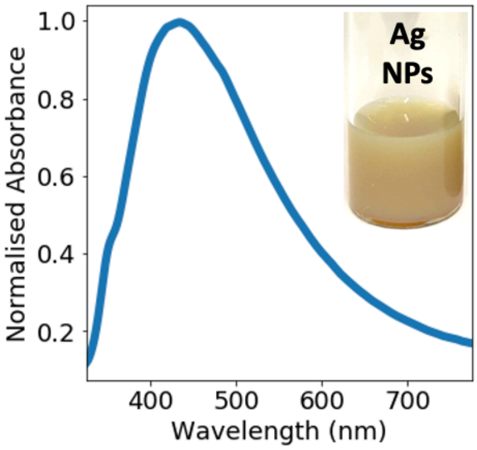

Figure 3.2: UV-vis spectra of Ag NPs plotted with normalised absorbance. (Inset) Photograph of colloidal Ag NP solution.

Transmission electron microscopy (TEM) confirmed the formation of polydisperse Ag NPs (Figure 3.3). The NPs were quasi-spherical with some rods and trapeziums also present, which is typical for Ag NPs synthesised using the Lee and Meisel method.[201] ImageJ was used to manually measure the area of 1,026 particles from TEM images and the diameter of each particle was calculated by assuming the particles were spherical. The mean diameter calculated in this way was 79 nm ± 25 nm and a histogram of the diameter distribution is plotted in Figure 3.4. Clearly, this measurement method is an approximation as the particles are not all spherical. This is highlighted by the "tail" of the histogram at large NP diameters. These values likely come from very long nanorods (>200 nm), which are occasionally present (Figure 3.3e).

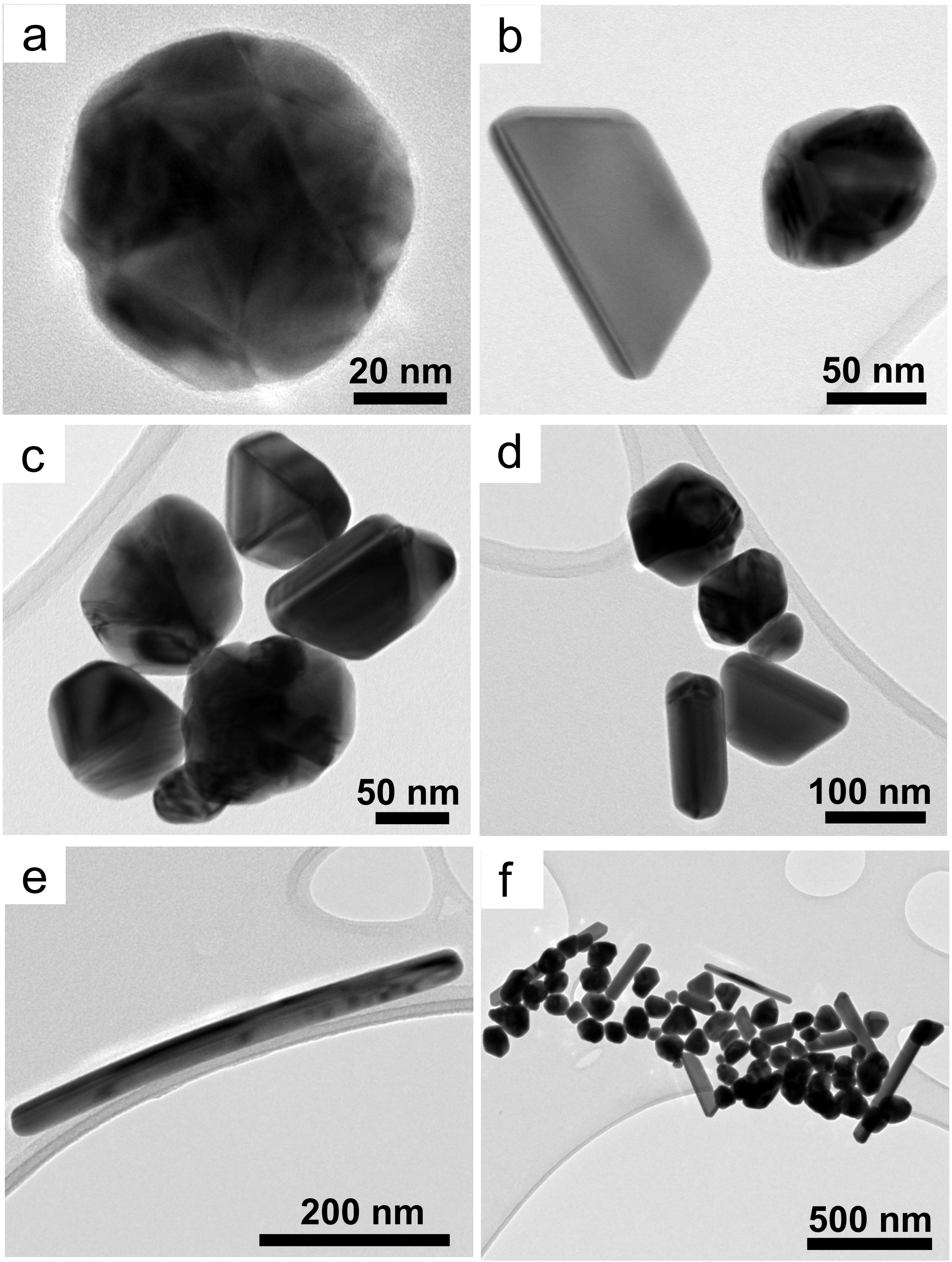

Figure 3.3: TEM images of as-synthesised Ag NPs.

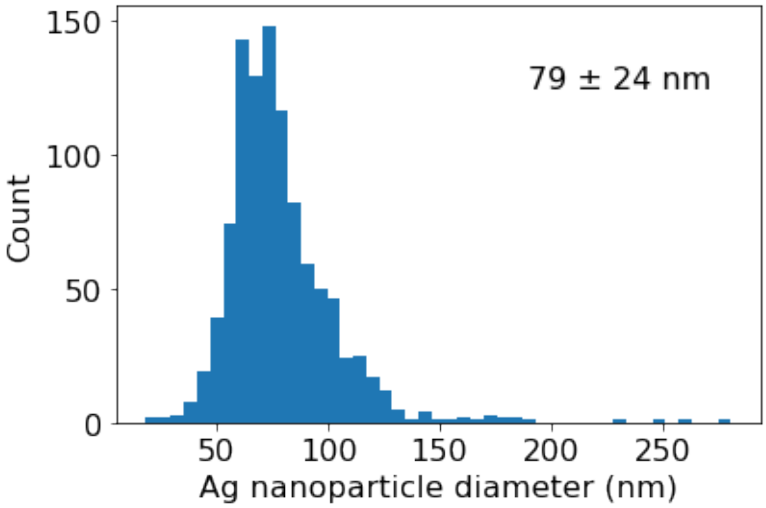

Figure 3.4: Size distribution of the as-synthesised Ag NPs. The areas of 1,026 particles were measured from TEM images using ImageJ and the diameter of each particle was calculated by assuming the particles were spherical.

3.2.2 Electrode characterisation

The Ag NP electrodes were fabricated by drop-casting a concentrated (ca. 230 mg/mL) colloidal solution of Ag NPs onto conductive FTO-coated glass (Figure 3.5). Scanning electron microscope (SEM) images of the FTO-coated glass (Figure 3.6a) show that it has a rough surface with nanoscale angular protrusions. The SEM images of the Ag NP film show a densely packed compact layer of NPs (Figure 3.6). The closely packed arrangement of the particles creates “hot spots” that are crucial for SERS enhancement. However, the gap size is not consistent for all the particles, which can lead to variability in the SERS signal across the surface. Some undulations are also observed in the nanoparticle layer, which may be attributed to the rough FTO surface.

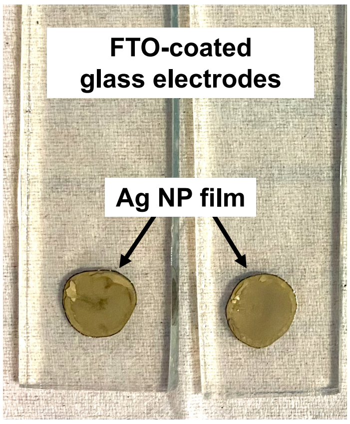

Figure 3.5: Photograph of Ag NP electrodes. Concentrated colloidal Ag NP solution is drop-cast on FTO-coated glass slides.

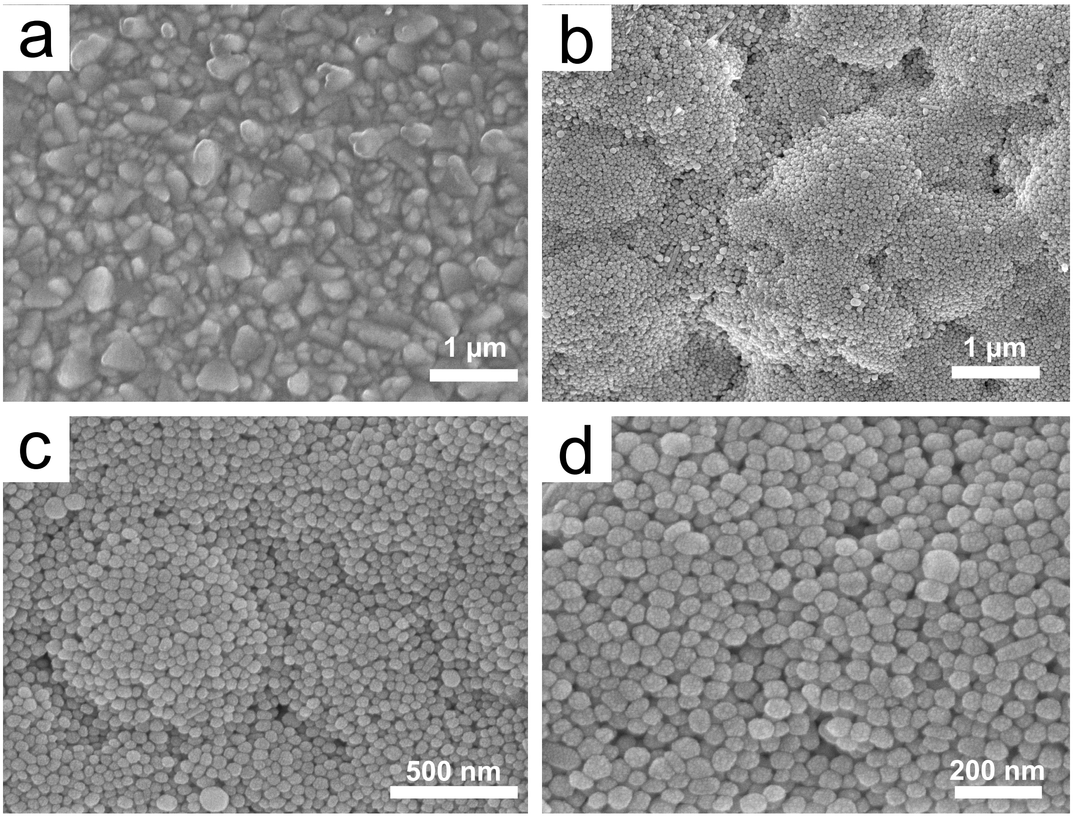

Figure 3.6: SEM images of (a) FTO-coated glass and (b,c,d) Ag NP film deposited on FTO-coated glass.

3.3 Detection of uric acid

3.3.1 Raman and SERS

Prior to conducting E-SERS analysis of uric acid, the Raman spectra of solid UA powder (Figure 3.7a) and SERS spectra of a 0.5 mM UA solution (Figure 3.7b) were recorded to identify the characteristic peaks. The band assignments for the Raman and SERS peaks are given in

Table 3.1. The UA SERS spectra recorded using the Ag NP electrodes have two main characteristic UA peaks at 636 cm^{-1} and 1138 cm^{-1}, which are assigned to skeletal ring deformation and C-N vibration, respectively. There is another prominent peak at 931 cm^{-1}, consistently observed in both the UA and the NaF solutions, which is attributed to the citrate ions that remain on the surface of the Ag NPs after synthesis.[209,211] This is discussed further in section 3.3.3.

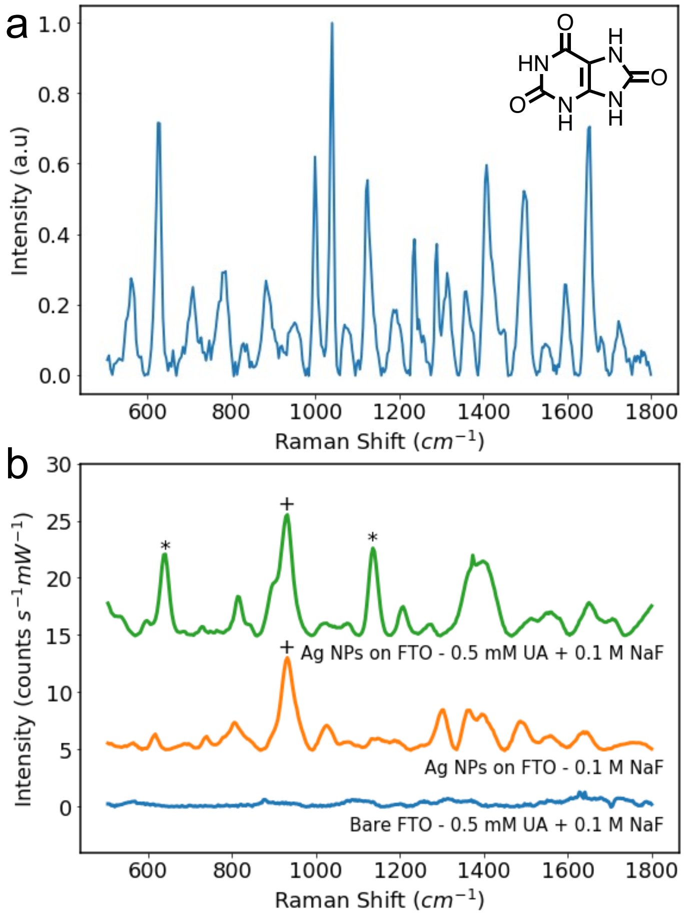

*Figure 3.7: Raman spectrum of solid uric acid powder. (b) SERS spectra of (blue) an aqueous solution of 0.5 mM UA and 0.1 M NaF (the supporting electrolyte) on a bare FTO-coated glass electrode, (orange) 0.1 M NaF$_{(aq)}$ on an Ag NP/FTO electrode, (green) 0.5 mM UA and 0.1 M NaF $_{(aq)}$ on an Ag NP/FTO electrode. The characteristic UA and citrate peaks are indicated with a * and a +, respectively.*

Table 3.1: Band assignments for Raman and SERS uric acid peaks. Raman spectra were recorded using pure UA powder and SERS spectra were recorded using 0.5 mM UA and 0.1 M NaF $_{(aq)}$ on Ag NP/FTO electrodes.[124,208,253,314]

Raman Peak (cm^{-1})	SERS Peak (cm^{-1})	Band assignment
560	592	Ring breathing mode
624	636	Skeletal ring deformation
708	727	N-H bending
786	813	Ring vibration
882	886	N-H bending
999	1017	Ring vibration
1039	1073	Mixed vibrations
1124	1138	C-N vibration
1236	1207	N-C-C stretching and bending
1496	1503	CC stretching
1594	1557	CN stretching
1653	1656	C=O stretching

3.3.2 E-SERS

The Ag NP electrodes were used to record E-SERS spectra of an aqueous solution containing 0.5 mM uric acid and 0.1 M NaF. The SERS spectra were recorded using a 633 nm, 22 mW laser with an integration time of 7s. The applied potential was stepped from 0 to 0.5V and from 0 to -0.8V in 100 mV increments. The E-SERS spectra were recorded by holding the potential at each step for 5 minutes. Spectra recorded in the first 75 seconds were not included in the analysis to give the system time to equilibrate, this resulted in 3 spectra that were included in the analysis for each potential step. The spectra recorded at each potential were averaged before plotting (Figure 3.8). The most negative potential at which spectra were recorded was -0.8V because the Ag NP film started to become detached from the FTO electrodes at potentials below -0.8V. This is likely because the Ag NPs are only attached *via* van der Waals forces, and the NPs are negatively charged due to the stabilisers on the surface and are therefore repelled by the large negative potentials. This is discussed further in section 3.6.2.

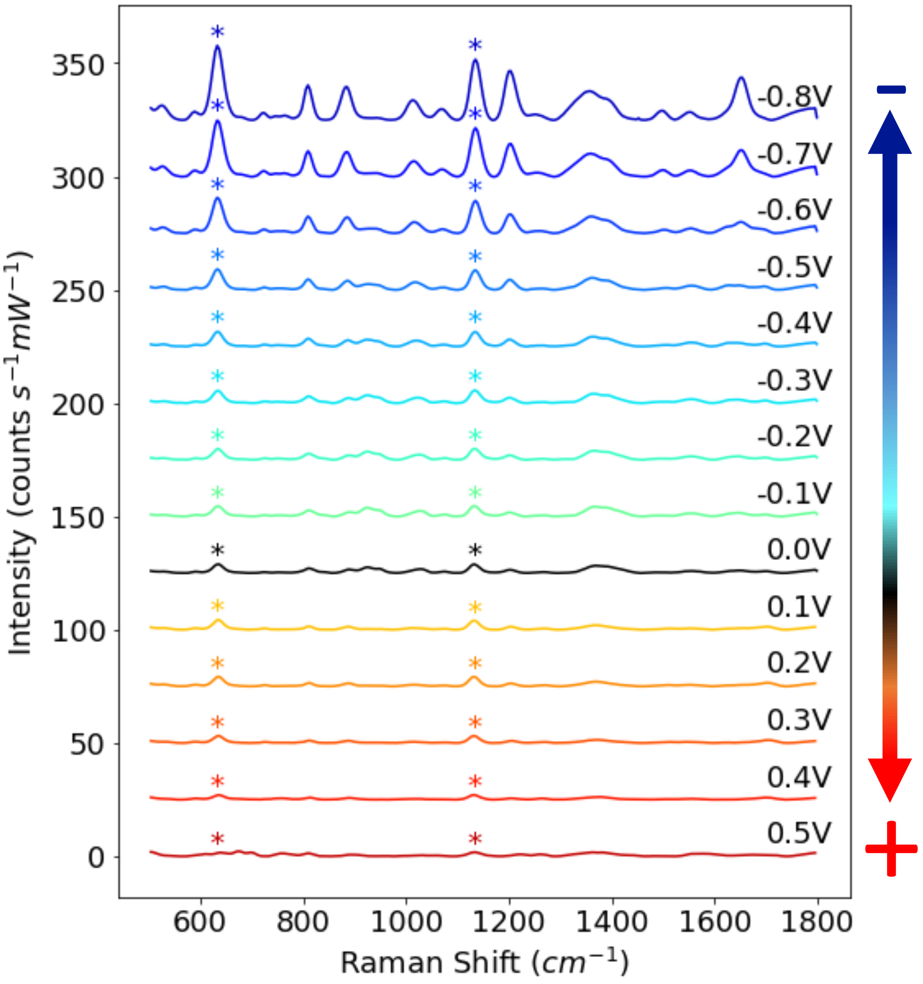

*Figure 3.8: E-SERS spectra of 0.5 mM UA with 0.1 M NaF as the supporting electrolyte. The applied potential was stepped from 0 to 0.5V and from 0 to -0.8V in 100 mV increments. The characteristic UA peaks are indicated with a *. (RE: Ag/AgCl; WE: Ag NPs on FTO; CE: platinum plate).*

The characteristic uric acid peaks at 636 cm^{-1} and 1138 cm^{-1} were identified in the initial spectra recorded at 0V (Figure 3.9a).[124,208,253] As the applied potential becomes more negative, the magnitude of the SERS peaks increase, reaching a maximum at -0.8V. In contrast, the magnitude of the SERS peaks decrease as the applied potential becomes more positive.

The height of the characteristic uric acid peak at 636 cm^{-1} is plotted against applied potential in Figure 3.9b. The dramatic increase in the magnitude of the SERS peak with negative applied potential is clearly shown. The magnitude of the 636 cm^{-1} peak increases by over 9 times from 3.8 to 32.7 counts s^{-1} mW^{-1} demonstrating the advantage offered by E-SERS over conventional SERS.

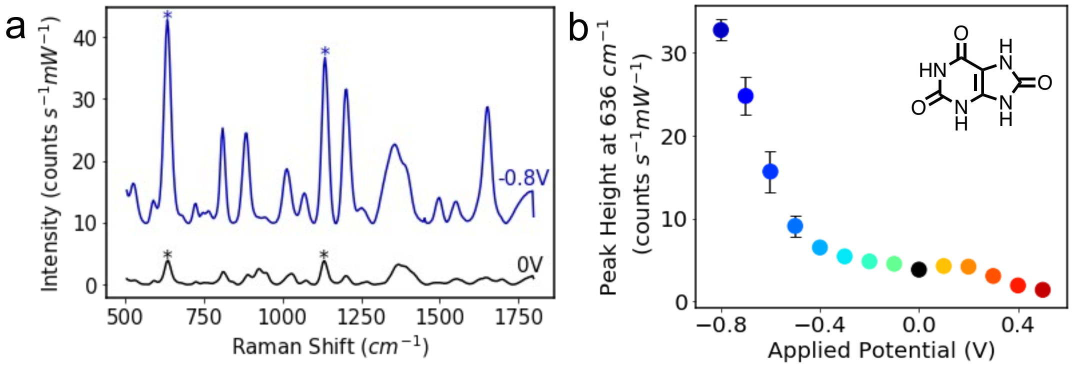

*Figure 3.9: E-SERS spectra of a 0.5 mM UA solution at 0V and -0.8V. The characteristic UA peaks are indicated with a *. (b) The mean height of the characteristic UA peak at 636 cm^{-1} plotted against applied potential. The magnitude of the error bars is equal to the standard deviation in the peak height from 3 spectra measured at each potential. (RE: Ag/AgCl; WE: Ag NPs on FTO; CE: platinum plate; supporting electrolyte: 0.1 M NaF).*

3.3.3 Discussion of E-SERS enhancement

As discussed in section 1.4.1, it can be difficult to determine the reasons for the E-SERS enhancement for a particular system as it is often a combination of surface adsorption, electromagnetic, and charge transfer effects. For this system, there seems to be several factors which influence the observed enhancement. The first relates to the sodium citrate which is used to reduce the silver nitrate during the Ag NP synthesis.[198,199] The citrate ions remain on the surface of the NPs after synthesis and act as electrostatic stabilisers for the colloidal solutions. The presence of citrate on the surface of the Ag NP/FTO electrodes can be identified by the characteristic peak at 931 cm^{-1}, which is observed for all solutions including those that do not contain UA or NaF (Appendix Figure A.1).[209,211]

When negative potentials are applied to the Ag NP/FTO electrodes, the negatively charged citrate ions are repelled from the surface.[209,211] This is shown in Figure 3.10 by the reduction in the 931 cm^{-1} peak height as the negative potential is applied (the same behaviour is also observed for solutions containing only NaF (Appendix Figure A.2)). The magnitude of the citrate peak remains constant over two subsequent applied potential cycles demonstrating that this process is irreversible. The reduction in the citrate peak is mirrored by an increase in the characteristic UA peak at 636 cm^{-1} (Figure 3.10). This implies that the removal of the citrate ions allows the uric acid molecules to get closer to the Ag NP surface and leads to an increased enhancement of the uric acid SERS signal. This is interesting because the pKa of uric acid is 5.6 which means the uric acid molecules are present as anionic urate ions with a charge of -1 in the aqueous solutions studied here. As such, the enhancement observed at negative potentials (-0.8V) may seem counterintuitive. However, the E-SERS enhancement is complex and there are several possible explanations for this behaviour, which has also been consistently observed in the literature.[208,209] Although the citrate and urate ions are both negatively charged, the citrate ions have a charge of -3 compared to the urate ions which have a charge of -1, so the citrate ions will experience a stronger repulsion force than the urate ions. This means the citrate ions will be preferentially removed, allowing the urate ions to adsorb onto the Ag NP surface.

However, this does not fully explain the E-SERS enhancement because, as Figure 3.10 shows, the UA peak height continues to increase with negative potential after the citrate ions have desorbed. However, the adsorption of the urate ions on the surface is not a binary on/off. The effect of surface orientation can have a significant impact on the SERS signal. The application of the negative potential may be causing a reorientation on the surface and changing the functional groups which are closest to the Ag NPs, enhancing particular SERS peaks. Secondly, it is also important to consider the possible impact of redox reactions. Cyclic voltammetry studies of uric acid have shown it exhibits an oxidation peak at 0.36V and a reduction peak at 0.33V.[315] The fact that the redox reactions appear to take place far from the enhancement potentials and no new peaks are observed in the SERS spectra implies that this is not the reason for the E-SERS enhancement. However, in the future, it would be useful to carry out a more extensive electrochemical characterisation of the analytes. Finally, the electromagnetic enhancement, where the free electron density increases due to the negative applied potential and strengthens the LSPR in the Ag NPs, is likely to also play a part.[316]

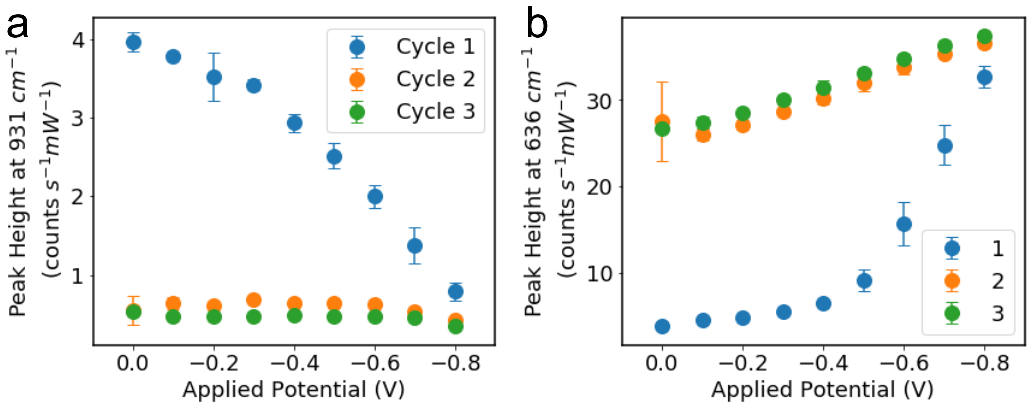

Figure 3.10: The height of the characteristic (a) citrate peak at 931 cm^{-1} and (b) uric acid peak at 636 cm^{-1} plotted against applied potential for an aqueous solution containing 0.5 mM UA and 0.1 M NaF. Three E-SERS scans were performed consecutively at the same point on the electrode. The magnitude of the error bars is equal to the standard deviation in the peak height from 3 spectra measured at each potential. (RE: Ag/AgCl; WE: Ag NPs on FTO; CE: platinum plate; supporting electrolyte: 0.1 M NaF).

Looking at this more closely, the characteristic UA peak height is plotted against time for an E-SERS test in Figure 3.11. The potential was scanned from 0V to -0.8V and then from 0V to 0.4V in 0.2 V increments. As expected, the peak height at 636 cm^{-1} increases dramatically as the negative potentials are applied, reaching a maximum of 24.2 counts s^{-1} mW^{-1} at -0.8V. When the potential is returned to 0V, there is a clear reduction in the peak height to 6.7 counts s^{-1} mW^{-1}. This is thought to be due to the reduction in the electron density in the Ag NPs, although there may also be some changes in surface adsorption.

Nevertheless, the peak is still clearly visible at 0V, implying that there is still significant UA adsorbed on the surface. As the positive potentials are applied, the UA peak height decreases further. This is likely to be due to the repulsion of the UA molecules from the Ag NP surface. When the potential returns to 0V, the peak height has returned to close to the original value at the beginning of the test, suggesting that the surface of the Ag NPs has been “cleaned” by the application of the positive potentials. This is a key observation as it will help to develop the experimental procedure for the E-SERS system.

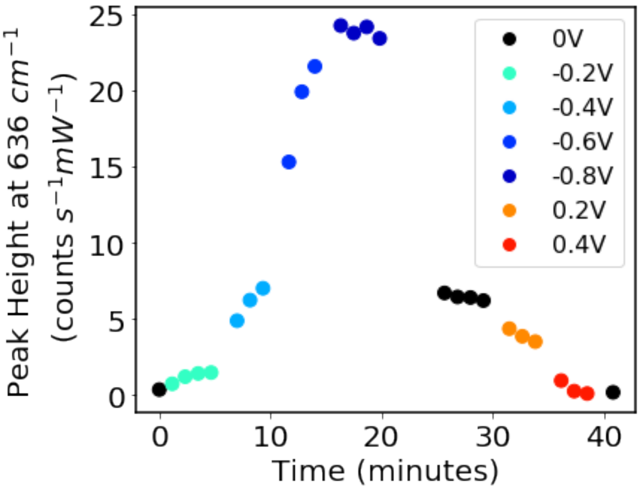

Figure 3.11: The characteristic UA peak height at 636 cm^{-1} plotted against time for an E-SERS test in 50 μM UA solution. The colour of the markers indicates the potential, which was scanned from 0V to -0.8V and then from 0V to 0.4V in 0.2 V increments. (RE: Ag/AgCl; WE: Ag NPs on FTO; CE: platinum plate; supporting electrolyte: 0.1 M NaF).

3.3.4 Uric acid quantification

Successive E-SERS scans from 0V to -0.6V were performed on an Ag NP/FTO electrode in a 0.1 M NaF solution as the uric acid concentration was gradually increased from 0 μM to 50 μM. The potential was only reduced as far -0.6V due to electrode durability issues which are discussed further in 3.6.2. The spectra recorded at -0.6V are shown in Figure 3.12.

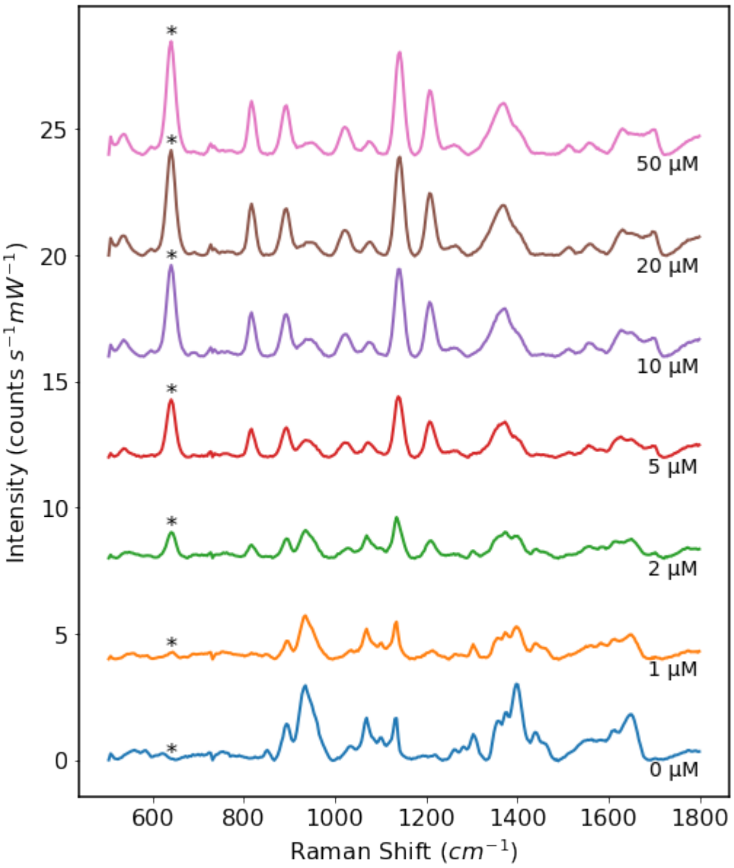

Figure 3.12: E-SERS spectra of UA solutions with concentrations ranging from 0 µM to 50 µM at an applied potential of -0.6V. The spectra plotted are an average of 3 spectra recorded over 5 minutes (with spectra in the first 75 seconds removed to allow for equilibration). The supporting electrolyte was 0.1 M NaF. (RE: Ag/AgCl; WE: Ag NPs on FTO; CE: Platinum plate).

The height of the 636 cm^{-1} peak is plotted against potential for each of the concentrations in Figure 3.13a. The characteristic peak is clearly visible for the solution containing 1 µM UA at -0.6V. This is not the case at 0V, illustrating the benefit of E-SERS over conventional SERS. The peak height at 636 cm^{-1} at -0.6V is plotted against UA concentration in Figure 3.13b. A linear relationship was fitted between log(UA concentration) and the peak height for concentrations from 1 µM to 50 µM with good correlation (R^2 = 0.98). This demonstrates that quantitative detection is possible with this system. 1 µM is significantly lower than the uric acid concentrations previously detected by colloidal NP E-SERS systems.[208,209]

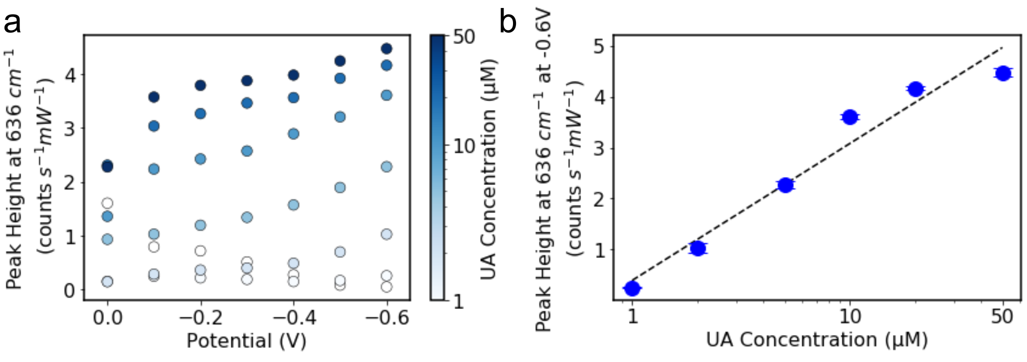

Figure 3.13: (a) Mean peak height at 636 cm^{-1} plotted against applied potential for each of the uric acid concentrations from 0 μM to 50 μM. (b) Peak height at 636 cm^{-1} plotted against uric acid concentration for the spectra recorded at -0.6V. A linear relationship is fitted between log(concentration) and peak height for concentrations from 1 μM to 50 μM (R^2 = 0.98) and plotted on a log x-axis. The magnitude of the error bars is equal to the standard deviation in the peak height from 3 spectra measured at each potential.

3.4 Detection of CRN

3.4.1 Raman and SERS

The Raman spectra of solid creatinine power and a SERS spectrum of 0.5 mM CRN solution are shown in Figure 3.14. Tentative band assignments for the Raman and SERS peaks are given in Table 3.2, along with the E-SERS peaks. The main characteristic CRN SERS peak is found at 684 cm^{-1} and is assigned to N-H bending.[317,318] As with the UA spectra, the characteristic citrate peak at 931 cm^{-1} is also observed.

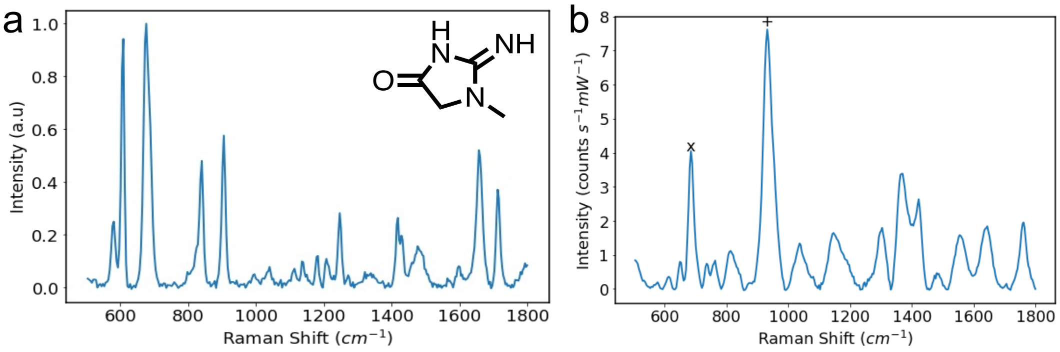

Figure 3.14: (a) Raman spectrum of solid creatinine powder. (b) SERS spectra of an aqueous solution of 0.5 mM CRN and 0.1 M NaF on an Ag NP/FTO electrode. The characteristic CRN and citrate peaks are indicated with an x and a +, respectively.

3.4.2 E-SERS

E-SERS spectra of an aqueous solution containing 0.5 mM creatinine and 0.1 M NaF were recorded with Ag NP/FTO electrodes. The applied potential was stepped from 0 to 0.5V and from 0 to -0.8V in 100 mV increments and the potential was held at each step for 5 minutes. Spectra recorded in the first 75 seconds were not included in the analysis to give the system time to equilibrate, this resulted in 3 spectra that were included in the analysis for each potential step. The spectra recorded at each potential were averaged before plotting (Figure 3.15).

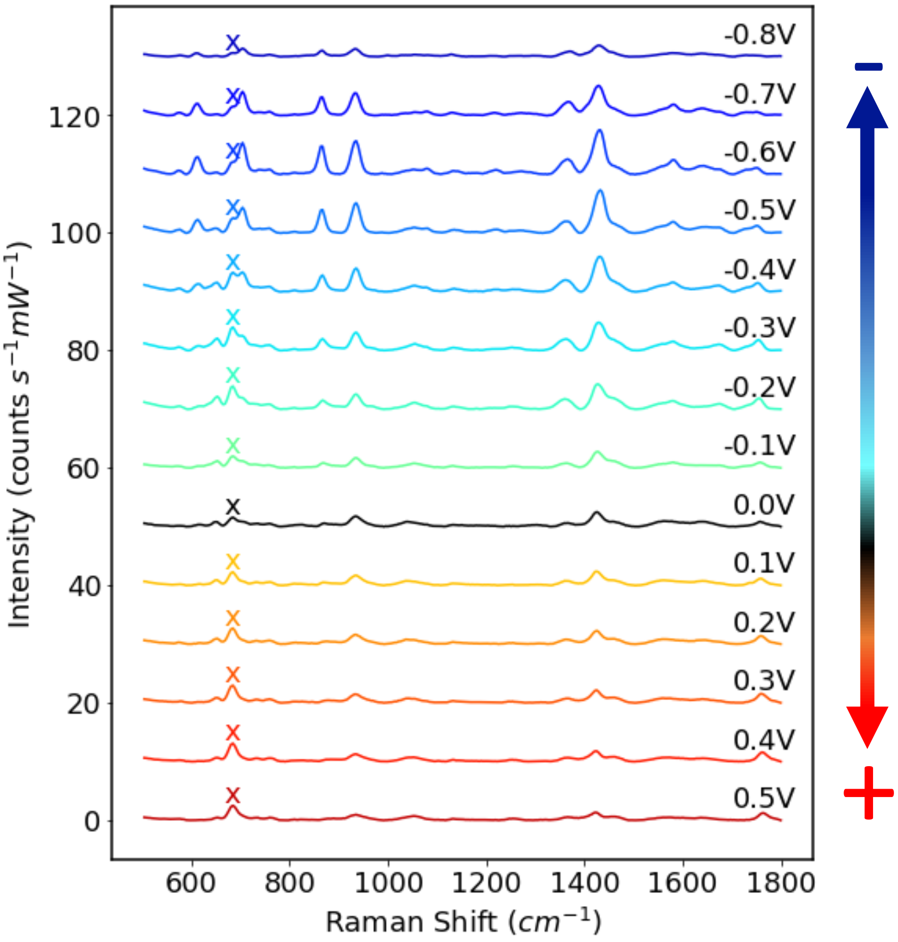

Figure 3.15: E-SERS spectra of 0.5 mM CRN$_{(aq)}$. The applied potential was stepped from 0 to 0.5V and from 0 to -0.8V in 100 mV increments. The characteristic CRN peak is indicated with an x. The spectra plotted are an average of 3 spectra recorded over 5 minutes (with spectra in the first 75 seconds removed to allow for equilibration). (RE: Ag/AgCl; WE: Ag NPs on FTO; CE: platinum plate; supporting electrolyte: 0.1 M NaF).

At 0V, a characteristic creatinine peak is observed at 684 cm^{-1} (Figure 3.16a). As the applied potential becomes more positive, the magnitude of this SERS peak starts to increase, reaching a maximum at 0.4V, and then decreases. During cathodic stepping, the peak at 684 cm^{-1} increases, reaching a maximum at -0.3V, after which it starts to decrease. Other notable changes are observed at the negative potentials. New peaks are recorded at 608 cm^{-1} and 863 cm^{-1} and the characteristic peaks at 684 cm^{-1} and 1421 cm^{-1} start to shift to the right (higher Raman shifts). These changes increase as the applied potential becomes more negative, reaching a maximum at -0.6V. Tentative band assignments of the E-SERS peaks at 0.4V and -0.6V are listed along with the Raman and SERS peaks in Table 3.2.

Table 3.2: Tentative band assignments for Raman, SERS and E-SERS creatinine peaks. Raman spectra were recorded using pure CRN powder and SERS and E-SERS spectra were recorded using 0.5 mM CRN and 0.1 M NaF $_{(aq)}$ on Ag NP/FTO electrodes.[317,318]

Raman Peak (cm^{-1})	**SERS Peak (cm^{-1})**	**E-SERS Peak at 0.4V (cm^{-1})**	**E-SERS Peak at -0.6V (cm^{-1})**	**Band assignment**
608	-	-	608	C-H bending
676	684	684	704	N-H bending
840	-	-	863	N-H bending
1418	1421	1421	1432	C-H bending
1656	1643	1640	1640	C-N stretching
1712	1760	1760	1751	C-O stretching

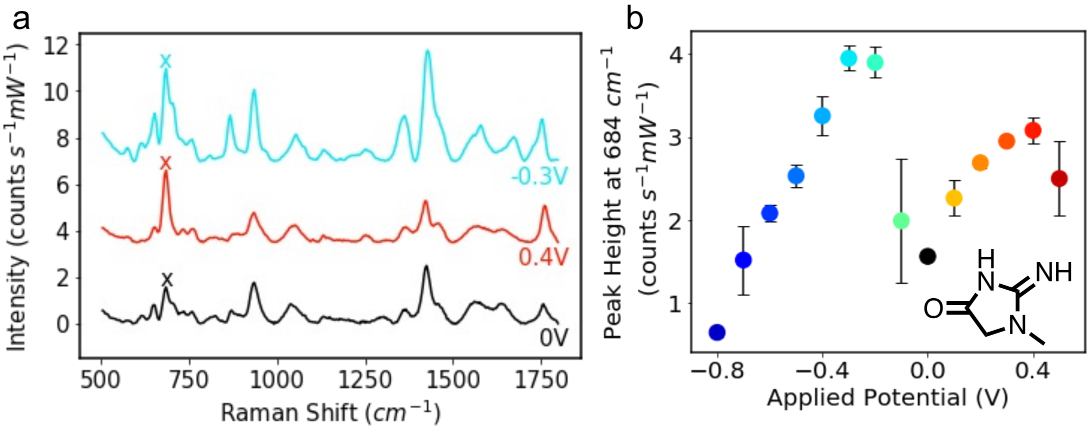

Figure 3.16: E-SERS spectra of a 0.5 mM CRN solution at 0V, 0.4V and -0.3V. The characteristic CRN peak is indicated with an x. (b) The mean height of the characteristic CRN peak at 684 cm^{-1} plotted against applied potential. The applied potential was stepped from 0 to 0.5V and then from 0 to -0.8V in 100 mV increments. The magnitude of the error bars is equal to the standard deviation in the peak height from 3 spectra measured at each potential. (RE: Ag/AgCl; WE: Ag NPs on FTO; CE: platinum plate; supporting electrolyte: 0.1 M NaF).

The two maxima in Figure 3.16b and additional peaks observed at the negative potentials illustrate the complex interactions between the different types of enhancement in the E-SERS system. For the 684 cm^{-1} characteristic peak, the maximum at 0.4V could be due to the adsorption of the CRN molecules onto the Ag NPs and the maximum at -0.3V may be the result of the increased electron density at the negative applied potential. The additional peaks and peak shifts observed at the negative potentials could be the result of a variety of phenomena. Creatinine has two pKa values, one at 4.8 for the imidazolidinone ring nitrogen and another at 12.7 for the amino group.[319] This means in the aqueous solutions studies here CRN exists as a zwitterion with the imidazolidinone ring nitrogen deprotonated and the amino group protonated, resulting in an overall neutral molecule with both positive and negative charges. This means the complex enhancement may be the result of changes in the orientation of the adsorbed CRN molecules due to the differently charged functional groups.[141] Change transfer may also occur between the CRN molecules and the Ag NPs leading to changes in the SERS chemical enhancement.[38] The possibility of redox reactions taking place should also be considered.[164,206,320] It was not possible to determine the oxidation and reduction potentials using cyclic voltammetry but this should be a priority for future work. There have been some reports of silver forming complexes with creatinine during electrochemical cycling so this could be an explanation for the additional peaks observed.[321,322]

3.4.3 Creatinine quantification

Successive E-SERS scans from 0V to 0.3V and then from 0V to -0.4V were performed on an Ag NP/FTO electrode in a 0.1 M NaF solution as the creatinine concentration was gradually increased from 0 μM to 50 μM. The spectra recorded at -0.2V are shown in Figure 3.17. The potential was only scanned between -0.4V and 0.3V and the concentration was only increased to 50 μM due to electrode durability issues, which are examined further in section 3.6.2.

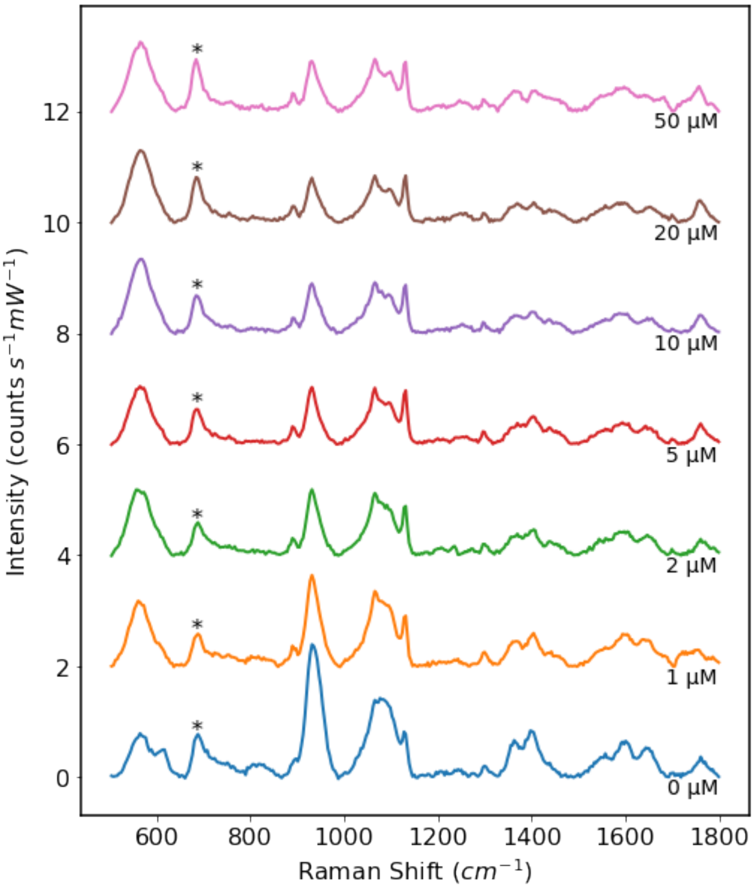

Figure 3.17: E-SERS spectra of CRN solutions with concentrations ranging from 0 µM to 50 µM at an applied potential of -0.2V. The spectra plotted are an average of 3 spectra recorded over 5 minutes (with spectra in the first 75 seconds removed to allow for equilibration). The supporting electrolyte was 0.1 M NaF. (RE: Ag/AgCl; WE: Ag NPs on FTO; CE: Platinum plate).

The height of the 684 cm^{-1} peak is plotted against potential for each of the concentrations in Figure 3.18a and against CRN concentration at -0.2V in Figure 3.18b. A linear relationship was fitted between log(CRN concentration) and the peak height for concentrations from 1 µM to 50 µM with good correlation ($R^2 = 0.97$). Although there is a decent relationship at this potential, the plot in Figure 3.18a is quite messy and there is not a consistent increase in the peak height with increasing CRN concentration for all the applied potentials. The spectra quality is also affected by a significant citrate peak observed at 931 cm^{-1} as discussed in section 3.3.3. These results show that quantitative detection of CRN is possible, but improvements are needed to achieve reliable measurement with this E-SERS system. This is investigated further later in this chapter.

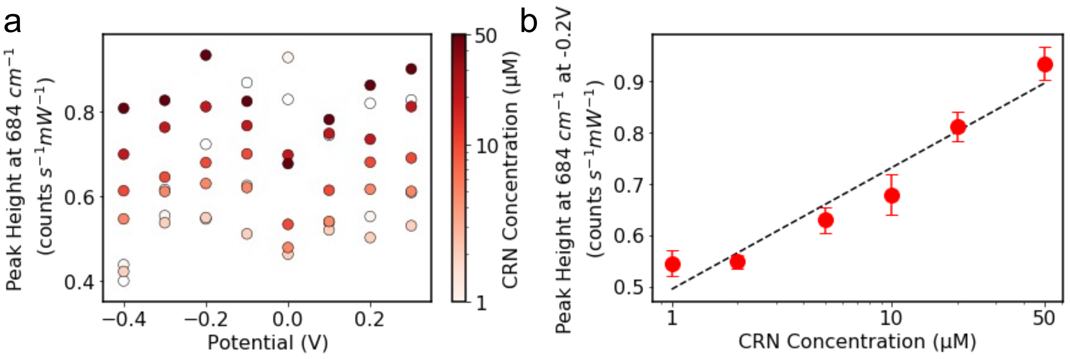

Figure 3.18: (a) Mean peak height at 684 cm^{-1} from 3 spectra plotted against applied potential for each creatinine concentration from 0 μM to 50 μM. (b) Peak height at 684 cm^{-1} plotted against CRN concentration for the spectra recorded at -0.2V. A linear relationship is fitted between log(concentration) and peak height for concentrations from 1 μM to 50 μM ($R^2 = 0.97$) and plotted on a log x-axis. The magnitude of the error bars is equal to the standard deviation in the peak height from 3 spectra measured at each potential.

3.5 Multiplexed detection

The aim of this work is to develop an E-SERS system for the multiplexed detection of analytes in solution. To investigate the feasibility of this idea, two solutions were prepared: the first contained 50 μM UA and 100 μM CRN and the second contained 100 μM UA and 50 μM CRN. For each solution, E-SERS scans were performed using 3 different Ag NP/FTO electrodes (6 electrodes tested in total). During the scans, the applied potential was first stepped in the anodic direction from 0V to 0.4V and then in the cathodic direction from 0V to -0.8V in 100 mV increments.

Figure 3.19b shows spectra from one of the electrodes submerged in solution 1 (50 μM UA and 100 μM CRN). In Figure 3.19a, the spectra are plotted between 550 and 800 cm^{-1}. This section of the spectra contains characteristic peaks for UA and CRN at 636 cm^{-1} and 684 cm^{-1}, indicated by a * and a x respectively. The relative magnitudes of the peaks vary with the applied potential, with the CRN peak being dominant at positive and slightly negative potentials and the UA peak overtaking it at more negative potentials (Figure 3.19c). This behaviour arises from changes in the analyte adsorption at different applied potentials, showcasing how particular analytes can be selectively enhanced through the application of potential, and illustrating the advantage E-SERS has over conventional SERS for detecting multiple analytes.

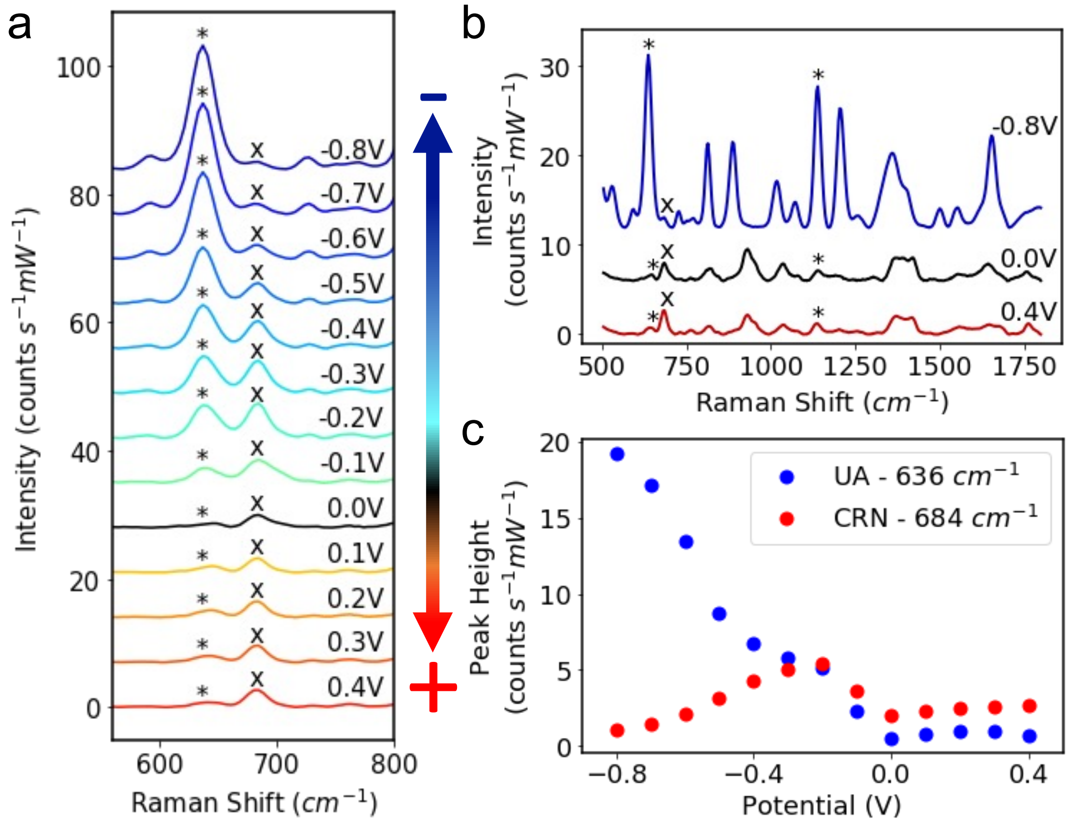

*Figure 3.19: (a) Representative E-SERS spectra of a solution containing 50 µM UA, 100 µM CRN and 0.1 M NaF plotted between 550 and 800 cm^{-1}. The characteristic uric acid and creatinine peaks are indicated by a * and a x respectively. The applied potential was stepped in the anodic direction from 0V to 0.4V and then in the cathodic direction from -0.1V to -0.8V in 0.1V increments. (b) The complete spectra for the same solution recorded at 0.4V, 0V and -0.8V. (c) The height of the characteristic UA and CRN peaks at 636 cm^{-1} and 684 cm^{-1}, respectively, plotted against applied potential. The spectra plotted are an average of 3 spectra recorded over 5 minutes (with spectra in the first 75 seconds removed to allow for equilibration). (RE: Ag/AgCl; WE: Ag NPs on FTO; CE: Platinum plate).*

Although this work focuses on two analytes exhibiting enhancement at positive and negative potentials respectively, the system is not limited to distinguishing between only negatively and positively charged analytes. Due to the complex nature of the E-SERS enhancement, different analytes—depending on their functional groups, charge distributions, and redox properties—respond differently to various applied potentials. These responses can include changes in surface orientation, adsorption, or redox state. Consequently, some analytes may exhibit their strongest SERS signals at slightly negative potentials, while others may show significant enhancement at very negative potentials. This variability is reflected in the diverse optimal potentials reported for different analytes in the E-SERS literature.[243,323] Therefore, it should be feasible to distinguish between three or more analytes. Future work should focus on this aspect, as detecting three or more analytes is crucial for validating multiplexed detection.

Figure 3.19 and the spectra for the other 5 electrodes (which are not included here but exhibited similar trends) demonstrate that simultaneous qualitative detection of uric acid and creatinine is possible with this system. However, the aim of this study was to determine whether reliable quantitative detection is possible. To demonstrate this, the difference between the spectra recorded for the two solutions needs to be larger than the variation between the electrodes. Figure 3.20 shows the peak height at the characteristic uric acid and creatinine peaks respectively plotted against the applied potential. The 3 electrodes which were submerged in solution 1 (50 μM UA and 100 μM CRN) are plotted in red and the 3 electrodes which were submerged in solution 2 (100 μM UA and 50 μM CRN) are plotted in blue. There is not a clear distinction between the red and blue markers for either of the analytes. This demonstrates that the variation in the peak height due to the variability in the Ag NP/FTO electrodes is larger than the variation caused by the difference in the analyte concentration in the two solutions. Therefore, reliable quantitative detection of uric acid and creatinine is not possible with this system in its current form.

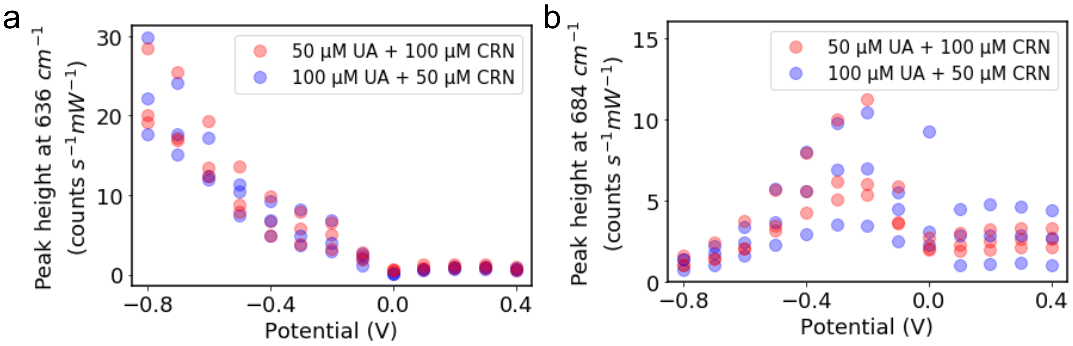

Figure 3.20: The peak height at the characteristic (a) uric acid and (b) creatinine peaks plotted against applied potential for the 6 electrodes used in the multiplexing feasibility study. The electrodes submerged in solution 1 (50 μM UA and 100 μM CRN) and solution 2 (100 μM UA and 50 μM CRN) are plotted in red and blue respectively. The potential was stepped from 0V to 0.4V and then from 0V to -0.8V in 100 mV increments. The spectra plotted are an average of 3 spectra recorded over 5 minutes (with spectra in the first 75 seconds removed to allow for equilibration).

There are many possible reasons for this variability. Firstly, from the TEM and SEM images in section 3.2, it is clear that there are differences in the nanoparticle shape, size and spacing across the electrode surface. This leads to significant differences in the electromagnetic field enhancement, and therefore the SERS signal. Secondly, as discussed in section 3.3.3, the citrate on the surface of the Ag NPs has a major impact on the adsorption of the target analytes onto the substrate, and consequently the SERS spectra. Electrochemical cycling can be used to mitigate this issue but there will still be some variability due to the differences between batches of nanoparticles. Finally, there is the issue of Ag NP ageing.

Silver nanoparticles are known to be vulnerable to photo-assisted oxidation of the surface Ag by O_2.[324,325] This is a concern when using Ag NPs for SERS as the presence of the surface oxide dampens the localised surface plasmon resonance and consequently can lead to reduced SERS enhancements. This is the reason Au NPs are often favoured for SERS; however, Ag NPs exhibit stronger plasmonic resonance than Au NPs and therefore, larger SERS signals which is important when trying to detect low concentrations of analytes. In Figure 3.21, the peak height of the characteristic uric acid peak at 636 cm^{-1} is plotted against applied potential. The number of days since each Ag NP/FTO electrode was fabricated is indicated by the colour of the marker. The older substrates (8 and 10 days since fabrication) generally exhibit slightly lower peak heights than the fresher substrates. It is not possible to determine whether this is a statistically significant effect given the number of samples and the intrinsic variation in the drop-cast Ag NP/FTO electrodes. However, this is an area to consider in the development of the E-SERS system.

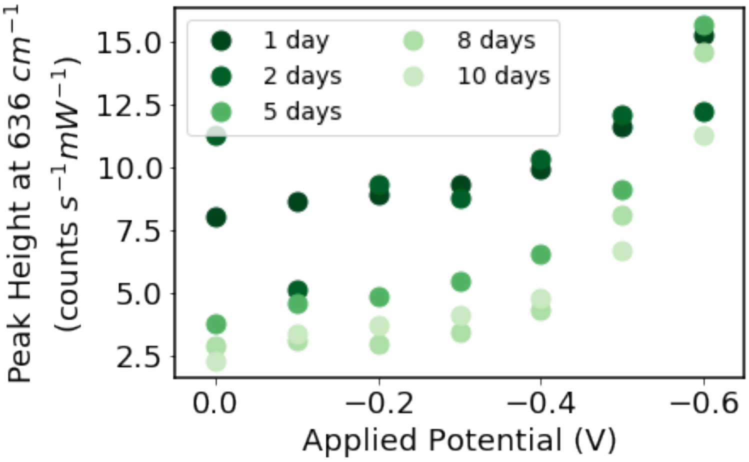

Figure 3.21: The height of the characteristic uric acid peak at 636 cm^{-1} is plotted against the applied potential for multiple E-SERS scans of an aqueous solution containing 0.5 mM UA and 0.1 M NaF. The colour of the marker indicates the number of days since the Ag NP/FTO substrate was fabricated. A different substrate was used for each scan, and this was the first scan for each substrate. In each scan, the applied potential was stepped in the cathodic direction from 0V to -0.6V in 100 mV increments (RE: Ag/AgCl; WE: Ag NPs on FTO; CE: platinum plate).

3.6 Improving the Ag NP/FTO electrodes

Clearly improvements need to be made to the Ag NP/FTO electrodes to achieve effective quantitative multiplexed detection. It is critical that the substrates exhibit reliable SERS enhancements across and between substrates. As discussed in section 1.4.2, this is an area which has been researched extensively and typically there is a trade-off between ease and affordability of fabrication and the magnitude and reliability of the SERS enhancement.[323] One of the key benefits of the Ag NP/FTO electrodes is the ease, speed, and accessibility of the simple drop-cast fabrication method. Improvements to the reliability of the electrode itself are likely to make the fabrication process more complex and potentially more expensive. Therefore, it is preferable to find a way to reduce the variation in the spectra without changing the electrode fabrication method.

3.6.1 Rhodamine 6G (R6G) internal standard

To mitigate the issue of variability without changing the electrode fabrication method, an internal standard can be used. In this approach, a known concentration of a molecule is added to every sample that is analysed and the height of the characteristic peak of that molecule is used to normalise the spectra.[28,45,326,327] Some of the Ag NP/FTO electrodes will have larger SERS enhancements for a variety of reasons including the NP distribution, the shapes of the Ag NPs and oxidation of the silver. Adding a known concentration of another analyte, which has a signal that will be similarly enhanced, means that the SERS signal can be normalised and the variation in the substrates is less problematic. Internal standards are regularly used in SERS systems to improve their quantitative detection.[28,45,326,327]

The key requirements for internal standards for SERS applications are that they are strong Raman scatterers, their SERS peaks do not overlap with the characteristic peaks of the target analytes and their adsorption does not interfere too much with the adsorption of the target analytes. It is also helpful if the standard is a molecule which has been well-studied. For these reasons, Rhodamine 6G (R6G) was chosen as the internal standard. R6G has been successfully used as an internal standard for SERS systems previously and has been studied extensively.[145,327–329] R6G is a highly fluorescent dye molecule and is known to exhibit resonance Raman due to a molecular electronic transition in the visible region (absorption maximum at 530 nm).[330] On the one hand, this means very large SERS signals can be observed which means reliable signals can be observed even at trace levels. This allows lower concentrations to be used for the internal standard minimising potential issues from competitive binding. However, the high levels of fluorescence observed for R6G, and the generally large peaks could also mean that the characteristic peaks of the target analytes are obscured and harder to identify.

The E-SERS spectra for a 10 μM R6G and 0.1 M NaF solution recorded using a Ag NP electrode are shown in Figure 3.22. The R6G exhibits strong E-SERS peaks. The largest peak is at 1362 cm^{-1} and is assigned to C-C stretching in the xanthene ring[15]. The magnitude of the R6G peaks varies with applied potential (Figure 3.23), with the largest peaks being observed at 0V and smaller peaks present at the greater applied potentials. This is likely due to the changes in the adsorption of the R6G molecules on the NP surface.

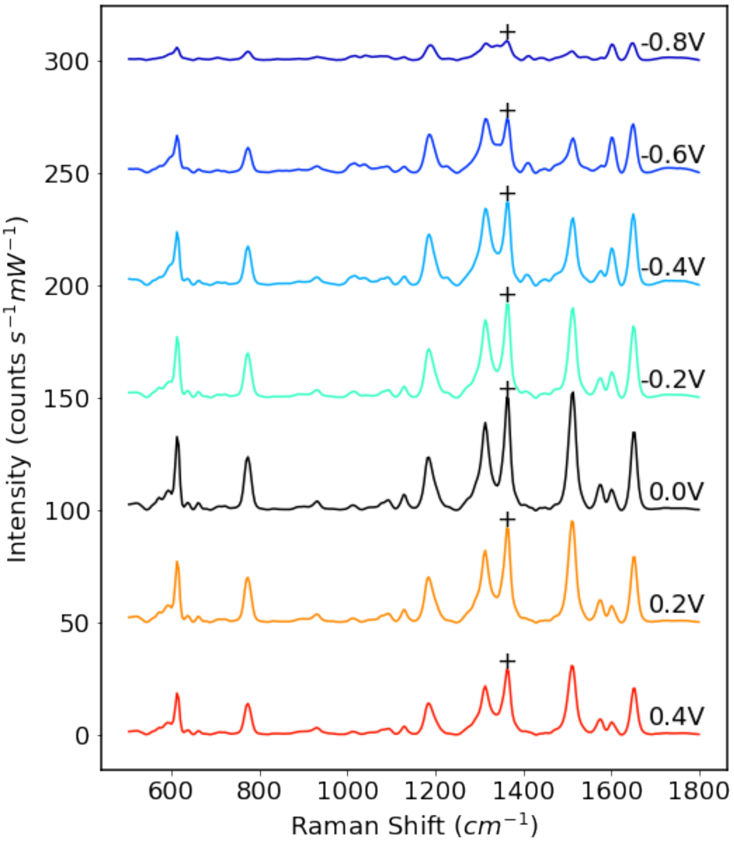

Figure 3.22: E-SERS spectra of a solution containing 10 μM R6G and 0.1 M NaF. The characteristic peak at 1362 cm^{-1} used for normalisation is indicated by a +. The applied potential was stepped in the anodic direction from 0V to 0.4V and then in the cathodic direction from -0.2V to -0.8V in 0.2V increments. The spectra plotted are an average of 3 spectra recorded over 5 minutes (with spectra in the first 75 seconds removed to allow for equilibration) (RE: Ag/AgCl; WE: Ag NPs on FTO; CE: Platinum plate).

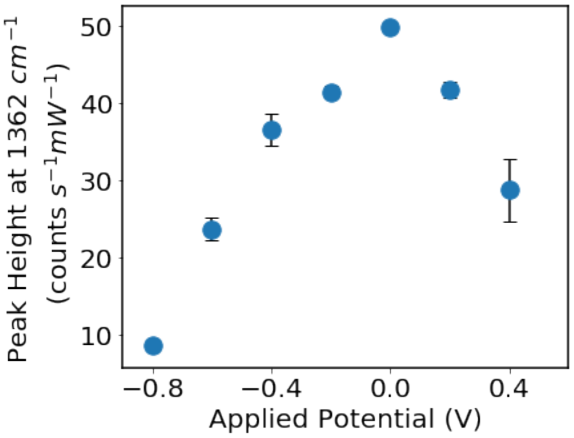

Figure 3.23: The height of the characteristic R6G peak at 1362 cm^{-1} plotted against applied potential for a solution containing 10 μM R6G and 0.1 M NaF. The magnitude of the error bars is equal to the standard deviation in the peak height from 3 spectra measured at each potential (RE: Ag/AgCl; WE: Ag NPs on FTO; CE: Platinum plate).

In theory, this variation with potential should not prevent the acquisition of quantitative E-SERS spectra providing it is consistent and reliable. If the R6G peaks are always changing in the same way, then they can be used to normalise the spectra and enable improved comparison between electrodes. However, there could potentially be an issue with competitive adsorption. High concentrations of the target analytes in the solution could affect the adsorption of the R6G onto the Ag NP surface. This could mean that the R6G peak is smaller than anticipated for a particular electrode and therefore, the normalisation would not give a representative peak height. Here, a low concentration of R6G (10 μM) was chosen as it gave reliable strong SERS peaks without obscuring the peaks of the target analytes or producing a very large fluorescent background. This should also hopefully reduce the potential impact of competitive adsorption. However, it is important to be aware of this issue and this is discussed further in section 4.2.2.

To test the feasibility of using R6G as an internal standard for the E-SERS system, an aqueous solution was prepared containing 100 μM uric acid, 10 μM R6G and 0.1 M NaF. E-SERS scans were performed in this solution using 3 different Ag NP/FTO electrodes. During the scans, the applied potential was first stepped in the anodic direction from 0V to 0.3V and then in the cathodic direction from 0V to -0.6V in 100 mV increments. The R6G peak at 1362 cm^{-1} was used as the reference peak for normalisation. The normalised spectra for one of the electrodes are shown in Figure 3.24. It was still possible to see the characteristic uric acid peak at 636 cm^{-1} and although it appears small relative to the R6G peaks, the height of the peak here is comparable to the height of the UA peak for a 100 μM UA solution when R6G is not present.

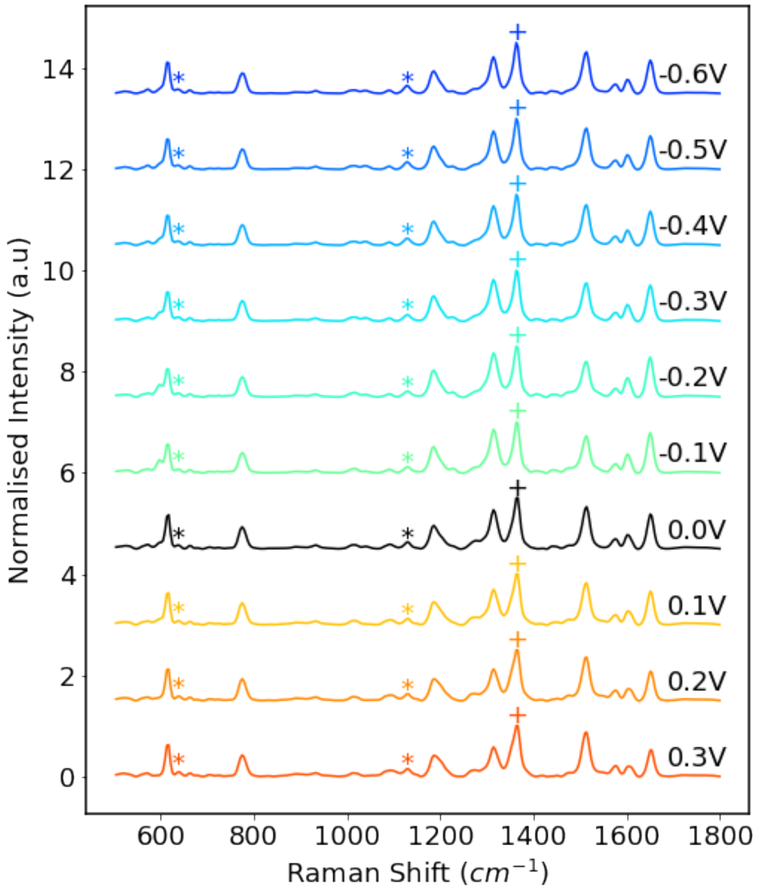

Figure 3.24: R6G normalised *E-SERS spectra of a solution containing 100 µM uric acid, 10 µM R6G and 0.1 M NaF. The characteristic* UA *and* R6G *peaks are indicated by a * and a + respectively. The applied potential was stepped in the anodic direction from 0V to 0.3V and then in the cathodic direction from -0.1V to -0.6V in 0.1V increments. The spectra plotted are an average of 3 spectra recorded over 5 minutes (with spectra in the first 75 seconds removed to allow for equilibration) (RE: Ag/AgCl; WE: Ag NPs on FTO; CE: Platinum plate).*

To assess whether the R6G had helped to improve the reliability of the uric acid detection, the spectra from the three electrodes were normalised using the 1362 cm^{-1} peak as the reference peak. The height of the characteristic uric acid peak at 636 cm^{-1} was extracted from each normalised spectra and the mean and standard deviation were calculated for the three electrodes. The standard deviation as a percentage of the mean peak height for the original and normalised spectra are plotted in Figure 3.25. The percentage standard deviation is significantly lower for the R6G normalised spectra than the original spectra at all potentials. In particular, at -0.6V the standard deviation for the R6G normalised spectra is over 4 times smaller than for the original spectra. This suggests that using R6G as an internal standard can alleviate the issue of electrode variability and help the E-SERS system to achieve quantitative multiplexed detection without increasing the cost or complexity of the electrodes.

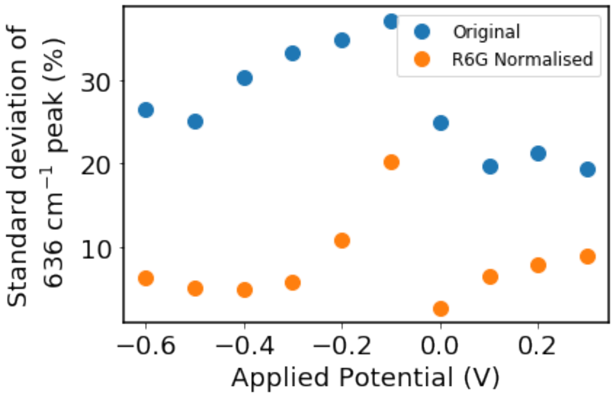

Figure 3.25: The standard deviation of the characteristic uric acid peak at 636 cm^{-1} as a percentage of the mean peak height for the original and R6G normalised spectra. The standard deviation is calculated for 3 Ag NP/FTO electrodes which were submerged in a 100 μM uric acid, 10 μM R6G, 0.1 M NaF (aq) solution. (RE: Ag/AgCl; WE: Ag NPs on FTO; CE: Platinum plate).

3.6.2 APTES coating to improve adhesion

Issues were identified with the adhesion of the Ag NP film onto the FTO-coated glass. Sometimes during the E-SERS scans, part or all of the Ag NP film would become detached and slide off the glass surface preventing any further experiments (Figure 3.26a). This is a particular problem when larger potentials are being applied (e.g. -0.8V or 0.5V) or if the electrode needs to be moved. This has limited the potentials which can be applied in the E-SERS scans and the number of scans that can be run on a single electrode.

(3-aminopropyl)triethoxysilane (APTES) is commonly used to improve the adhesion of Ag and Au nanoparticles on a variety of substrates.[331–335] The APTES molecules bond to the surface of the FTO-coated glass *via* their hydrolysable alkoxy groups and the exposed amine groups interact electrostatically with the surface of the Ag NPs.[331,335] To determine whether APTES could help to improve the adhesion of the Ag NP/FTO electrodes without affecting the E-SERS spectra, a short trial was conducted. An FTO-coated glass electrode was coated with APTES (following the procedure in section 2.3.2) and the concentrated Ag NP solution was drop-cast onto the surface as normal. The APTES coating made the surface slightly hydrophobic and the contact angle between the glass and the Ag NP solution was larger than normal. This led to the formation of a slightly smaller Ag NP film circle (~0.5 cm vs. ~0.8 cm diameter). This could be beneficial as the variation in the spread of the Ag NP solution could be contributing to the variability in the Ag NP/FTO electrodes.

To test the APTES-coated electrode, an E-SERS scan was performed from 0V to -0.8V to 0.4V to 0V in a 100 μM UA + 0.1 M NaF (aq) solution. After the scan, the electrode was removed from the solution and left to dry. The same process was performed on an Ag NP/FTO electrode fabricated without APTES. This procedure was repeated 4 times for each electrode. The APTES electrode showed no visible degradation after 4 E-SERS scans whereas the electrode without APTES showed considerable damage including sections where the NP film had flaked off the glass (Figure 3.26b). There was no significant difference between the E-SERS scans performed with and without APTES. The characteristic uric acid peak was clearly visible, and the SERS signal responded to the applied potential in the typical way (Appendix Figure A.3). This is a significant improvement which increases the likelihood that reliable quantitative multiplexed detection can be achieved with this E-SERS system. It also opens up new possibilities in terms of cleaning and reusing the Ag NP/FTO electrodes.

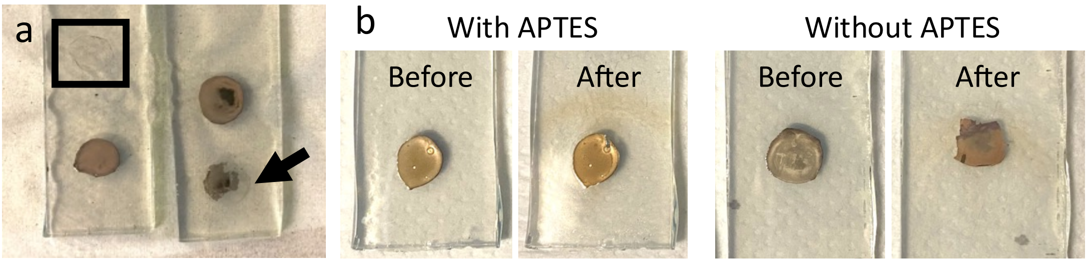

Figure 3.26: (a) Examples of degradation of the Ag NP/FTO electrodes after E-SERS scans. (b) Images of the electrodes from the APTES trial showing the two electrodes before and after 4 E-SERS scans.

3.7 Quantitative single analyte detection with improved electrodes

Based on the research detailed in this chapter, three key improvements were implemented in the E-SERS measurement procedure. First, the FTO-coated electrodes were coated with APTES to improve the adhesion of the Ag NP film on the surface. The improved adhesion also made it possible to measure spectra at a wider potential range (from -0.8V to 0.4V), which is beneficial as the optimal potential for multiplexed detection of UA and CRN are -0.8V and 0.4V, respectively. Second, a complete scan from 0 to +0.4 and from 0V to -0.8V was performed in the analyte solution before starting to measure SERS spectra to remove the adsorbed citrate from the Ag NP surface and allow improved detection of the target analytes. Lastly, 10 μM R6G was added to all analyte solutions and the characteristic R6G peak at 1362 cm^{-1} was used to normalise the spectra and enable better comparison between different electrodes.

To demonstrate the progress achieved by these improvements, quantitative single analyte detection tests were performed for UA and CRN (like those carried out in sections 3.3.4 and 0). Successive E-SERS scans were performed on Ag NP/FTO electrodes which had been coated in APTES before drop casting. The potential was scanned from 0V to 0.4V to -0.8V to 0V in steps of 0.2V. The scans were performed in a solution containing 10 μM R6G and 0.1 M NaF. The analyte concentration was gradually increased from 0 μM to 100 μM for UA and 0 - 1000 μM for CRN.

The R6G normalised characteristic peak heights are plotted against applied potential in Figure 3.27a and Figure 3.27c. For UA, the characteristic peak at 1138 cm^{-1} is used here (as opposed to the 636 cm^{-1}) as it is further from any of the R6G characteristics peaks. The R6G normalised 1138 cm^{-1} peak height at -0.8V is plotted against UA concentration in Figure 3.27b. A linear relationship is fitted between UA concentration and the peak height for concentrations from 1 μM to 100 μM ($R^2 = 0.99$) and then plotted on a log scale to improve readability and allow the lower concentration points to be distinguished. In Figure 3.27d, the normalised 684 cm^{-1} peak height at 0.4V is plotted against CRN concentration. A linear relationship is fitted between log(CRN concentration) and the peak height for concentrations from 1 μM to 1000 μM ($R^2 = 0.90$) and plotted on a log scale. For both of these plots, the limit of detection (LoD) was calculated as 3.3 times the standard error of the slope of the calibration line divided by the slope (i.e. $3.3\sigma/S$).[336] This resulted in a LoD of 0.13 μM for UA and 0.35 μM for CRN. These results are compared to literature reported values in Table 3.3 and Table 3.4. The LoDs reported here are significantly lower than those reported for drop-cast colloidal Ag NPs previously and are comparable to many of the results achieved for much more complex nanofabricated electrodes.

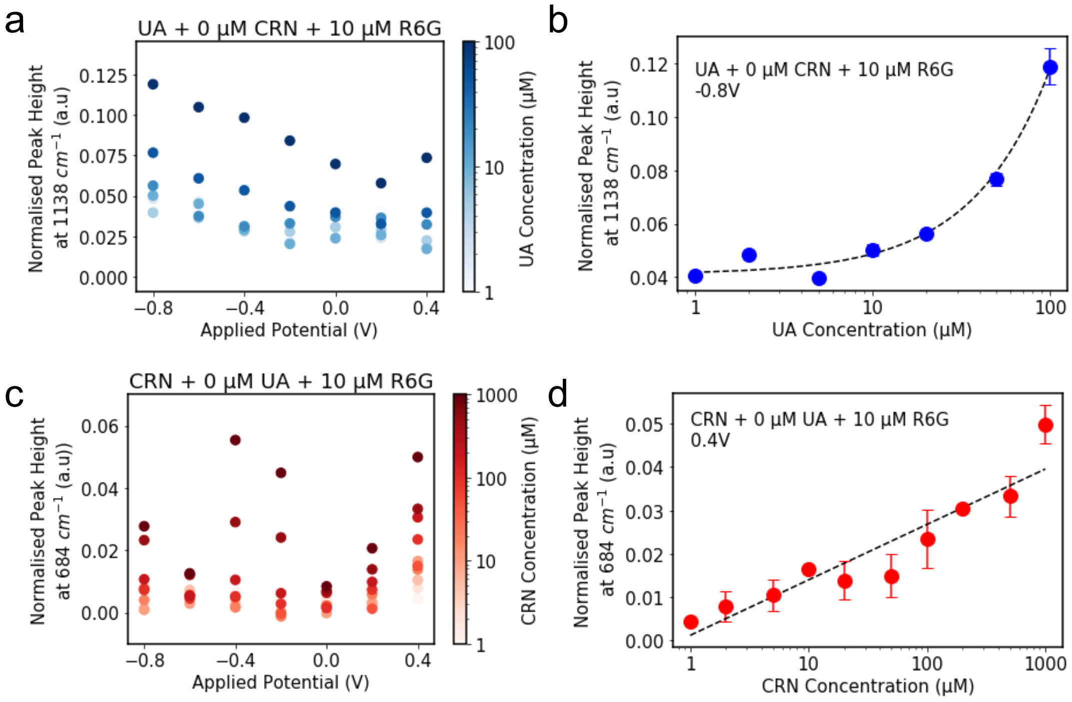

Figure 3.27: (a) The height of the characteristic UA peak at 1138 cm^{-1} plotted against applied potential for UA concentrations from 1 μM to 100 μM. The colour of the markers represents the UA concentration and is log-scaled. (b) The peak height at 1138 cm^{-1} plotted against UA concentration for the spectra recorded at -0.8V. A linear relationship is fitted between UA concentration and the peak height for concentrations from 1 μM to 100 μM ($R^2 = 0.988$) and then plotted on a log scale for readability. (c) The height of the characteristic CRN peak at 684 cm^{-1} plotted against applied potential for CRN concentrations from 1 μM to 1000 μM. The colour of the markers represents the CRN concentration and is log-scaled. (d) The peak height at 684 cm^{-1} plotted against CRN concentration for the spectra recorded at 0.4V. A linear relationship is fitted between log(CRN concentration) and the peak height for concentrations from 1 μM to 1000 μM ($R^2 = 0.902$). The spectra plotted are an average of 3 spectra recorded over 5 minutes (with spectra in the first 75 seconds removed to allow for equilibration) and the magnitude of the error bars is equal to the standard deviation in the peak height from the 3 spectra measured at each potential. (RE: Ag/AgCl; WE: Ag NPs on FTO; CE: platinum plate; supporting electrolyte: 0.1 M NaF).

Table 3.3: Detection of uric acid by SERS or E-SERS reported in the literature.

Method	**Material**	**Limit of detection (μM)**	**Linear range (μM)**	**Reference**
SERS	Ag NPs	110	0 - 3500	[279]
SERS	Ag NPs	5	5 - 1000	[337]
SERS	Ag NPs	1.7	5 - 1000	[338]
SERS	Ag NPs/ZnO/Fe3O4	0.365	0.5 - 10	[339]
SERS	Au NP:CB7 nanoaggregates	0.2	0.2 - 10	[124]
E-SERS	Au nanopillars	0.001	0.01 - 100	[340]
E-SERS	Multi-layered Au NPs/Ag NPs	100	100 - 1000	[209]
E-SERS	Polycarbonate nanocone array decorated with Au NPs	0.087	0.1 - 100	[242]
E-SERS	Ag NPs	0.13	1 - 100	This study

Table 3.4: Detection of creatinine by SERS reported in the literature.

Method	**Material**	**Limit of detection (μM)**	**Linear range (μM)**	**Reference**
SERS	Ag NPs	88.40	88.40 - 2475	[341]
SERS	Jaffe complex on Ag film	25	25 – 150	[311]
SERS	Boron nitride/Au nanocomposite	10	10 - 200	[342]
SERS	Ag NPs	5	5 - 1000	[337]
SERS	Au NP-coated blu-ray DVD	1.77	1.77 – 8.84	[343]
SERS	Au NP:CB7 nanoaggregates	0.53	0.53 – 13.26	[122]
SERS	Nanoporous Au disk	0.1	0.1 - 100	[344]
SERS	Au dendritic nanostructure	0.97	17.7 - 2829	[345]
SERS	Polyelectrolyte multilayers over Au film	0.29	1 - 1000	[317]
E-SERS	Ag NPs	0.35	1 - 1000	This study

3.8 Conclusion

In this chapter, the quantitative detection of uric acid and creatinine using E-SERS was demonstrated. Applying a potential to the SERS electrodes results in significant enhancement of the Raman signal of these analytes and enables lower concentrations to be detected compared to conventional SERS. During this research, issues were identified with the Ag NP/FTO electrodes relating to the durability and variability of the Ag NP film. These problems would have prevented the electrodes from being used successfully for reliable multiplexed detection. To improve the adhesion of the Ag NP film on the FTO-coated glass, the substrates were coated with APTES which allowed larger potentials to be applied to the electrodes and increased their lifespan. To overcome the variability issues, R6G was used as an internal standard to normalise the E-SERS spectra. This reduced the variation in the SERS signal and enabled reliable quantitative detection. Application of negative potentials was also used to remove the citrate adsorbed on the surface of the Ag NPs and allow improved detection of the target analytes.

These improvements enabled the quantitative detection of UA and CRN. At the optimal applied potentials, limits of detection of 0.127 μM (UA) and 0.354 μM (CRN) were achieved. With linear ranges of 1 – 100 μM and 1 – 1000 μM for UA and CRN, respectively. The LoD achieved for UA is significantly lower than the concentrations previously detected by colloidal Ag NP E-SERS systems (0.1 mM)[208,209] and comparable to many of the results achieved for much more complex nanofabricated electrodes. Quantitative E-SERS detection of CRN has not been reported previously but LoD compares favourably to the results achieved for sophisticated SERS set-ups. The LoDs and linear ranges are well within the clinically relevant ranges for these biomarkers[300,346] indicating that urine samples could be diluted significantly before testing, therefore minimising the disruption to the Raman signal caused by other analytes in the complex matrix.[122] This is investigated in the next chapter of this thesis.

Preliminary tests were performed for solutions containing both UA and CRN. It was possible to clearly identify the peaks of both analytes in the multiplexed solutions, with the applied potential enabling the effective modulation of the spectra and enhancement of the peaks of a particular analyte. The next step is to investigate the quantitative multiplexed detection of uric acid and creatinine using E-SERS. This is the focus of the next chapter of this thesis.

Chapter 4 Quantitative multiplexed detection of uric acid and creatinine with E-SERS and machine learning

4.1 Motivation

In the previous chapter, an E-SERS system was developed which could detect low concentrations (down to 1 μM) of uric acid and creatinine and demonstrated promise for multiplexed detection. The next step is to investigate the system's potential for quantitative detection of the two analytes. To do this, extensive E-SERS testing of solutions containing varying concentrations of uric acid and creatinine is needed to build up a large dataset of spectra. This dataset can then be used to investigate the capacity of the E-SERS system for quantitative multiplexed detection.

Up until now, quantitative detection of multiple analytes using E-SERS has not been reported and is likely to be difficult without additional functionalities within the system. Machine learning (ML) for SERS analysis is growing rapidly, with techniques such as partial least squares regression (PLSR), and artificial neural networks (ANNs) being employed to recognise subtle patterns in SERS datasets and identify the presence or concentration of analytes in unseen spectra. ML approaches have been used to classify or quantify biomarkers[49,265], bacteria[268,269], and food products[48,270,271]. In addition to improving interpretation, it reduces the need for time-consuming visual inspection of SERS spectra by trained operators, increasing the practicality of SERS as an analytical technique. Machine learning has recently been used for E-SERS classification of fentanyl-related compounds[347], but it is yet to be applied to quantitative E-SERS. However, the additional complexity within the datasets, which comes from the applied potential, makes it an ideal application for these techniques.

In this chapter, a large E-SERS dataset (> 2,300 spectra) is recorded using the optimised Ag NP/FTO electrodes for solutions containing various concentrations of UA and CRN. Three different machine learning approaches are then applied to interpret the spectra and predict the analyte concentrations from unseen spectra. The different ML approaches are compared and discussed. Finally, proof-of-concept experiments are performed in dilute synthetic urine to demonstrate the detection of clinically relevant concentrations of UA and CRN.

4.2 Multiplexed E-SERS dataset

Extensive E-SERS testing was performed to build up a dataset of spectra for solutions containing different concentrations of uric acid and creatinine. All the SERS spectra were recorded using the electrodes fabricated by drop-casting Ag NPs onto APTES-coated FTO-coated glass and a 633 nm, 22 mW laser with an integration time of 7s. The supporting electrolyte was 0.1 M NaF and a leakless Ag/AgCl reference electrode and a platinum plate counter electrode were used. All solutions contained 10 μM R6G and the peak at 1362 cm^{-1} was used to normalise the spectra.

The applied potential was scanned from 0V to 0.4V and from 0V to -0.8V in increments of 0.2V and the potential was held for 5 minutes to allow multiple SERS spectra to be recorded before the next potential was applied. Spectra recorded in the first 75s were not included in the analysis to give the system time to equilibrate, this resulted in 3 spectra which were included in the analysis for each potential step. From looking at the chronoamperometry curves, the current appears to stabilise within this time and the spectra do not change significantly after this point (Appendix Figure A.4). As discussed in section 3.3.3, a full potential scan was performed on each electrode before recording any spectra to counter the issue of citrate desorption.

The UA concentrations tested were 0, 1, 2, 5, 10, 20, 50 and 100 μM. For CRN, the same concentrations were tested, plus 200, 500 and 1000 μM. Spectra were recorded using 20 different electrodes for 86 unique concentration combinations. In total, the dataset contained 2,348 spectra. The concentration ranges tested using each electrode are detailed in Table 4.1. Occasionally, despite the improvements achieved by the APTES coating, the Ag NP film would become detached from the substrate after multiple E-SERS scans. This is why some electrodes do not cover the full concentration range.

Table 4.1: Details of the electrodes used, and UA and CRN concentrations tested to build the multiplexed E-SERS dataset.

Electrode	UA Concentration (μM)	CRN Concentration (μM)
1	0	0 - 1000
2	1	0 - 1000
3	2	0 - 500
4	5	0 - 1000
5	10	0 - 1000
6	20	0 - 500
7	50	0 - 1000
8	100	0 - 1000
9	100	0 -100
10	0 - 100	0
11	0 - 200	0
12	0 - 10	10
13	0 - 100	20
14	0 - 50	50
15	0 - 100	100
16	0 - 50	100
17	0 - 100	200
18	0 - 5	500
19	0 - 10	1000
20	50 - 100	1000

4.2.1 Example of quantitative multiplexed detection

Examples of the results from the multiplexed E-SERS tests are shown in Figure 4.1. In these tests, the concentration of one analyte was held at 20 μM whilst the concentration of the other was gradually increase (from 0 μM to 100 μM for UA and from 0 μM to 100 μM for CRN). All the spectra recorded were normalised using the characteristic R6G peak at 1362 cm^{-1} and the characteristic peak height at the optimal potential is plotted against analyte concentration (1138 cm^{-1} at -0.8V for UA and 684 cm^{-1} at 0.4V for CRN). The point plotted is the mean peak height and the magnitude of the errors bars is ± the standard deviation.

A linear relationship is fitted between UA concentration and the peak height for concentrations from 1 μM to 100 μM (R^2 = 0.99) (Figure 4.1a). It is difficult to distinguish between concentration up to 5 μM but concentrations above 10 μM can be clearly differentiated. For CRN, a linear relationship is fitted between log(CRN concentration) and the peak height for concentrations from 1 μM to 1000 μM (R^2 = 0.88) (Figure 4.1b). The CRN peak is clearly identified for all solution concentrations down to 1 μM.

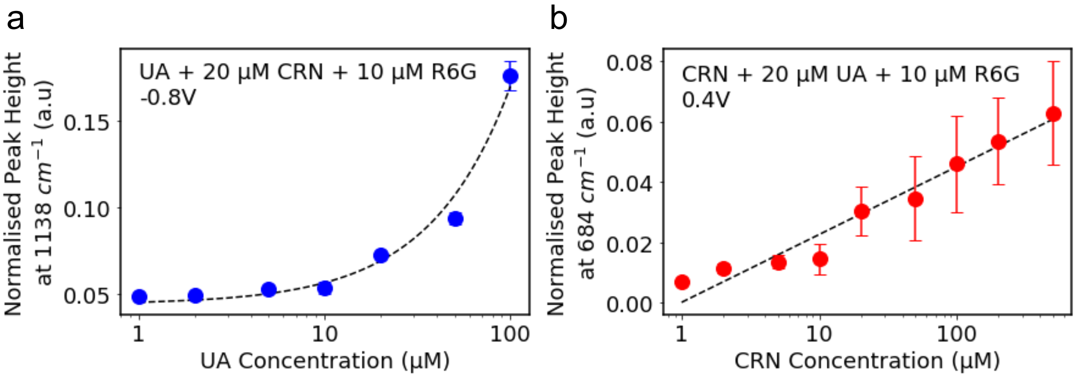

Figure 4.1: (a) *The* mean *1138 cm^{-1} UA peak height normalised using the R6G peak at 1362 cm^{-1} and plotted against UA concentration for the spectra recorded at -0.8V for a solution containing 20 μM CRN and 10 μM R6G. A linear relationship is fitted between UA concentration and the peak height for concentrations from 1 μM to 100 μM (R^2 = 0.99) and then plotted on a log scale for readability.* (b) *The* mean *R6G normalised peak height at 684 cm^{-1} plotted against CRN concentration for the spectra recorded at 0.4V for a solution containing 20 μM UA and 10 μM R6G. A linear relationship is fitted between log(CRN concentration) and the peak height for concentrations from 1 μM to 1000 μM (R^2 = 0.88). The magnitude of the error bars is equal to the standard deviation in the peak height from 3 spectra measured at each potential (RE: Ag/AgCl; WE: Ag NPs on FTO; CE: Platinum plate).*

The results included here exhibit clearly identifiable peaks and a strong correlation between the peak height and analyte concentration. However, the results for some of the electrodes were less impressive. The characteristic peak height did increase with concentration but, in some cases, the relationship was weaker (lower R^2s) and the characteristic peak heights were smaller. This is likely due to the variations in the quality of the electrodes.

4.2.2 Quantitative multiplexed with full dataset

In Figure 4.2, all the spectra recorded using the electrodes detailed in Table 4.1 (2,348 spectra in total) are combined and the height of the characteristic peaks are plotted against analyte concentration at the optimal potential. A linear relationship is fitted between UA concentration and the 1138 cm^{-1} peak height at -0.8V (R^2 = 0.66) and between log(CRN concentration) and the 684 cm^{-1} peak height at 0.4V (R^2 = 0.39). Clearly, these R^2 values are low, and the errors bars shown in Figure 4.2 are very large. However, it is important to note that these spectra were recorded using different electrodes and a wide variety of analyte concentrations, unlike the results in Figure 4.1 which were recorded with one electrode and a constant second analyte concentration. It is promising to observe that there is a consistent trend, with the characteristic peak heights increasing with concentration, and although the standard deviation in the peak heights is large, the mean values show a positive relationship.

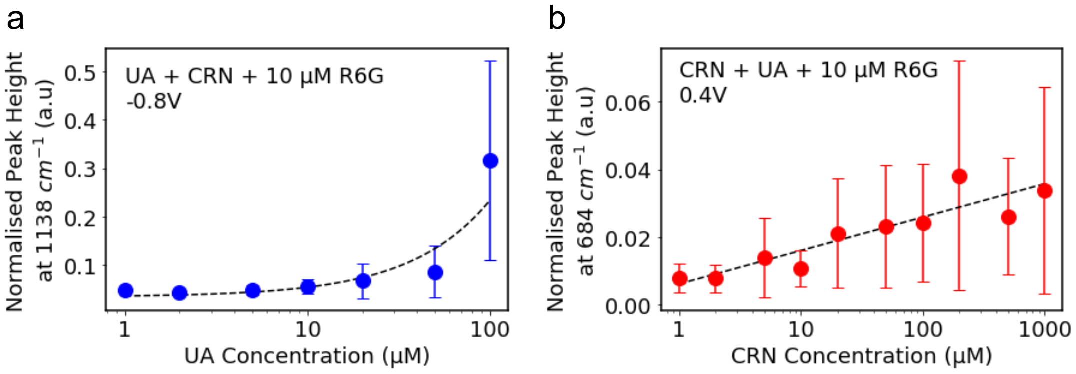

Figure 4.2: (a) The mean R6G normalised peak height at 1138 cm^{-1} plotted against UA concentration for the spectra recorded at -0.8V for solutions containing between 0 – 1000 μM CRN and 10 μM R6G. A linear relationship is fitted between UA concentration and the peak height for concentrations from 1 μM to 100 μM (R^2 = 0.66) and then plotted on a log scale for readability. (b) The R6G normalised peak height at 684 cm^{-1} plotted against CRN concentration for the spectra recorded at 0.4V for a solution containing between 0 - 100 μM UA and 10 μM R6G. A linear relationship is fitted between log(CRN concentration) and the peak height for concentrations from 1 μM to 1000 μM (R^2 = 0.39). The magnitude of the error bars is equal to the standard deviation in the peak height from 3 spectra measured at each potential (RE: Ag/AgCl; WE: Ag NPs on FTO; CE: Platinum plate).

The use of the R6G as an internal standard has helped to improve the results. The R^2 for the UA peak height/concentration plot is 0.23 without R6G normalisation, compared to 0.66 with normalisation. For CRN, the R^2 without normalisation is 0.21 compared to 0.39 with normalisation. When the idea of using R6G as an internal standard was initially presented in section 3.6.1, the potential issue of competitive adsorption was raised. The presence of the other analytes (UA and CRN) could impede the adsorption of the R6G onto the surface of the Ag NPs and therefore, reduce the magnitude of the characteristic R6G peak in the SERS spectra. This would be a problem as it would reduce the validity of the R6G normalisation.

In Figure 4.3, the height of the characteristic R6G peak at 1362 cm^{-1} in spectra recorded at 0V is plotted against the total analyte concentration (sum of UA and CRN concentration). Generally, there is significant variation in the peak height due the variability of the Ag NP/FTO electrodes. However, there is a weak negative correlation (R^2 = -0.47) between the peak height and the log(total analyte concentration). This implies that the R6G peaks are being affected to some extent by the adsorption of the target analytes on the surface. There could also be other factors affecting this, including the fact that the higher concentrations are more commonly tested later in the E-SERS measurement cycle so electrode ageing or adhesion could be playing a part too. This result is not particularly pronounced and is unlikely to have a substantial effect on the results considering the variability in the other parts of the E-SERS system. However, it would be an area to investigate in the future. A possible improvement could be to use a smaller molecule as the internal standard or a molecule which binds less strongly to the Ag surface, which may be less likely to prevent adsorption of target analytes on the NP surface.

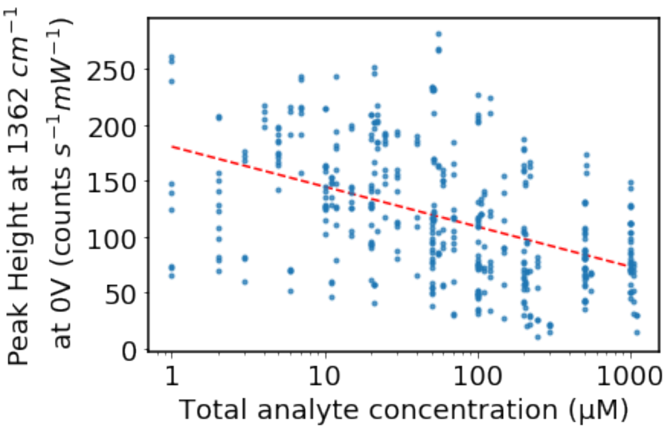

Figure 4.3: The R6G characteristic peak height at 1362 cm^{-1} plotted against total analyte concentration (UA + CRN) for the spectra recorded at 0V for solutions containing 10 µM R6G and between 0 - 100 µM UA and 0 – 1000 µM CRN. A linear relationship is fitted between log(total analyte concentration) and the peak height for concentrations from 1 µM to 1100 µM (R^2 = -0.47).(RE: Ag/AgCl; WE: Ag NPs on FTO; CE: Platinum plate).

The issue of competitive adsorption also applies to the target analytes. The concentration of one analyte (e.g. UA) will likely affect the adsorption of the other analyte (e.g. CRN) on the Ag NP surface and therefore influence the characteristic peak height of the latter. Attempts were made to investigate this phenomenon by examining how the characteristic peak heights of each analyte changed with increasing concentrations of the other analyte. However, the variation in the E-SERS system and differences between the electrodes meant that it was not possible to observe a consistent trend. This suggests that it may not be a major obstacle for the quantitative multiplexed detection of UA and CRN. Nevertheless, competitive adsorption likely influences the system to some extent and is likely to be a bigger issue in clinical samples which contain larger components, such as proteins. This is an area which should be investigated further. Some attempts have been made to investigate this behaviour in SERS systems. For example, Grys *et al.* developed an automated robotic system which was able to study the competitive binding of methylviologen and its deuterated isomer in a solution-based cucuit[*n*]uril-Au NP system.[348] The use of the automated robotic system enabled the collection of sufficiently reproducible data to study this sensitive interaction. To my knowledge, similar work has not been attempted with a E-SERS system, which has the added complication of the applied potential, but this would be an interesting area of future research.

Despite some encouraging results for the multiplexed detection (Figure 4.1), significant variation was observed when comparing the spectra recorded with different electrodes and mixtures of analytes (Figure 4.2). It is evident that achieving reliable quantitative multiplexed detection using the type of conventional calibration curve plots shown in Figure 4.2, would not be possible. However, these plots are only looking at the height of a single peak at a single potential. This disregards valuable information present in the rest of the SERS spectra that can aid in identifying the analyte concentration. Machine learning algorithms, on the other hand, leverage the entire spectra to identify subtle patterns and make more accurate predictions. This is a particularly effective approach in complex, multi-analyte solutions.

4.3 Machine learning approaches for quantitative detection

4.3.1 Linear regression

To set a benchmark for the investigation into different machine learning models, a simple linear regression-based approach was tested first. The spectra recorded at the optimal potentials (-0.8V for UA and 0.4 for CRN) were selected from the multiplexed E-SERS dataset and separated into training and test dataset (80:20). The R6G normalised characteristic peak heights (1138 cm^{-1} for UA and 684 cm^{-1} for CRN) were extracted and the training dataset was used to fit a linear regression model. This linear regression was then used to predict the analyte concentrations from the test dataset. The prediction accuracies were 0.26 and 0.018 for UA and CRN respectively (Appendix Figure A.5). Clearly, this is unacceptably low, and a different approach is needed to improve the prediction accuracy.

4.3.2 Partial least squares regression

As discussed in section 1.5.1, partial least squares regression (PLSR) is a popular supervised machine learning approach which is commonly used to analyse SERS datasets. It works by reducing the dimensionality of the predictor (X) variables by finding new latent variables (or components) which best describe the variation in the response (Y) variables.[258] The new variables are linear functions of those in the original dataset, with each variable successively increasing the total variance explained by the latent variables.

When employing a PLSR model, it is important to choose the number of components carefully to avoid over or under-fitting. To find the optimal number of components, partial least squares regression was performed on the multiplexed E-SERS dataset with 1 to 31 components, and the R^2 was calculated. 5-fold cross validation was used to give representative results for the whole dataset. As expected, the cross-validated R^2 increases with the number of PLSR components. Figure 4.4 shows that the cross-validated R^2 starts to plateau above 14 components. Therefore, to avoid overfitting, 14 components was used for the PLSR model.

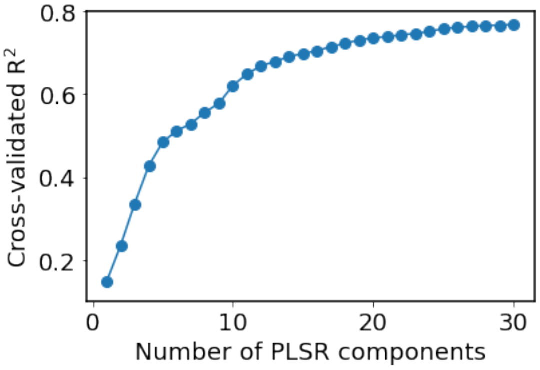

Figure 4.4: The cross-validated R^2 values for PLSR regression models with varying numbers of PLSR components. The R^2 values were calculated using 5-fold cross-validation.

The prediction results for the PLSR model with 14 components are shown in Figure 4.5. The overall R^2 value for the two analytes was 0.72. This is a significantly improvement on the simple linear regression model and clearly shows the benefit of utilising the entire SERS spectra. However, the prediction accuracy of 0.72 is not especially high and there were some concentrations where the predictions differ significantly from the true values, for example the higher CRN concentrations.

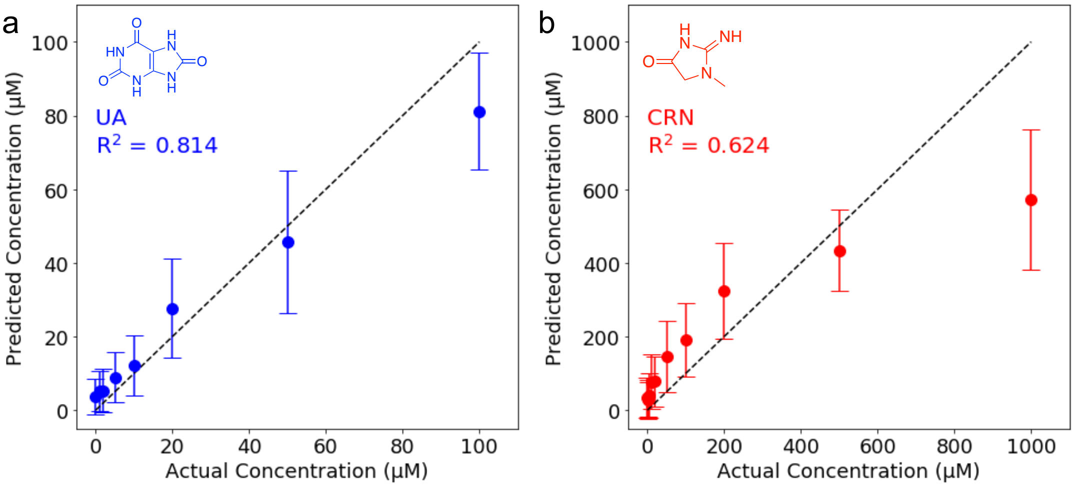

Figure 4.5: A comparison of the actual concentrations and the predicted concentrations for *the* 14-component PLSR model *for (*a*) UA and (*b*) CRN. The magnitude of the error bars is equal to the standard deviation of the predictions. The dotted y=x line represents perfect agreement between the actual and predicted concentrations.*

4.3.3 Multilayer perceptron

Multilayer perceptrons (MLPs) are a simple type of feed-forward artificial neural network, which consist of three layers of neurons – an input layer, one or more hidden layers and an output layer.[117,263] In MLPs, each neuron in one layer is connected to every neuron in the following layer.[255] Initially, the connections between neurons are assigned random weights.[117] When the network is presented with a training dataset, back-propagation is used to iteratively adjust the weights to reduce the difference between the output results and the actual results.[117,255,263] This process is repeated until the error is below an acceptable level. The resulting trained network can then be used to determine the output for a new unseen input dataset.

The scikit-learn MLP Regressor has various parameters that can be optimised for a particular dataset. The parameters used in this test are detailed in Table 4.2. The activation function is the function that is applied to the weighted sum of the node inputs to generate the node output. The rectified linear unit (ReLU) function is currently the most popular activation function in ANNs.[349] It is defined as:[349]

$$f(x) = max\ (0, x) \qquad \text{Equation 20}$$

where x is the input to the neuron or node. ReLU was chosen for this work because it is faster and simpler than the more traditional sigmoid activation function. The limited-memory Broyden-Fletcher-Goldfarb-Shanno (L-BFGS) algorithm was used for the weight optimisation as it is recommended over more commonly used stochastic gradient descent methods for small datasets because it converges faster and performs better.[349,350]

Table 4.2: Optimised parameters used for the multilayer perceptron.

Parameter	**Value**
Number of input nodes	361 (The number wavenumber shifts in the SERS spectra after pre-processing plus the applied potential)
Number of output nodes	2 (The number of analytes)
Hidden layer nodes	16, 64, 64 (Determined by Bayesian optimisation)
Activation function	ReLU (Rectified Linear Function)
Algorithm for weight optimisation	Limited-memory BFGS

A Bayesian optimiser using Gaussian processes was employed to find the optimal hidden layer architecture for the MLP. Bayesian optimisation is a strategy that can be used to efficiently determine the optimal parameters for a machine learning algorithm.[349,351] It involves testing different parameters and quantifying their performance to identify the best one. Unlike random or grid search, the choice of which parameter to try next is based on the results of all the previous tests which makes it much more efficient.[260,349] Bayesian optimisation with Gaussian processes constructs a probabilistic (surrogate) model of the objective function using a Gaussian process which is updated after every test.[352] The choice of parameters for each trial is based on the probability that they will give an improvement over the current best result.

When selecting the hyperparameters for ML, it is important to avoid overfitting, so the test dataset was selected and removed at the beginning and 5-fold cross validation was employed to find the optimal parameters using the remaining data. Here, the Bayesian optimiser was set up so the MLP could have between 1 and 3 layers and each layer could have 4, 8, 16, 32 or 64 nodes. This results in 155 possible options. During the optimisation, a possible MLP architecture was selected from these options. The performance of this MLP model was then quantified by calculating the R^2 from 5 K-fold splits of the training dataset.[295] As the optimisation progressed, the selection started to converge. After 50 selections, the architecture that resulted in the highest R^2 was returned and this was used to build the final MLP model.

For the Bayesian optimiser described here, the highest cross-validated R^2 of 0.80 was found for a hidden layer architecture of (16, 32). Figure 4.6 shows how the R^2 evolved over the optimisation process. This hidden layer architecture was used to build an MLP which was trained on the entire training set and then used to predict the analyte concentrations from the unseen spectra in the test dataset. The prediction accuracy (R^2) was 0.75 and the results for the MLP are plotted in Figure 4.7.

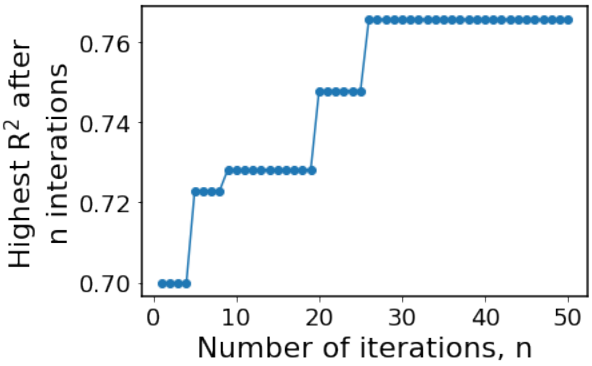

Figure 4.6: The highest R^2 after n iterations of the 50 iterations of the Bayesian optimisation with Gaussian processes for the MLP.

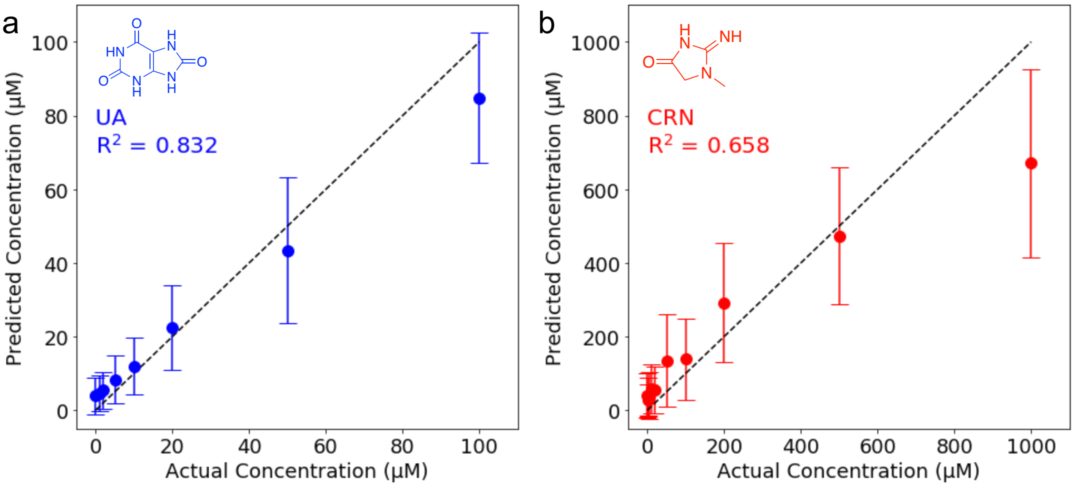

Figure 4.7: A comparison of the actual concentrations and the predicted concentrations for *the* MLP model *for* (a) *UA and* (b) *CRN. The magnitude of the error bars is equal to the standard deviation of the predictions. The dotted y=x line represents perfect agreement between the actual and predicted concentrations.*

4.3.4 Two-step PLSR-MLP algorithm

The results for the PLSR and MLP models were promising but they were still not achieving especially high prediction accuracies. In an attempt to combine the merits of the two approaches, a two-step PLSR-MLP algorithm was devised. In this approach, PLSR is used to reduce the dimensionality of the SERS spectra, and then the new latent variables are combined with the applied potential to create the input layer for the MLP.

For the PLSR, the dataset (excluding the applied potentials) is split into a m x n **X** matrix and a p x n **Y** matrix where n is the number of spectra, m is the number of wavenumber shifts in the SERS spectra after pre-processing (360, from 500 - 1800 cm^{-1}, equally spaced) and p is the number of analytes, which is 2.[258,259] The dimensionality of the **X** matrix is then reduced to a specified number of latent variables (k) which best describes the variance in the **Y** matrix. The result is a k x n **T** matrix. The **T** matrix is then combined with the applied potential to create a $(k+1)$ x n **T+P** matrix. The **T+P** matrix is the input layer for the MLP which is used to make the concentration predictions. The two-step PLSR-MLP algorithm is illustrated in Figure 4.8.

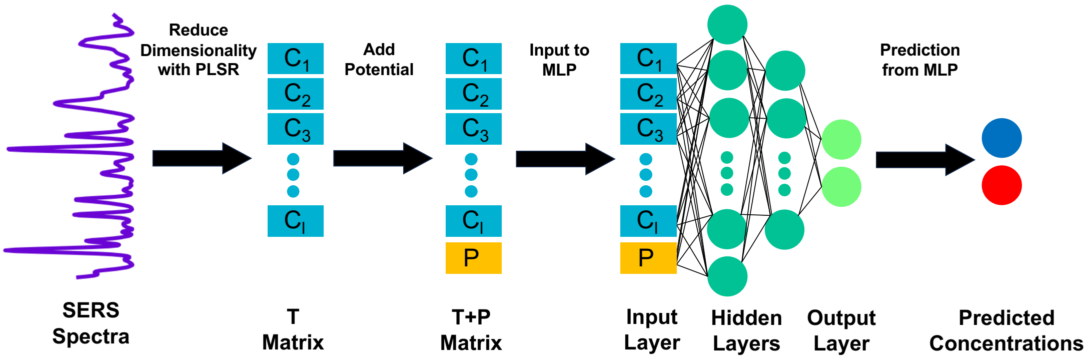

Figure 4.8: Schematic diagram illustrating the two-step PLSR-MLP algorithm which was used to predict the UA and CRN concentrations from unseen E-SERS spectra.

As with the MLP, a Bayesian optimiser using Gaussian processes was employed to find the optimal hyperparameters. Here, it was used to determine the number of latent variables for the PLSR and the hidden layer architecture for the MLP. The PLSR could have between 5 and 60 latent variables (or components) and the MLP could have between 1 and 3 layers. Each layer could have 4, 8, 16, 32 or 64 nodes. This results in 8525 possible options. As with the MLP, the performance of each option was quantified by calculating the R^2 from 5 K-fold splits of the training dataset.[295] 150 iterations were tested in this case as there were more possible options. The highest R^2 values were achieved for 44 PLSR components and a MLP hidden layer architecture of (32,32,32).

Figure 4.9a shows how the R^2 evolved over the optimisation process. The R^2 values for different numbers of PLSR components are plotted in Figure 4.9b. Generally, the prediction accuracy increases with the number of PLSR components as the total variance explained increases as additional components are added. However, when over 50 PLSR components were used, the R^2 started to decrease, which is likely due to overfitting.

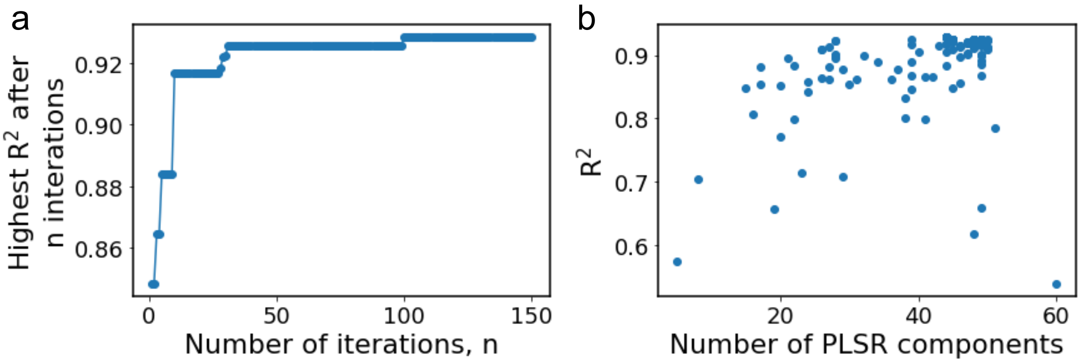

Figure 4.9: (a) The highest R^2 after n iterations of the 150 iterations of the Bayesian optimisation with Gaussian processes for the two-step PLSR-MLP algorithm. (b) The R^2 values achieved for the different numbers of PLSR components tested in the Bayesian optimisation of the two-step PLSR-MLP algorithm.

The optimal parameters identified by the Bayesian optimiser (44 PLSR components and a MLP hidden layer architecture of (32, 32, 32)) were used to construct the two-step PLSR-MLP algorithm. The model was trained on the entire training set and then used to predict the analyte concentrations from the unseen spectra in the test dataset. The prediction accuracy (R^2) was 0.94 and the results for the two-step PLSR-MLP model are plotted in Figure 4.10. The predicted concentrations are plotted against the actual concentrations and the points are very close to the y = x line, indicating excellent prediction accuracy. The R^2s for UA and CRN were 0.96 and 0.91, respectively. The prediction accuracies for the three ML algorithms tested are compared in Table 4.3.

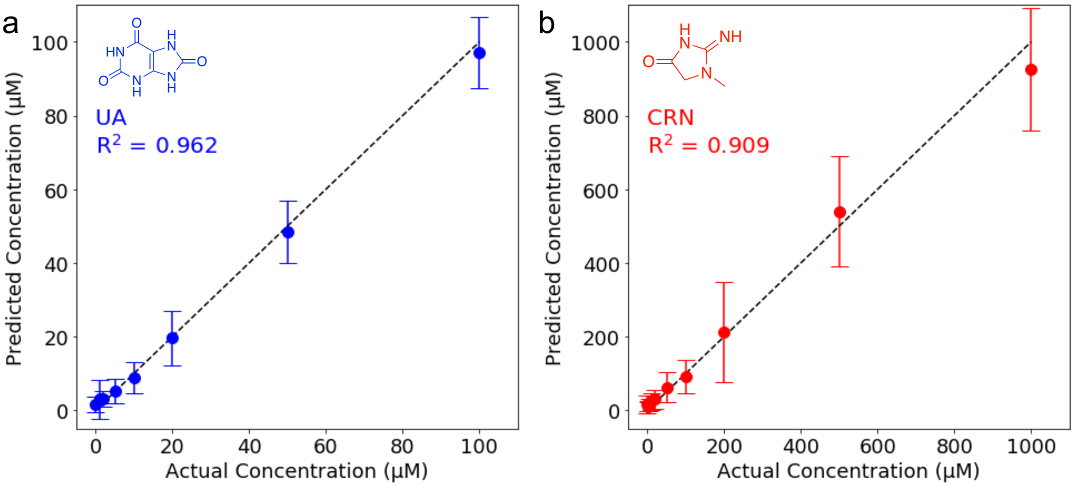

Figure 4.10: A comparison of the actual concentrations and the predicted concentrations for the two-step PLSR-MLP model for (a) UA and (b) CRN. The magnitude of the error bars is equal to the standard deviation of the predictions. The dotted y=x line represents perfect agreement between the actual and predicted concentrations.

Table 4.3: Comparison of the prediction accuracies (R^2s) of the different machine learning algorithms: partial least squares regression (PLSR), multilayer perceptron (MLP), and the two-step PLSR-MLP model.

Model	**UA prediction accuracy (*R*^{2})**	**CRN prediction accuracy (*R*^{2})**
PLSR	0.81	0.62
MLP	0.83	0.66
PLSR-MLP	0.96	0.91

To evaluate the effect of the applied potential, the same process was used to build a two-step PLSR-MLP algorithm using only the spectra recorded at 0V. The prediction accuracy for this dataset was 0.50, which is significantly lower than the 0.94 achieved when all spectra recorded at different potentials are included (Appendix Figure A.6). Indeed, the fact that the dataset has been shrunk significantly (482 vs. 2,348 spectra) will influence the performance of the model, however, the same test was performed using only the spectra recorded at -0.8V and 0.4V and they achieved prediction accuracies of 0.92 and 0.86, respectively. This highlights that the benefits offered by E-SERS over SERS in standard spectral analysis also apply when machine learning is used.

For machine learning models, the root mean square error of prediction (RMSEP) can be taken as an indication of the limit of detection of the system. The RMSEP of the two-step PLSR-MLP algorithm was 5.93 μM for UA and 84.7 μM for CRN. These results are comparable to those reported in the literature for single analyte detection of uric acid (Table 3.3) and creatinine (Table 3.4) using Ag NP SERS. It is encouraging to see that by combining E-SERS with machine learning, it is possible to achieve similar levels of quantitative detection for more complex solutions containing multiple analytes.

The concentration ranges studied in this work are well within the clinically relevant range for uric acid[300,353,354] and creatinine[346,353,354]. This is beneficial as it means samples could be diluted significantly before testing, minimising any disruption to the Raman signal caused by other analytes in the complex matrix.[122]

4.3.5 Interpretation of ML models

It is important to try and understand how ML algorithms are making their predictions. For PLSR, it is possible to investigate this by looking at the coefficient plots. These plots show the coefficients which relate the X variables (spectra) to the Y variables (analyte). The coefficients are not directly used to make the predictions but are a function of all the latent variables in the regressor. The coefficient plots for the PLSR part of the two-step PLSR-MLP algorithm are shown in Figure 4.11 alongside representative spectra of the uric acid and creatinine at the optimal potentials. The magnitude of the coefficients at a particular wavenumber indicates their importance in predicting the concentration of the analyte. Large positive coefficients show that a wavenumber has a strong positive correlation with the concentration or presence of an analyte.

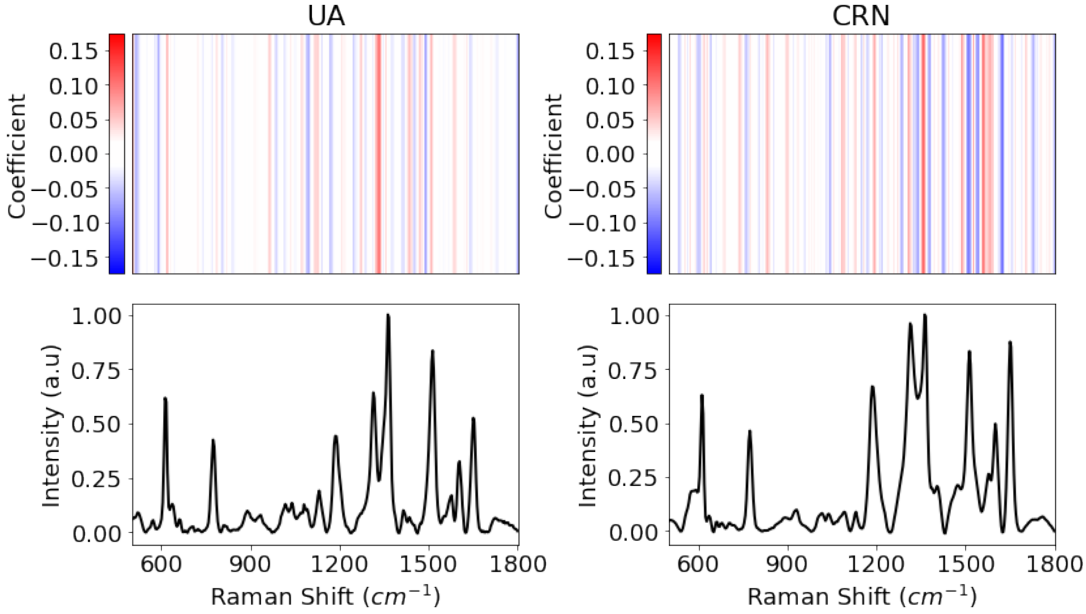

Figure 4.11: Coefficient plots for UA and CRN for the PLSR part of the two-step PLSR-MLP algorithm shown above representative SERS spectra of the analytes. Brighter colours indicate a stronger relationship between a specific wavenumber and the concentration of the analyte.

The results in Figure 4.11 are not particularly clear but it is possible to see a correlation between the larger coefficients (brighter colours) and the peaks in the spectra. The fact that the R6G peaks dominate the spectra makes it harder to interpret the coefficient plots, but it is possible to see a difference between the UA and CRN plots with larger coefficients being observed around the analyte's characteristic peaks.

It is much harder to investigate the MLP part of the two-step PLSR-MLP model. MLPs, or more generally ANNs, are often described as "black boxes" because it is hard to determine how a particular model makes its predictions.[355] Unlike PLSR models, ANNs are difficult to interpret and identifying which predictor values are the most important and how they relate to the response variables is challenging. This can lead to famous failures such as when a deep neural network that claimed to be able to diagnose skin cancer from pictures of skin lesions with impressive accuracy was revealed to be making its predictions partly based on whether there was a ruler in the image.[356,357] ANNs are also prone to over-fitting and often lack robustness. This is illustrated by the example of a deep neural network which will change its classification of a picture of a horse to a frog when a single pixel is altered.[358,359]

Overfitting is a particular problem when the training dataset is small. Machine learning, and neural networks especially, rely on large training datasets to build robust models and overfitting is much more likely to occur when the dataset is small. Although the E-SERS dataset contains 2,348 spectra, this is still small in ML terms. Recent leading work in the field of ML for SERS has utilized training datasets of over 10,000 SERS spectra and achieved impressive results.[268,360] It is difficult to collect datasets of this size without automation or large-scale collaboration. However, if it were possible to do this in the future, it would improve the robustness of the model and its predictions.

4.4 Detection in synthetic urine

To assess the potential of E-SERS for the detection of UA and CRN in clinical settings, E-SERS tests were performed in synthetic urine (SU). The SU contained urea, NaCl, KCl, NaH_2PO_4, citric acid and albumin.[279,280] Initially, spectra were recorded for SU which did not contain UA or CRN (Figure 4.12a). Generally, the spectra are quite noisy compared to the spectra recorded in deionised water. This is attributed to the presence of many additional molecules in the solution, particularly the albumin, as large molecules like proteins are known to have noisy SERS spectra due to the number of different vibrational modes present.[125] A large peak is observed at 1002 cm^{-1}, which is attributed to the symmetric N-C-N bond stretching in urea.[361] Next, E-SERS spectra were recorded for a synthetic urine solution which also contained 0.5 mM UA and 0.5 mM CRN (Figure 4.12b). NaF was omitted as the supporting electrolyte since the SU contains many ions that can sustain the flow of charge within the system. Even though high concentrations of the target analytes were present, it is difficult to identify the characteristic peaks in the noisy spectra. It is slightly easier to see the UA peaks at -0.8V but they are still too small to ensure reliable quantification.

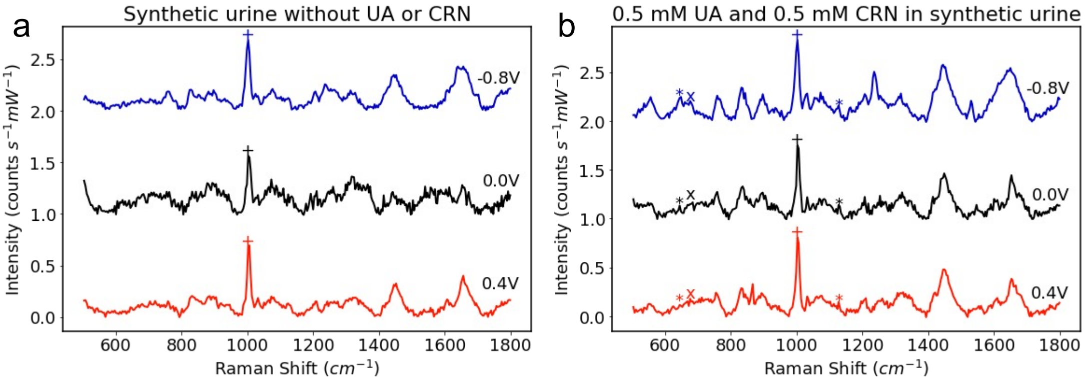

*Figure 4.12: E-SERS spectra of (a) synthetic urine and (b) 0.5 mM UA and 0.5 mM CRN in synthetic urine. The characteristic UA, CRN and urea peaks are indicated with a *, x, and + respectively. The spectra plotted are an average of 3 spectra recorded over 5 minutes (with spectra in the first 75 seconds removed to allow for equilibration) (RE: Ag/AgCl; WE: Ag NPs on FTO; CE: platinum plate; supporting electrolyte: 0.1 M NaF).*

The previous tests have established that the Ag NP electrode/E-SERS system could detect low concentrations of UA and CRN (LODs of 0.13 μM and 0.35 μM respectively). Therefore, it was possible to dilute the synthetic urine and still record spectra for clinically relevant concentrations of UA and CRN, which reduces the potential for interference from the other molecules in the SU.[300,346,353,354] In Figure 4.13, E-SERS spectra for a 10% SU solution containing 20 μM UA, 1000 μM CRN, 10 μM R6G, and 0.1 M NaF are plotted. This corresponds to urinary UA and CRN concentrations of 0.2 mM and 10 mM, which are within the normal healthy ranges for adults. The characteristic UA and CRN peaks can be clearly identified in the diluted SU E-SERS spectra. There is no major interference from other molecules, although it is still possible to identify the urea peak at 1002 cm^{-1}. The CRN peak is significantly easier to identify at the optimal applied potential, -0.4V, than at 0V, which further highlights the benefits of E-SERS over conventional SERS for the multiplexed detection of analytes in complex solutions. These results show that it is possible to detect clinically relevant concentrations of UA and CRN in dilute synthetic urine using the Ag NP electrode/E-SERS system. This implies that, if a large enough dataset of E-SERS spectra was recorded, it could be possible to train a two-step PLSR-ANN algorithm to quantitively detect clinically relevant concentrations of UA and CRN in urine.

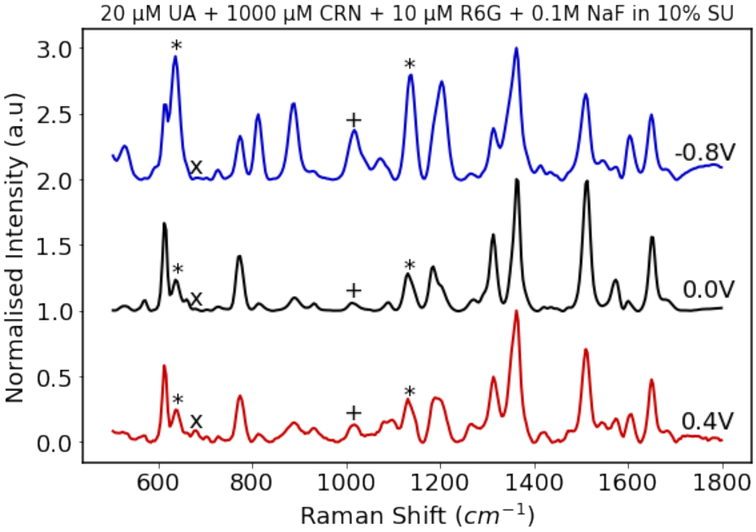

*Figure 4.13: E-SERS spectra of a solution containing 20 μM UA, 1000 μM CRN, 10 μM R6G, and 0.1 M NaF in a 10% synthetic urine solution. The characteristic UA, CRN and urea peaks are indicated with a *, x, and + respectively. The spectra plotted are an average of 3 spectra recorded over 5 minutes (with spectra in the first 75 seconds removed to allow for equilibration) (RE: Ag/AgCl; WE: Ag NPs on FTO; CE: platinum plate; supporting electrolyte: 0.1 M NaF).*

It is important to note that real urine is much more complex than synthetic urine and contains a much larger range of components. Bouatra *et al.* created a database which contains 2651 confirmed human urine metabolite species.[362] These include amino acids, peptides, lipids, carbohydrates, isoflavones, and thiols. Therefore, to properly assess the capabilities of the E-SERS system, tests would need to be carried out with real human urine.

4.5 Conclusion

This chapter has demonstrated the quantitative multiplexed detection of uric acid and creatinine through E-SERS and machine learning using simple Ag NP electrodes. An extensive multiplexed E-SERS dataset was collected, and different machine learning approaches were applied to interpret the spectra. A two-step PLSR-MLP machine learning algorithm was developed which was able to predict the analyte concentrations of unseen spectra with a prediction accuracy of 0.94. The RMSEP, which can be taken as an indication of the limit of detection of the system, was 5.93 μM for UA and 84.7 μM for CRN. Finally, proof-of-concept experiments were performed in dilute synthetic urine to demonstrate the detection of clinically relevant concentrations of UA and CRN.

The next step would be to build up a similar E-SERS dataset for UA and CRN in synthetic urine (or potentially clinical urine samples). This dataset could then be used to train a two-step PLSR-MLP machine learning algorithm which could perform multiplexed quantification. Ideally, this dataset would be larger than the one described in this chapter (over 5,000 spectra) to improve the robustness of the model. The same approach could also be applied to other biomarkers in urine (or other bodily fluids). Studies should also be carried out with three or more biomarker to verify multiplex detection. This work demonstrates the potential that E-SERS and ML have in trace analyte detection and highlights the benefits they offer over conventional SERS analysis.

Chapter 5 Hybrid tin dioxide coated silver nanoparticles for SERS

5.1 Motivation

In recent years, there has been growing interest in hybrid plasmonic metal–semiconductor nanomaterials for SERS.[57,58] These hybrid systems combine the large electromagnetic enhancements achieved by plasmonic metals, with additional chemical enhancements (CE) resulting from charge transfer between the semiconductor and metal or adsorbed molecules. A key example of hybrid SERS is photo-induced enhanced Raman scattering (PIERS), developed by the Parkin group in 2016 (section 1.3.5).[60] In PIERS, Au or Ag colloids are deposited on top of metal oxide films, which have been irradiated with UV light to create oxygen vacancies (V_o). The V_os increase the CE by enabling additional charge transfer resulting in signals which are ca. 1 order of magnitude higher than conventional SERS. TiO_2, the standard PIERS substrate, does not exhibit the additional enhancement without UV-irradiation and when the UV-light is removed the enhancement disappears after approximately an hour.

So far, PIERS has been used to detect explosives[60], pollutants[60,66], and biomarkers.[60,67,68] Zhang *et al.* developed a TiO_2-Ag PIERS substrate to detect the fungicide, thiram, which demonstrated an up to 27.8-fold enhancement over conventional SERS with a limit of detection of 10 nM.[66] PIERS has also been used as a characterization method to study oxygen vacancy behaviour in photocatalytic materials.[62,363,364]

SnO_2 is an n-type, wide band gap (3.6 eV) semiconductor oxide which contains intrinsic oxygen vacancies.[365] This means it can exhibit photo-induced charge transfer without UV-irradiation. Recently, our group demonstrated that colloidal SnO_2-coated gold nanotriangles (Au NTs) can achieve significant enhancements in Raman signal over bare Au NTs without UV-activation due to charge transfer from the SnO_2 to the Au which is made possible by the intrinsic oxygen vacancies in the SnO_2.[366] The hybrid system achieved a limit of detection of 88 nM for an explosive marker (2,4-DNT) in water, exhibiting signals 16 times stronger than those of bare Au NTs.

Building on this work, the idea of using colloidal Ag nanoparticles coated with SnO_2 (Ag@SnO_2 NPs) in a solid electrode was investigated as a possible extension of the E-SERS research described in Chapters 3 and 4. While no notable improvements were seen for the E-SERS system, a significant and unexpected enhancement was observed as a result of in-situ laser irradiation with the Raman laser (Figure 5.1). This phenomenon is investigated in this chapter, along with discussion of the possible mechanism and some potential applications.

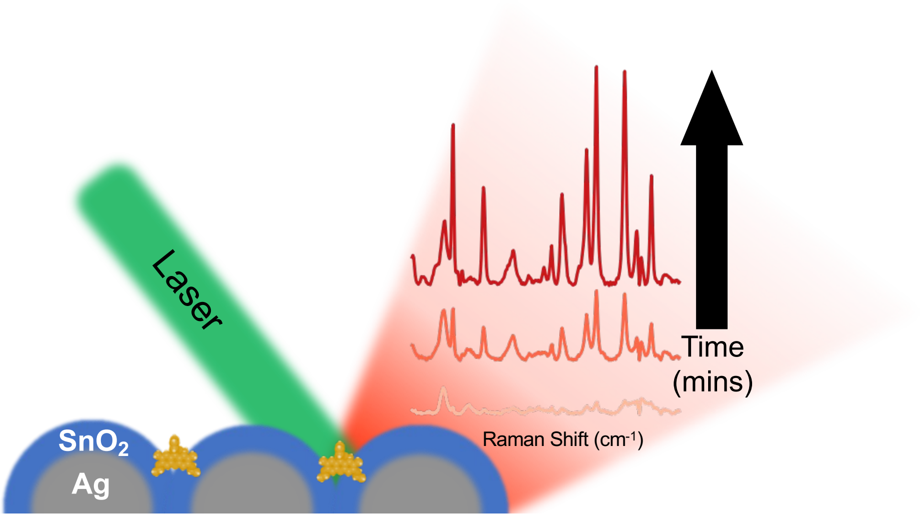

Figure 5.1: Schematic diagram illustrating the in-situ laser enhancement of the SERS signal from a Ag@SnO$_2$ *substrate.*

5.2 Characterisation

5.2.1 Nanoparticle characterisation

Tin dioxide coated silver nanoparticles (Ag@SnO$_2$ NPs) were produced by synthesising Ag NPs and then coating them with SnO$_2$. The Ag NPs were synthesised using the same Lee and Meisel-based citrate reduction method described in section 2.2.1. The UV-vis spectrum of the as-synthesised Ag NPs showed a LSPR peak at ca. 434 nm (Figure 5.2) and the TEM images confirmed the formation of polydisperse Ag NPs with a mean diameter of 79 nm ± 25 nm (Figure 3.3). Further details of the characterisation of these NPs can be found in section 3.2.1.

The as-synthesised citrate-stabilised Ag NPs were then coated with SnO$_2$ via a modified version of the precipitation method described by Oldfield et al.[275] The coating process was repeated twice to form a thicker coating of SnO$_2$. The Ag@SnO2 NPs were not purified further via repeat centrifugation and were used as-synthesised. The effect of the coating thickness is discussed further in section 5.3.2. The LSPR peak of the Ag@SnO_2 NPs in the UV-VIS spectra is observed at ca. 486 nm (Figure 5.2). This redshift is understood to be the result of the increase in the refractive index around the Ag NPs due to the metal oxide coating.[367]

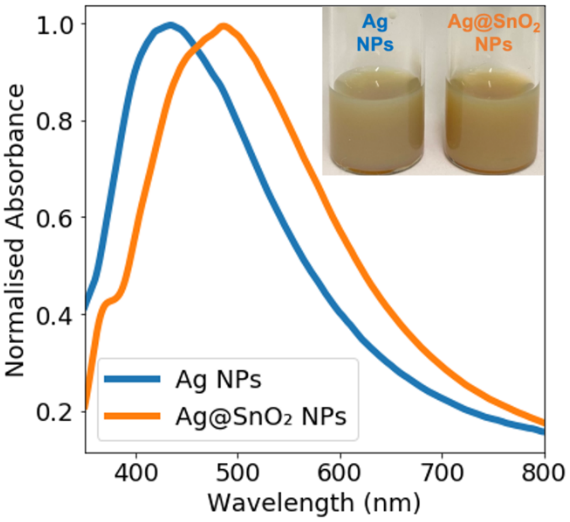

Figure 5.2: UV-vis spectra of Ag NPs (blue) and Ag@SnO_2 NPs (orange) plotted with normalised absorbance. (Inset) Photographs of colloidal Ag NP and Ag@SnO_2 NPs solutions.

Transmission electron microscopy verified the coating of the Ag NPs with SnO_2 (Figure 5.3). The images showed that there had been no significant change in the size or shape of the Ag NPs during the coating process. The SnO_2 coating is clearly visible and was measured to have a mean thickness of 16 nm ± 3 nm (Appendix Figure A.7). The coating is not particularly dense and contains some voids. However, these voids have previously been shown to be beneficial for hybrid SERS as they allow the analyte molecules to access the surface of the plasmonic metal.[366] Brunauer-Emmett-Teller (BET) analysis could also be used in the future to determine the surface area and porosity of the NPs.

The as-synthesised colloidal Ag@SnO_2 solution also contained SnO_2 NPs (approximately 35 nm in diameter) that are not attached to a Ag NP, which is typical for this coating method (Figure 5.3d).[368] These SnO_2 NPs did not form part of the final drop-cast substrates as they were removed during the centrifugation process because they are less dense than the Ag@SnO_2 NPs.

However, it would be interesting to investigate whether further purification *via* centrifugation before concentrating the solution improves the results. Removing more of the SnO_2 NPs may improve the uniformity of the Ag@SnO_2 films.

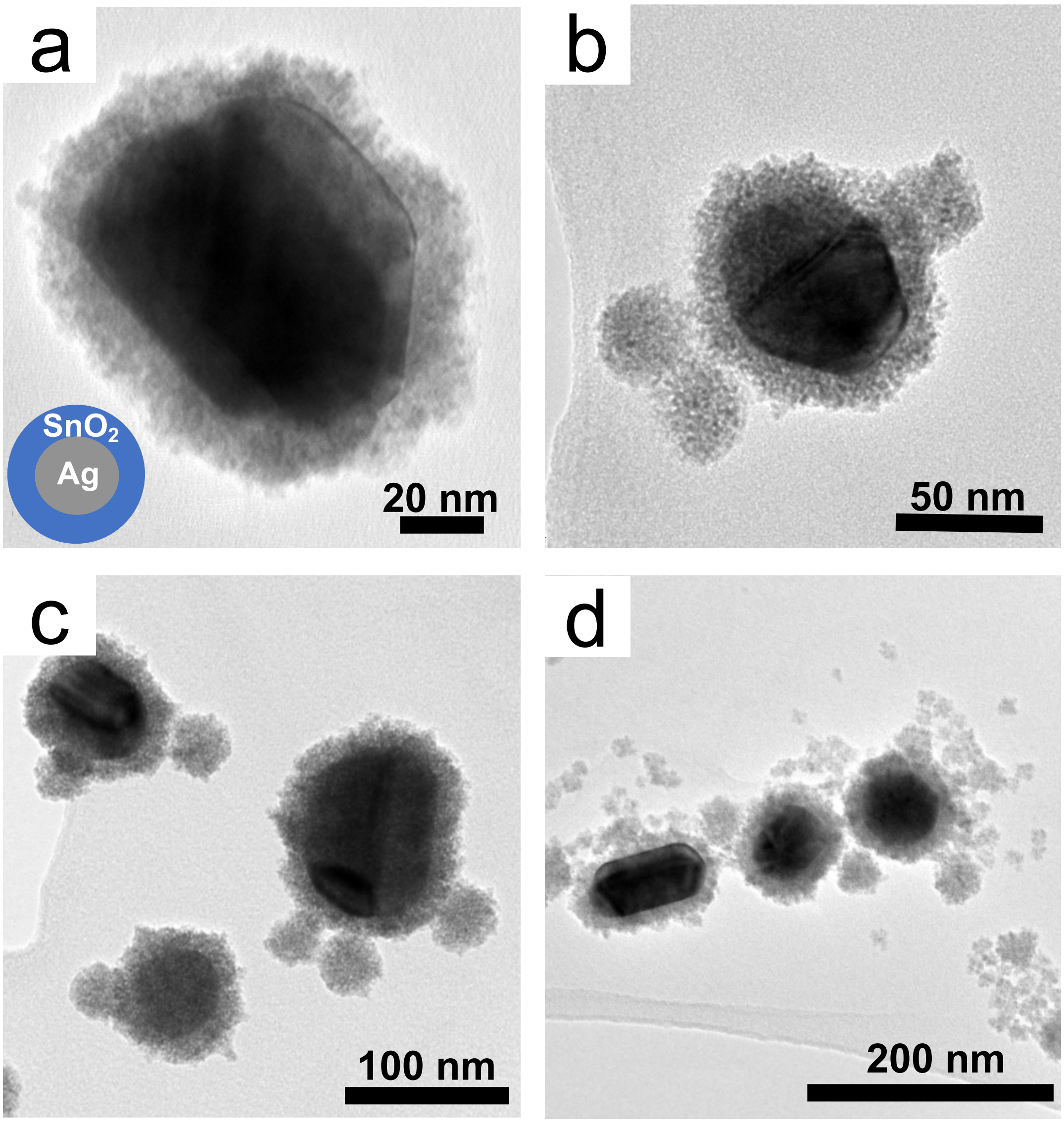

Figure 5.3: TEM images of as-synthesised tin dioxide coated silver nanoparticles (Ag@SnO_2 NPs).

5.2.2 Electrode characterisation

The Ag@SnO_2 substrates were fabricated by concentrating the colloidal Ag@SnO_2 solution and then drop-casting it onto glass slides. The dried Ag@SnO_2 NP films had a distinctive reflective silvery-blue colour (Figure 5.4).

Scanning electron microscope (SEM) images of the substrate show a densely packed compact film of NPs (Figure 5.5). Some cracks are present in the film (Figure 5.5a) but there are regular areas of over 5 μm^2, which show a consistent covering of Ag@SnO$_2$ NPs. ImageJ was used to manually measure the area of 365 particles from the SEM images and the diameter of each particle was calculated by assuming the particles were spherical. The mean diameter calculated in this way was 102 nm ± 21 nm and a histogram of the diameter distribution is plotted in Appendix Figure A.8. X-ray photoelectron spectroscopy (XPS) of the Ag@SnO$_2$ NP films confirmed the presence of silver, tin, and oxygen (Figure 5.6). XPS is discussed further in section 5.5.3.4.

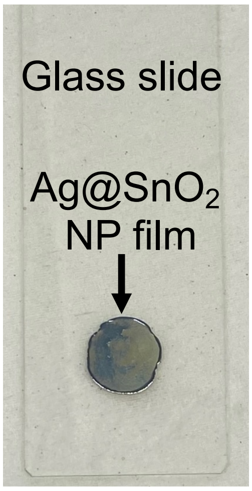

Figure 5.4: Photograph of a Ag@SnO$_2$ NP substrate. Concentrated colloidal Ag@SnO$_2$ NP solution is drop-cast on a glass slide.

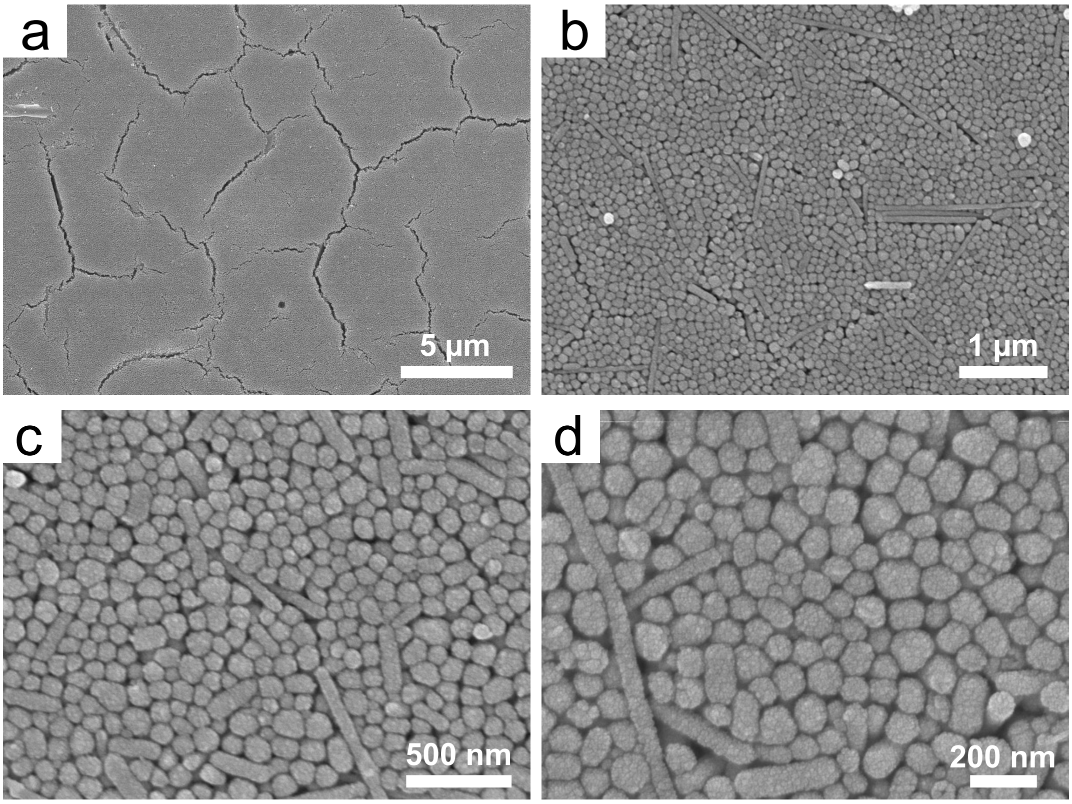

Figure 5.5: SEM images of Ag@SnO_2 NP film deposited on glass.

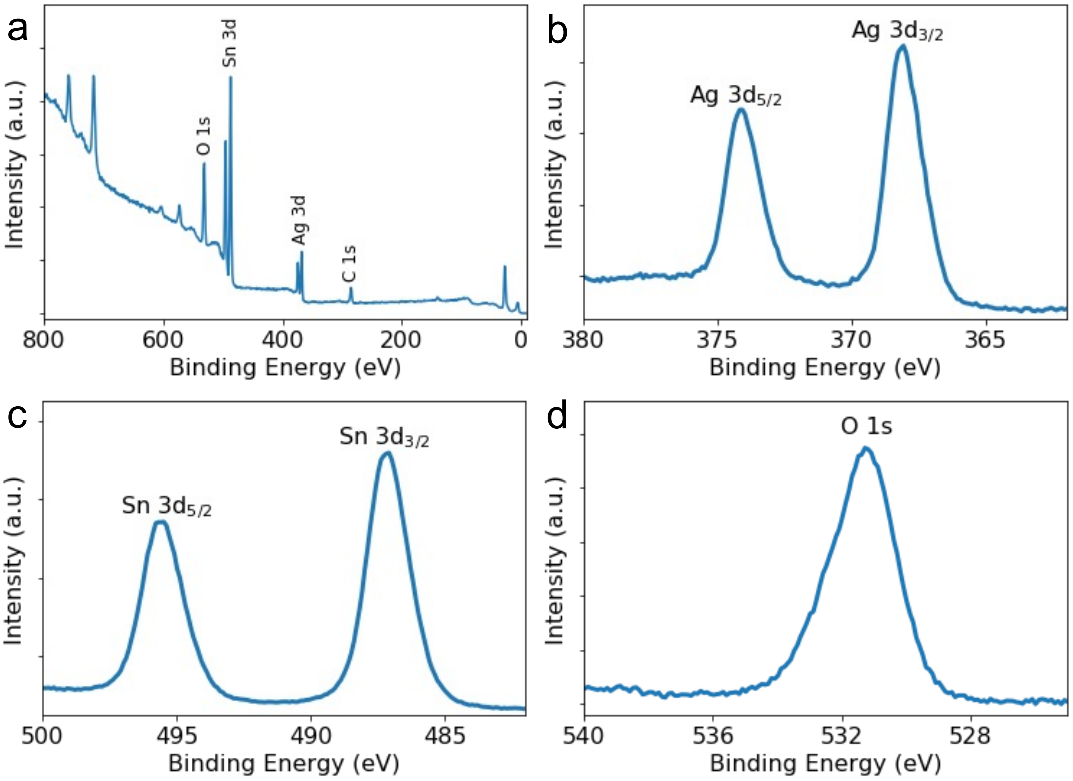

Figure 5.6: The XPS (a) survey spectrum and core level spectra of the (b) Ag 3d peaks, (c) Sn 3d peaks, and (d) O 1s peak of an Ag@SnO$_2$ NP substrate.

5.3 SERS of uric acid with Ag@SnO$_2$ substrates

The Ag@SnO$_2$ substrates were submerged in an aqueous 0.1 mM UA solution and the SERS spectra were recorded using a 633 nm, 22 mW laser with an integration time of 7s. The characteristic uric acid peaks at 636 cm^{-1} and 1138 cm^{-1}, which are attributed to skeletal ring deformation and C-N deformation respectively, were identified in the first spectrum recorded (Figure 5.7).[124,208,253] The broad peak at 573 cm^{-1} is attributed to the SnO$_2$ and is discussed further in section 5.5.5.

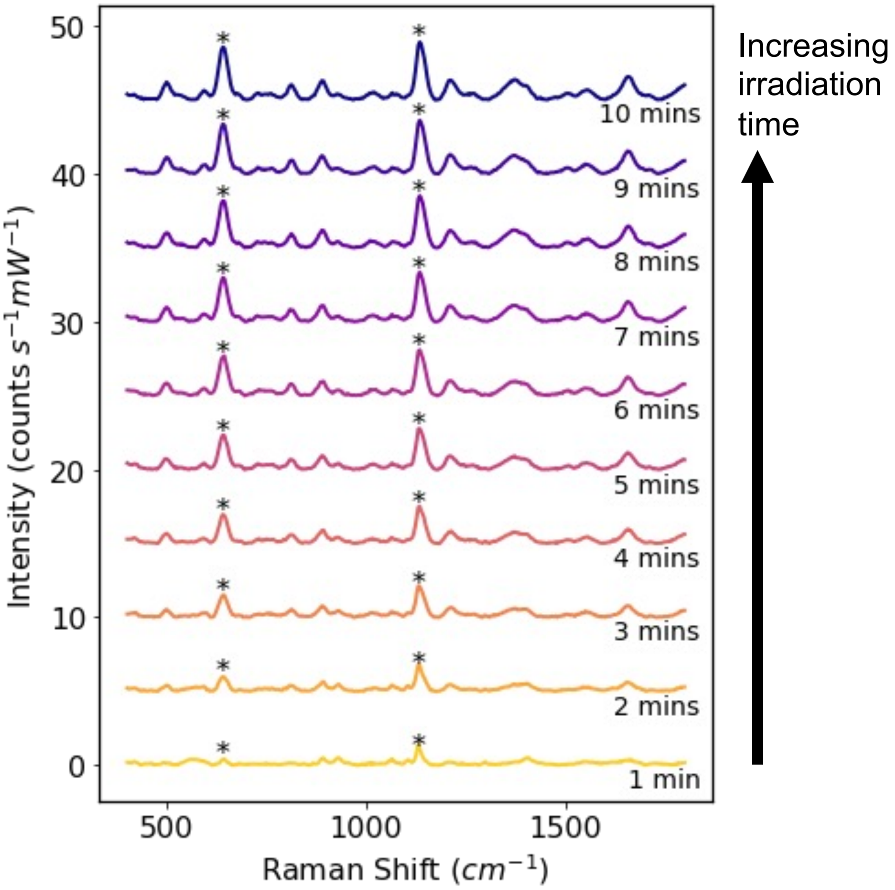

Figure 5.7: Successive SERS spectra of an aqueous 0.1 mM uric acid solution recorded over 10 minutes with a Ag@SnO$_2$ substrate.

As successive SERS spectra were acquired, under continuous irradiation from the 633 nm laser, the magnitude of these peaks started to increase (Figure 5.8). This was unexpected as SERS spectra typically remain constant over time or decrease due to damage to the substrate. The rate of increase was fastest over the first 15 minutes and then started to slow. After 1 hour of irradiation, the magnitude of the 636 cm^{-1} peak increased by over 19 times from 0.298 to 5.846 counts mW^{-1} s^{-1} (Figure 5.8a). This is a significant observation as increases in the SERS peak heights for a particular analyte could enable the detection of lower concentrations. No shifts in the positions of the UA peaks were observed and no new peaks were detected (Figure 5.8b).

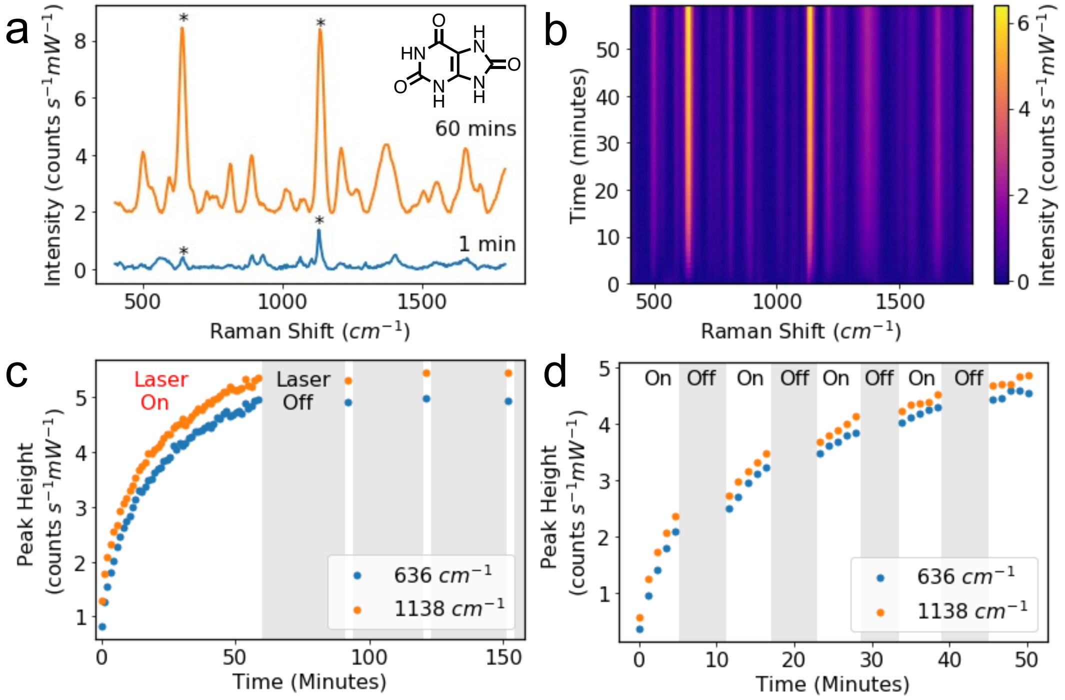

*Figure 5.8: (a) Comparison of the 0.1 mM UA spectra recorded with a Ag@SnO$_2$ substrate after 1 minute (blue) and 60 minutes (orange) of irradiation with the 633 nm laser. The characteristic UA peaks are indicated with a *. (b) A heat map showing how the 0.1 mM UA spectra change over 1 hour of irradiation. (c and d) The characteristic UA peak heights plotted against time. The grey areas indicate when the 633 nm laser was turned off.*

After irradiating a spot on the Ag@SnO$_2$ NP substrate for 1 hour, the laser was turned off and the substrate was left in place for 30 minutes. When the SERS measurement was re-started, there was no significant reduction in the UA characteristic peak heights (Figure 5.8c). This cycle was repeated 3 times and the peak heights remained consistent. A test was also performed where the laser was switched on and off approximately every 5 minutes (Figure 5.8d). Here, it was clear that the enhancement was the result of the Raman laser as the height of the peaks increased when the laser was on and remained constant when the laser was turned off. Further tests have shown that this enhancement is stable for at least 12 hours (Appendix Figure A.9).

The increase in the SERS peaks with irradiation was consistently observed regardless of how long the substrate had been submerged in the analyte solution (providing the initial 15 minutes equilibration time was given), implying that this phenomenon is not simply due to adsorption of the analyte molecules on the NP surface. This is highlighted in Figure 5.9, where the 636 cm^{-1} peak height is plotted against irradiation time for a Ag@SnO$_2$ substrate that had just been placed in the UA solution (no equilibration time) and another spot on the same substrate after it had been submerged in the solution for 72 hours. The laser-induced increase is still observed after the substrate had been submerged in the solution for 72 hours. The increase is faster for the 72-hour measurement, confirming that adsorption of the UA molecules on the surface is needed to observe the large peaks, which is expected as SERS is a surface selective effect. When the substrate was left to equilibrate, a similar increase in SERS signal was observed after 4 and 18 hours in solution (Appendix Figure A.10).

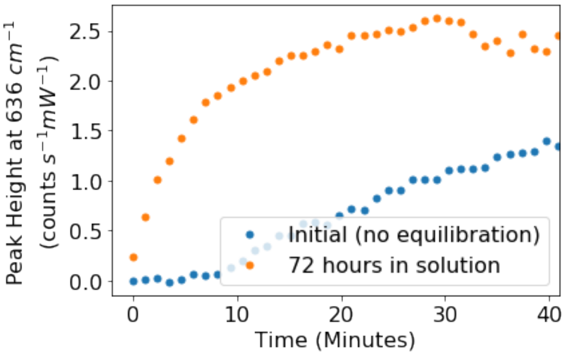

Figure 5.9: The height of the characteristic UA peak at 636 cm^{-1} plotted against time for a 0.1 mM uric acid solution. The blue line was recorded immediately after the Ag@SnO$_2$ substrate was placed in the solution, and the orange line was recorded after it had been submerged for 72 hours.

5.3.1 Comparison to other nanoparticle substrates

As a comparison, substrates were also made using the as-synthesised colloidal Ag NPs, SnO$_2$ NPs, a physical mixture of Ag NPs and SnO$_2$ NPs and Ag@SiO$_2$ NPs via the same drop-casting method. The Ag@SiO$_2$ NPs were included to compare the effect of a semiconductor shell (SnO$_2$) and an insulator shell (SiO$_2$). UV-vis spectra and TEM images of the Ag@SiO$_2$ NPs are included in the appendix (Appendix Figure A.11 and Appendix Figure A.12) along with TEM images of the SnO$_2$ NPs (Appendix Figure A.13). SERS spectra were recorded for 1 hour from 3 different positions on each substrate in a 0.1 mM UA solution.

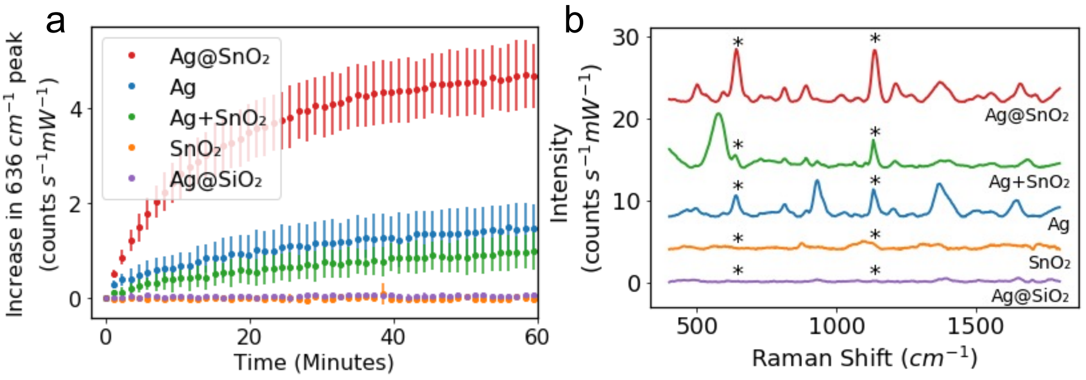

Figure 5.10: (a) The increase in the characteristic UA peak at 636 cm^{-1} over irradiation time for drop-cast substrates fabricated using Ag@SnO$_2$ NPs (red), Ag NPs (blue), a mixture of Ag and SnO$_2$ NPs (green), SnO$_2$ NPs (orange) and Ag@SiO$_2$ NPs (purple). The analyte solution was 0.1 mM UA and the error bars are equal to ± the standard deviation of three measurements. (b) The SERS spectra recorded after 1 hour of irradiation with the 633 nm laser for the same substrates.

The dramatic increases seen for the Ag@SnO$_2$ NPs were not observed for any of the other NPs (Figure 5.10a). The SnO$_2$ substrates did not exhibit any UA peaks, which is unsurprising as metal oxides typically have vastly smaller SERS enhancement than plasmonic metals (Figure 5.10b). Similarly, the Ag@SiO$_2$ did not exhibit significant UA peaks (Figure 5.10b). This is probably because the SiO$_2$ layer was quite thick (approximately 50 nm) and did not contain the voids which are present in the SnO$_2$ coating. This means the UA molecules are unable to get close enough to the plasmonic metal cores to experience the electromagnetic enhancement needed for large SERS signals. However, this does also highlight that there is something interesting taking place with the Ag@SnO$_2$ NPs as the SERS signal from these NPs does not appear to be hindered by the fact that the analyte molecules are further from the plasmonic metal core. This is discussed further in section 5.3.2.

The Ag substrates displayed moderate UA peaks (Figure 5.10b). However, they were smaller than the final peaks recorded from the laser-enhanced Ag@SnO$_2$ substrates (2.49 ± 0.74 vs. 5.10 ± 0.54 counts mW^{-1} s^{-1} after 1 hour irradiation). Again, this demonstrates that there is an additional enhancement present in the hybrid system which is enabling larger SERS signals to be recorded. Some increase was seen in the UA peaks for the Ag substrate (1.44 ± 0.74 counts mW^{-1} s^{-1} over 1 hour irradiation) (Figure 5.10a). This is likely to be due to the removal of citrate ions from the NP surface. As discussed in section 3.3.3, citrate ions remain on the surface of Ag NPs prepared using the Lee and Meisel method after synthesis. This reduces the SERS signals of target analytes as the citrate ions prevent the analyte molecules from adsorbing onto the plasmonic metal surface. Here, a reduction in the citrate characteristic SERS peak at 931 cm^{-1} is observed over time which tracks with the increase in the UA peaks for the Ag substrates (Appendix Figure A.14). The reason for the desorption of the citrate ions from the Ag surface with laser irradiation is unknown, but it is possibly due to plasmonic heating in the Ag NPs, which is discussed further in section 5.5.2. The increase in the Ag NP UA SERS signal could also be related to the thermal reduction and removal of the Ag_2O layer that forms on the Ag NPs as they age.[369]

The Ag + SnO_2 substrates showed modest UA peaks which were smaller than those observed for the Ag@SnO_2 and Ag substrates and did not exhibit the dramatic enhancement over time observed for the Ag@SnO_2 NPs (Figure 5.10a). This indicates that close contact is needed between the plasmonic metal and metal oxide to benefit from the hybrid enhancement effect. The SnO_2 NPs may also separate the Ag NPs reducing the number of hot spots. Overall, after 1 hour irradiation, the largest peaks were observed for the Ag@SnO_2 substrates, which highlights the potential of this hybrid nanostructure.

5.3.2 Optimisation of the SnO_2 coating thickness

The precipitation method used to coat the Ag NPs with SnO_2 can be repeated multiple times to form a thicker SnO_2 layer. An investigation was carried out to determine the optimal number of coating cycles. The normalised UV-vis spectra for NPs produced using different numbers of SnO_2 coating cycles are shown in Figure 5.11. As the number of coating cycles increases, the LSPR peak is red-shifted. This is to be expected as the thickness of the SnO_2 layer has increased, increasing the diameter of the particles and the refractive index around the Ag NPs. Figure 5.12 shows TEM images of the singly, doubly, and triply coated Ag@SnO_2 NPs. The thickness, density, and uniformity of the SnO_2

shell increase with the number of coating cycles. The thickness of the coating was generally less than 5 nm for the single-coated nanoparticles and approximately 20 nm for the triply-coated NPs.

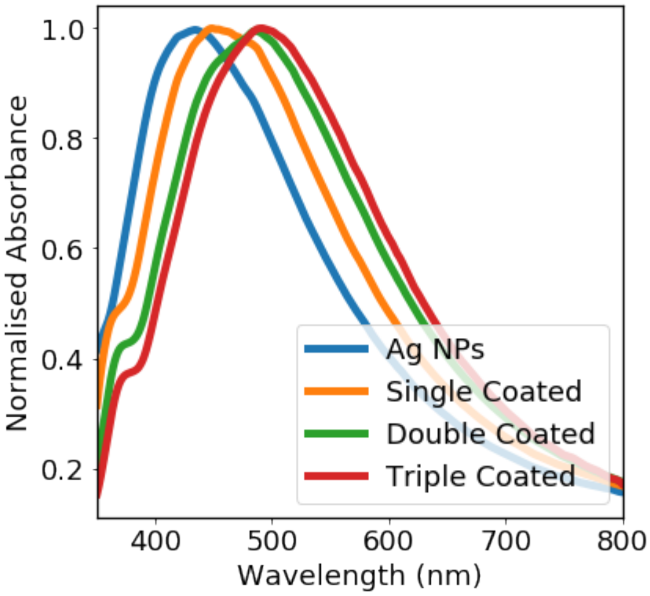

Figure 5.11: UV-vis spectra of the Ag NPs (blue) and the single (orange), double (green) and triple (red) coated Ag@SnO$_2$ NPs.

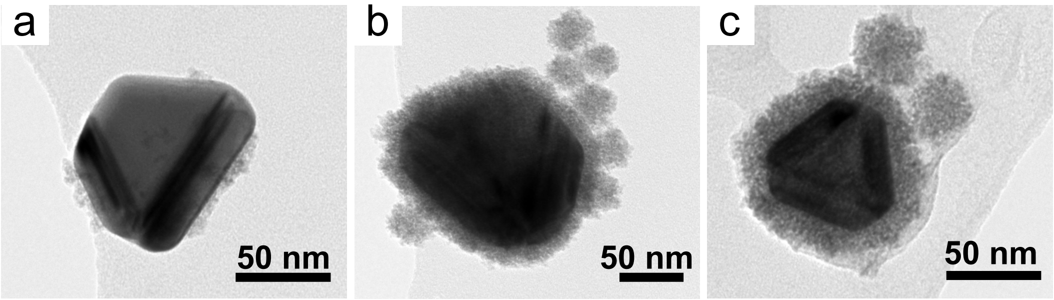

Figure 5.12: TEM images of as-synthesised single (a), double (b) and triple (c) coated Ag@SnO$_2$ NPs.

Drop-cast substrates were fabricated by centrifuging the 3 different colloidal NP solutions. 1 ml aliquots of the as-synthesised Ag@SnO$_2$ NP solution were added to 1.5 ml Eppendorf tubes and each tube was centrifuged at 3600 rpm for 15 minutes. The supernatant was then removed and discarded, and another aliquot of the colloidal solution was added. This was repeated 10 times. After the solution was centrifuged for the 10th time, almost all the supernatant was removed, leaving ~0.03 ml of concentrated NP solution. The concentrated NP solution was drop-cast onto a glass slide in three 10 μL aliquots. The substrate was then left to dry overnight prior to use.

The substrates were then tested in a 0.1 mM UA solution. All 3 substrates displayed the distinctive Ag@SnO_2 in-situ laser enhancement (Figure 5.13). The double-coated particles exhibited the largest and quickest increase in peak height. This behaviour likely arises from the double-coated particles having the optimal coating thickness to benefit from the enhancement offered by the hybrid system without the UA molecules being too far from the plasmonic Ag NP cores to experience the electromagnetic enhancement. The SnO_2 coating is also likely to become less porous with increasing coating cycles which means it can be harder for the analyte molecules to reach the plasmonic NPs in the triple-coated particles. BET analysis could be used to study this in the future. Additionally, the separation between the Ag NP cores in the NP film is likely to be larger for the triple-coated NPs which would reduce the electromagnetic SERS enhancement. Therefore, the double-coated particles were used to fabricate the Ag@SnO_2 substrates described in this work.

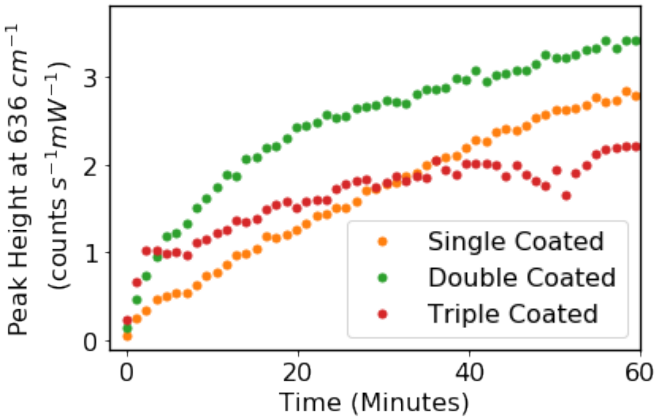

Figure 5.13: (a) The height of the characteristic UA peak at 636 cm^{-1} over irradiation time for drop-cast substrates fabricated using single (orange), double (green) and triple (red) coated Ag@SnO$_2$ NPs. The analyte solution was 0.1 mM UA.

5.4 SERS of other analytes with Ag@SnO$_2$ NP substrates

After studying the laser-induced enhancement for UA, other analyte molecules were tested to determine whether the same phenomenon was observed. The molecules chosen were widely used Raman reporters or molecules with well-studied Raman spectra. They included 4-mercaptobenzoic acid (4-MBA), 4-mercaptopyridine (4-MPY), rhodamine 6G (R6G), adenine, methyl viologen (MV) and 2,4-dinitrotoulene (2,4-DNT). The analyte concentrations tested depended on the size of the characteristic SERS peaks. Larger concentrations were used for tested for weaker Raman scatterers. The SERS spectra recorded after 1 minute and 60 minutes of laser irradiation are plotted in Figure 5.14.

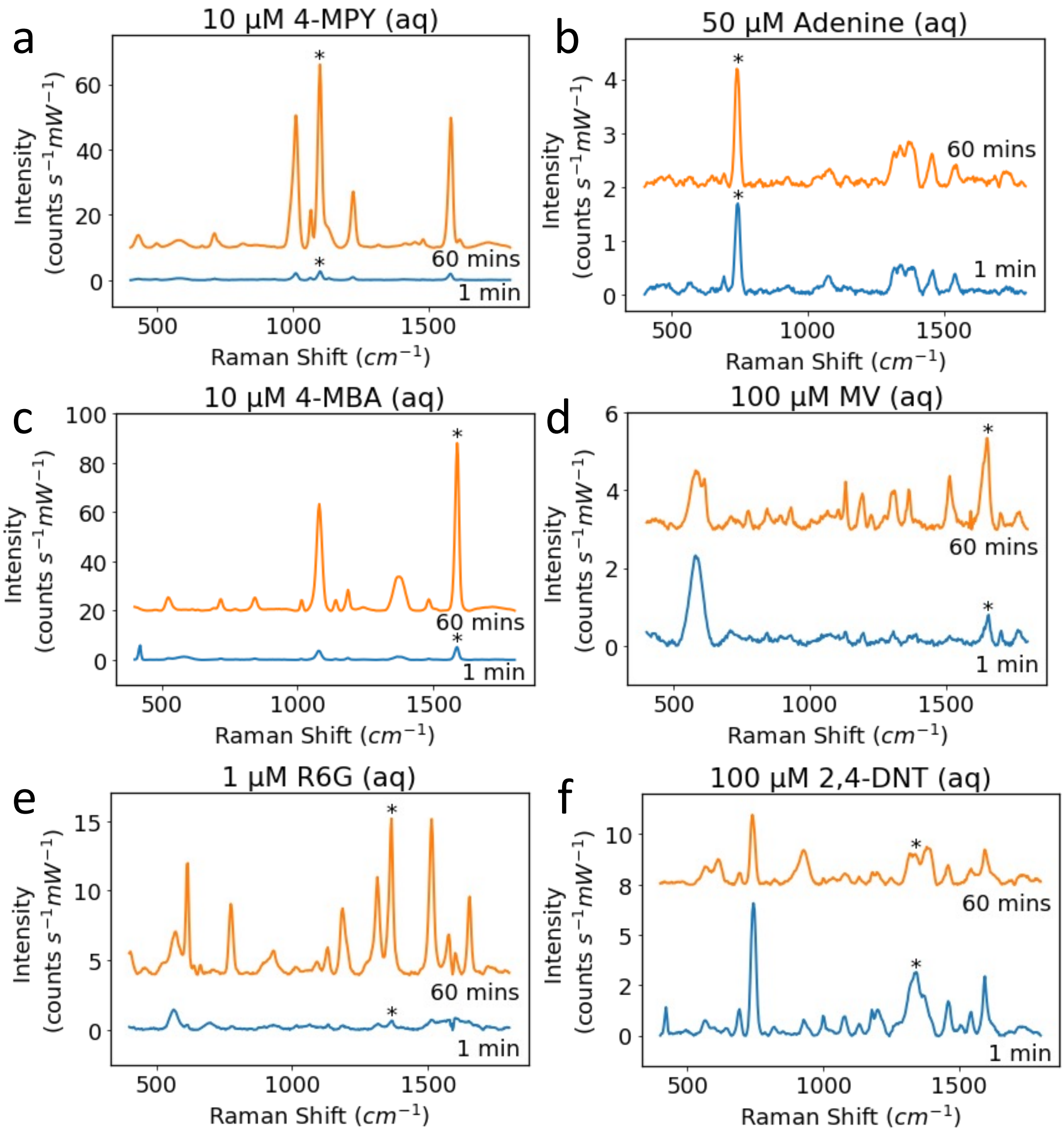

*Figure 5.14: Comparison of the SERS spectra recorded from the Ag@SnO$_2$ substrates after 1 minute (blue) and 60 minutes (orange) irradiation with the 633 nm laser for aqueous solutions containing (a) 10 µM 4-mercaptopyridine, (b) 50 µM adenine, (c) 10 µM 4-mercaptobenzoic acid, (d) 100 µM methyl viologen, (e) 1 µM rhodamine 6G and (f) 100 µM 2,4-dinitrotoulene. The largest characteristic peaks are indicated with a *.*

When the Ag@SnO$_2$ substrates were tested in solutions containing these molecules, two distinct behaviours were observed. One group of analytes displayed the laser-induced enhancement in the SERS signal as recorded for UA, and the other did not display any significant changes in the spectra over time. The molecules in these groups were categorised as “active” and “inactive”, respectively. The relative increase in the largest characteristic Raman peaks for the “active” and “inactive” molecules are plotted in Figure

5.15. For the “active” molecules, the characteristic peaks typically increased by 12 – 20 times over 60 minutes.

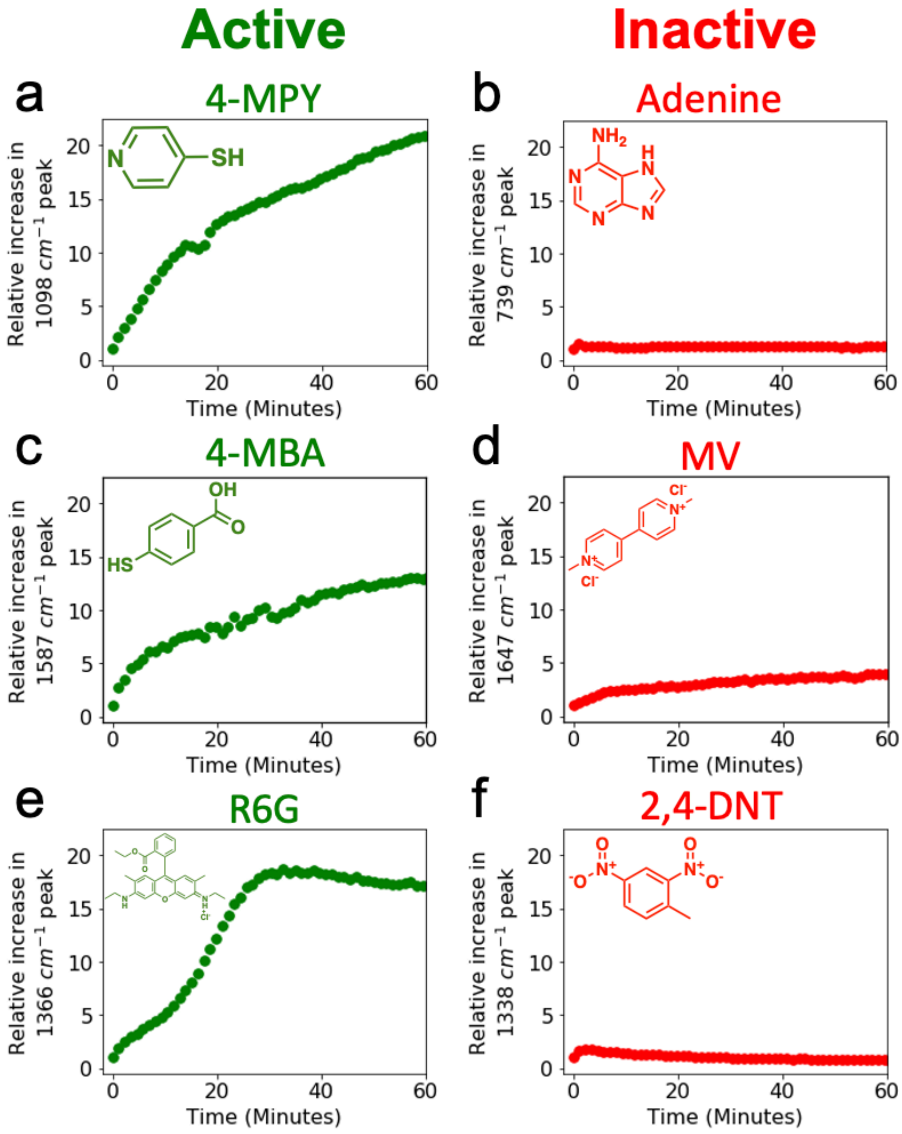

Figure 5.15: The relative increase in the largest characteristic peak is plotted against irradiation time for (a) 10 µM 4-mercaptopyridine, (b) 50 µM adenine, (c) 10 µM 4-mercaptobenzoic acid, (d) 100 µM methyl viologen, (e) 1 µM rhodamine 6G and (f) 100 µM2,4-dinitrotoulene. The analytes are separated into molecules which display the laser-induced enhancement (active) shown in green and those which do not (inactive) shown in red.

The key question is what determines whether an analyte is “active” or “inactive”. Based on the molecules which have been tested so far, the current hypothesis is that the difference in behaviour of these two groups of molecules is related to their redox properties. The “active” molecules are generally mildly reducing, and the “inactive” molecules are more oxidising. For example, looking at the literature, uric acid has an onset oxidation potential of ~300 mV whereas adenine has an onset oxidation potential of around 900 mV.[370,371] The “active’ molecules also often contain carbonyl groups. Testing of wider variety of molecules is needed to gain a deeper understanding of this phenomenon but this preliminary work will help to determine the reasons behind the in-situ laser enhancement observed in the hybrid system (section 5.5).

5.4.1 Activation of the laser enhancement

To further understand the behaviour of the different groups of molecules, tests were performed where both “active” and “inactive” molecules were present. First, a Ag@SnO_2 substrate was submerged in an aqueous solution containing 50 μM adenine and irradiated for 1 hour. The characteristic adenine peak at 735 cm^{-1} is clearly visible but its height does not exhibit any significant changes with irradiation (Figure 5.16). Then, 0.1 mM uric acid (an “active” molecule) was added to the solution. A sudden and significant increase in the adenine characteristic peak is observed (from 0.56 to 5.23 counts mW^{-1} s^{-1}) (Figure 5.16b). The UA peaks at 636 cm^{-1} and 1138 cm^{-1} are also present in these spectra (Figure 5.16a).

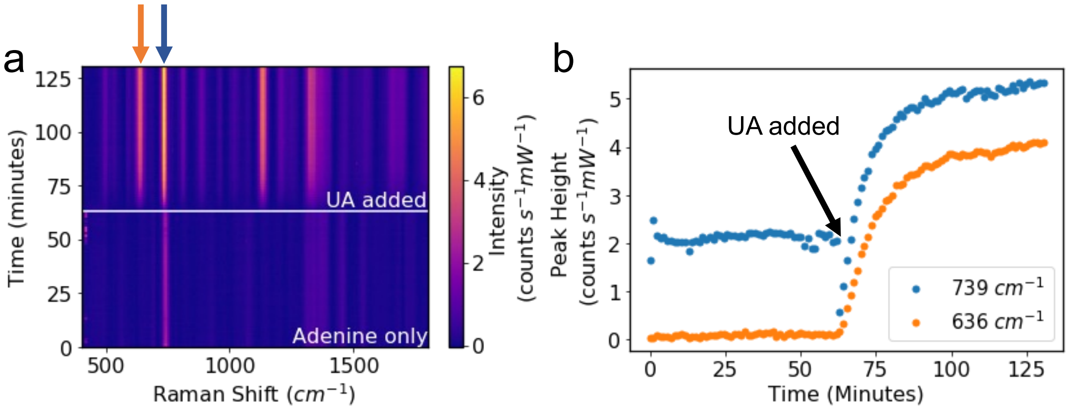

Figure 5.16: (a) A heatmap showing how the spectra of a 50 μM adenine solution recorded using a Ag@SnO₂ substrate change over time with the addition of 0.1 mM UA after 1 hour. (b) The characteristic adenine (blue) and uric acid (orange) peak heights are plotted against time. The position of these peaks in the spectra in (a) are indicated with blue and orange arrows.

To record laser enhanced adenine spectra without the presence of additional peaks, the same test was performed with acetone as the “activator” molecule. Acetone was chosen because it is a simple, well-understood ketone (containing a carbonyl group like many of the “active” molecules) but does not have a particularly strong Raman signal. As in the tests with UA, the acetone “activated” the system and resulted in large enhancements in the adenine peak (Figure 5.17). The discovery that the in-situ laser enhancement can be activated using particular molecules is a significant finding which can help to determine the mechanism behind the behaviour. This phenomenon could also be harnessed for the indirect detection of molecules without strong Raman signals. This is discussed further in section 5.6.2.

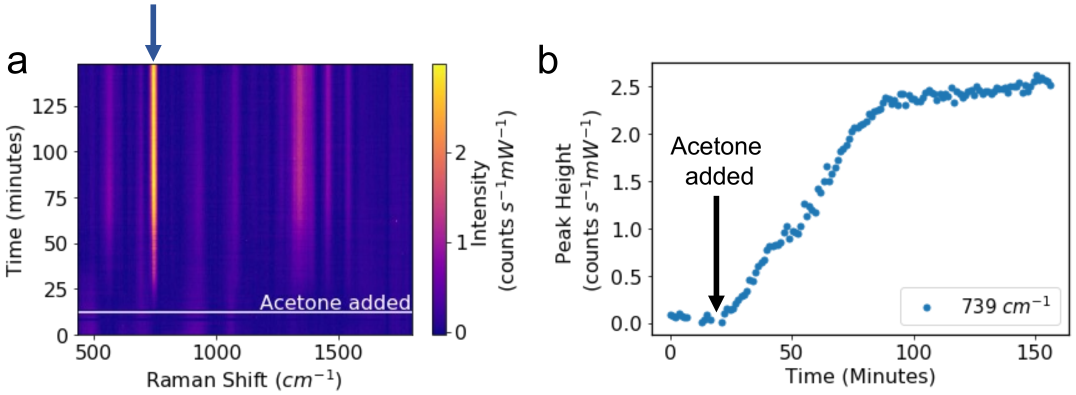

Figure 5.17: (a) A heatmap showing how the spectra of a 10 μM adenine solution recorded using a Ag@SnO₂ substrate change over time with the addition of 0.5 mM acetone after 20 minutes. (b) The characteristic adenine peak height is plotted against time. The position of this peak in the spectra in (a) is indicated with a blue arrow.

5.5 Understanding the enhancement mechanism

The work presented in this chapter thus far has shown that the Ag@SnO_2 NP substrates exhibit an additional in-situ SERS enhancement when irradiated with the Raman laser. This behaviour is interesting and potentially advantageous for the detection of trace concentrations of analytes. However, it is important to understand the mechanism behind this phenomenon. Based on the results in the first half of this chapter, the following statements can be made about the Ag@SnO_2 hybrid SERS enhancement:

- It is laser-induced – the increase in the SERS peaks starts when the NPs are irradiated with the 633 nm laser (regardless of how long the substrate has been submerged in the solution) and no increase is observed when the laser is turned off.

- It is irreversible (at least for the time periods and conditions tested) – when the laser is turned off, the enhancement remains for at least 12 hours.

- It has only been observed for Ag@SnO_2 NPs – it is not observed for uncoated Ag NPs, SnO_2 NPs or Ag@SiO_2 NPs and appears to be unique to the hybrid system. However, there may be other NPs that have not been tested, that exhibit this behaviour, particularly other plasmonic-metal metal oxide systems.

- It appears to be specific to solid substrates and has not been observed for colloidal substrates (Appendix Figure A.15).

- It is analyte dependent – some molecules exhibit the laser-induced increase ("active") and others do not ("inactive"). Currently, the active molecules appear to be mildly reducing.

- It is not analyte specific – it is possible to "induce" the SERS enhancement for an "inactive" analyte by adding an "active" molecule.

Based on these observations and other research in the literature, particularly PIERS research[60] and our group's previous work using SnO_2-coated gold nanotriangles for SERS[366], two general possible explanations were considered. The first is that over time, there is a laser-induced increase in the oxygen vacancy density in the SnO_2, enabling additional charge transfer and boosting the electromagnetic and chemical enhancement of SERS. The second suggestion is a laser-induced change in the geometry of the nanostructure, which increases the electromagnetic enhancement component of SERS. To investigate these possible mechanisms as well as understand and characterise other observations which had been made, a series of experiments were performed which are presented in the following section.

5.5.1 SERS with 785 nm laser

Since the $Ag@SnO_2$ enhancement is understood to be laser-induced, tests were carried out to determine whether the time-dependent enhancement is also observed for a 785 nm Raman laser as well as the usual 633 nm laser. The measurement conditions were kept consistent with a laser power of 22 mW and an integration time of 7s. A standard $Ag@SnO_2$ NP substrate was tested in a 0.1 mM UA solution. The time-dependent enhancement was still observed (Figure 5.18) with the 636 cm^{-1} peak increasing from 0.009 to 1.098 counts mW^{-1} s^{-1} after 1 hour irradiation. The characteristic SERS peaks are generally lower than those recorded with the 633 nm laser (~1 vs. ~5 counts mW^{-1} s^{-1} after 1 hour), which is to be expected as the Raman scattering intensity is proportional to λ^{-4} and 785 nm is further from the resonant wavelength of the Ag@SnO$_2$ NPs. The fact that the laser-induced enhancement is observed for both 633 nm and 785 nm irradiation is notable as it implies that the behaviour does not rely on a particular laser wavelength, unlike resonance Raman scattering for example.[372]

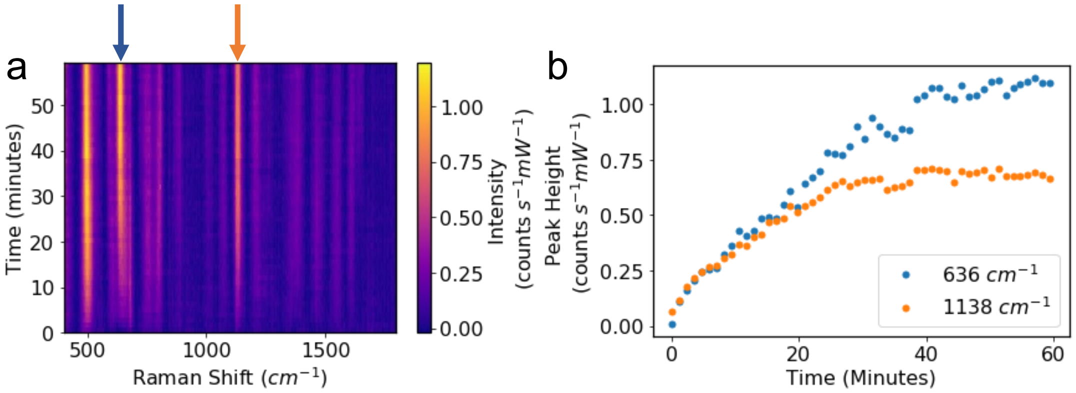

Figure 5.18: (a) A heatmap showing how the 785 nm laser SERS spectra of a 0.1 mM UA solution recorded using a Ag@SnO$_2$ substrate change over time. (b) The characteristic UA peak heights are plotted against time. The positions of these peaks in the spectra in (a) are indicated with an orange and blue arrow.

Unlike the 633 nm HeNe laser which had a fixed power, it was possible to adjust the power of the 785 nm solid-state laser in this set-up. A series of tests were carried out where a Ag@SnO$_2$ substrate was irradiated for 15 minutes in a 0.1 mM UA solution with a 785 nm laser at different laser powers from 10 mW to 130 mW. These laser powers are higher than those typically used in most SERS measurements. However, due to the set-up of the sample holder, the measurements are being taken at a focal distance with a large laser spot size (~ 400 µM in diameter) so the energy density at the laser spot is well below the recommended 1 mW/µm^2 limit.[373]

The peak height at 636 cm^{-1} is plotted against time for the different 785 nm laser powers shown in Figure 5.19. The peaks height is normalised for the laser power (i.e. plotted in counts mW^{-1} s^{-1}). For laser powers up to 70 mW, the enhancement in the 636 cm^{-1} peak height after 15 minutes irradiation increases with laser power. Above 70 mW, the enhancement starts to level off and then decreases at 130 mW. The rate of peak height increase also rises with higher laser powers with the lower laser powers (50 mW and below) exhibiting linear increases over the 15 minutes whereas the higher powers (above 70 mW) increase quickly in the first 5 minutes and then start to plateau.

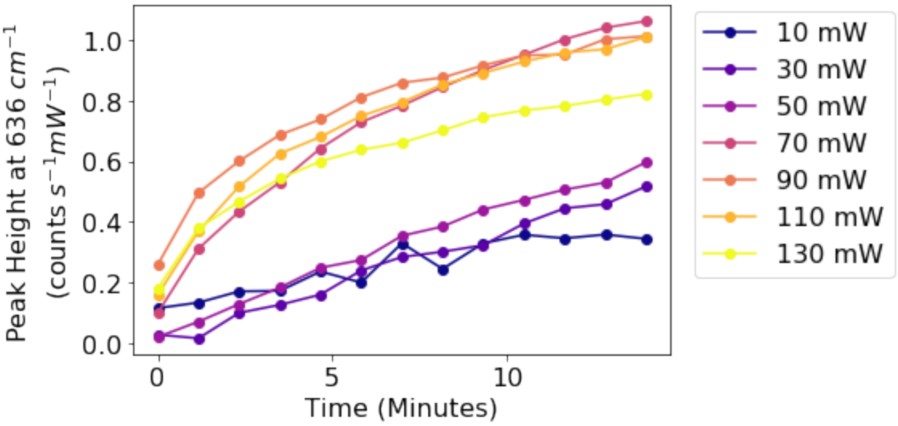

Figure 5.19: The height of the characteristic UA peak at 636 cm^{-1} plotted against time for a Ag@SnO$_2$ substrate irradiated for 15 minutes in a 0.1 mM UA solution with a 785 nm laser at different laser powers from 10 mW to 130 mW.

The fact the magnitude and rate of the enhancement both increase with laser power further supports the belief that this phenomenon is laser-induced. It also indicates that this behaviour could be related to plasmonic heating (section 1.3.6) as the heat generated through LSPR in a plasmonic nanoparticle increases with higher laser powers. The lower peak heights observed at the highest laser powers (above 70 mW) could indicate that the substrate is being damaged by the laser, for example melting or sintering of the Ag NPs. However, in this case, the spectra would likely exhibit a significant deterioration rather than a slight reduction in signal intensity. It is also possible that the adsorption of the analyte on the surface is being affected by the higher laser powers (and increased temperatures). The possibility of substrate damage is discussed further in section 5.5.3.

5.5.2 External heating investigation

Given the time dependence of the SERS signal increase and its correlation with laser power, it seemed plausible that plasmonic heating, where heat is generated due to local surface plasmon resonance, could be playing a role in the enhancement. Additionally, the absence of laser-induced enhancement for colloidal substrates (Appendix Figure A.16), where particle diffusion leads to less localized heating, further supports the idea that the enhancement could be linked to plasmonic heating. To investigate this, a series of experiments were carried out where the Ag@SnO_2 substrates were soaked in 0.1 mM UA solutions of different temperatures. In these tests, a Ag@SnO_2 substrate was submerged in a room temperature 0.1 mM UA solution and initial spectra were recorded at three different positions (each spot was irradiated for 70 seconds). The substrate was then placed in a centrifuge tube containing 0.1 mM UA solution and held at a defined temperature (20, 40, 60 or 80 °C) for 1 hour. Subsequently, the substrate was removed from the heated solution and returned to the measurement holder containing room temperature UA solution. The substrate was left to equilibrate for 15 minutes and then spectra were recorded from three different positions on the surface. As a control, the same process was carried out with another substrate but instead of removing the substrate from the measurement holder and placing it in a heated solution, it was irradiated with the 633 nm laser for 1 hour in three different positions.

The results of the heating tests are shown in Figure 5.20. The enhancement due to the laser irradiation is much more significant than the enhancement due to external heating. However, there is an increase in the 636 cm^{-1} peak height with heating. The substrate held at 80 °C displays an approximately 2x enhancement in the SERS signal compared to the substrate held at 20 °C (0.95 ± 0.12 vs. 0.40 ± 0.08 counts mW^{-1} s^{-1} at 636 cm^{-1}).

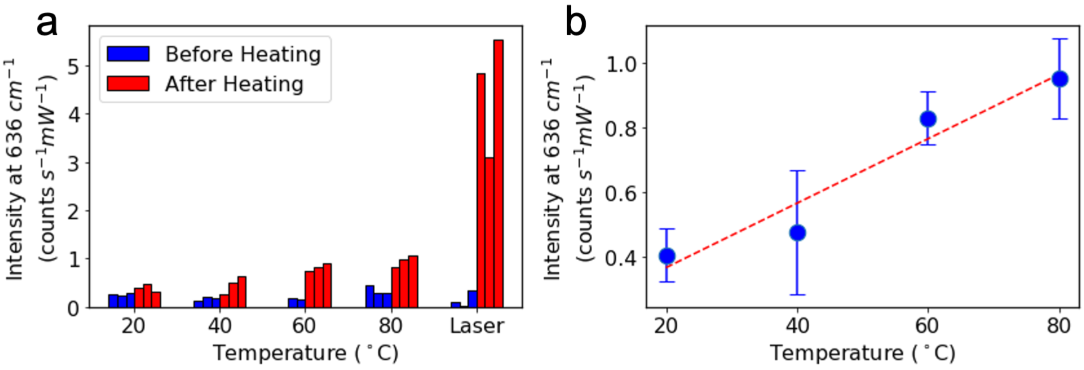

Figure 5.20: (a) The intensity of the characteristic UA peak at 636 cm^{-1} before and after external heating or laser irradiation in 0.1 mM UA solution. 3 points were measured on each substrate. (b) The mean intensity of 636 cm^{-1} peak after external heating plotted again temperature. The error bars are equal to ± the standard deviation of three measurements.

In Figure 5.20b, there is a positive relationship between the external temperature and the 636 cm^{-1} peak height. A simple linear regression is fitted to the data with moderate agreement ($R^2 = 0.78$). Extrapolating this line to find the temperature needed to reach the mean peak height observed for the laser-irradiated substrate results in a predicted temperature of 433 °C. This is higher than the temperatures typically reported in the literature for plasmonic heating (although a wide range of temperatures can be achieved depending on the laser power and material, size, shape, and arrangement of the nanoparticles).[70] However, the relationship between the enhancement and the temperature may not be linear. If the enhancement is the result of a chemical reaction taking place between the analyte and the SnO_2, then the rate of the reaction would depend exponentially on temperature, as described by the Arrhenius equation ($\mathrm{k} \propto \exp(\frac{\mathrm{E_a}}{\mathrm{RT}})$), where k is the rate constant, E_a is the activation energy, R is the gas constant and T is temperature). If this is the case, then it is possible that the peak heights achieved by the laser irradiation could be matched at a much lower temperature, which may be within the typical plasmonic heating range for continuous laser irradiation (~<250 °C).[374]

It is difficult to draw conclusions from the current data as it was only possible to test low temperatures (80 °C and below) with the equipment available. Ideally, it would be better to measure the temperature of the system during laser irradiation. However, it can be very difficult to measure the temperature at the surface of the NPs during plasmonic heating[70] and it was not possible to measure the bulk temperature in-situ with the time and equipment available. This is an area for further research but based on the positive relationship between external temperature and the peak height increase as well as the previous investigations into the laser power, it seems likely that plasmonic heating is playing a role in the enhancement observed.

Another factor to consider is the potential role of hot electrons or hot carriers. This is an area of significant debate that accompanies much of the discussion around plasmonic heating.[148] Hot carriers are formed when a metal nanoparticle absorbs a photon and promotes one electron from below the Fermi level to a state high above the Fermi level.[103,104] The energy gained by the electron is equal to that of the incident photon (a few electronvolts in the visible-NIR range). The electron-hole pair formed in this process only exists for tens of femtoseconds due to collisions with other unexcited electrons in the particle. However, in that time they can be transferred to molecules adsorbed on the surface of the NP and activate chemical reactions.[101,375] Plasmonic hot-carrier chemistry has been an area of substantial interest over the last few years with researchers suggesting it has applications in nanochemistry[102,376], water splitting[377–379] and artificial photosynthesis[380–382]. However, there is still significant debate over the underlying mechanism and the question of whether plasmonic heat generation or hot charge carriers play a more significant role in the catalysis remains.

In the case of this work, there is a possibility that hot electrons play a part in the observed enhancement, particularly as hot carriers can exist for longer in hybrid plasmonic-metal metal oxide systems than plasmonic metal nanostructures.[383–385] This is due to electron-hole separation which delays recombination. However, even in hybrid systems, the lifetime of hot carriers is typically less than 100 femtoseconds.[383] Considering that the laser-induced enhancement typically increases for around an hour, it seems unlikely that hot carriers are the primary reason for the enhancement. Nevertheless, there is still a possibility that hot carriers are catalysing a reaction which leads to the enhancement. It could be possible to investigate this further by studying the SERS spectra of probe molecules that are particularly sensitive to hot carriers. For example, the conversion of p-nitrothiophenol to 4,4′-dimercaptoazobenzene is known to be triggered by hot carriers, so this reaction is commonly used to study plasmon-induced photocatalysis.[386,387]

5.5.3 Morphological changes to the nanoparticle film

5.5.3.1 Observation of “dark spots”

As discussed above, the prolonged laser irradiation and the likely plasmonic heating mean it is important to consider whether morphological changes are taking place in the NP film. In particular, there is a possibility that the Ag NPs are reshaping or sintering, which could lead to changes in the plasmonic hot spots and consequently, the electromagnetic SERS enhancement. Another key reason this possibility was considered is the presence of circular “dark spots” which appear on the Ag@SnO_2 film at the measurement site after sustained laser irradiation (Figure 5.21). The “dark spots” are approximately 0.6 mm in diameter (Appendix Figure A.16) and can be clearly identified as the Ag@SnO_2 normally has a silvery-blue appearance, and the “dark spots” are black-brown.

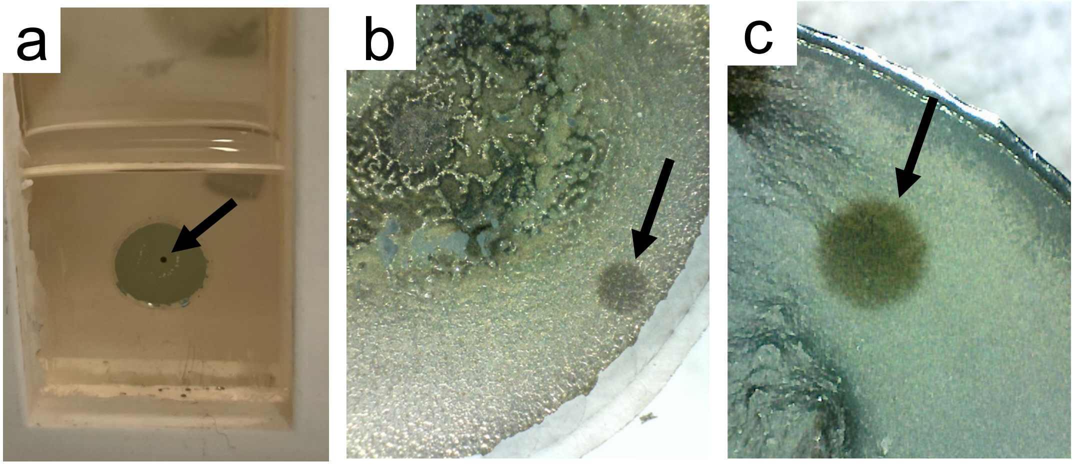

Figure 5.21: Optical images of the "dark spot" which appears on the Ag@SnO$_2$ film at the SERS measurement site after sustained 633 nm laser irradiation for 1 hour in 0.1 mM UA solution. The "dark spot" is indicated with a black arrow.

These "dark spots" could be the results of morphological changes, either through an increase in surface roughness resulting in increased light scattering or a change in the size or shape of the plasmonic nanoparticles causing a colour change. However, there may be other reasons for the colour change. SnO$_2$ nanostructures with a high concentration of oxygen vacancies can appear black so the "dark spot" could be due to an increase in the oxygen vacancy density in the SnO$_2$.[388,389] This would support the theory that the observed enhancement is the result of an increase in the oxygen vacancy density in the SnO$_2$, enabling additional charge transfer and boosting the chemical enhancement component of SERS.

5.5.3.2 SEM imaging of irradiated areas

To investigate the possible morphological changes at the "dark spots", SEM images were taken of the Ag@SnO$_2$ film after 1 hour irradiation with the 633 nm laser (ca. 22 mW) in a 0.1 mM UA solution (Figure 5.22). Comparing the SEM images from the "dark spot" and the rest of the Ag@SnO$_2$ NP film, there is a noticeable difference in the nanostructure. The images from the "dark spot" show a more irregular arrangement of NPs with more variation in the NP size and spacing than the unirradiated area. Additionally, the images from the "dark spot" display more variation in depth, resulting in a rougher appearance in contrast to the flatter and smother unirradiated areas. This could be increasing the light scattering at the surface and causing the area to appear darker.

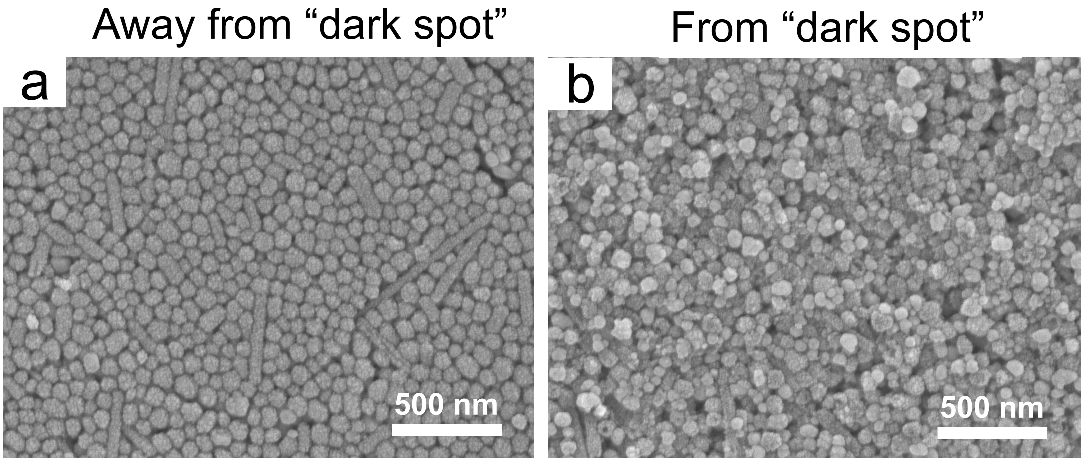

Figure 5.22: SEM images of a Ag@SnO$_2$ NP substrate that had been used to measure SERS spectra of 0.1 mM UA for 1 hour with a 633 nm laser. (a) was taken from an area away from the measurement position and (b) was taken from the “dark spot” which had been irradiated with the 633 nm laser for 1 hour. Accelerating voltage of 10 kV.

The next step was to try to understand whether these morphological changes were the reason for the observed enhancement. To do this, a test was carried out where a Ag@SnO$_2$ film was submerged in deionized water and a spot was irradiated for 1 hour. The deionized water was then removed and replaced with 0.1 mM UA solution and SERS spectra were recorded from the same spot for 1 hour. If the enhancement is caused by laser-induced morphological changes, the expectation would be to observe large UA peaks from the start (without the time-dependent increase) as the pre-irradiation in water would have already altered the nanostructure.

The results from the test are shown in Figure 5.23 and the time-dependent laser-induced increase in the UA peaks is still observed despite the pre-irradiation in water. These results are similar to those presented in section 5.4.1, where the enhancement of “inactive” molecules was activated through the addition of “active” molecules. This observation further supports the idea that the analytes molecules are playing an important part in the enhancement, implying that the observed behaviour is not simply due to a morphological change in the nanostructure.

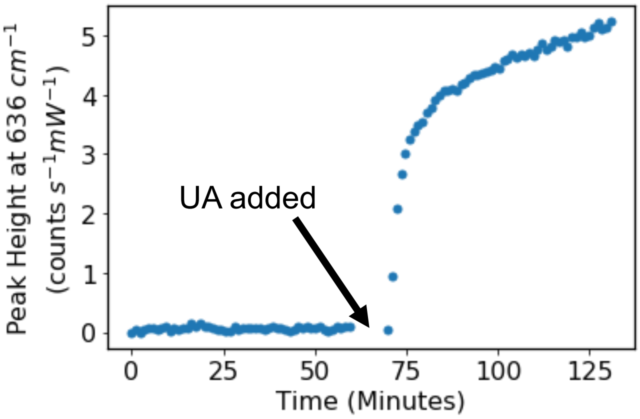

Figure 5.23: The height of the characteristic UA peak at 636 cm^{-1} plotted against time for a Ag@SnO2 substrate. For the first 60 minutes, the SERS measurements are recorded in deionized water. Then, the deionized water is removed and replaced with a 0.1 mM UA solution and the same position is irradiated for a further 60 minutes.

When the Ag@SnO$_2$ film was irradiated in deionized water, the “dark spot” was still observed and the same change in the nanostructure morphology can be seen in the SEM images (Figure 5.24). This implies that the change in the morphology is separate from the analyte-dependent enhancement which is observed in the SERS signal.

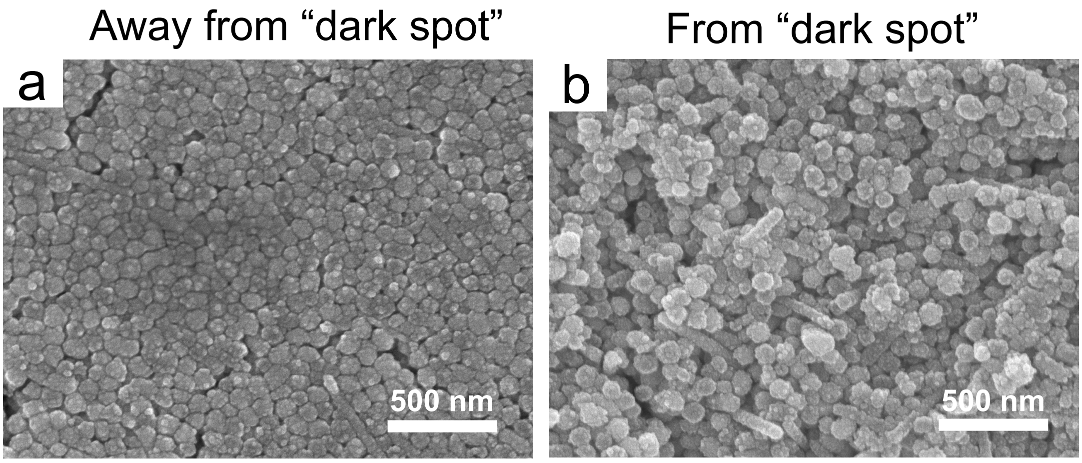

Figure 5.24: SEM images of a Ag@SnO$_2$ NP substrate that had been used to measure SERS spectra of deionized water for 1 hour. (a) was taken from an area away from the measurement position and (b) was taken from the “dark spot” which had been irradiated with the 633 nm laser (ca. 22 mW) for 1 hour. Accelerating voltage of 10 kV.

5.5.3.3 TEM imaging of irradiated nanoparticles

To further investigate the changes in morphology observed in the SEM images, TEM images were taken of the Ag@SnO$_2$ NPs before and after irradiation. To do this, a needle was used to remove NPs from the substrate, either in an area which had been irradiated for 1 hour (the “dark spot”) or in an area which had not been irradiated. The entire substrate had previously been submerged in 0.1 mM UA solution. The NPs which were removed from the substrate were mixed with water and then sonicated to re-disperse the particles. The colloidal solutions were then drop-cast onto TEM grids and imaged. The re-dispersed Ag@SnO$_2$ NPs can be clearly seen in the TEM images (Figure 5.25).

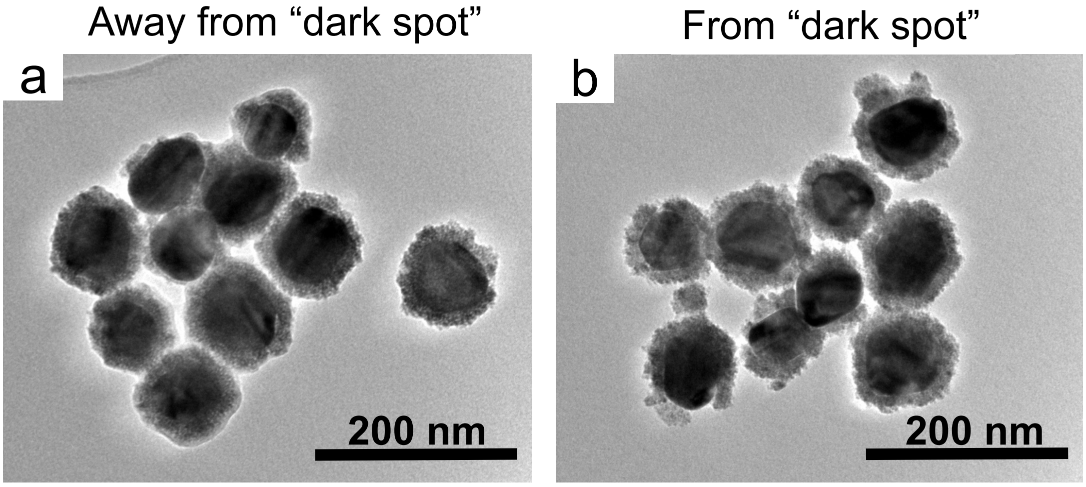

Figure 5.25: TEM images of Ag@SnO$_2$ NPs which had been removed from the glass substrates and re-dispersed. (a) shows particles which were taken from an area away from the measurement position and the NPs in (b) were taken from the “dark spot” which had been irradiated with the 633 nm laser for 1 hour in a 0.1 mM UA solution.

Comparing the images of the NPs from the “dark spot” and the rest of the film, no significant differences were observed between the two sets of images in terms of the size, shape, or coating of the nanoparticles. This was surprising considering the differences observed in the SEM images (Figure 5.22). These images are only a snapshot of the many thousands of particles in the substrate, and it is difficult to ensure that only particles from the “dark spot” were removed with the needle. So, there could be a difference which has not been captured in these images. Alternatively, rather than causing a change in the NPs themselves, the irradiation could be causing NPs to become detached from the NP film. This would explain the difference in roughness observed in the SEM images. Ideally, to understand this further, it would be helpful to TEM image the same particles before and after irradiation. This may be possible with very careful preparation the TEM grids and precise control of the laser position and would be a valuable area of future research.

5.5.3.4 XPS of irradiated areas

To further investigate the “dark spots”, XPS was performed on six points on the same Ag@SnO$_2$ substrate which had been submerged in a 0.1 mM UA solution. Three of the points had been irradiated with the 633 nm laser for 1 hour (“dark spots”) and the other three points had not been irradiated. The normalized O 1s, Sn 3d and Ag 3d spectra are shown in Figure 5.26. No consistent differences were observed in the spectra from the two areas.

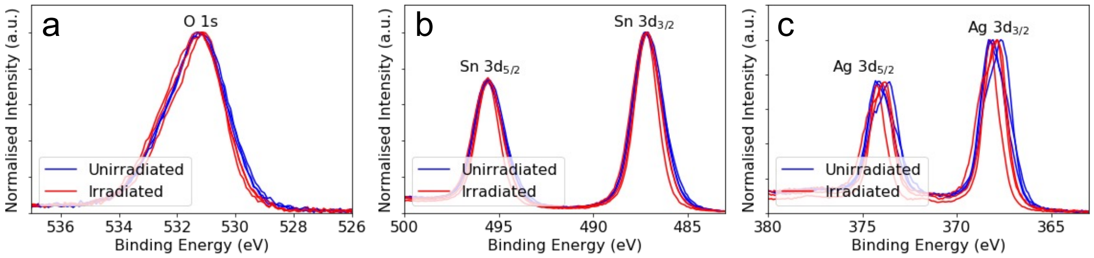

Figure 5.26: The XPS core level spectra of the (a) O 1s peak, (b) Sn 3d peaks, and (c) Ag 3d peak from three irradiated spots (red) and three unirradiated spots (blue) on an Ag@SnO_2 NP substrate which had been submerged in 0.1 mM UA. The spectra are min-max normalised, and the binding energy scale was calibrated to the C 1s peak at 284.8 eV.

It should be noted that the literature contains many examples of researchers using the O 1s XPS to identify the presence of oxygen vacancies in SnO_2.[390–392] However, this has now been debunked by XPS specialists.[393–395] XPS relies on measuring the kinetic energy of an electron removed from the core or valence levels of an atom in a material. Therefore, it is not possible to measure a photoelectron signal originating from a missing oxygen atom. The peak which is erroneously attributed to oxygen vacancies (around 531 – 532 eV) is actually the result of surface hydroxyls.[393]

5.5.4 Quantifying the degree of charge transfer

The discussion of the mechanism thus far has suggested two general possible explanations. The first is a laser-induced increase in the oxygen vacancy density in the SnO_2, enabling additional charge transfer and boosting the chemical enhancement component of SERS. The second suggestion is a laser-induced change in the geometry of the nanostructure, which increases the electromagnetic enhancement component of SERS. To try and determine which of these explanations is more plausible or exhibits a major contribution, it is important to establish whether the chemical or electromagnetic component is responsible for the observed enhancement. Lombardi proposed a method to determine the degree of charge transfer taking place in a SERS measurement by comparing the b_2 (non-totally symmetric) and a_1 (totally symmetric) vibrational modes of a probe molecule.[396] This approach is commonly used to study charge transfer in hybrid SERS systems.[397–400]

In the charge transfer model proposed by Lombardi, the Frank-Condon principle (LSPR - electromagnetic enhancement) is only responsible for the enhancement of the totally symmetric vibrational modes of a molecule, while the Herzberg-Teller effect (charge transfer - chemical enhancement) can enhance totally and non-totally symmetric vibrational modes.[396] Therefore, the degree of charge transfer (p_{CT}) can be calculated using the following equation:

$$p_{CT} = \frac{I^k(CT) - I^k(SPR)}{I^k(CT) + I^0(SPR)} \qquad \text{Equation 21}$$

Where k is an identifier for a Raman band and $I^k(CT)$ is the intensity of a Raman band which is affected by charge transfer. $I^0(SPR)$ is the intensity of a totally symmetric line which is only enhanced by LSPR. If the Raman band, k, is totally symmetric, then $I^k(SPR)$ = $I^0(SPR)$. If it is not totally symmetric, then $I^k(SPR)$ is the intensity of the Raman band, k, without charge-transfer contributions. Under normal conditions, $I^k(SPR)$ is expected to be small or zero, while $I^0(SPR)$ is larger.[399] Therefore, Equation 21 can be simplified to calculate the p_{CT} of a b_2 line to give:

$$p_{CT} = \frac{R}{R+1}\text{, where } R = \frac{I_{b_2}}{I_{a_1}} \qquad \text{Equation 22}$$

4-mercaptobenzoic acid (4-MBA) was chosen as the probe molecule for this study as it has a well characterised Raman spectra.[401] When choosing the a_1 and b_2 peaks for analysis it is important to choose peaks which are in the same region of the spectra with comparable heights to minimise disruption due to other factors in the SERS measurement. Here, the a_1 peak at 1185 cm^{-1} and the b_2 peak at 1142 cm^{-1} were used.[397,401] SERS spectra were recorded with a Ag@SnO$_2$ NP substrate in a 10 μM 4-MBA solution for 1 hour.

The spectra are shown in Figure 5.27 and the peaks used for the charge transfer analysis are highlighted in Figure 5.27b. The degree of charge transfer was calculated using equation 22 and is plotted with the characteristic peak at 1587 cm^{-1} in Figure 5.28. There is a clear increase in the degree of charge transfer with irradiation time (from 0.307 to 0.338 over 1 hour). This increase in the degree of charge transfer is mirrored by the increase in the characteristic 4-MBA peak at 1587 cm^{-1}. These results indicate that additional charge transfer is responsible for the observed enhancement. This supports the idea that an increase in the oxygen vacancy density in the SnO_2 could be causing the improvement in the SERS spectra.

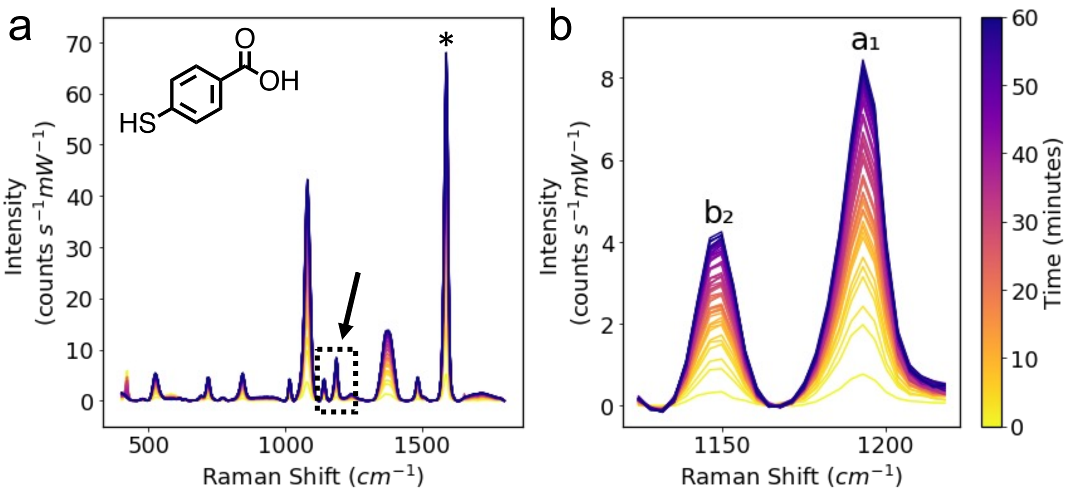

*Figure 5.27: Successive SERS spectra of an aqueous 10 μM 4-MBA solution recorded over 1 hour with a Ag@SnO$_2$ substrate. The colour of the spectra indicates the irradiation time with the initial spectra plotted in yellow and the final spectra plotted in blue. (a) shows the spectra across the full Raman shift range and (b) shows the section of the spectra which is used to calculate the degree of charge transfer. The largest characteristic 4-MBA peak at 1587 cm^{-1} is indicated with a * in (a) and the a$_1$ and b$_2$ peaks used for the charge transfer calculation are labelled in (b).*

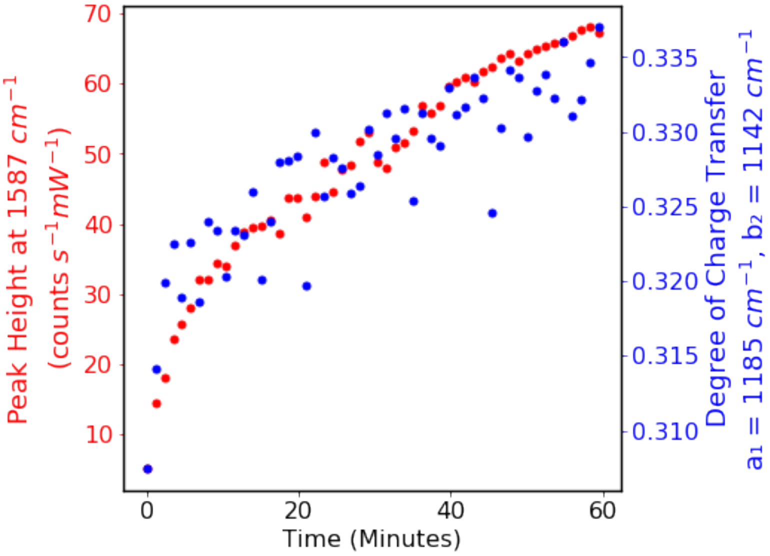

Figure 5.28: The characteristic 4-MBA peak at 1587 cm^{-1} and the degree of charge transfer calculated using the a$_1$ peak at 1185 cm^{-1} and the b$_2$ peak at 1142 cm^{-1} are both plotted against time for spectra recorded in a 10 μM 4-MBA solution with a Ag@SnO$_2$ substrate.

5.5.5 Investigation of the SnO$_2$ SERS peaks

The changes in the relative peak heights indicate that the observed enhancement is the result of charge transfer processes. Previous research into hybrid SERS, particularly the PIERS work, has shown that charge transfer in plasmonic-metal metal oxide systems is often due to oxygen vacancies, which create donor states in the metal oxide and enable the excitation of electrons from the semiconductor to the plasmonic metal.[60,61] To determine whether the oxygen vacancies (V_o) are responsible for the enhancement, it would be helpful to observe how the oxygen vacancy density changes during laser irradiation. However, it can be challenging to characterize the oxygen vacancies in a metal oxide – by definition, it is difficult to measure the absence of an atom and ex-situ characterization is problematic due to vacancy healing.[62] One approach is to look at the Raman signal of the SnO_2 itself. There has been some work linking the SnO_2 peaks to different types of oxygen vacancies in SnO_2 nanostructures.[402–405] Liu et al. studied Raman spectra of spherical SnO_2 nanocrystals annealed at different temperatures and identified peaks at 573 cm^{-1} and 618 cm^{-1}.[402] They linked the 573 cm^{-1} peak (A_s) to the presence of in-plane V_o and suggested that the peak at 618 cm^{-1} was due to a downshifting of the A_{1g} mode in the presence of bridging V_o. However, it is important to note that there is limited published work in this area and these assignments may not necessarily be reliable.

The SERS spectra recorded using the Ag@SnO_2 NP substrates normally contain the broad SnO_2 peak at 573 cm^{-1}. However, it can often be difficult to study as it can become obscured by more dominant analyte peaks and it is hard to distinguish increases in this peak from the general SERS signal enhancement observed with sustained laser irradiation. To avoid these disruptions, a SERS test was carried out in 0.1 mM acetone. Acetone was chosen as it is known to be a “active” molecule (section 5.4.1) and has a simple SERS spectrum which is dominated by one peak at 788 cm^{-1}. The SERS spectra in the wavelength range of interest are plotted in Figure 5.29. The broad SnO_2 peak at 573 cm^{-1} (A_s) can be clearly identified, it increases initially before plateauing and shifting slightly to the right (larger Raman shifts). The A_{1g} peak is not visible initially but increases with irradiation time until a clear shoulder is observed in the SnO_2 peak.

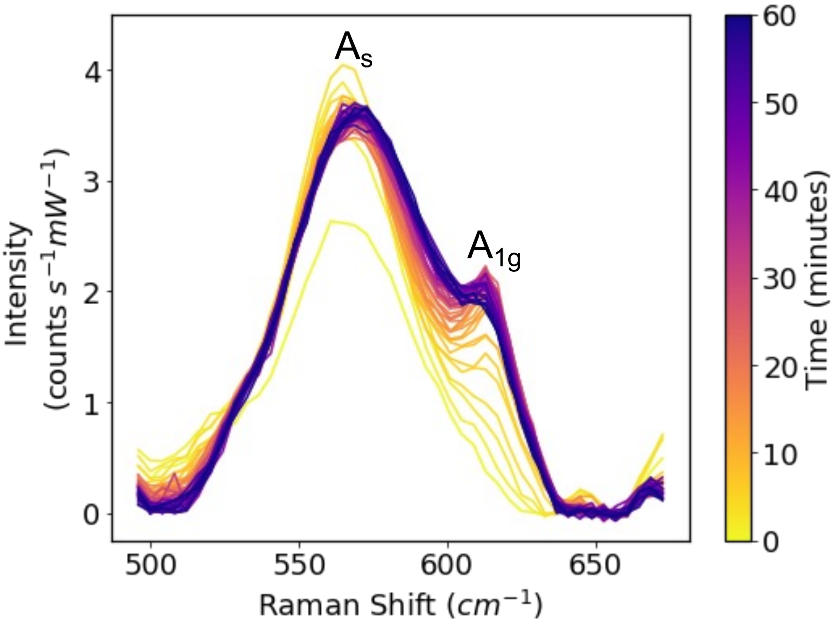

Figure 5.29: A zoomed-in section of successive SERS spectra recorded over 1 hour in an aqueous 0.1 mM acetone solution with a Ag@SnO₂ substrate. The colour of the spectra indicates the irradiation time with the initial spectra plotted in yellow and the final spectra plotted in blue. The A_s and A_{1g} peaks, linked to SnO_2 containing in-plane and bridging oxygen vacancies respectively, are labelled.

The height of the A_s and A_{1g} peaks are plotted in Figure 5.30 along with the ratio of the two peaks. The relative height of the A_{1g} increases with irradiation time, rising rapidly in the first 15 minutes and then plateauing. Based on the previous work relating the Raman peaks to the SnO_2 defects, these results imply that the relative density of bridging oxygen vacancies is increasing with laser irradiation.[402,403] With the information currently available, it is difficult to discern how this relates to the enhanced SERS signals. However, studying the literature related to SnO_2 gas sensors (the focus of most SnO_2 research), it seems that bridging oxygen vacancies play a more significant role in charge transfer processes than in-plane oxygen vacancies.[365,406] If this is also the case in this system, then this could help to explain the observed enhancement. In theory, laser irradiation could increase the density of bridging oxygen vacancies, enabling additional charge transfer, and boosting the chemical enhancement component of SERS. However, more research is needed to substantiate this theory and it is possible that this observation may be an incidental consequence of the enhancement mechanism rather than its primary cause.

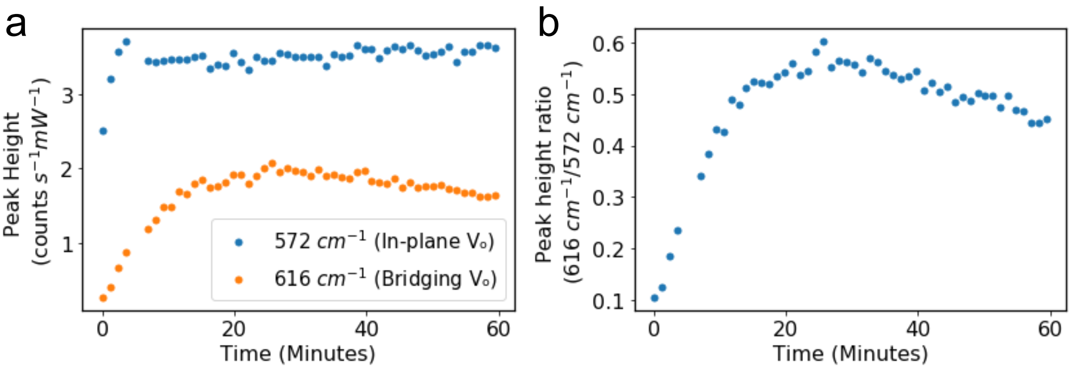

Figure 5.30: (a) The height of the SnO_2 peaks linked to in-plane (blue) and bridging (orange) oxygen vacancies are plotted against irradiation time for spectra recorded in a 1 mM acetone solution with a Ag@SnO_2 substrate. (b) shows the ratio of the two peak heights (616 cm^{-1}/572 cm^{-1}).

5.5.6 Mechanism discussion

The current theory for the in-situ laser induced SERS enhancement is that an increase in the bridging oxygen vacancy density in the SnO_2 results in additional charge transfer. The next question is how does the laser irradiation increase the oxygen vacancy density? The results in section 5.4 revealed that the enhancement is analyte dependent, and an “active” molecule is needed to observe the increase in the SERS signal. The “active” molecules are generally reducing and have lower oxidation potentials than the “inactive” molecules. Therefore, it seems plausible that a redox reaction between the “active” molecule and the SnO_2 is creating the additional oxygen vacancies. Reducing molecules have been shown to generate oxygen vacancies in SnO_2, either through the adsorption of reducing gases in SnO_2 gas sensors[365,407] or pre-treatment with strong reducing agents like $NaBH_4$[408–411]. It is possible that this redox reaction is being made possible by plasmonic heating, which would help explain the laser dependence of the observed behaviour and the plasmonic heating results in section 5.5.2. Based on all the results presented in this section, the current proposed mechanism is as follows: The reducing “active” molecules undergo a redox reaction at the SnO_2 surface, which generates additional bridging oxygen vacancies. This reaction is made possible by plasmonic heating in the Ag NPs. The additional oxygen vacancies enhance the SERS signal by boosting the chemical enhancement through additional charge transfer.

This is a tentative proposed mechanism, and more research is needed to substantiate it. It would be beneficial to gain a deeper understanding of the behaviour of the "active" and "inactive" molecules to give a clearer picture of the redox reactions taking place. Testing a wider variety of analytes would help with this and it would also be interesting to study how the concentration of the different analytes influence the enhancement. It was not possible to study how the UV-vis spectrum of the Ag@SnO_2 NP films changed with laser irradiation with the available time and equipment. However, this approach has been used previously to study the change in the electron density of the plasmonic nanoparticles in hybrid systems and could be a useful way of substantiating the current proposed mechanism.[60,366,412] Finally, it would be interesting to explore other plasmonic-metal metal oxide core-shell nanoparticles, particularly Ag@TiO_2 NPs, to ascertain whether similar enhancements are seen for these systems.

5.6 Applications

5.6.1 Uric acid quantification

After discovering the in-situ laser enhancement of the Ag@SnO_2 NP substrates and delving into the mechanism behind this behaviour, the final step was to investigate the potential applications of this phenomenon. The detection of uric acid with the Ag@SnO_2 NP substrates has already been studied and significant laser-induced enhancements were observed. As discussed extensively in Chapter 3 and Chapter 4, UA is an important biomarker for several conditions, including preeclampsia, gout, and cardiovascular disease. An investigation was carried out to assess whether the Ag@SnO_2 NP substrates could be used for the quantitative detection of UA and evaluate whether their LoD could rival that achieved by the Ag NP E-SERS system. The concentration of the UA solution was gradually increased from 0 μM to 100 μM and a new position was irradiated on the Ag@SnO_2 NP substrate for each concentration. The characteristic peak at 636 cm^{-1} is plotted against time for each UA concentration in Figure 5.31 and the spectra recorded after 60 minutes irradiation are compared in Figure 5.32. The UA characteristic peak increases over irradiation time for all the UA concentrations. After 60 minutes irradiation, the peaks can be clearly distinguished for all the UA concentrations including the 1 μM solution.

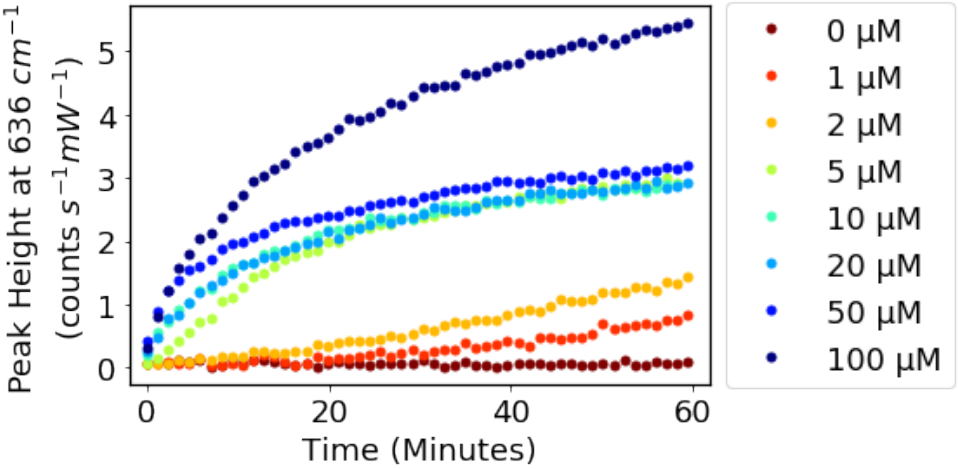

Figure 5.31: The height of the characteristic UA peak at 636 cm^{-1} plotted against time for a Ag@SnO$_2$ substrate irradiated for 60 minutes in a solution containing between 0 - 100 μM UA.

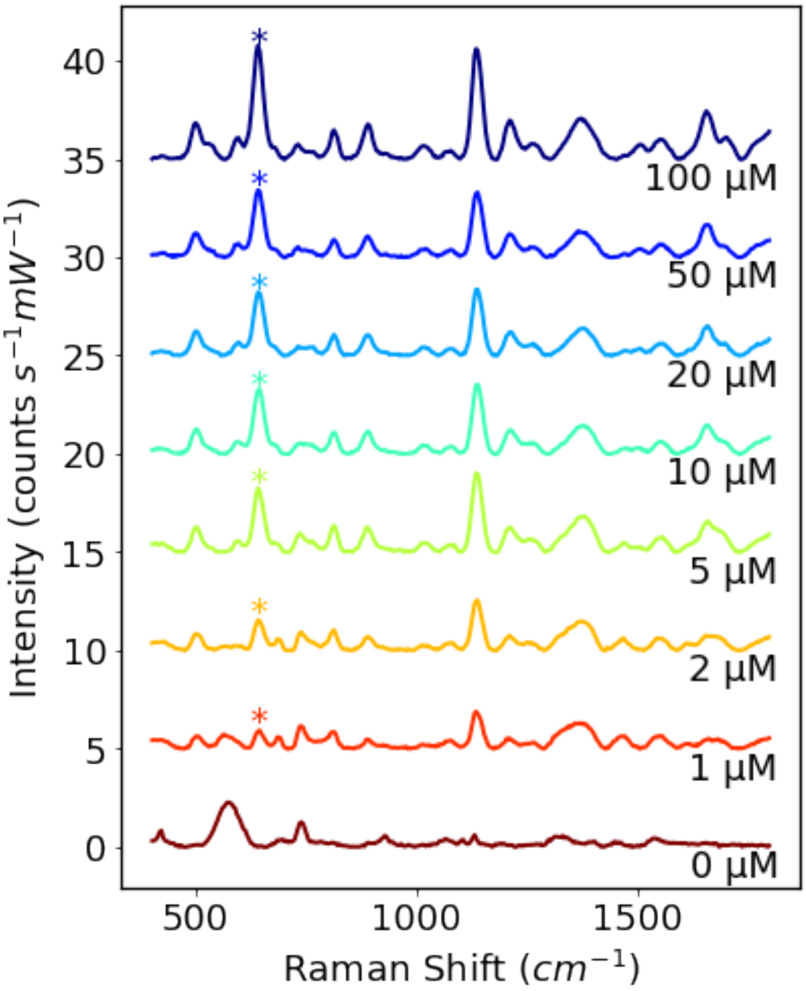

*Figure 5.32: SERS spectra of UA solutions with concentrations ranging from 0 μM to 100 μM recorded after 1 hour of irradiation. The characteristic UA peak is indicated with a *.*

The heights of the 636 cm^{-1} peak in the initial spectra and the final spectra are compared in Figure 5.33a. This clearly illustrated the benefit offered by the in-situ laser enhancement. Without laser irradiation, it is not possible to distinguish between the different UA concentrations but after 1 hour irradiation, there is a clear positive correlation between the peak height and the analyte concentration. However, the relationship is not particularly strong ($R^2 = 0.81$). For the higher concentrations, the 636 cm^{-1} peak height started to plateau after around 20 minutes and there was not a significant difference in the final heights for the 5 – 50 μM solutions. However, it was possible to observe a difference in the initial rate of increase of the characteristic peak. The initial gradient of the 636 cm^{-1} peak increase is plotted against UA concentration in Figure 5.33b. This shows a much stronger relationship ($R^2 = 0.98$), although it should be noted that only one measurement was performed for each concentration due to time constraints and much more testing would be needed to properly assess the quantitative sensing ability of this system.

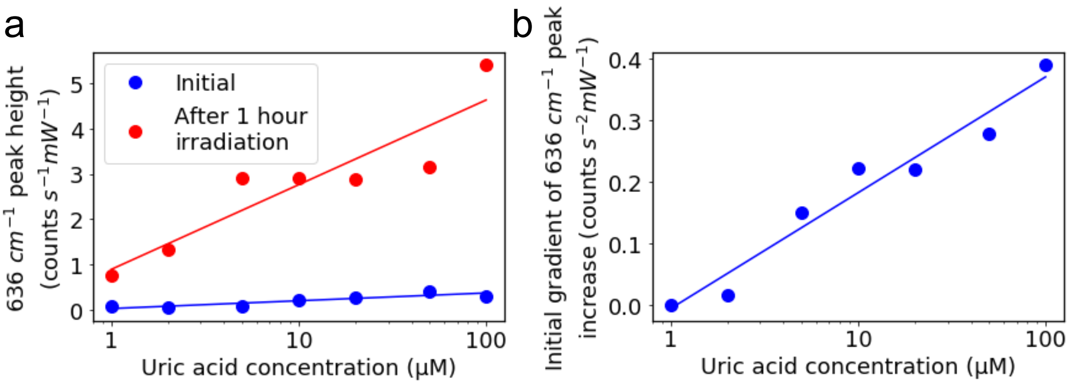

Figure 5.33: (a) The peak height at 636 cm^{-1} *plotted against UA concentration for the initial spectra recorded using the Ag@SnO*$_2$ *NP substrate (blue) and the spectra recorded after 60 minutes of irradiation. A linear relationship is fitted between log(concentration) and peak height for concentrations from 1 µM to 100 µM. (b) The initial gradient of the 636 cm*$^{-1}$ *peak height increase plotted against UA concentration. A linear relationship is fitted between log(concentration) and gradient for concentrations from 1 µM to 100 µM.*

The strong relationship between the rate of increase and the analyte concentration shows how the dynamic nature of the Ag@SnO$_2$ SERS spectra could be utilised for quantitative detection. The LoD was calculated as 3.3 times the standard error of the slope in Figure 5.33b (divided by the slope (i.e. 3.3σ/S).[336] This resulted in a LoD of 0.32 µM. As a comparison, the UA LoD for the Ag NP E-SERS system was 0.13 µM. It is promising to see that the initial tests of the Ag@SnO$_2$ system can achieve comparable limits of detection to the optimised E-SERS system without the need for external applied potential. However, more testing is needed to give a representative R^2 and LoD, and properly assess the performance of this system.

5.6.2 Detection of 3-hydroxybutanoic acid

The "activation" tests in section 5.4.1 demonstrated that the addition of an "active" molecule could be used to induce the laser enhancement of an "inactive" molecule. The "activator" molecule does not need to be a strong Raman scatterer itself, so the possibility that the Ag@SnO$_2$ system could be used to indirectly detect weak Raman scatterers was explored. This is a similar approach to the one used in SERS tag systems.[28]

Ketosis is a metabolic state that is characterized by increased levels of ketone bodies (acetone, acetoacetic acid and 3-hydroxybutanoic acid (3-HB)) in the blood or urine and is the result of low glucose availability.[20] The uncontrolled production of ketones can result in ketoacidosis, a serious medical condition which most commonly affects people with diabetes. 3-HB is the ketosis biomarker detected in commercial sensors and blood 3-HB concentrations of over 1 mM indicate elevated levels of ketosis.[20] Many of the hybrid SERS "active" molecules are ketones or carboxylic acids and the ketone bodies produced by ketosis are not strong Raman scatterers so the feasibility of using laser-enhanced Ag@SnO_2 SERS to detect ketoacidosis was investigated.

A Ag@SnO_2 substrate was submerged in an aqueous solution containing 10 μM adenine (an "inactive molecule") and irradiated for 60 minutes. 1 mM of 3-HB was then added and a rapid increase in the adenine peak at 735 cm^{-1} was recorded (Figure 5.34). The adenine peak increased by over 16 times from 2.28 to 37.05 counts mW^{-1} s^{-1} over 60 minutes. No new peaks from the 3-HB were observed.

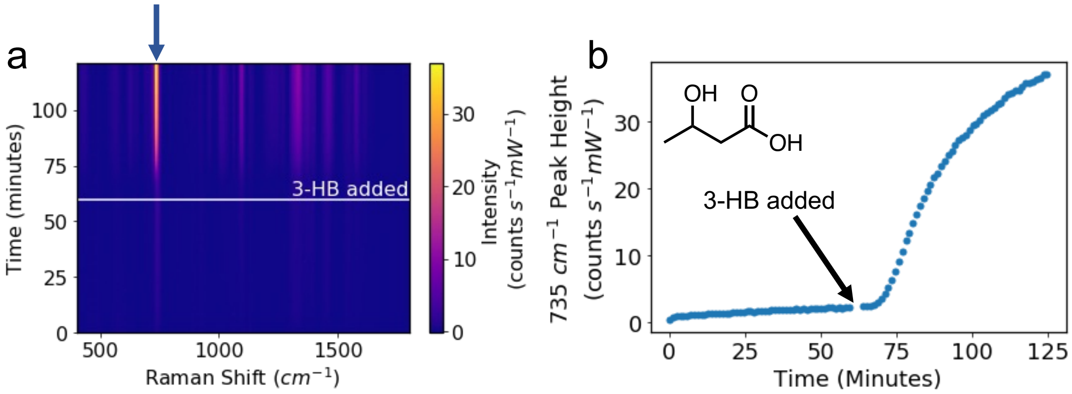

Figure 5.34: (a) A heatmap showing how the spectra of a 10 μM adenine solution recorded using a Ag@SnO₂ substrate change over time with the addition of 1 mM 3-hydroxybutanoic acid after 60 minutes. (b) The characteristic adenine peak height is plotted against time. The position of this peak in the spectra in (a) is indicated with a blue arrow.

This indirect detection approach is not specific as it is only possible to detect the general presence of “active” molecules rather than a “fingerprint” of a particular analyte as in SERS. However, since ketoacidosis is characterised by significantly elevated levels of ketones and the Ag@SnO_2 system is particularly sensitive to ketones, it may be possible to measure a difference in the laser-induced SERS enhancement for patients in ketoacidosis versus healthy patients. Initial tests were carried out in human blood serum to assess the feasibility of this idea. As expected, the SERS spectra of undiluted human blood serum recorded using the Ag@SnO_2 substrates were extremely noisy, and it was not possible to identify any specific peaks (Figure 5.35a). However, when the serum was diluted 100x with deionized water, it was possible to identify some SERS peaks including the SnO_2 peak at 573 cm^{-1}. Unsurprisingly considering the plethora of different molecules in human blood serum, the peaks increased with laser irradiation (Figure 5.35b).

A series of tests were then carried out with a solution containing 100x diluted human blood serum (1%) and 1 μM adenine. Different concentrations of 3-HB were then added based on 100x dilutions of clinically relevant levels. These concentrations ranged between 5 μM and 50 μM which correspond to serum concentrations of 0.5 – 5 mM; over 1 mM is an indicator of ketosis. A significant laser enhancement was observed for all the concentrations (Figure 5.35b). However, it was not possible to identify a quantitative relationship between the

3-HB concentration and the magnitude or increase in the adenine characteristic peak. This is probably because human blood serum itself has a high concentration of “active” molecules, so the relatively low concentrations of additional 3-HB do not make a discernible difference to the enhancement. The variability observed across and between the substrates means that a significant difference in SERS response is needed for sensitive quantitative detection. The prospect of ketosis detection using the Ag@SnO_2 substrates could be revisited if additional functionalities, such as analyte filtering or separation within the blood serum, are incorporated into the system.

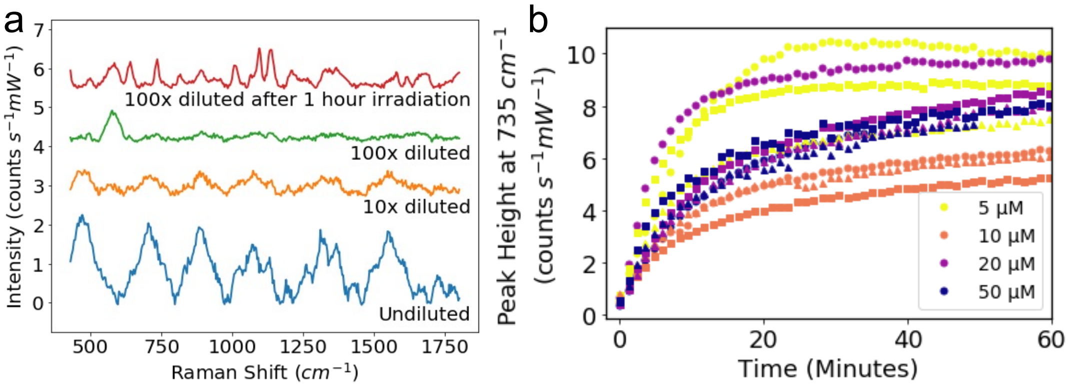

Figure 5.35: (a) SERS spectra recorded using Ag@SnO_2 substrates in undiluted (blue), 10x diluted (10%) (orange), and 100x diluted (1%) (green) human blood serum. The red line shows the spectra for 100x diluted human blood serum after 1 hour of laser irradiation. (b) The height of the characteristic adenine peak at 735 cm^{-1} plotted against time for a Ag@SnO_2 substrate irradiated for 60 minutes in a solution containing between 5 - 50 μM 3-hydroxybutanoic acid (3-HB) and 1% human blood serum.

5.6.3 Detection of ketamine

5.6.3.1 Detection in water

Ketamine is a dissociative anaesthetic commonly used in veterinary and human medicine.[413] It has also gained popularity as a recreational drug due to its hallucinogenic and dissociative effects. Driving under the influence of ketamine is an area of increasing concern as the drug can induce sedation, alter perception of time and space, and impair judgment.[413–415] Current detection methods include lateral flow-based rapid oral fluid test kits, which are not quantitative and have limited sensitivity, and specialised and expensive lab-based techniques, such as liquid chromatography–mass spectrometry

(LC-MS). As such, there is a need for quick, cost-effective, quantitative ketamine sensors.

An investigation was carried out to determine whether laser-enhanced Ag@SnO$_2$ NP substrates could be used to detect ketamine. The Ag@SnO$_2$ NP substrates were submerged in solutions containing 1 µM to 100 µM ketamine and irradiated for 60 minutes. Characteristic ketamine Raman peaks were identified at 612, 770, 1313, 1366, and 1513 cm^{-1} with the largest being observed at 1513 cm^{-1} (Figure 5.36).

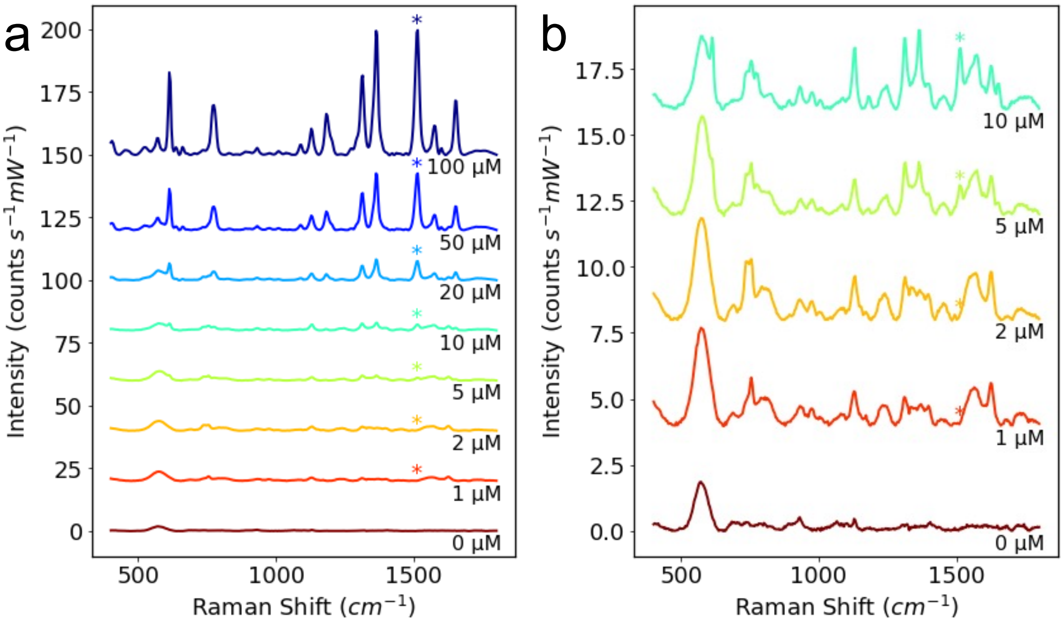

*Figure 5.36: (a) SERS spectra of ketamine solutions with concentrations ranging from 0 µM to 100 µM recorded after 1 hour of irradiation with Ag@SnO$_2$ NP substrates. The characteristic ketamine peak is indicated with a *. (b) A zoomed-in section showing the spectra for the 0 µM to 10 µM ketamine solutions.*

These peaks display the typical in-situ laser enhancement (Appendix Figure A.17) and after 60 minutes irradiation can be clearly distinguished at concentrations down to 5 µM. There is a strong relationship between the intensity of the 1513 cm^{-1} peak and the ketamine concentration (Figure 5.37). However, more tests are needed to give a representative R^2 and properly assess the performance of this system. There was also a good correlation between the initial gradient of the peak increase and the concentration

(Appendix Figure A.18). These results were compared to previous data collected by a member of our group, Alice Cozens, using Ag NPs to detect ketamine (Appendix Figure A.19). The Ag NPs displayed much smaller characteristic SERS peaks (10.5 vs 49.8 counts mW^{-1} s^{-1} for a 100 μM solution) and it was only possible to distinguish the ketamine peaks for solutions with concentrations greater than 20 μM. This highlights the benefits offered by the laser-enhanced Ag@SnO$_2$ system for the detection of trace analytes.

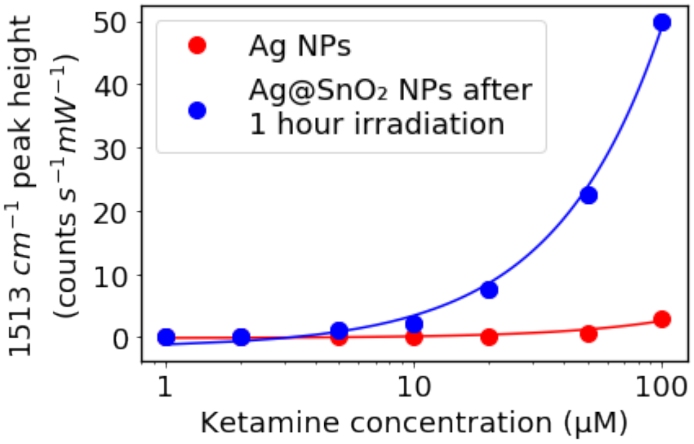

Figure 5.37: (a) The peak height at 1513 cm^{-1} plotted against ketamine concentration for the spectra recorded using Ag@SnO$_2$ NP substrates after 1 hour laser irradiation (blue) and the spectra recorded using Ag NP substrates collected by Alice Cozens (red). A linear relationship is fitted between the concentration and peak height for concentrations from 1 μM to 100 μM.

5.6.3.2 Detection in synthetic saliva

After the success of the initial ketamine detection tests, the next step was to carry out tests in synthetic saliva to simulate real-world use. The synthetic saliva contained KH_2PO_4, NaCl, $CaCl_2$ and NaOH and was used undiluted.[281] Real human saliva is much more complicated than this, however, this was used as a starting point to test the system. The Ag@SnO$_2$ NP substrates were submerged in ketamine-spiked synthetic saliva solutions and irradiated for 60 minutes. The characteristic ketamine peaks could be clearly identified, and they were actually significantly larger than those recorded in the aqueous solutions (Figure 5.38). The reason for this is unclear. One possibility is that the salts present in the synthetic saliva could be enhancing the SERS signals, potentially through reduction reactions which form additional oxygen vacancies as discussed in section 5.5.6. Alternatively, it could be attributed to the general improvements that had been made to the Ag@SnO_2 substrate fabrication process as these results were collected much later in the project. Due to time constraints, it was not possible to investigate this further.

SERS spectra were recorded from three different positions on an Ag@SnO_2 NP substrates submerged in a synthetic saliva solution containing between 0.05 μM and 1 μM. It was possible to distinguish the characteristic peak for all the ketamine solutions. There is a strong relationship between the intensity of the 1513 cm^{-1} peak and the ketamine concentration (Figure 5.39). A linear relationship is fitted between log(concentration) and peak height for concentrations from 0.05 μM to 1 μM with good agreement (R^2 = 0.91).

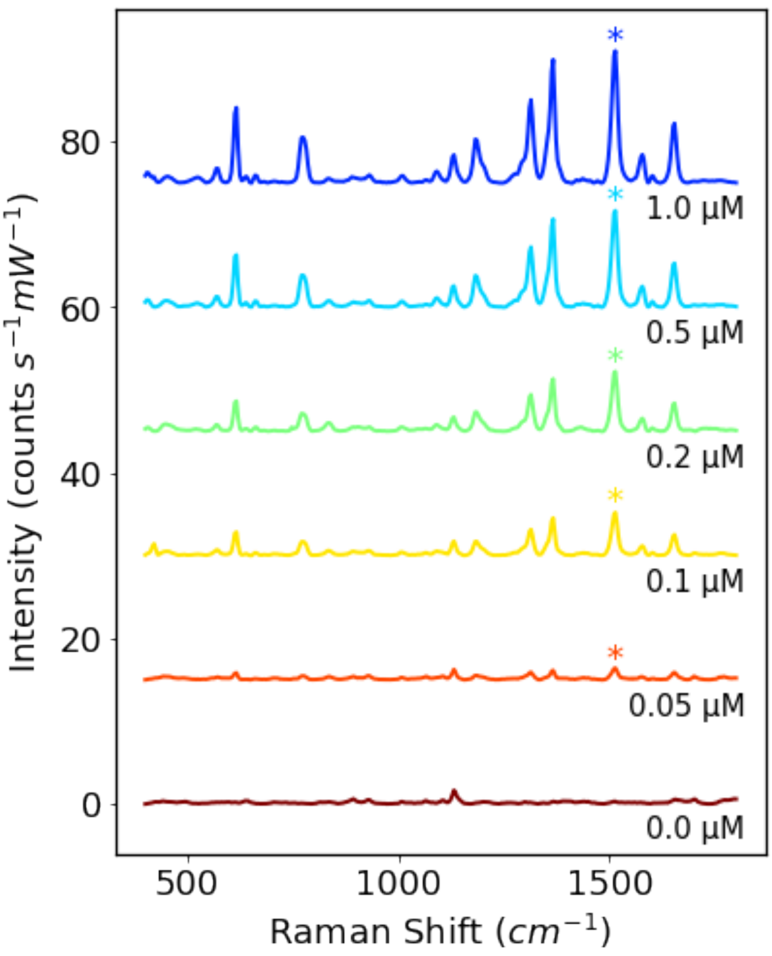

*Figure 5.38: (a) SERS spectra of synthetic saliva solutions containing between 0 μM to 1 μM ketamine recorded after 1 hour of irradiation with Ag@SnO$_2$ NP substrates. The spectra plotted are the mean spectra calculated from three different spots on the substrates. The characteristic ketamine peak is indicated with a *.*

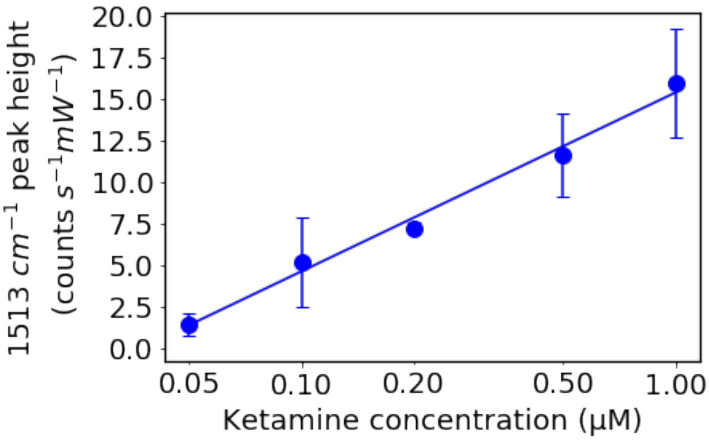

Figure 5.39: (a) The peak height at 1513 cm^{-1} plotted against ketamine concentration for the spectra recorded using Ag@SnO$_2$ NP substrates after 1 hour laser irradiation. A linear relationship is fitted between the log(concentration) and peak height for concentrations from 0.05 μM to 1 μM.

5.6.3.3 Improved measurement conditions

The results presented above were encouraging; however, the practicality of the Ag@SnO_2 system is limited by the need for approximately 1 hour of irradiation to reach the maximum peak heights. The 785 nm laser tests in section 5.5.1 had shown that increasing the laser power could speed up the in-situ enhancement and give large SERS signals. The 633 nm laser had a fixed power; however, the measurement setup was adapted so that spectra could be recorded at a focal distance which was closer to the focal point of the laser. This reduced the laser spot size and increased the power density within the measurement area. Using these new measurement conditions, the maximum peak heights were reached within 15 minutes (Appendix Figure A.20) and much larger peaks were recorded (~30x larger) which enabled the detection of lower concentrations of ketamine.

SERS spectra were recorded from three different positions on a Ag@SnO_2 NP substrates submerged in a synthetic saliva solution containing between 0.5 nM and 200 nM. The substrates were irradiated for 15 minutes. The new measurement conditions meant it was possible to distinguish the characteristic peak for all the ketamine solutions, down to 0.5 nM (Figure 5.40). Unfortunately, due to the sensitivity of the system and the fact that the 3D-printed PLA substrate holder is difficult to properly clean, there were some contamination issues, and occasionally ketamine peaks were detected in the pure synthetic saliva solution (0 nM ketamine). However, they were still smaller than the peaks observed for the lowest concentration ketamine solution (the 1513 cm^{-1} peak was 29.0 ± 0.03 for the 0.5 nM solution and 23.0 ± 14.8 for the "0 nM" solution). Improving the robustness of the measurement set-up in the future should be able to eliminate this problem.

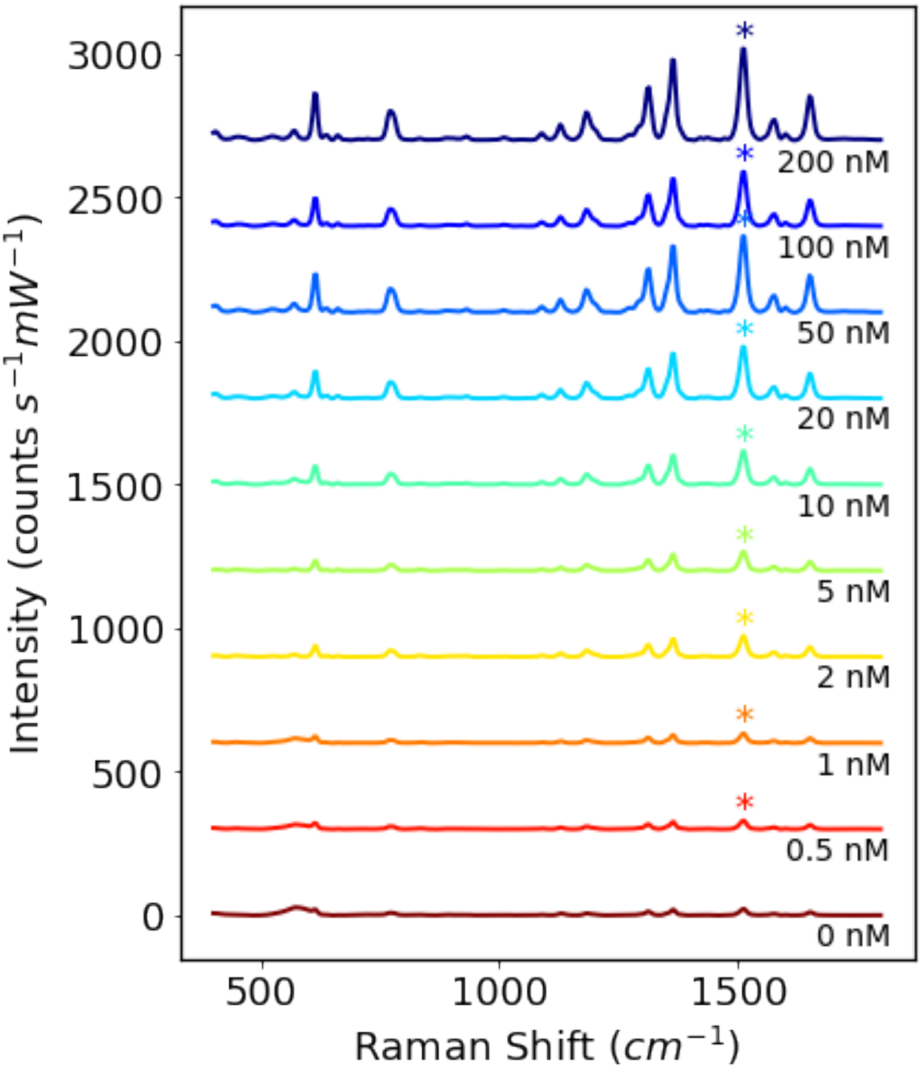

*Figure 5.40: SERS spectra of synthetic saliva solutions containing between 0 nM to 200 nM ketamine recorded after 15 minutes irradiation with Ag@SnO$_2$ NP substrates using the improved measurement position. The spectra plotted are the mean spectra calculated from three different spots on the substrates. The characteristic ketamine peak is indicated with a *.*

There is a strong relationship between the intensity of the 1513 cm^{-1} peak and the ketamine concentration (Figure 5.41). A linear relationship is fitted between log(concentration) and peak height for concentrations from 0.5 nM to 200 nM with good agreement (R^2 = 0.87). The limit of detection (LoD) was calculated as 3.3 times the standard error of the slope of the calibration line divided by the slope (i.e. 3.3σ/S). The LoD for the detection of ketamine using Ag@SnO$_2$ substrates after 15 minutes irradiation was 0.342 nM.

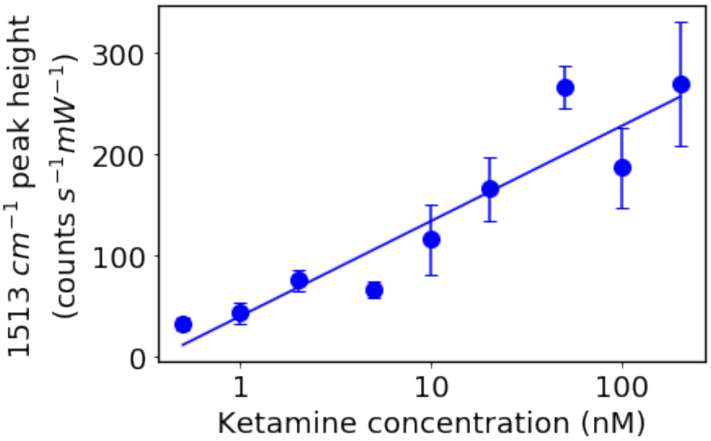

Figure 5.41: (a) The peak height at 1513 cm^{-1} plotted against ketamine concentration for the spectra recorded in synthetic saliva using Ag@SnO$_2$ NP substrates after 15 minutes irradiation at the improved measurement position. A linear relationship is fitted between the log(concentration) and peak height for concentrations from 0.5 nM to 200 nM. The error bars are equal to ± the standard deviation of three measurements.

The LoD of 0.342 nM offers a significant improvement over the current non-quantitative commercial sensors. The advertised ketamine cut-off values for three rapid oral fluid testing devices, the DrugWipe® 6S, Ora-Check® and SalivaScreen®, are 21 nM, 210 nM and 105 nM respectively.[416] However, a study by Tang et al. evaluated these devices and found that they had poor sensitivity – 43% for DrugWipe® 6S, 60% for Ora-Check® and 71% for SalivaScreen®.[416] Studies testing the saliva of ketamine users have found concentrations from ~25 nM to ~230 μM with median concentrations of approximately 1 μM.[416,417] As these typical concentrations are significantly higher than the 0.311 nM LoD, it may be possible to dilute the saliva before performing SERS measurements, which could help to minimise disruption from possible polluting molecules in the saliva. This study is preliminary, and more research is needed to determine the sensor's performance with real human saliva samples. Nevertheless, the laser-enhanced hybrid SERS system offers a promising tool for rapid, inexpensive illicit drug detection.

5.7 Conclusions

This chapter has demonstrated the in-situ laser enhancement of hybrid Ag@SnO$_2$ NP substrates for SERS. An unexpected, time-dependent increase in the SERS signal was observed when the Ag@SnO$_2$ NP substrates were irradiated with a 633 nm laser. For a 0.1 mM UA solution, the characteristic SERS peak increased by 19x over 60 minutes of irradiation and the enhancement was stable for at least 12 hours. Analysis of uncoated Ag NPs, SnO_2 NPs or Ag@SiO_2 NPs revealed that this behaviour was only observed for Ag@SnO_2 NPs. The laser-induced enhancement was revealed to be analyte dependent (reducing molecules were generally “active” whilst oxidising molecules were normally “inactive), but not analyte specific as it was possible to “induce” the SERS enhancement for an “inactive” analyte by adding an “active” molecule.

Extensive testing was carried out to determine the mechanism behind this enhancement using SEM, TEM, XPS and in-depth analysis of the SERS spectra. Based on this work, the proposed mechanism is that reducing “active” molecules undergo a redox reaction at the SnO_2 surface, which generates additional bridging oxygen vacancies. This reaction is made possible by plasmonic heating in the Ag NPs. The additional oxygen vacancies enhance the SERS signal by boosting the chemical enhancement through additional charge transfer. To further substantiate this theory, more investigation is needed into the potential redox reactions taking place at the surface and it would also be useful to determine whether this phenomenon is observed for other hybrid systems.

Potential applications of the Ag@SnO_2 NP system were investigated. Quantitative detection of uric acid using the rate of increase of the characteristic SERS peaks was demonstrated. A preliminary LoD of 0.32 μM was achieved, which is only slightly higher than the 0.13 μM detection limit realised by the optimised Ag NP E-SERS system, and crucially the hybrid system does not require an external applied potential. The indirect detection of the ketosis biomarker, 3-hydroxybutanoic acid, was also explored. This was successful in an aqueous detection but was not practical in human blood serum due to the other activator molecules present in the complex fluid. Finally, quantitative detection of ketamine in synthetic saliva was demonstrated. A limit of detection of 0.342 nM was achieved, which offers a significant improvement over the current non-quantitative commercial sensors.

Chapter 6 Conclusions and future work

6.1 Conclusions

SERS is a powerful analytical technique that has been the focus of significant research over the last 50 years. Despite its potential, it is still yet to achieve clinical use. This thesis has explored ways to boost the sensitivity, selectivity, and interpretability of SERS using electrochemistry, hybrid nanomaterials, and machine learning for the detection of biomarkers and other trace analytes.

Simple Ag NP electrodes were fabricated and used to detect uric acid and creatinine with E-SERS. Applying a potential to the SERS electrodes resulted in significant enhancement of the Raman signal of these analytes and enabled lower concentrations to be detected compared to conventional SERS. Crucially, the applied potential also facilitated the controlled adsorption of UA and CRN on the Ag NP surface, which enabled the selective enhancement of particular characteristic peaks and therefore, the simultaneous detection of the analytes.

Research was carried out to assess the reliability and robustness of the Ag NP/FTO electrodes. A series of improvements were implemented including coating the FTO-coated glass with APTES to improve the adhesion of the Ag NP film; using R6G as an internal standard to normalise the E-SERS spectra and applying negative potentials to remove the adsorbed citrate on the Ag NP surface. These improvements enabled the quantitative detection of UA and CRN. At the optimal applied potentials, the E-SERS system achieved limits of detection of 0.127 μM (UA) and 0.354 μM (CRN) with linear ranges of 1 – 100 μM and 1 – 1000 μM, respectively. The LoD for UA is significantly lower than the concentrations previously detected by colloidal Ag NP E-SERS systems (0.1 mM)[208,209] and comparable to many of the results achieved for more complex nanofabricated electrodes.[242,340] Quantitative E-SERS detection of CRN has not been reported previously but the LoD compares favourably to the results achieved for sophisticated SERS set-ups.[317,342–345]

Despite the improvements implemented, there are still issues with the variability in the SERS signal across and between electrodes which reduces the reliability of the quantitative detection. Although using R6G as an internal standard helps reduce this issue, there are concerns over the competitive adsorption of the target analytes and the R6G molecules and the consistency of the enhancement of the R6G signal at different applied potentials.

An extensive UA/CRN E-SERS dataset was collected, and different machine learning approaches were applied to interpret the spectra. ML has not previously been used for quantitative E-SERS but it is a promising approach as the applied potential offers an additional dimension for the ML analysis, enabling greater differentiation between the spectra recorded from complex multiplexed solutions. Using ML-based concentration prediction also reduces the need for time-consuming visual inspection of SERS spectra by trained operators, increasing the practicality of SERS as an analytical technique.

A two-step PLSR-MLP algorithm was developed which was able to predict the analyte concentrations of unseen spectra with a prediction accuracy of 0.94. The root mean square error of prediction (RMSEP), which can be taken as an indication of the limit of detection of the system, was 5.93 μM for UA and 84.7 μM for CRN. To our knowledge, this is the first demonstration of quantitative, multiplexed detection using E-SERS. These are promising results; however, machine learning relies on large datasets to make reliable predictions. Increasing the size of the UA/CRN E-SERS dataset (to > 10,000 spectra) would help to improve the robustness of the model and reduce the RMSEP. It is also important to recognise that ML models can sometimes be “black boxes” and it is difficult to know how they are making their predictions so care must be taken to make sure the dataset is reliable and representative.

Finally, proof-of-concept experiments were performed in dilute synthetic urine to demonstrate the detection of clinically relevant concentrations of UA and CRN. These tests were preliminary, and more work is needed to achieve quantitative detection of these analytes in complex media. Competitive adsorption of other molecules in urine would likely dampen the detection of the target analytes and synthetic urine is still much simpler than real human urine which is highly variable. Furthermore, to verify multiplexed detection three or more analytes would need to be studied.

Recent work has demonstrated that hybrid plasmonic metal-metal oxide systems can be used to boost the chemical component of the SERS enhancement. Building on this work, tin dioxide-coated silver nanoparticles (Ag@SnO_2 NPs) substrates were fabricated and tested. An unexpected increase in the SERS signal was observed when the Ag@SnO_2 NP substrates were irradiated with the Raman laser, resulting in a ~20x enhancement in the analyte peak heights. The laser-induced enhancement was stable for at least 12 hours and only observed for Ag@SnO_2 NPs.

Extensive testing was conducted to determine the mechanism behind this enhancement using in-depth analysis of the SERS spectra, SEM, TEM and XPS. Based on this work, the proposed mechanism is that reducing molecules undergo a redox reaction at the SnO_2 surface, which generates additional bridging oxygen vacancies. This reaction is made possible by plasmonic heating in the Ag NPs. The additional oxygen vacancies enhance the SERS signal by boosting the chemical enhancement through additional charge transfer. However, this is a tentative proposal, and other factors, particularly morphological changes in the nanostructure, could play a part in the enhancement.

The large peaks observed for the in-situ enhanced Ag@SnO_2 NP substrates meant that they could be used to detect trace concentrations of target analytes. The rate of increase of the characteristic SERS peaks was used to quantitatively detect uric acid, achieving a preliminary LoD of 0.32 μM. This is only slightly higher than the 0.13 μM detection limit achieved by the optimised Ag NP E-SERS system, and crucially the hybrid system does not require an external applied potential.

The indirect detection of the ketosis biomarker, 3-hydroxybutanoic acid, was also explored. This was successful in an aqueous solution but was not practical in human blood serum due to the plethora of other molecules present in the complex fluid. Finally, quantitative detection of ketamine in synthetic saliva was demonstrated. A limit of detection of 0.342 nM was achieved, which offers a significant improvement over the current non-quantitative commercial sensors. However, it is important to recognise that the Ag@SnO_2 NP system is extremely sensitive to the presence of other reducing molecules, and it may struggle to achieve the same results in real human saliva.

6.2 Future work

The variability in the SERS signal across and between the Ag NP/FTO electrodes is still a concern which limits the reliability of the E-SERS system. The drop-cast colloidal NP fabrication approach was chosen due to its accessibility and simplicity. However, more sophisticated methods such as nanosphere lithography can produce much more uniform nanostructures but rely on specialist equipment. Going forward, it would be useful to properly evaluate the cost of these fabrication processes on a larger scale and the improvements they offer to determine if this would be a better approach for low-cost healthcare sensing.

In terms of the E-SERS detection of UA and CRN, the next step would be to build up a similar E-SERS dataset in synthetic urine. This dataset could then be used to train a two-step PLSR-MLP machine learning algorithm which could perform multiplexed quantification. Ideally, this dataset would be larger than the one described in this chapter (over 10,000 spectra) to improve the robustness of the model. A more representative test would be to perform the same process with clinical urine samples. This would be very valuable for determining how complex solutions might affect the E-SERS spectra, either through competitive adsorption on the Ag NP surface or the overlapping of characteristic peaks, and illustrating how the applied potential might overcome some of these issues. It will also be important to study how the ML algorithms handle the variability which is present in real human samples. More broadly, these approaches could be employed to detect a variety of biomarkers in urine (or other bodily fluids). Combining E-SERS and ML with portable Raman spectrometers could bring SERS closer to a clinical reality as a fast, cost-effective tool for biomarker detection.

In Chapter 5, the reason for the in-situ laser-enhancement of the Ag@SnO_2 NPs SERS signal was investigated. A proposed mechanism was presented which centred around the generation of additional oxygen vacancies; however, more investigation is needed to substantiate this theory. In particular, greater understanding is needed of the redox reactions taking place at the SnO_2 surface. It would be useful to perform a more in-depth study of the “active” and “inactive” molecules, potentially by analysing the behaviour of a series of molecules which only differ by one functional group. It may also be helpful to perform some tests in a much smaller measurement cell to see whether it is possible to identify any changes in the SERS spectra as the analyte molecules undergo the redox reactions.

Looking at the nanostructure itself, it would be interesting to investigate how the UV-vis spectrum of the Ag@SnO_2 NP films changed with laser irradiation. This approach has been used previously to study the change in the electron density of the plasmonic nanoparticles in hybrid systems and could be a useful way of substantiating the current proposed mechanism.[60,366,412] It would also be helpful to observe the Ag@SnO_2 NP under the TEM before and after irradiation to determine whether any changes in shape or size are occurring. This may be possible with very careful preparation of the TEM grids and precise control of the laser position or with sophisticated in-situ TEM. Finally, it would be interesting to explore other plasmonic-metal metal oxide core-shell nanoparticles, particularly Au@SnO_2 and Ag@TiO_2 NPs, to ascertain whether similar enhancements are seen for these systems.

For the applications of the Ag@SnO_2 SERS system, further testing should be performed to accurately determine the detection limit for UA and experiments should also be performed in synthetic urine to assess how the presence of other molecules affects the enhancement. The results for the detection of ketamine in synthetic saliva are promising. However, it is important to perform tests in actual human saliva as the Ag@SnO_2 NP system is highly sensitive and may face challenges in achieving reliable performance in variable, complex media.

Bibliography

(1) Etzioni, R.; Urban, N.; Ramsey, S.; McIntosh, M.; Schwartz, S.; Reid, B.; Radich, J.; Anderson, G.; Hartwell, L. The Case for Early Detection. *Nat Rev Cancer* **2003**, *3* (4), 243–252. https://doi.org/10.1038/nrc1041.

(2) Yager, P.; Domingo, G. J.; Gerdes, J. Point-of-Care Diagnostics for Global Health. *Annual Review of Biomedical Engineering* **2008**, *10* (1), 107–144. https://doi.org/10.1146/annurev.bioeng.10.061807.160524.

(3) *NHS England » NHS Long Term Plan ambitions for cancer*. https://www.england.nhs.uk/cancer/strategy/ (accessed 2023-12-05).

(4) FDA-NIH Biomarker Working Group. *Diagnostic Biomarker*; Food and Drug Administration (US), 2016.

(5) Bravo-Merodio, L.; Acharjee, A.; Russ, D.; Bisht, V.; Williams, J. A.; Tsaprouni, L. G.; Gkoutos, G. V. Translational Biomarkers in the Era of Precision Medicine. In *Advances in Clinical Chemistry*; Elsevier, 2021; Vol. 102, pp 191–232. https://doi.org/10.1016/bs.acc.2020.08.002.

(6) Huang, J.; Sokolikova, M.; Ruiz-Gonzalez, A.; Kong, Y.; Wang, Y.; Liu, Y.; Xu, L.; Wang, M.; Mattevi, C.; Davenport, A.; Lee, T.-C.; Li, B. Ultrasensitive Colorimetric Detection of Creatinine via Its Dual Binding Affinity for Silver Nanoparticles and Silver Ions. *RSC Adv.* **2024**, *14* (13), 9114–9121. https://doi.org/10.1039/D3RA08736K.

(7) I, H.; Cho, J.-Y. Chapter Three - Lung Cancer Biomarkers. In *Advances in Clinical Chemistry*; Makowski, G. S., Ed.; Elsevier, 2015; Vol. 72, pp 107–170. https://doi.org/10.1016/bs.acc.2015.07.003.

(8) Simrén, J.; Elmgren, A.; Blennow, K.; Zetterberg, H. Chapter Six - Fluid Biomarkers in Alzheimer’s Disease. In *Advances in Clinical Chemistry*; Makowski, G. S., Ed.; Elsevier, 2023; Vol. 112, pp 249–281. https://doi.org/10.1016/bs.acc.2022.09.006.

(9) Bravo-Merodio, L.; Acharjee, A.; Russ, D.; Bisht, V.; Williams, J. A.; Tsaprouni, L. G.; Gkoutos, G. V. In *Advances in Clinical Chemistry*; Elsevier, 2021; Vol. 102, pp 191–232. https://doi.org/10.1016/bs.acc.2020.08.002.

(10) Kenny, L. C.; Broadhurst, D. I.; Dunn, W.; Brown, M.; North, R. A.; McCowan, L.; Roberts, C.; Cooper, G. J. S.; Kell, D. B.; Baker, P. N. Robust Early Pregnancy Prediction of Later Preeclampsia Using Metabolomic Biomarkers. *Hypertension* **2010**, *56* (4), 741–749. https://doi.org/10.1161/HYPERTENSIONAHA.110.157297.

(11) Roberts, J. M.; Gammill, H. S. Preeclampsia: Recent Insights. *Hypertension* **2005**, *46* (6), 1243–1249. https://doi.org/10.1161/01.HYP.0000188408.49896.c5.

(12) Johnson, R. J.; Kanbay, M.; Kang, D.-H.; Lozada, L. G.-S.; Feig, D. Uric Acid: A Clinically Useful Marker to Distinguish Preeclampsia from Gestational Hypertension. *Hypertension* **2011**, *58* (4), 548–549. https://doi.org/10.1161/HYPERTENSIONAHA.111.178921.

(13) Roberts, J. M.; Bodnar, L. M.; Lain, K. Y.; Hubel, C. A.; Markovic, N.; Ness, R. B.; Powers, R. W. Uric Acid Is as Important as Proteinuria in Identifying Fetal Risk in Women With Gestational Hypertension. *Hypertension* **2005**, *46* (6), 1263–1269. https://doi.org/10.1161/01.HYP.0000188703.27002.14.

(14) Carty, D. M.; Delles, C.; Dominiczak, A. F. Novel Biomarkers for Predicting Preeclampsia. *Trends Cardiovasc Med* **2008**, *18* (5), 186–194. https://doi.org/10.1016/j.tcm.2008.07.002.

(15) Roberts, J. M.; Cooper, D. W. Pathogenesis and Genetics of Pre-Eclampsia. *Lancet* **2001**, *357* (9249), 53–56. https://doi.org/10.1016/s0140-6736(00)03577-7.

(16) Lytvyn, Y.; Perkins, B. A.; Cherney, D. Z. I. Uric Acid as a Biomarker and a Therapeutic Target in Diabetes. *Can J Diabetes* **2015**, *39* (3), 239–246. https://doi.org/10.1016/j.jcjd.2014.10.013.

(17) Feig, D. I.; Kang, D.-H.; Johnson, R. J. Uric Acid and Cardiovascular Risk. *N Engl J Med* **2008**, *359* (17), 1811–1821. https://doi.org/10.1056/NEJMra0800885.

(18) Puig, J. G.; Martínez, M. A.; Mora, M.; Fraile, J. M.; Montoya, F.; Torres, R. J. Serum Urate, Metabolic Syndrome, and Cardiovascular Risk Factors. A Population-Based Study. *Nucleosides, Nucleotides & Nucleic Acids* **2008**, *27* (6–7), 620–623. https://doi.org/10.1080/15257770802138582.

(19) Fraile, J. M.; Puig, J. G.; Torres, R. J.; de Miguel, E.; Martínez, P.; Vázquez, J. J. Uric Acid Metabolism in Patients with Primary Gout and the Metabolic Syndrome. *Nucleosides Nucleotides Nucleic Acids* **2010**, *29* (4–6), 330–334. https://doi.org/10.1080/15257771003741273.

(20) Kilpatrick, E. S.; Butler, A. E.; Ostlundh, L.; Atkin, S. L.; Sacks, D. B. Controversies Around the Measurement of Blood Ketones to Diagnose and Manage Diabetic Ketoacidosis. *Diabetes Care* **2022**, *45* (2), 267–272. https://doi.org/10.2337/dc21-2279.

(21) Heller, A.; Feldman, B. Electrochemical Glucose Sensors and Their Applications in Diabetes Management. *Chem. Rev.* **2008**, *108* (7), 2482–2505. https://doi.org/10.1021/cr068069y.

(22) Koczula, K. M.; Gallotta, A. Lateral Flow Assays. *Essays Biochem* **2016**, *60* (1), 111–120. https://doi.org/10.1042/EBC20150012.

(23) Song, Y.; Wei, W.; Qu, X. Colorimetric Biosensing Using Smart Materials. *Advanced Materials* **2011**, *23* (37), 4215–4236. https://doi.org/10.1002/adma.201101853.

(24) Denoroy, L.; Zimmer, L.; Renaud, B.; Parrot, S. Ultra High Performance Liquid Chromatography as a Tool for the Discovery and the Analysis of Biomarkers of Diseases: A Review. *Journal of Chromatography B* **2013**, *927*, 37–53. https://doi.org/10.1016/j.jchromb.2012.12.005.

(25) Wang, X.; Sun, H.; Zhang, A.; Wang, P.; Han, Y. Ultra-Performance Liquid Chromatography Coupled to Mass Spectrometry as a Sensitive and Powerful Technology for Metabolomic Studies. *Journal of Separation Science* **2011**, *34* (24), 3451–3459. https://doi.org/10.1002/jssc.201100333.

(26) Crutchfield, C. A.; Thomas, S. N.; Sokoll, L. J.; Chan, D. W. Advances in Mass Spectrometry-Based Clinical Biomarker Discovery. *Clinical Proteomics* **2016**, *13* (1), 1. https://doi.org/10.1186/s12014-015-9102-9.

(27) Higson, S. *Analytical Chemistry*; Oxford University Press: Oxford ; New York, 2003.

(28) Langer, J.; Jimenez de Aberasturi, D.; Aizpurua, J.; Alvarez-Puebla, R. A.; Auguié, B.; Baumberg, J. J.; Bazan, G. C.; Bell, S. E. J.; Boisen, A.;

Brolo, A. G.; Choo, J.; Cialla-May, D.; Deckert, V.; Fabris, L.; Faulds, K.; García de Abajo, F. J.; Goodacre, R.; Graham, D.; Haes, A. J.; Haynes, C. L.; Huck, C.; Itoh, T.; Käll, M.; Kneipp, J.; Kotov, N. A.; Kuang, H.; Le Ru, E. C.; Lee, H. K.; Li, J.-F.; Ling, X. Y.; Maier, S. A.; Mayerhöfer, T.; Moskovits, M.; Murakoshi, K.; Nam, J.-M.; Nie, S.; Ozaki, Y.; Pastoriza-Santos, I.; Perez-Juste, J.; Popp, J.; Pucci, A.; Reich, S.; Ren, B.; Schatz, G. C.; Shegai, T.; Schlücker, S.; Tay, L.-L.; Thomas, K. G.; Tian, Z.-Q.; Van Duyne, R. P.; Vo-Dinh, T.; Wang, Y.; Willets, K. A.; Xu, C.; Xu, H.; Xu, Y.; Yamamoto, Y. S.; Zhao, B.; Liz-Marzán, L. M. Present and Future of Surface-Enhanced Raman Scattering. *ACS Nano* **2020**, *14* (1), 28–117. https://doi.org/10.1021/acsnano.9b04224.

(29) Le Ru, E. C.; Etchegoin, P. G. *Principles of Surface-Enhanced Raman Spectroscopy: And Related Plasmonic Effects*, 1st ed.; Elsevier: Amsterdam ; Boston, 2009.

(30) *Surface Enhanced Raman Spectroscopy: Analytical, Biophysical and Life Science Applications*; Schlücker, S., Ed.; Wiley-VCH Verlag: Weinheim, Germany, 2011.

(31) Vandenabeele, P. *Practical Raman Spectroscopy: An Introduction*; Wiley: The Atrium, Southern Gate, Chichester, West Sussex, United Kingdom, 2013.

(32) Atkins, P. W.; De Paula, J. *Physical Chemistry*; Oxford University Press: Oxford, 2006.

(33) Smekal, A. Zur Quantentheorie der Dispersion. *Naturwissenschaften* **1923**, *11* (43), 873–875. https://doi.org/10.1007/BF01576902.

(34) Smith, E.; Dent, G. *Modern Raman Spectroscopy: A Practical Approach*; J. Wiley: Hoboken, NJ, 2005.

(35) Raman, C. V.; Krishnan, K. S. A New Type of Secondary Radiation. *Nature* **1928**, *121* (3048), 501–502. https://doi.org/10.1038/121501c0.

(36) Larkin, P. Chapter 1 - Introduction: Infrared and Raman Spectroscopy. In *Infrared and Raman Spectroscopy*; Larkin, P., Ed.; Elsevier: Oxford, 2011; pp 1–5. https://doi.org/10.1016/B978-0-12-386984-5.10001-1.

(37) Fleischmann, M.; Hendra, P. J.; McQuillan, A. J. Raman Spectra of Pyridine Adsorbed at a Silver Electrode. *Chemical Physics Letters* **1974**, *26* (2), 163–166. https://doi.org/10.1016/0009-2614(74)85388-1.

(38) Wu, D.-Y.; Li, J.-F.; Ren, B.; Tian, Z.-Q. Electrochemical Surface-Enhanced Raman Spectroscopy of Nanostructures. *Chem. Soc. Rev.* **2008**, *37* (5), 1025. https://doi.org/10.1039/b707872m.

(39) Pilot; Signorini; Durante; Orian; Bhamidipati; Fabris. A Review on Surface-Enhanced Raman Scattering. *Biosensors* **2019**, *9* (2), 57. https://doi.org/10.3390/bios9020057.

(40) Schlücker, S. Surface-Enhanced Raman Spectroscopy: Concepts and Chemical Applications. *Angew. Chem. Int. Ed.* **2014**, *53* (19), 4756–4795. https://doi.org/10.1002/anie.201205748.

(41) Petryayeva, E.; Krull, U. J. Localized Surface Plasmon Resonance: Nanostructures, Bioassays and Biosensing—A Review. *Analytica Chimica Acta* **2011**, *706* (1), 8–24. https://doi.org/10.1016/j.aca.2011.08.020.

(42) Ghosh, S. K.; Pal, T. Interparticle Coupling Effect on the Surface Plasmon Resonance of Gold Nanoparticles: From Theory to

Applications. *Chem. Rev.* **2007**, *107* (11), 4797–4862. https://doi.org/10.1021/cr0680282.

(43) Kelly, K. L.; Coronado, E.; Zhao, L. L.; Schatz, G. C. The Optical Properties of Metal Nanoparticles: The Influence of Size, Shape, and Dielectric Environment. *J. Phys. Chem. B* **2003**, *107* (3), 668–677. https://doi.org/10.1021/jp026731y.

(44) Louis, C.; Pluchery, O. *Gold Nanoparticles For Physics, Chemistry And Biology (Second Edition)*; World Scientific, 2017.

(45) Isabel Pérez-Jiménez, A.; Lyu, D.; Lu, Z.; Liu, G.; Ren, B. Surface-Enhanced Raman Spectroscopy: Benefits, Trade-Offs and Future Developments. *Chemical Science* **2020**, *11* (18), 4563–4577. https://doi.org/10.1039/D0SC00809E.

(46) Moskovits, M. Surface-Enhanced Raman Spectroscopy: A Brief Retrospective. *Journal of Raman Spectroscopy* **2005**, *36* (6–7), 485–496. https://doi.org/10.1002/jrs.1362.

(47) Xu, H.; Aizpurua, J.; Käll, M.; Apell, P. Electromagnetic Contributions to Single-Molecule Sensitivity in Surface-Enhanced Raman Scattering. *Phys. Rev. E* **2000**, *62* (3), 4318–4324. https://doi.org/10.1103/PhysRevE.62.4318.

(48) Chio, W.-I. K.; Liu, J.; Jones, T.; Perumal, J.; Dinish, U. S.; Parkin, I. P.; Olivo, M.; Lee, T.-C. SERS Multiplexing of Methylxanthine Drug Isomers via Host–Guest Size Matching and Machine Learning. *J. Mater. Chem. C* **2021**, *9* (37), 12624–12632. https://doi.org/10.1039/D1TC02004H.

(49) Davison, G.; Jones, T.; Liu, J.; Kim, J.; Yin, Y.; Kim, D.; Chio, W. K.; Parkin, I. P.; Jeong, H.; Lee, T. Computer-Aided Design and Analysis of Spectrally Aligned Hybrid Plasmonic Nanojunctions for SERS Detection of Nucleobases. *Adv Materials Technologies* **2023**, 2201400. https://doi.org/10.1002/admt.202201400.

(50) Zhu, W.; Esteban, R.; Borisov, A. G.; Baumberg, J. J.; Nordlander, P.; Lezec, H. J.; Aizpurua, J.; Crozier, K. B. Quantum Mechanical Effects in Plasmonic Structures with Subnanometre Gaps. *Nature Communications* **2016**, *7* (1), 11495. https://doi.org/10.1038/ncomms11495.

(51) Jones, T.; Davison, G.; Jeong, H.-H.; Lee, T.-C. Chapter 2. Engineered Gold Nanoparticles for Photothermal Applications. In *Nanoscience & Nanotechnology Series*; Ye, E., Li, Z., Eds.; Royal Society of Chemistry: Cambridge, 2022; pp 33–80. https://doi.org/10.1039/9781839165177-00033.

(52) Hao, E.; Schatz, G. C. Electromagnetic Fields around Silver Nanoparticles and Dimers. *The Journal of Chemical Physics* **2004**, *120* (1), 357–366. https://doi.org/10.1063/1.1629280.

(53) Hu, J.; Jiang, R.; Zhang, H.; Guo, Y.; Wang, J.; Wang, J. Colloidal Porous Gold Nanoparticles. *Nanoscale* **2018**, *10* (39), 18473–18481. https://doi.org/10.1039/C8NR06149A.

(54) Chen, X.; Jiang, C.; Yu, S. Nanostructured Materials for Applications in Surface-Enhanced Raman Scattering. *CrystEngComm* **2014**, *16* (43), 9959–9973. https://doi.org/10.1039/C4CE01383B.

(55) Reguera, J.; Langer, J.; Aberasturi, D. J. de; Liz-Marzán, L. M. Anisotropic Metal Nanoparticles for Surface Enhanced Raman

Scattering. *Chem. Soc. Rev.* **2017**, *46* (13), 3866–3885. https://doi.org/10.1039/C7CS00158D.

(56) Zong, C.; Xu, M.; Xu, L.-J.; Wei, T.; Ma, X.; Zheng, X.-S.; Hu, R.; Ren, B. Surface-Enhanced Raman Spectroscopy for Bioanalysis: Reliability and Challenges. *Chem. Rev.* **2018**, *118* (10), 4946–4980. https://doi.org/10.1021/acs.chemrev.7b00668.

(57) Liu, Y.; Ma, H.; Han, X. X.; Zhao, B. Metal–Semiconductor Heterostructures for Surface-Enhanced Raman Scattering: Synergistic Contribution of Plasmons and Charge Transfer. *Mater. Horiz.* **2021**, *8* (2), 370–382. https://doi.org/10.1039/D0MH01356K.

(58) Lee, H. K.; Lee, Y. H.; Koh, C. S. L.; Phan-Quang, G. C.; Han, X.; Lay, C. L.; Sim, H. Y. F.; Kao, Y.-C.; An, Q.; Ling, X. Y. Designing Surface-Enhanced Raman Scattering (SERS) Platforms beyond Hotspot Engineering: Emerging Opportunities in Analyte Manipulations and Hybrid Materials. *Chem. Soc. Rev.* **2019**, *48* (3), 731–756. https://doi.org/10.1039/C7CS00786H.

(59) Jiang, X.; Li, X.; Jia, X.; Li, G.; Wang, X.; Wang, G.; Li, Z.; Yang, L.; Zhao, B. Surface-Enhanced Raman Scattering from Synergistic Contribution of Metal and Semiconductor in TiO2/MBA/Ag(Au) and Ag(Au)/MBA/TiO2 Assemblies. *J. Phys. Chem. C* **2012**, *116* (27), 14650–14655. https://doi.org/10.1021/jp302139e.

(60) Ben-Jaber, S.; Peveler, W. J.; Quesada-Cabrera, R.; Cortés, E.; Sotelo-Vazquez, C.; Abdul-Karim, N.; Maier, S. A.; Parkin, I. P. Photo-Induced Enhanced Raman Spectroscopy for Universal Ultra-Trace Detection of Explosives, Pollutants and Biomolecules. *Nat Commun* **2016**, *7* (1), 12189. https://doi.org/10.1038/ncomms12189.

(61) Zhao, J.; Wang, Z.; Lan, J.; Khan, I.; Ye, X.; Wan, J.; Fei, Y.; Huang, S.; Li, S.; Kang, J. Recent Advances and Perspectives in Photo-Induced Enhanced Raman Spectroscopy. *Nanoscale* **2021**, *13* (19), 8707–8721. https://doi.org/10.1039/D1NR01255J.

(62) Glass, D.; Cortés, E.; Ben-Jaber, S.; Brick, T.; Peveler, W. J.; Blackman, C. S.; Howle, C. R.; Quesada-Cabrera, R.; Parkin, I. P.; Maier, S. A. Dynamics of Photo-Induced Surface Oxygen Vacancies in Metal-Oxide Semiconductors Studied Under Ambient Conditions. *Adv Sci (Weinh)* **2019**, *6* (22), 1901841. https://doi.org/10.1002/advs.201901841.

(63) Al-Shammari, R. M.; Baghban, M. A.; Al-attar, N.; Gowen, A.; Gallo, K.; Rice, J. H.; Rodriguez, B. J. Photoinduced Enhanced Raman from Lithium Niobate on Insulator Template. *ACS Appl. Mater. Interfaces* **2018**, *10* (36), 30871–30878. https://doi.org/10.1021/acsami.8b10076.

(64) Ye, J.; Arul, R.; Nieuwoudt, M. K.; Dong, J.; Zhang, T.; Dai, L.; Greenham, N. C.; Rao, A.; Hoye, R. L. Z.; Gao, W.; Simpson, M. C. Understanding the Chemical Mechanism behind Photoinduced Enhanced Raman Spectroscopy. *J. Phys. Chem. Lett.* **2023**, *14* (19), 4607–4616. https://doi.org/10.1021/acs.jpclett.3c00478.

(65) Brognara, A.; Bricchi, B. R.; William, L.; Brinza, O.; Konstantakopoulou, M.; Bassi, A. L.; Ghidelli, M.; Lidgi-Guigui, N. New Mechanism for Long Photo-Induced Enhanced Raman Spectroscopy in Au Nanoparticles Embedded in TiO2. *Small* **2022**, *18* (25), 2201088. https://doi.org/10.1002/smll.202201088.

(66) Zhang, M.; Sun, H.; Chen, X.; Yang, J.; Shi, L.; Chen, T.; Bao, Z.; Liu, J.; Wu, Y. Highly Efficient Photoinduced Enhanced Raman Spectroscopy (PIERS) from Plasmonic Nanoparticles Decorated 3D Semiconductor Arrays for Ultrasensitive, Portable, and Recyclable Detection of Organic Pollutants. *ACS Sens* **2019**, *4* (6), 1670–1681. https://doi.org/10.1021/acssensors.9b00562.

(67) Man, T.; Lai, W.; Xiao, M.; Wang, X.; Chandrasekaran, A. R.; Pei, H.; Li, L. A Versatile Biomolecular Detection Platform Based on Photo-Induced Enhanced Raman Spectroscopy. *Biosensors and Bioelectronics* **2020**, *147*, 111742. https://doi.org/10.1016/j.bios.2019.111742.

(68) Mai, Q. D.; Nguyen, H. A.; Phung, T. L. H.; Xuan Dinh, N.; Tran, Q. H.; Doan, T. Q.; Pham, A. T.; Le, A.-T. Photoinduced Enhanced Raman Spectroscopy for the Ultrasensitive Detection of a Low-Cross-Section Chemical, Urea, Using Silver–Titanium Dioxide Nanostructures. *ACS Appl. Nano Mater.* **2022**, *5* (10), 15518–15530. https://doi.org/10.1021/acsanm.2c03524.

(69) Davison, G.; Yin, Y.; Jones, T.; Parkin, I. P.; Peveler, W. J.; Lee, T.-C. Multi-Mode Enhanced Raman Scattering Spectroscopy Using Aggregation-Free Hybrid Metal/Metal-Oxide Nanoparticles with Intrinsic Oxygen Vacancies. *J. Mater. Chem. C* **2023**. https://doi.org/10.1039/D2TC05069B.

(70) Jauffred, L.; Samadi, A.; Klingberg, H.; Bendix, P. M.; Oddershede, L. B. Plasmonic Heating of Nanostructures. *Chem. Rev.* **2019**, *119* (13), 8087–8130. https://doi.org/10.1021/acs.chemrev.8b00738.

(71) Baffou, G.; Quidant, R. Thermo-Plasmonics: Using Metallic Nanostructures as Nano-Sources of Heat. *Laser & Photonics Reviews* **2013**, *7* (2), 171–187. https://doi.org/10.1002/lpor.201200003.

(72) Vilches, C.; Quidant, R. Chapter 12 - Targeted Hyperthermia with Plasmonic Nanoparticles. In *Frontiers of Nanoscience*; Parak, W. J., Feliu, N., Eds.; Colloids for Nanobiotechnology; Elsevier, 2020; Vol. 16, pp 307–352. https://doi.org/10.1016/B978-0-08-102828-5.00012-7.

(73) Sangnier, A. P.; Walle, A. V. de; Aufaure, R.; Fradet, M.; Motte, L.; Guénin, E.; Lalatonne, Y.; Wilhelm, C. Endosomal Confinement of Gold Nanospheres, Nanorods, and Nanoraspberries Governs Their Photothermal Identity and Is Beneficial for Cancer Cell Therapy. *Advanced Biosystems* **2020**, *4* (4), 1900284. https://doi.org/10.1002/adbi.201900284.

(74) Hwang, S.; Nam, J.; Jung, S.; Song, J.; Doh, H.; Kim, S. Gold Nanoparticle-Mediated Photothermal Therapy: Current Status and Future Perspective. *Nanomedicine* **2014**, *9* (13), 2003–2022. https://doi.org/10.2217/nnm.14.147.

(75) Vines, J. B.; Yoon, J.-H.; Ryu, N.-E.; Lim, D.-J.; Park, H. Gold Nanoparticles for Photothermal Cancer Therapy. *Front Chem* **2019**, *7*, 167. https://doi.org/10.3389/fchem.2019.00167.

(76) Parakhonskiy, B. V.; Parak, W. J.; Volodkin, D.; Skirtach, A. G. Hybrids of Polymeric Capsules, Lipids, and Nanoparticles: Thermodynamics and Temperature Rise at the Nanoscale and Emerging Applications. *Langmuir* **2019**, *35* (26), 8574–8583. https://doi.org/10.1021/acs.langmuir.8b04331.

(77) Carregal-Romero, S.; Ochs, M.; Rivera-Gil, P.; Ganas, C.; Pavlov, A. M.; Sukhorukov, G. B.; Parak, W. J. NIR-Light Triggered Delivery of Macromolecules into the Cytosol. *Journal of Controlled Release* **2012**, *159* (1), 120–127. https://doi.org/10.1016/j.jconrel.2011.12.013.

(78) Ambrosone, A.; Marchesano, V.; Carregal-Romero, S.; Intartaglia, D.; Parak, W. J.; Tortiglione, C. Control of Wnt/β-Catenin Signaling Pathway in Vivo via Light Responsive Capsules. *ACS Nano* **2016**, *10* (4), 4828–4834. https://doi.org/10.1021/acsnano.5b07817.

(79) Kyrsting, A.; Bendix, P. M.; Stamou, D. G.; Oddershede, L. B. Heat Profiling of Three-Dimensionally Optically Trapped Gold Nanoparticles Using Vesicle Cargo Release. *Nano Lett.* **2011**, *11* (2), 888–892. https://doi.org/10.1021/nl104280c.

(80) Anderson, L.; Hansen, E.; Lukianova-Hleb, E. Y.; Hafner, J. H.; Lapotko, D. O. Optically Guided Controlled Release from Liposomes With Tunable Plasmonic Nanobubbles. *J Control Release* **2010**, *144* (2), 151–158. https://doi.org/10.1016/j.jconrel.2010.02.012.

(81) Wijaya, A.; Schaffer, S. B.; Pallares, I. G.; Hamad-Schifferli, K. Selective Release of Multiple DNA Oligonucleotides from Gold Nanorods. *ACS Nano* **2009**, *3* (1), 80–86. https://doi.org/10.1021/nn800702n.

(82) Delcea, M.; Sternberg, N.; Yashchenok, A. M.; Georgieva, R.; Bäumler, H.; Möhwald, H.; Skirtach, A. G. Nanoplasmonics for Dual-Molecule Release through Nanopores in the Membrane of Red Blood Cells. *ACS Nano* **2012**, *6* (5), 4169–4180. https://doi.org/10.1021/nn3006619.

(83) Li, W.; Chen, X. Gold Nanoparticles for Photoacoustic Imaging. *Nanomedicine (Lond)* **2015**, *10* (2), 299–320. https://doi.org/10.2217/nnm.14.169.

(84) Liu, W.-W.; Li, P.-C. Photoacoustic Imaging of Cells in a Three-Dimensional Microenvironment. *Journal of Biomedical Science* **2020**, *27* (1), 3. https://doi.org/10.1186/s12929-019-0594-x.

(85) Song, J.; Kim, J.; Hwang, S.; Jeon, M.; Jeong, S.; Kim, C.; Kim, S. “Smart” Gold Nanoparticles for Photoacoustic Imaging: An Imaging Contrast Agent Responsive to the Cancer Microenvironment and Signal Amplification via pH-Induced Aggregation. *Chem. Commun.* **2016**, *52* (53), 8287–8290. https://doi.org/10.1039/C6CC03100E.

(86) Cheng, X.; Sun, R.; Yin, L.; Chai, Z.; Shi, H.; Gao, M. Light-Triggered Assembly of Gold Nanoparticles for Photothermal Therapy and Photoacoustic Imaging of Tumors In Vivo. *Advanced Materials* **2017**, *29* (6), 1604894. https://doi.org/10.1002/adma.201604894.

(87) Han, S.; Bouchard, R.; Sokolov, K. V. Molecular Photoacoustic Imaging with Ultra-Small Gold Nanoparticles. *Biomed Opt Express* **2019**, *10* (7), 3472–3483. https://doi.org/10.1364/BOE.10.003472.

(88) Chen, Y.-S.; Zhao, Y.; Yoon, S. J.; Gambhir, S. S.; Emelianov, S. Miniature Gold Nanorods for Photoacoustic Molecular Imaging in the Second Near-Infrared Optical Window. *Nature Nanotechnology* **2019**, *14* (5), 465–472. https://doi.org/10.1038/s41565-019-0392-3.

(89) García-Álvarez, R.; Chen, L.; Nedilko, A.; Sánchez-Iglesias, A.; Rix, A.; Lederle, W.; Pathak, V.; Lammers, T.; von Plessen, G.; Kostarelos, K.; Liz-Marzán, L. M.; Kuehne, A. J. C.; Chigrin, D. N. Optimizing the Geometry of Photoacoustically Active Gold Nanoparticles for Biomedical

Imaging. *ACS Photonics* **2020**, *7* (3), 646–652. https://doi.org/10.1021/acsphotonics.9b01418.

(90) Jokerst, J. V.; Cole, A. J.; Van de Sompel, D.; Gambhir, S. S. Gold Nanorods for Ovarian Cancer Detection with Photoacoustic Imaging and Resection Guidance via Raman Imaging in Living Mice. *ACS Nano* **2012**, *6* (11), 10366–10377. https://doi.org/10.1021/nn304347g.

(91) Cai, K.; Zhang, W.; Foda, M. F.; Li, X.; Zhang, J.; Zhong, Y.; Liang, H.; Li, H.; Han, H.; Zhai, T. Miniature Hollow Gold Nanorods with Enhanced Effect for In Vivo Photoacoustic Imaging in the NIR-II Window. *Small* **2020**, *16* (37), 2002748. https://doi.org/10.1002/smll.202002748.

(92) Ge, X.; Fu, Q.; Su, L.; Li, Z.; Zhang, W.; Chen, T.; Yang, H.; Song, J. Light-Activated Gold Nanorod Vesicles with NIR-II Fluorescence and Photoacoustic Imaging Performances for Cancer Theranostics. *Theranostics* **2020**, *10* (11), 4809–4821. https://doi.org/10.7150/thno.44376.

(93) Liu, F.; Lai, Y.; Zhao, B.; Bradley, R.; Wu, W. Photothermal Materials for Efficient Solar Powered Steam Generation. *Front. Chem. Sci. Eng.* **2019**, *13* (4), 636–653. https://doi.org/10.1007/s11705-019-1824-1.

(94) Lin, Y.; Xu, H.; Shan, X.; Di, Y.; Zhao, A.; Hu, Y.; Gan, Z. Solar Steam Generation Based on the Photothermal Effect: From Designs to Applications, and Beyond. *J. Mater. Chem. A* **2019**, *7* (33), 19203–19227. https://doi.org/10.1039/C9TA05935K.

(95) Guo, A.; Fu, Y.; Wang, G.; Wang, X. Diameter Effect of Gold Nanoparticles on Photothermal Conversion for Solar Steam Generation. *RSC Adv.* **2017**, *7* (8), 4815–4824. https://doi.org/10.1039/C6RA26979F.

(96) Neumann, O.; Urban, A. S.; Day, J.; Lal, S.; Nordlander, P.; Halas, N. J. Solar Vapor Generation Enabled by Nanoparticles. *ACS Nano* **2013**, *7* (1), 42–49. https://doi.org/10.1021/nn304948h.

(97) Fortenbaugh, R. J.; Lear, B. J. On-Demand Curing of Polydimethylsiloxane (PDMS) Using the Photothermal Effect of Gold Nanoparticles. *Nanoscale* **2017**, *9* (25), 8555–8559. https://doi.org/10.1039/C7NR01423F.

(98) Osaka, Y.; Sugano, S.; Hashimoto, S. Plasmonic-Heating-Induced Nanofabrication on Glass Substrates. *Nanoscale* **2016**, *8* (42), 18187–18196. https://doi.org/10.1039/C6NR06543K.

(99) Fedoruk, M.; Meixner, M.; Carretero-Palacios, S.; Lohmüller, T.; Feldmann, J. Nanolithography by Plasmonic Heating and Optical Manipulation of Gold Nanoparticles. *ACS Nano* **2013**, *7* (9), 7648–7653. https://doi.org/10.1021/nn402124p.

(100) Cao, L.; Barsic, D. N.; Guichard, A. R.; Brongersma, M. L. Plasmon-Assisted Local Temperature Control to Pattern Individual Semiconductor Nanowires and Carbon Nanotubes. *Nano Lett.* **2007**, *7* (11), 3523–3527. https://doi.org/10.1021/nl0722370.

(101) Shin, H.-H.; Koo, J.; Lee, K.; Kim, Z. Chemical Reactions Driven by Plasmon-Induced Hot Carriers. *Applied Materials Today* **2019**, *16*, 112–119. https://doi.org/10.1016/j.apmt.2019.04.018.

(102) Qiu, J.; Wei, W. D. Surface Plasmon-Mediated Photothermal Chemistry. *J. Phys. Chem. C* **2014**, *118* (36), 20735–20749. https://doi.org/10.1021/jp5042553.

(103) Baffou, G.; Cichos, F.; Quidant, R. Applications and Challenges of Thermoplasmonics. *Nature Materials* **2020**, *19* (9), 946–958. https://doi.org/10.1038/s41563-020-0740-6.

(104) Kuppe, C.; Rusimova, K. R.; Ohnoutek, L.; Slavov, D.; Valev, V. K. “Hot” in Plasmonics: Temperature-Related Concepts and Applications of Metal Nanostructures. *Advanced Optical Materials* **2020**, *8* (1), 1901166. https://doi.org/10.1002/adom.201901166.

(105) Naresh, V.; Lee, N. A Review on Biosensors and Recent Development of Nanostructured Materials-Enabled Biosensors. *Sensors* **2021**, *21* (4), 1109. https://doi.org/10.3390/s21041109.

(106) Ke, S.; Kan, C.; Zhu, X.; Wang, C.; Wang, X.; Chen, Y.; Zhu, X.; Li, Z.; Shi, D. Synthesis of Porous Au–Ag Alloy Nanorods with Tunable Plasmonic Properties and Intrinsic Hotspots for Surface-Enhanced Raman Scattering. *CrystEngComm* **2021**. https://doi.org/10.1039/D1CE00258A.

(107) Bi, L.; Wang, X.; Cao, X.; Liu, L.; Bai, C.; Zheng, Q.; Choo, J.; Chen, L. SERS-Active Au@Ag Core-Shell Nanorod (Au@AgNR) Tags for Ultrasensitive Bacteria Detection and Antibiotic-Susceptibility Testing. *Talanta* **2020**, *220*, 121397. https://doi.org/10.1016/j.talanta.2020.121397.

(108) Kumar, G. V. P.; Shruthi, S.; Vibha, B.; Reddy, B. A. A.; Kundu, T. K.; Narayana, C. Hot Spots in Ag Core−Au Shell Nanoparticles Potent for Surface-Enhanced Raman Scattering Studies of Biomolecules. *J. Phys. Chem. C* **2007**, *111* (11), 4388–4392. https://doi.org/10.1021/jp068253n.

(109) Lagona, J.; Mukhopadhyay, P.; Chakrabarti, S.; Isaacs, L. The Cucurbit[n]Uril Family. *Angewandte Chemie International Edition* **2005**, *44* (31), 4844–4870. https://doi.org/10.1002/anie.200460675.

(110) Taylor, R. W.; Lee, T.-C.; Scherman, O. A.; Esteban, R.; Aizpurua, J.; Huang, F. M.; Baumberg, J. J.; Mahajan, S. Precise Subnanometer Plasmonic Junctions for SERS within Gold Nanoparticle Assemblies Using Cucurbit[n]Uril “Glue.” *ACS Nano* **2011**, *5* (5), 3878–3887. https://doi.org/10.1021/nn200250v.

(111) Cao, L.; Šekutor, M.; Zavalij, P. Y.; Mlinarić-Majerski, K.; Glaser, R.; Isaacs, L. Cucurbit[7]uril·Guest Pair with an Attomolar Dissociation Constant. *Angewandte Chemie International Edition* **2014**, *53* (4), 988–993. https://doi.org/10.1002/anie.201309635.

(112) Lambert, H.; Mohan, N.; Lee, T.-C. Ultrahigh Binding Affinity of a Hydrocarbon Guest inside Cucurbit[7]Uril Enhanced by Strong Host–Guest Charge Matching. *Physical Chemistry Chemical Physics* **2019**, *21* (27), 14521–14529. https://doi.org/10.1039/C9CP01762C.

(113) Nau, W. M.; Florea, M.; Assaf, K. I. Deep Inside Cucurbiturils: Physical Properties and Volumes of Their Inner Cavity Determine the Hydrophobic Driving Force for Host–Guest Complexation. *Israel Journal of Chemistry* **2011**, *51* (5–6), 559–577. https://doi.org/10.1002/ijch.201100044.

(114) Lee, T.-C.; Scherman, O. A. Formation of Dynamic Aggregates in Water by Cucurbit[5]Uril Capped with Gold Nanoparticles. *Chem. Commun.* **2010**, *46* (14), 2438–2440. https://doi.org/10.1039/B925051D.

(115) Lee, T.-C.; Scherman, O. A. A Facile Synthesis of Dynamic Supramolecular Aggregates of Cucurbit[n]Uril (N=5–8) Capped with Gold Nanoparticles in Aqueous Media. *Chemistry – A European Journal* **2012**, *18* (6), 1628–1633. https://doi.org/10.1002/chem.201102675.

(116) Tao, C.; An, Q.; Zhu, W.; Yang, H.; Li, W.; Lin, C.; Xu, D.; Li, G. Cucurbit[n]Urils as a SERS Hot-Spot Nanocontainer through Bridging Gold Nanoparticles. *Chem. Commun.* **2011**, *47* (35), 9867. https://doi.org/10.1039/c1cc12474a.

(117) Kasera, S.; Herrmann, L. O.; Barrio, J. del; Baumberg, J. J.; Scherman, O. A. Quantitative Multiplexing with Nano-Self-Assemblies in SERS. *Sci Rep* **2015**, *4* (1), 6785. https://doi.org/10.1038/srep06785.

(118) Kasera, S.; Biedermann, F.; Baumberg, J. J.; Scherman, O. A.; Mahajan, S. Quantitative SERS Using the Sequestration of Small Molecules Inside Precise Plasmonic Nanoconstructs. *Nano Lett.* **2012**, *12* (11), 5924–5928. https://doi.org/10.1021/nl303345z.

(119) de Nijs, B.; Kamp, M.; Szabó, I.; Barrow, S. J.; Benz, F.; Wu, G.; Carnegie, C.; Chikkaraddy, R.; Wang, W.; Deacon, W. M.; Rosta, E.; Baumberg, J. J.; Scherman, O. A. Smart Supramolecular Sensing with Cucurbit[*n*]Urils: Probing Hydrogen Bonding with SERS. *Faraday Discuss.* **2017**, *205*, 505–515. https://doi.org/10.1039/C7FD00147A.

(120) Chio, W.-I. K.; Peveler, W. J.; Assaf, K. I.; Moorthy, S.; Nau, W. M.; Parkin, I. P.; Olivo, M.; Lee, T.-C. Selective Detection of Nitroexplosives Using Molecular Recognition within Self-Assembled Plasmonic Nanojunctions. *J. Phys. Chem. C* **2019**, *123* (25), 15769–15776. https://doi.org/10.1021/acs.jpcc.9b02363.

(121) Peveler, W. J.; Jia, H.; Jeen, T.; Rees, K.; Macdonald, T. J.; Xia, Z.; Chio, W.-I. K.; Moorthy, S.; Parkin, I. P.; Carmalt, C. J.; Algar, W. R.; Lee, T.-C. Cucurbituril-Mediated Quantum Dot Aggregates Formed by Aqueous Self-Assembly for Sensing Applications. *Chem. Commun.* **2019**, *55* (38), 5495–5498. https://doi.org/10.1039/C9CC00410F.

(122) Chio, W.-I. K.; Moorthy, S.; Perumal, J.; U. S., D.; Parkin, I. P.; Olivo, M.; Lee, T.-C. Dual-Triggered Nanoaggregates of Cucurbit[7]Uril and Gold Nanoparticles for Multi-Spectroscopic Quantification of Creatinine in Urinalysis. *J. Mater. Chem. C* **2020**, *8* (21), 7051–7058. https://doi.org/10.1039/D0TC00931H.

(123) de Nijs, B.; Carnegie, C.; Szabó, I.; Grys, D.-B.; Chikkaraddy, R.; Kamp, M.; Barrow, S. J.; Readman, C. A.; Kleemann, M.-E.; Scherman, O. A.; Rosta, E.; Baumberg, J. J. Inhibiting Analyte Theft in Surface-Enhanced Raman Spectroscopy Substrates: Subnanomolar Quantitative Drug Detection. *ACS Sens.* **2019**, *4* (11), 2988–2996. https://doi.org/10.1021/acssensors.9b01484.

(124) Chio, W.-I. K.; Davison, G.; Jones, T.; Liu, J.; Parkin, I. P.; Lee, T.-C. Quantitative SERS Detection of Uric Acid via Formation of Precise Plasmonic Nanojunctions within Aggregates of Gold Nanoparticles and Cucurbit[n]Uril. *JoVE* **2020**, No. 164, 61682. https://doi.org/10.3791/61682.

(125) Haynes, C. L.; Yonzon, C. R.; Zhang, X.; Van Duyne, R. P. Surface-Enhanced Raman Sensors: Early History and the Development of Sensors for Quantitative Biowarfare Agent and Glucose Detection.

Journal of Raman Spectroscopy **2005**, *36* (6–7), 471–484. https://doi.org/10.1002/jrs.1376.

(126) Liu, H.; Gao, X.; Xu, C.; Liu, D. SERS Tags for Biomedical Detection and Bioimaging. *Theranostics* **2022**, *12* (4), 1870–1903. https://doi.org/10.7150/thno.66859.

(127) Kahraman, M.; Mullen, E. R.; Korkmaz, A.; Wachsmann-Hogiu, S. Fundamentals and Applications of SERS-Based Bioanalytical Sensing. *Nanophotonics* **2017**, *6* (5), 831–852. https://doi.org/10.1515/nanoph-2016-0174.

(128) Pollap, A.; Świt, P. Recent Advances in Sandwich SERS Immunosensors for Cancer Detection. *Int J Mol Sci* **2022**, *23* (9), 4740. https://doi.org/10.3390/ijms23094740.

(129) Verdin, A.; Sloan-Dennison, S.; Malherbe, C.; Graham, D.; Eppe, G. SERS Nanotags for Folate Receptor α Detection at the Single Cell Level: Discrimination of Overexpressing Cells and Potential for Live Cell Applications. *Analyst* **2022**, *147* (14), 3328–3339. https://doi.org/10.1039/D2AN00706A.

(130) Wiercigroch, E.; Swit, P.; Brzozka, A.; Pięta, Ł.; Malek, K. Dual-Enhancement and Dual-Tag Design for SERS-Based Sandwich Immunoassays: Evaluation of a Metal–Metal Effect in 3D Architecture. *Microchim Acta* **2021**, *189* (1), 32. https://doi.org/10.1007/s00604-021-05125-0.

(131) Blanco-Covián, L.; Montes-García, V.; Girard, A.; Fernández-Abedul, M. T.; Pérez-Juste, J.; Pastoriza-Santos, I.; Faulds, K.; Graham, D.; Blanco-López, M. C. Au@Ag SERRS Tags Coupled to a Lateral Flow Immunoassay for the Sensitive Detection of Pneumolysin. *Nanoscale* **2017**, *9* (5), 2051–2058. https://doi.org/10.1039/C6NR08432J.

(132) Fu, X.; Wen, J.; Li, J.; Lin, H.; Liu, Y.; Zhuang, X.; Tian, C.; Chen, L. Highly Sensitive Detection of Prostate Cancer Specific PCA3 Mimic DNA Using SERS-Based Competitive Lateral Flow Assay. *Nanoscale* **2019**, *11* (33), 15530–15536. https://doi.org/10.1039/C9NR04864B.

(133) Kim, K.; Kashefi-Kheyrabadi, L.; Joung, Y.; Kim, K.; Dang, H.; Chavan, S. G.; Lee, M.-H.; Choo, J. Recent Advances in Sensitive Surface-Enhanced Raman Scattering-Based Lateral Flow Assay Platforms for Point-of-Care Diagnostics of Infectious Diseases. *Sensors and Actuators B: Chemical* **2021**, *329*, 129214. https://doi.org/10.1016/j.snb.2020.129214.

(134) Sloan-Dennison, S.; O'Connor, E.; Dear, J. W.; Graham, D.; Faulds, K. Towards Quantitative Point of Care Detection Using SERS Lateral Flow Immunoassays. *Anal Bioanal Chem* **2022**, *414* (16), 4541–4549. https://doi.org/10.1007/s00216-022-03933-8.

(135) Wang, R.; Kim, K.; Choi, N.; Wang, X.; Lee, J.; Jeon, J. H.; Rhie, G.; Choo, J. Highly Sensitive Detection of High-Risk Bacterial Pathogens Using SERS-Based Lateral Flow Assay Strips. *Sensors and Actuators B: Chemical* **2018**, *270*, 72–79. https://doi.org/10.1016/j.snb.2018.04.162.

(136) Wang, X.; Choi, N.; Cheng, Z.; Ko, J.; Chen, L.; Choo, J. Simultaneous Detection of Dual Nucleic Acids Using a SERS-Based Lateral Flow

Assay Biosensor. *Anal. Chem.* **2017**, *89* (2), 1163–1169. https://doi.org/10.1021/acs.analchem.6b03536.

(137) *Developments in Electrochemistry*, 1st ed.; John Wiley & Sons, Ltd, 2014. https://doi.org/10.1002/9781118694404.

(138) Compton, R. G.; Laborda, E.; Ward, K. R.; World Scientific (Firm). *Understanding Voltammetry: Simulation of Electrode Processes*; Imperial College Press ; Distributed by World Scientific Pub. Co.: London; Singapore, 2014.

(139) Elgrishi, N.; Rountree, K. J.; McCarthy, B. D.; Rountree, E. S.; Eisenhart, T. T.; Dempsey, J. L. A Practical Beginner's Guide to Cyclic Voltammetry. *J. Chem. Educ.* **2018**, *95* (2), 197–206. https://doi.org/10.1021/acs.jchemed.7b00361.

(140) *Advances in Electrochemical Science and Engineering*, 1st ed.; John Wiley & Sons, Ltd, 2017. https://doi.org/10.1002/9783527340934.

(141) Willets, K. A. Probing Nanoscale Interfaces with Electrochemical Surface-Enhanced Raman Scattering. *Current Opinion in Electrochemistry* **2019**, *13*, 18–24. https://doi.org/10.1016/j.coelec.2018.10.005.

(142) Fu, B.; Van Dyck, C.; Zaleski, S.; Van Duyne, R. P.; Ratner, M. A. Single Molecule Electrochemistry: Impact of Surface Site Heterogeneity. *J. Phys. Chem. C* **2016**, *120* (48), 27241–27249. https://doi.org/10.1021/acs.jpcc.6b05252.

(143) Oyamada, N.; Minamimoto, H.; Murakoshi, K. In Situ Observation of Unique Bianalyte Molecular Behaviors at the Gap of a Single Metal Nanodimer Structure via Electrochemical Surface-Enhanced Raman Scattering Measurements. *J. Phys. Chem. C* **2019**, *123* (40), 24740–24745. https://doi.org/10.1021/acs.jpcc.9b07361.

(144) Zhou, L.; Chen, X.; Ren, G.; Chen, L.; Xu, W.; Gu, C.; Zhang, W.; Li, Y.; Tian, Z.; Zhou, J.; Han, J. Electrically Tunable SERS Based on Plasmonic Gold Nanorod-Graphene/Ion-Gel Hybrid Structure with a Low Voltage. *Carbon* **2022**, *187*, 425–431. https://doi.org/10.1016/j.carbon.2021.11.040.

(145) Zaleski, S.; Cardinal, M. F.; Chulhai, D. V.; Wilson, A. J.; Willets, K. A.; Jensen, L.; Van Duyne, R. P. Toward Monitoring Electrochemical Reactions with Dual-Wavelength SERS: Characterization of Rhodamine 6G (R6G) Neutral Radical Species and Covalent Tethering of R6G to Silver Nanoparticles. *J. Phys. Chem. C* **2016**, *120* (43), 24982–24991. https://doi.org/10.1021/acs.jpcc.6b09022.

(146) Wang, Y.-H.; Zheng, S.; Yang, W.-M.; Zhou, R.-Y.; He, Q.-F.; Radjenovic, P.; Dong, J.-C.; Li, S.; Zheng, J.; Yang, Z.-L.; Attard, G.; Pan, F.; Tian, Z.-Q.; Li, J.-F. In Situ Raman Spectroscopy Reveals the Structure and Dissociation of Interfacial Water. *Nature* **2021**, *600* (7887), 81–85. https://doi.org/10.1038/s41586-021-04068-z.

(147) *Citation report - 9,053 - Web of Science Core Collection*. https://www.webofscience.com/wos/woscc/citation-report/d75ce886-44c1-4ab9-977f-700bfe4d8164-acc37272 (accessed 2023-10-19).

(148) Tian, Z.-Q.; Ren, B.; Wu, D.-Y. Surface-Enhanced Raman Scattering: From Noble to Transition Metals and from Rough Surfaces to Ordered

Nanostructures. *J. Phys. Chem. B* **2002**, *106* (37), 9463–9483. https://doi.org/10.1021/jp0257449.

(149) Shi, R.; Liu, X.; Ying, Y. Facing Challenges in Real-Life Application of Surface-Enhanced Raman Scattering: Design and Nanofabrication of Surface-Enhanced Raman Scattering Substrates for Rapid Field Test of Food Contaminants. *J. Agric. Food Chem.* **2018**, *66* (26), 6525–6543. https://doi.org/10.1021/acs.jafc.7b03075.

(150) Gao, P.; Gosztola, D.; Leung, L.-W. H.; Weaver, M. J. Surface-Enhanced Raman Scattering at Gold Electrodes: Dependence on Electrochemical Pretreatment Conditions and Comparisons with Silver. *Journal of Electroanalytical Chemistry and Interfacial Electrochemistry* **1987**, *233* (1–2), 211–222. https://doi.org/10.1016/0022-0728(87)85017-9.

(151) Wang, J.; Qiu, C.; Mu, X.; Pang, H.; Chen, X.; Liu, D. Ultrasensitive SERS Detection of Rhodamine 6G and P-Nitrophenol Based on Electrochemically Roughened Nano-Au Film. *Talanta* **2020**, *210*, 120631. https://doi.org/10.1016/j.talanta.2019.120631.

(152) Martín-Yerga, D.; Pérez-Junquera, A.; González-García, M. B.; Perales-Rondon, J. V.; Heras, A.; Colina, A.; Hernández-Santos, D.; Fanjul-Bolado, P. Quantitative Raman Spectroelectrochemistry Using Silver Screen-Printed Electrodes. *Electrochimica Acta* **2018**, *264*, 183–190. https://doi.org/10.1016/j.electacta.2018.01.060.

(153) Zhu, Z.; Yoshikawa, H.; Saito, M.; Fan, B.; Tamiya, E. Fabrication of Surface-Enhanced Raman Spectroscopy (SERS) – Active Electrodes by Silver Sputtering Deposition for Electrochemical SERS Analysis. *Electroanalysis* **2018**, *30* (7), 1432–1437. https://doi.org/10.1002/elan.201800003.

(154) Ibáñez, D.; Pérez-Junquera, A.; González-García, M. B.; Hernández-Santos, D.; Fanjul-Bolado, P. Spectroelectrochemical Elucidation of B Vitamins Present in Multivitamin Complexes by EC-SERS. *Talanta* **2020**, *206*, 120190. https://doi.org/10.1016/j.talanta.2019.120190.

(155) Martín-Yerga, D.; Pérez-Junquera, A.; Hernández-Santos, D.; Fanjul-Bolado, P. In Situ Activation of Thick-Film Disposable Copper Electrodes for Sensitive Detection of Malachite Green Using Electrochemical Surface-Enhanced Raman Scattering (EC-SERS). *Electroanalysis* **2018**, *30* (6), 1095–1099. https://doi.org/10.1002/elan.201800023.

(156) Moldovan, R.; Milenko, K.; Vereshchagina, E.; Iacob, B.-C.; Schneider, K.; Farcău, C.; Bodoki, E. EC-SERS Detection of Thiabendazole in Apple Juice Using Activated Screen-Printed Electrodes. *Food Chemistry* **2022**, 134713. https://doi.org/10.1016/j.foodchem.2022.134713.

(157) Ott, C.; Burns, A.; Sisco, E.; Arroyo, L. E. Targeted Fentanyl Screening Utilizing Electrochemical Surface-Enhanced Raman Spectroscopy (EC-SERS) Applied to Authentic Seized Drug Casework Samples. *NIST* **2023**.

(158) Ott, C. E.; Perez-Estebanez, M.; Hernandez, S.; Kelly, K.; Dalzell, K. A.; Arcos-Martinez, M. J.; Heras, A.; Colina, A.; Arroyo, L. E. Forensic Identification of Fentanyl and Its Analogs by Electrochemical-Surface Enhanced Raman Spectroscopy (EC-SERS) for the Screening of Seized Drugs of Abuse. *Frontiers in Analytical Science* **2022**, *2*.

(159) Dai, X.; Nekrassova, O.; Hyde, M. E.; Compton, R. G. Anodic Stripping Voltammetry of Arsenic(III) Using Gold Nanoparticle-Modified Electrodes. 6.

(160) Wang, J.; Cao, X.; Li, L.; Li, T.; Wang, R. Electrochemical Seed-Mediated Growth of Surface-Enhanced Raman Scattering Active Au(111)-Like Nanoparticles on Indium Tin Oxide Electrodes. *J. Phys. Chem. C* **2013**, *117* (30), 15817–15828. https://doi.org/10.1021/jp400633k.

(161) Ye, W.; Wang, D.; Zhang, H.; Zhou, F.; Liu, W. Electrochemical Growth of Flowerlike Gold Nanoparticles on Polydopamine Modified ITO Glass for SERS Application. *Electrochimica Acta* **2010**, *55* (6), 2004–2009. https://doi.org/10.1016/j.electacta.2009.11.022.

(162) Dendisová, M. EC-SERS Study of Phenolic Acids Sorption Behavior on Au, Ag and Cu Substrates – Effect of Applied Potential and Metal Used. *Applied Surface Science* **2019**, 8.

(163) Clarke, O. J. R.; St. Marie, G. J. H.; Brosseau, C. L. Evaluation of an Electrodeposited Bimetallic Cu/Ag Nanostructured Screen Printed Electrode for Electrochemical Surface-Enhanced Raman Spectroscopy (EC-SERS) Investigations. *J. Electrochem. Soc.* **2017**, *164* (5), B3091–B3095. https://doi.org/10.1149/2.0131705jes.

(164) Tsai, M.-H.; Lin, Y.-K.; Luo, S.-C. Electrochemical SERS for *in Situ* Monitoring the Redox States of PEDOT and Its Potential Application in Oxidant Detection. *ACS Appl. Mater. Interfaces* **2019**, *11* (1), 1402–1410. https://doi.org/10.1021/acsami.8b16989.

(165) Dong, P.; Lin, Y.; Deng, J.; Di, J. Ultrathin Gold-Shell Coated Silver Nanoparticles onto a Glass Platform for Improvement of Plasmonic Sensors. *ACS Appl. Mater. Interfaces* **2013**, *5* (7), 2392–2399. https://doi.org/10.1021/am4004254.

(166) Bian, J.; Shu, S.; Li, J.; Huang, C.; Li, Y. Y.; Zhang, R.-Q. Reproducible and Recyclable SERS Substrates: Flower-like Ag Structures with Concave Surfaces Formed by Electrodeposition. *Applied Surface Science* **2015**, *333*, 126–133. https://doi.org/10.1016/j.apsusc.2015.02.007.

(167) Dai, X.; Compton, R. G. Direct Electrodeposition of Gold Nanoparticles onto Indium Tin Oxide Film Coated Glass: Application to the Detection of Arsenic(III). *Anal. Sci.* **2006**, *22* (4), 567–570. https://doi.org/10.2116/analsci.22.567.

(168) Ibáñez, D.; González-García, M. B.; Hernández-Santos, D.; Fanjul-Bolado, P. Detection of Dithiocarbamate, Chloronicotinyl and Organophosphate Pesticides by Electrochemical Activation of SERS Features of Screen-Printed Electrodes. *Spectrochimica Acta Part A: Molecular and Biomolecular Spectroscopy* **2021**, *248*, 119174. https://doi.org/10.1016/j.saa.2020.119174.

(169) Cheng, Z.-Q.; Li, Z.-W.; Xu, J.-H.; Yao, R.; Li, Z.-L.; Liang, S.; Cheng, G.-L.; Zhou, Y.-H.; Luo, X.; Zhong, J. Morphology-Controlled Fabrication of Large-Scale Dendritic Silver Nanostructures for Catalysis and SERS Applications. *Nanoscale Research Letters* **2019**, *14* (1), 89. https://doi.org/10.1186/s11671-019-2923-0.

(170) Subhadarshini, S.; Singh, R.; Goswami, D. K.; Das, A. K.; Das, N. Ch. Electrodeposited Cu_2O Nanopetal Architecture as a Superhydrophobic

and Antibacterial Surface. *Langmuir* **2019**, *35* (52), 17166–17176. https://doi.org/10.1021/acs.langmuir.9b03024.

(171) Paunovic, M.; Schlesinger, M. *Fundamentals of Electrochemical Deposition*; John Wiley & Sons, 2006.

(172) Su, S.; Wu, Y.; Zhu, D.; Chao, J.; Liu, X.; Wan, Y.; Su, Y.; Zuo, X.; Fan, C.; Wang, L. On-Electrode Synthesis of Shape-Controlled Hierarchical Flower-Like Gold Nanostructures for Efficient Interfacial DNA Assembly and Sensitive Electrochemical Sensing of MicroRNA. *Small* **2016**, *12* (28), 3794–3801. https://doi.org/10.1002/smll.201601066.

(173) Tang, S.; Meng, X.; Wang, C.; Cao, Z. Flowerlike Ag Microparticles with Novel Nanostructure Synthesized by an Electrochemical Approach. *Materials Chemistry and Physics* **2009**, *114* (2–3), 842–847. https://doi.org/10.1016/j.matchemphys.2008.10.048.

(174) Bian, J.-C.; Chen, Z.-D.; Li, Z.; Yang, F.; He, H.-Y.; Wang, J.; Tan, J. Z. Y.; Zeng, J.-L.; Peng, R.-Q.; Zhang, X.-W.; Han, G.-R. Electrodeposition of Hierarchical Ag Nanostructures on ITO Glass for Reproducible and Sensitive SERS Application. *Applied Surface Science* **2012**, *258* (17), 6632–6636. https://doi.org/10.1016/j.apsusc.2012.03.093.

(175) Hulteen, J. C.; Van Duyne, R. P. Nanosphere Lithography: A Materials General Fabrication Process for Periodic Particle Array Surfaces. *Journal of Vacuum Science & Technology A: Vacuum, Surfaces, and Films* **1995**, *13* (3), 1553–1558. https://doi.org/10.1116/1.579726.

(176) Willets, K. A.; Van Duyne, R. P. Localized Surface Plasmon Resonance Spectroscopy and Sensing. *Annual Review of Physical Chemistry* **2007**, *58* (1), 267–297. https://doi.org/10.1146/annurev.physchem.58.032806.104607.

(177) Zhang, X.; Yonzon, C. R.; Van Duyne, R. P. Nanosphere Lithography Fabricated Plasmonic Materials and Their Applications. *J. Mater. Res.* **2006**, *21* (5), 1083–1092. https://doi.org/10.1557/jmr.2006.0136.

(178) Du, Y.; Shi, L.; He, T.; Sun, X.; Mo, Y. SERS Enhancement Dependence on the Diameter and Aspect Ratio of Silver-Nanowire Array Fabricated by Anodic Aluminium Oxide Template. *Applied Surface Science* **2008**, *255* (5, Part 1), 1901–1905. https://doi.org/10.1016/j.apsusc.2008.06.140.

(179) Sammi, H.; Nair, R. V.; Sardana, N. Recent Advances in Nanoporous AAO Based Substrates for Surface-Enhanced Raman Scattering. *Materials Today: Proceedings* **2021**, *41*, 843–850. https://doi.org/10.1016/j.matpr.2020.09.233.

(180) Zhao, C.; Zhu, Y.; Chen, L.; Zhou, S.; Su, Y.; Ji, X.; Chen, A.; Gui, X.; Tang, Z.; Liu, Z. Multi-Layer Nanoarrays Sandwiched by Anodized Aluminium Oxide Membranes: An Approach to an Inexpensive, Reproducible, Highly Sensitive SERS Substrate. *Nanoscale* **2018**, *10* (34), 16278–16283. https://doi.org/10.1039/C8NR05875J.

(181) Sun, K.; Deng, Q.; Tang, H. AAO Template-Assisted Fabrication of Ordered Ag Nanoparticles-Decorated Au Nanotubes Array for Surface-Enhanced Raman Scattering Detection. *Sustainability* **2022**, *14* (3), 1305. https://doi.org/10.3390/su14031305.

(182) Dick, L. A.; McFarland, A. D.; Haynes, C. L.; Van Duyne, R. P. Metal Film over Nanosphere (MFON) Electrodes for Surface-Enhanced Raman

Spectroscopy (SERS): Improvements in Surface Nanostructure Stability and Suppression of Irreversible Loss. *J. Phys. Chem. B* **2002**, *106* (4), 853–860. https://doi.org/10.1021/jp013638l.

(183) Zaleski, S.; Clark, K. A.; Smith, M. M.; Eilert, J. Y.; Doty, M.; Van Duyne, R. P. Identification and Quantification of Intravenous Therapy Drugs Using Normal Raman Spectroscopy and Electrochemical Surface-Enhanced Raman Spectroscopy. *Anal. Chem.* **2017**, *89* (4), 2497–2504. https://doi.org/10.1021/acs.analchem.6b04636.

(184) Zhang, X.; Yonzon, C. R.; Duyne, R. P. V. An Electrochemical Surface-Enhanced Raman Spectroscopy Approach to Anthrax Detection. In *Plasmonics: Metallic Nanostructures and Their Optical Properties*; International Society for Optics and Photonics, 2003; Vol. 5221, pp 82–91. https://doi.org/10.1117/12.508519.

(185) Falamas, A.; Cuibus, D.; Tosa, N.; Brezestean, I.; Muntean, C. M.; Milenko, K.; Vereshchagina, E.; Moldovan, R.; Bodoki, E.; Farcau, C. Toward Microfluidic SERS and EC-SERS Applications via Tunable Gold Films over Nanospheres. *Discover Nano* **2023**, *18* (1), 73. https://doi.org/10.1186/s11671-023-03851-3.

(186) Bartlett, P. N.; Baumberg, J. J.; Coyle, S.; Abdelsalam, M. E. Optical Properties of Nanostructured Metal Films. *Faraday Disc.* **2004**, *125*, 117. https://doi.org/10.1039/b304116f.

(187) Mahajan, S.; Abdelsalam, M.; Suguwara, Y.; Cintra, S.; Russell, A.; Baumberg, J.; Bartlett, P. Tuning Plasmons on Nano-Structured Substrates for NIR-SERS. *Phys. Chem. Chem. Phys.* **2007**, *9* (1), 104–109. https://doi.org/10.1039/B611803H.

(188) Bassetto, V. C.; Russell, A. E.; Kubota, L. T.; Bartlett, P. N. Preparation of Copper Sphere Segment Void Templates for Electrochemical SERS and Their Use to Study the Interaction of Amino Acids with Copper under Potentiostatic Control. *Electrochimica Acta* **2014**, *144*, 400–405. https://doi.org/10.1016/j.electacta.2014.08.066.

(189) Dong, X.; Ohnoutek, L.; Yang, Y.; Feng, Y.; Wang, T.; Tahir, M. A.; Valev, V. K.; Zhang, L. Cu/Ag Sphere Segment Void Array as Efficient Surface Enhanced Raman Spectroscopy Substrate for Detecting Individual Atmospheric Aerosol. *Anal. Chem.* **2019**, *91* (21), 13647–13657. https://doi.org/10.1021/acs.analchem.9b02840.

(190) Abdelsalam, M. E.; Bartlett, P. N.; Baumberg, J. J.; Cintra, S.; Kelf, T. A.; Russell, A. E. Electrochemical SERS at a Structured Gold Surface. *Electrochemistry Communications* **2005**, *7* (7), 740–744. https://doi.org/10.1016/j.elecom.2005.04.028.

(191) Abdelsalam, M.; Bartlett, P. N.; Russell, A. E.; Baumberg, J. J.; Calvo, E. J.; Tognalli, N. G.; Fainstein, A. Quantitative Electrochemical SERS of Flavin at a Structured Silver Surface. *Langmuir* **2008**, *24* (13), 7018–7023. https://doi.org/10.1021/la800410x.

(192) Vezvaie, M.; Brosseau, C. L.; Lipkowski, J. Electrochemical SERS Study of a Biomimetic Membrane Supported at a Nanocavity Patterned Ag Electrode. *Electrochimica Acta* **2013**, *110*, 120–132. https://doi.org/10.1016/j.electacta.2013.03.139.

(193) Peters, R. F.; Gutierrez-Rivera, L.; Dew, S. K.; Stepanova, M. Surface Enhanced Raman Spectroscopy Detection of Biomolecules Using EBL

Fabricated Nanostructured Substrates. *JoVE* **2015**, No. 97, 52712. https://doi.org/10.3791/52712.

(194) Sheffield, U. of. *Overview - EBL Patterning - Electron Beam Lithography - The University of Sheffield*. https://www.sheffield.ac.uk/ebl/patterning (accessed 2020-02-07).

(195) Prakash, S.; Yeom, J. Advanced Fabrication Methods and Techniques. In *Nanofluidics and Microfluidics*; Elsevier, 2014; pp 87–170. https://doi.org/10.1016/B978-1-4377-4469-9.00004-4.

(196) Abu Hatab, N. A.; Oran, J. M.; Sepaniak, M. J. Surface-Enhanced Raman Spectroscopy Substrates Created *via* Electron Beam Lithography and Nanotransfer Printing. *ACS Nano* **2008**, *2* (2), 377–385. https://doi.org/10.1021/nn7003487.

(197) Ward, D. R.; Grady, N. K.; Levin, C. S.; Halas, N. J.; Wu, Y.; Nordlander, P.; Natelson, D. Electromigrated Nanoscale Gaps for Surface-Enhanced Raman Spectroscopy. *Nano Lett.* **2007**, *7* (5), 1396–1400. https://doi.org/10.1021/nl070625w.

(198) Turkevich, J.; Stevenson, P. C.; Hillier, J. A Study of the Nucleation and Growth Processes in the Synthesis of Colloidal Gold. *Discuss. Faraday Soc.* **1951**, *11* (0), 55–75. https://doi.org/10.1039/DF9511100055.

(199) Frens, G. Controlled Nucleation for the Regulation of the Particle Size in Monodisperse Gold Suspensions. *Nature Physical Science* **1973**, *241* (105), 20–22. https://doi.org/10.1038/physci241020a0.

(200) Bastús, N. G.; Comenge, J.; Puntes, V. Kinetically Controlled Seeded Growth Synthesis of Citrate-Stabilized Gold Nanoparticles of up to 200 Nm: Size Focusing versus Ostwald Ripening. *Langmuir* **2011**, *27* (17), 11098–11105. https://doi.org/10.1021/la201938u.

(201) Lee, P. C.; Meisel, D. Adsorption and Surface-Enhanced Raman of Dyes on Silver and Gold Sols. *J. Phys. Chem.* **1982**, *86* (17), 3391–3395. https://doi.org/10.1021/j100214a025.

(202) Almatroudi, A. Silver Nanoparticles: Synthesis, Characterisation and Biomedical Applications. *Open Life Sci* **2020**, *15* (1), 819–839. https://doi.org/10.1515/biol-2020-0094.

(203) Wuithschick, M.; Paul, B.; Bienert, R.; Sarfraz, A.; Vainio, U.; Sztucki, M.; Kraehnert, R.; Strasser, P.; Rademann, K.; Emmerling, F.; Polte, J. Size-Controlled Synthesis of Colloidal Silver Nanoparticles Based on Mechanistic Understanding. *Chem. Mater.* **2013**, *25* (23), 4679–4689. https://doi.org/10.1021/cm401851g.

(204) Thanh, N. T. K.; Maclean, N.; Mahiddine, S. Mechanisms of Nucleation and Growth of Nanoparticles in Solution. *Chem. Rev.* **2014**, *114* (15), 7610–7630. https://doi.org/10.1021/cr400544s.

(205) Alarcon, E. I.; Griffith, M.; Udekwu, K. I. *Silver Nanoparticle Applications: In the Fabrication and Design of Medical and Biosensing Devices*; Springer, 2015.

(206) Cortés, E.; Etchegoin, P. G.; Le Ru, E. C.; Fainstein, A.; Vela, M. E.; Salvarezza, R. C. Monitoring the Electrochemistry of Single Molecules by Surface-Enhanced Raman Spectroscopy. *J. Am. Chem. Soc.* **2010**, *132* (51), 18034–18037. https://doi.org/10.1021/ja108989b.

(207) Zong, C.; Chen, C.-J.; Zhang, M.; Wu, D.-Y.; Ren, B. Transient Electrochemical Surface-Enhanced Raman Spectroscopy: A Millisecond

Time-Resolved Study of an Electrochemical Redox Process. *J. Am. Chem. Soc.* **2015**, *137* (36), 11768–11774. https://doi.org/10.1021/jacs.5b07197.

(208) Goodall, B. L.; Robinson, A. M.; Brosseau, C. L. Electrochemical-Surface Enhanced Raman Spectroscopy (E-SERS) of Uric Acid: A Potential Rapid Diagnostic Method for Early Preeclampsia Detection. *Phys. Chem. Chem. Phys.* **2013**, *15* (5), 1382–1388. https://doi.org/10.1039/C2CP42596C.

(209) Zhao, L.; Blackburn, J.; Brosseau, C. L. Quantitative Detection of Uric Acid by Electrochemical-Surface Enhanced Raman Spectroscopy Using a Multilayered Au/Ag Substrate. *Anal. Chem.* **2015**, *87* (1), 441–447. https://doi.org/10.1021/ac503967s.

(210) Smith, S. R.; Seenath, R.; Kulak, M. R.; Lipkowski, J. Characterization of a Self-Assembled Monolayer of 1-Thio-β- D -Glucose with Electrochemical Surface Enhanced Raman Spectroscopy Using a Nanoparticle Modified Gold Electrode. *Langmuir* **2015**, *31* (36), 10076–10086. https://doi.org/10.1021/acs.langmuir.5b02767.

(211) Lynk, T. P.; Sit, C. S.; Brosseau, C. L. Electrochemical Surface-Enhanced Raman Spectroscopy as a Platform for Bacterial Detection and Identification. *Anal. Chem.* **2018**, *90* (21), 12639–12646. https://doi.org/10.1021/acs.analchem.8b02806.

(212) Robinson, A. M.; Harroun, S. G.; Bergman, J.; Brosseau, C. L. Portable Electrochemical Surface-Enhanced Raman Spectroscopy System for Routine Spectroelectrochemical Analysis. *Anal. Chem.* **2012**, *84* (3), 1760–1764. https://doi.org/10.1021/ac2030078.

(213) Bindesri, S. D.; Alhatab, D. S.; Brosseau, C. L. Development of an Electrochemical Surface-Enhanced Raman Spectroscopy (EC-SERS) Fabric-Based Plasmonic Sensor for Point-of-Care Diagnostics. *Analyst* **2018**, *143* (17), 4128–4135. https://doi.org/10.1039/C8AN01117F.

(214) Yu, W. W.; White, I. M. Inkjet-Printed Paper-Based SERS Dipsticks and Swabs for Trace Chemical Detection. *Analyst* **2013**, *138* (4), 1020–1025. https://doi.org/10.1039/C2AN36116G.

(215) Robinson, A. M.; Zhao, L.; Shah Alam, M. Y.; Bhandari, P.; Harroun, S. G.; Dendukuri, D.; Blackburn, J.; Brosseau, C. L. The Development of “Fab-Chips” as Low-Cost, Sensitive Surface-Enhanced Raman Spectroscopy (SERS) Substrates for Analytical Applications. *Analyst* **2015**, *140* (3), 779–785. https://doi.org/10.1039/C4AN01633E.

(216) Albarghouthi, N.; Eisnor, M. M.; Pye, C. C.; Brosseau, C. L. Electrochemical Surface-Enhanced Raman Spectroscopy (EC-SERS) and Computational Study of Atrazine: Toward Point-of-Need Detection of Prevalent Herbicides. *J. Phys. Chem. C* **2022**, *126* (23), 9836–9842. https://doi.org/10.1021/acs.jpcc.2c02337.

(217) Greene, B. H. C.; Alhatab, D. S.; Pye, C. C.; Brosseau, C. L. Electrochemical-Surface Enhanced Raman Spectroscopic (EC-SERS) Study of 6-Thiouric Acid: A Metabolite of the Chemotherapy Drug Azathioprine. *J. Phys. Chem. C* **2017**, *121* (14), 8084–8090. https://doi.org/10.1021/acs.jpcc.7b01179.

(218) M. Eisnor, M.; R. McLeod, K. E.; Bindesri, S.; A. Svoboda, S.; L. Wustholz, K.; L. Brosseau, C. Electrochemical Surface-Enhanced

Raman Spectroscopy (EC-SERS): A Tool for the Identification of Polyphenolic Components in Natural Lake Pigments. *Physical Chemistry Chemical Physics* **2022**, *24* (1), 347–356. https://doi.org/10.1039/D1CP03301H.

(219) Jeong, H.-H.; Choi, E.; Ellis, E.; Lee, T.-C. Recent Advances in Gold Nanoparticles for Biomedical Applications: From Hybrid Structures to Multi-Functionality. *J. Mater. Chem. B* **2019**, *7* (22), 3480–3496. https://doi.org/10.1039/C9TB00557A.

(220) Silvestri, A.; Lay, L.; Psaro, R.; Polito, L.; Evangelisti, C. Fluidic Manufacture of Star-Shaped Gold Nanoparticles. *Chemistry – A European Journal* **2017**, *23* (41), 9732–9735. https://doi.org/10.1002/chem.201701617.

(221) Jahn, M.; Patze, S.; Hidi, I. J.; Knipper, R.; Radu, A. I.; Mühlig, A.; Yüksel, S.; Peksa, V.; Weber, K.; Mayerhöfer, T.; Cialla-May, D.; Popp, J. Plasmonic Nanostructures for Surface Enhanced Spectroscopic Methods. *Analyst* **2016**, *141* (3), 756–793. https://doi.org/10.1039/C5AN02057C.

(222) Li, J.-F.; Zhang, Y.-J.; Ding, S.-Y.; Panneerselvam, R.; Tian, Z.-Q. Core–Shell Nanoparticle-Enhanced Raman Spectroscopy. *Chem. Rev.* **2017**, *117* (7), 5002–5069. https://doi.org/10.1021/acs.chemrev.6b00596.

(223) Ghosh Chaudhuri, R.; Paria, S. Core/Shell Nanoparticles: Classes, Properties, Synthesis Mechanisms, Characterization, and Applications. *Chem. Rev.* **2012**, *112* (4), 2373–2433. https://doi.org/10.1021/cr100449n.

(224) Loiseau, A.; Asila, V.; Boitel-Aullen, G.; Lam, M.; Salmain, M.; Boujday, S. Silver-Based Plasmonic Nanoparticles for and Their Use in Biosensing. *Biosensors* **2019**, *9* (2), 78. https://doi.org/10.3390/bios9020078.

(225) Hartman, T.; Wondergem, C. S.; Kumar, N.; van den Berg, A.; Weckhuysen, B. M. Surface- and Tip-Enhanced Raman Spectroscopy in Catalysis. *J. Phys. Chem. Lett.* **2016**, *7* (8), 1570–1584. https://doi.org/10.1021/acs.jpclett.6b00147.

(226) Anker, J. N.; Hall, W. P.; Lyandres, O.; Shah, N. C.; Zhao, J.; Van Duyne, R. P. Biosensing with Plasmonic Nanosensors. *Nat Mater* **2008**, *7* (6), 442–453. https://doi.org/10.1038/nmat2162.

(227) Jiang, H.-L.; Akita, T.; Xu, Q. A One-Pot Protocol for Synthesis of Non-Noble Metal-Based Core–Shell Nanoparticles under Ambient Conditions: Toward Highly Active and Cost-Effective Catalysts for Hydrolytic Dehydrogenation of NH3BH3. *Chem. Commun.* **2011**, *47* (39), 10999–11001. https://doi.org/10.1039/C1CC13989D.

(228) Hu, Y.; Zhang, A.-Q.; Li, H.-J.; Qian, D.-J.; Chen, M. Synthesis, Study, and Discrete Dipole Approximation Simulation of Ag-Au Bimetallic Nanostructures. *Nanoscale Res Lett* **2016**, *11* (1), 209. https://doi.org/10.1186/s11671-016-1435-4.

(229) Steinbrück, A.; Stranik, O.; Csaki, A.; Fritzsche, W. Sensoric Potential of Gold–Silver Core–Shell Nanoparticles. *Anal Bioanal Chem* **2011**, *401* (4), 1241. https://doi.org/10.1007/s00216-011-5177-y.

(230) Liu, B.; Han, G.; Zhang, Z.; Liu, R.; Jiang, C.; Wang, S.; Han, M.-Y. Shell Thickness-Dependent Raman Enhancement for Rapid Identification and

Detection of Pesticide Residues at Fruit Peels. *Anal. Chem.* **2012**, *84* (1), 255–261. https://doi.org/10.1021/ac202452t.

(231) Pande, S.; Ghosh, S. K.; Praharaj, S.; Panigrahi, S.; Basu, S.; Jana, S.; Pal, A.; Tsukuda, T.; Pal, T. Synthesis of Normal and Inverted Gold−Silver Core−Shell Architectures in β-Cyclodextrin and Their Applications in SERS. *J. Phys. Chem. C* **2007**, *111* (29), 10806–10813. https://doi.org/10.1021/jp0702393.

(232) Wu, P.; Gao, Y.; Lu, Y.; Zhang, H.; Cai, C. High Specific Detection and Near-Infrared Photothermal Therapy of Lung Cancer Cells with High SERS Active Aptamer–Silver–Gold Shell–Core Nanostructures. *Analyst* **2013**, *138* (21), 6501. https://doi.org/10.1039/c3an01375h.

(233) Sugawa, K.; Akiyama, T.; Tanoue, Y.; Harumoto, T.; Yanagida, S.; Yasumori, A.; Tomita, S.; Otsuki, J. Particle Size Dependence of the Surface-Enhanced Raman Scattering Properties of Densely Arranged Two-Dimensional Assemblies of Au(Core)–Ag(Shell) Nanospheres. *Phys. Chem. Chem. Phys.* **2015**, *17* (33), 21182–21189. https://doi.org/10.1039/C4CP05058D.

(234) Zhao, Y.; Zhang, Y.-J.; Meng, J.-H.; Chen, S.; Panneerselvam, R.; Li, C.-Y.; Jamali, S. B.; Li, X.; Yang, Z.-L.; Li, J.-F.; Tian, Z.-Q. A Facile Method for the Synthesis of Large-Size Ag Nanoparticles as Efficient SERS Substrates. *Journal of Raman Spectroscopy* **2016**, *47* (6), 662–667. https://doi.org/10.1002/jrs.4879.

(235) Wang, L.; Patskovsky, S.; Gauthier-Soumis, B.; Meunier, M. Porous Au–Ag Nanoparticles from Galvanic Replacement Applied as Single-Particle SERS Probe for Quantitative Monitoring. *Small n/a* (n/a), 2105209. https://doi.org/10.1002/smll.202105209.

(236) Wang, H.; Levin, C. S.; Halas, N. J. Nanosphere Arrays with Controlled Sub-10-Nm Gaps as Surface-Enhanced Raman Spectroscopy Substrates. *J. Am. Chem. Soc.* **2005**, *127* (43), 14992–14993. https://doi.org/10.1021/ja055633y.

(237) Smith, S. R.; Lipkowski, J. Guided Assembly of Two-Dimensional Arrays of Gold Nanoparticles on a Polycrystalline Gold Electrode for Electrochemical Surface-Enhanced Raman Spectroscopy. *J. Phys. Chem. C* **2018**, *122* (13), 7303–7311. https://doi.org/10.1021/acs.jpcc.8b01309.

(238) Wu, M.; Jing, T.; Tian, J.; Qi, H.; Shi, D.; Zhao, C.; Chen, T.; Zhao, Z.; Zhang, P.; Guo, Z. Synergistic Effect of Silver Plasmon Resonance and P-n Heterojunction Enhanced Photoelectrochemical Aptasensing Platform for Detecting Chloramphenicol. *Adv Compos Hybrid Mater* **2022**, *5* (3), 2247–2259. https://doi.org/10.1007/s42114-021-00377-z.

(239) Zhu, Z.; Espulgar, W. V.; Yoshikawa, H.; Saito, M.; Fan, B.; Dou, X.; Tamiya, E. Electrochemically Modulated Surface-Enhanced Raman Spectra of Aminoglutethimide (AGI) on a Ag-Sputtered Electrode. *BCSJ* **2018**, *91* (11), 1579–1585. https://doi.org/10.1246/bcsj.20180172.

(240) McLeod, K. E. R.; Lynk, T. P.; Sit, C. S.; Brosseau, C. L. On the Origin of Electrochemical Surface-Enhanced Raman Spectroscopy (EC-SERS) Signals for Bacterial Samples: The Importance of Filtered Control Studies in the Development of New Bacterial Screening Platforms. *Anal. Methods* **2019**, *11* (7), 924–929. https://doi.org/10.1039/C8AY02613K.

(241) Zaleski, S.; Clark, K. A.; Smith, M. M.; Eilert, J. Y.; Doty, M.; Van Duyne, R. P. Identification and Quantification of Intravenous Therapy Drugs Using Normal Raman Spectroscopy and Electrochemical Surface-Enhanced Raman Spectroscopy. *Anal. Chem.* **2017**, *89* (4), 2497–2504. https://doi.org/10.1021/acs.analchem.6b04636.

(242) Huang, C.-Y.; Hsiao, H.-C. Integrated EC-SERS Chip with Uniform Nanostructured EC-SERS Active Working Electrode for Rapid Detection of Uric Acid. *Sensors (Basel)* **2020**, *20* (24), 7066. https://doi.org/10.3390/s20247066.

(243) Brosseau, C. L.; Colina, A.; Perales-Rondon, J. V.; Wilson, A. J.; Joshi, P. B.; Ren, B.; Wang, X. Electrochemical Surface-Enhanced Raman Spectroscopy. *Nat Rev Methods Primers* **2023**, *3* (1), 1–21. https://doi.org/10.1038/s43586-023-00263-6.

(244) Wright, D.; Lin, Q.; Berta, D.; Földes, T.; Wagner, A.; Griffiths, J.; Readman, C.; Rosta, E.; Reisner, E.; Baumberg, J. J. Mechanistic Study of an Immobilized Molecular Electrocatalyst by in Situ Gap-Plasmon-Assisted Spectro-Electrochemistry. *Nat Catal* **2021**, *4* (2), 157–163. https://doi.org/10.1038/s41929-020-00566-x.

(245) Santos Jr., V. O.; Leite, I. R.; Brolo, A. G.; Rubim, J. C. The Electrochemical Reduction of CO2 on a Copper Electrode in 1-n-Butyl-3-Methyl Imidazolium Tetrafluoroborate (BMI.BF4) Monitored by Surface-Enhanced Raman Scattering (SERS). *Journal of Raman Spectroscopy* **2016**, *47* (6), 674–680. https://doi.org/10.1002/jrs.4871.

(246) Henckel, D. A.; Counihan, M. J.; Holmes, H. E.; Chen, X.; Nwabara, U. O.; Verma, S.; Rodríguez-López, J.; Kenis, P. J. A.; Gewirth, A. A. Potential Dependence of the Local pH in a CO2 Reduction Electrolyzer. *ACS Catal.* **2021**, *11* (1), 255–263. https://doi.org/10.1021/acscatal.0c04297.

(247) Shan, W.; Liu, R.; Zhao, H.; He, Z.; Lai, Y.; Li, S.; He, G.; Liu, J. In Situ Surface-Enhanced Raman Spectroscopic Evidence on the Origin of Selectivity in CO2 Electrocatalytic Reduction. *ACS Nano* **2020**, *14* (9), 11363–11372. https://doi.org/10.1021/acsnano.0c03534.

(248) An, H.; Wu, L.; Mandemaker, L. D. B.; Yang, S.; de Ruiter, J.; Wijten, J. H. J.; Janssens, J. C. L.; Hartman, T.; van der Stam, W.; Weckhuysen, B. M. Sub-Second Time-Resolved Surface-Enhanced Raman Spectroscopy Reveals Dynamic CO Intermediates during Electrochemical CO2 Reduction on Copper. *Angewandte Chemie International Edition* **2021**, *60* (30), 16576–16584. https://doi.org/10.1002/anie.202104114.

(249) Hy, S.; Felix; Chen, Y.-H.; Liu, J.; Rick, J.; Hwang, B.-J. In Situ Surface Enhanced Raman Spectroscopic Studies of Solid Electrolyte Interphase Formation in Lithium Ion Battery Electrodes. *Journal of Power Sources* **2014**, *256*, 324–328. https://doi.org/10.1016/j.jpowsour.2014.01.092.

(250) Gajan, A.; Lecourt, C.; Torres Bautista, B. E.; Fillaud, L.; Demeaux, J.; Lucas, I. T. Solid Electrolyte Interphase Instability in Operating Lithium-Ion Batteries Unraveled by Enhanced-Raman Spectroscopy. *ACS Energy Lett.* **2021**, *6* (5), 1757–1763. https://doi.org/10.1021/acsenergylett.1c00436.

(251) Chen, D.; Mahmoud, M. A.; Wang, J.-H.; Waller, G. H.; Zhao, B.; Qu, C.; El-Sayed, M. A.; Liu, M. Operando Investigation into Dynamic Evolution of Cathode–Electrolyte Interfaces in a Li-Ion Battery. *Nano Lett.* **2019**, *19* (3), 2037–2043. https://doi.org/10.1021/acs.nanolett.9b00179.

(252) Zhong, J.-H.; Zhang, J.; Jin, X.; Liu, J.-Y.; Li, Q.; Li, M.-H.; Cai, W.; Wu, D.-Y.; Zhan, D.; Ren, B. Quantitative Correlation between Defect Density and Heterogeneous Electron Transfer Rate of Single Layer Graphene. *J. Am. Chem. Soc.* **2014**, *136* (47), 16609–16617. https://doi.org/10.1021/ja508965w.

(253) Westley, C.; Xu, Y.; Thilaganathan, B.; Carnell, A. J.; Turner, N. J.; Goodacre, R. Absolute Quantification of Uric Acid in Human Urine Using Surface Enhanced Raman Scattering with the Standard Addition Method. *Anal. Chem.* **2017**, *89* (4), 2472–2477. https://doi.org/10.1021/acs.analchem.6b04588.

(254) Goodacre, R.; Graham, D.; Faulds, K. Recent Developments in Quantitative SERS: Moving towards Absolute Quantification. *TrAC Trends in Analytical Chemistry* **2018**, *102*, 359–368. https://doi.org/10.1016/j.trac.2018.03.005.

(255) Lussier, F.; Thibault, V.; Charron, B.; Wallace, G. Q.; Masson, J.-F. Deep Learning and Artificial Intelligence Methods for Raman and Surface-Enhanced Raman Scattering. *TrAC Trends in Analytical Chemistry* **2020**, *124*, 115796. https://doi.org/10.1016/j.trac.2019.115796.

(256) Guo, S.; Popp, J.; Bocklitz, T. Chemometric Analysis in Raman Spectroscopy from Experimental Design to Machine Learning–Based Modeling. *Nat Protoc* **2021**, *16* (12), 5426–5459. https://doi.org/10.1038/s41596-021-00620-3.

(257) Wold, S.; Sjöström, M.; Eriksson, L. PLS-Regression: A Basic Tool of Chemometrics. *Chemometrics and Intelligent Laboratory Systems* **2001**, *58* (2), 109–130. https://doi.org/10.1016/S0169-7439(01)00155-1.

(258) Kreeger, P. K. Using Partial Least Squares Regression to Analyze Cellular Response Data. *Sci. Signal.* **2013**, *6* (271), tr7–tr7. https://doi.org/10.1126/scisignal.2003849.

(259) Eriksson, L.; Byrne, T.; Johansson, E.; Trygg, J.; Vikström, C. *Multi- and Megavariate Data Analysis Basic Principles and Applications*; Umetrics Academy, 2013.

(260) Nguyen, C. Q. Machine Learning for SERS Quantitative Detection of Pyocyanin, UC Irvine, 2018. https://escholarship.org/uc/item/6pt967sf#page=4 (accessed 2020-07-14).

(261) *6.7. Introduction to Projection to Latent Structures (PLS) — Process Improvement using Data*. https://learnche.org/pid/latent-variable-modelling/projection-to-latent-structures/index (accessed 2020-07-14).

(262) Dunn, K. Process Improvement Using Data. **2023**.

(263) Hallinan, J. S. Chapter 1 - Computational Intelligence in the Design of Synthetic Microbial Genetic Systems. In *Methods in Microbiology*; Harwood, C., Wipat, A., Eds.; Microbial Synthetic Biology; Academic Press, 2013; Vol. 40, pp 1–37. https://doi.org/10.1016/B978-0-12-417029-2.00001-7.

(264) Bishop, C. M.; Bishop, P. of N. C. C. M. *Neural Networks for Pattern Recognition*; Clarendon Press, 1995.

(265) Xie, Y.; Su, X.; Wen, Y.; Zheng, C.; Li, M. Artificial Intelligent Label-Free SERS Profiling of Serum Exosomes for Breast Cancer Diagnosis and Postoperative Assessment. *Nano Lett.* **2022**, *22* (19), 7910–7918. https://doi.org/10.1021/acs.nanolett.2c02928.

(266) Erzina, M.; Trelin, A.; Guselnikova, O.; Dvorankova, B.; Strnadova, K.; Perminova, A.; Ulbrich, P.; Mares, D.; Jerabek, V.; Elashnikov, R.; Svorcik, V.; Lyutakov, O. Precise Cancer Detection via the Combination of Functionalized SERS Surfaces and Convolutional Neural Network with Independent Inputs. *Sensors and Actuators B: Chemical* **2020**, *308*, 127660. https://doi.org/10.1016/j.snb.2020.127660.

(267) Ryzhikova, E.; Ralbovsky, N. M.; Halámková, L.; Celmins, D.; Malone, P.; Molho, E.; Quinn, J.; Zimmerman, E. A.; Lednev, I. K. Multivariate Statistical Analysis of Surface Enhanced Raman Spectra of Human Serum for Alzheimer's Disease Diagnosis. *Applied Sciences* **2019**, *9* (16), 3256. https://doi.org/10.3390/app9163256.

(268) Ho, C.-S.; Jean, N.; Hogan, C. A.; Blackmon, L.; Jeffrey, S. S.; Holodniy, M.; Banaei, N.; Saleh, A. A. E.; Ermon, S.; Dionne, J. Rapid Identification of Pathogenic Bacteria Using Raman Spectroscopy and Deep Learning. *Nat Commun* **2019**, *10* (1), 4927. https://doi.org/10.1038/s41467-019-12898-9.

(269) Nguyen, C. Q.; Thrift, W. J.; Bhattacharjee, A.; Ranjbar, S.; Gallagher, T.; Darvishzadeh-Varcheie, M.; Sanderson, R. N.; Capolino, F.; Whiteson, K.; Baldi, P.; Hochbaum, A. I.; Ragan, R. Longitudinal Monitoring of Biofilm Formation via Robust Surface-Enhanced Raman Scattering Quantification of Pseudomonas Aeruginosa-Produced Metabolites. *ACS Appl. Mater. Interfaces* **2018**, *10* (15), 12364–12373. https://doi.org/10.1021/acsami.7b18592.

(270) Alharbi, O.; Xu, Y.; Goodacre, R. Simultaneous Multiplexed Quantification of Caffeine and Its Major Metabolites Theobromine and Paraxanthine Using Surface-Enhanced Raman Scattering. *Anal Bioanal Chem* **2015**, *407* (27), 8253–8261. https://doi.org/10.1007/s00216-015-9004-8.

(271) Leong, Y. X.; Lee, Y. H.; Koh, C. S. L.; Phan-Quang, G. C.; Han, X.; Phang, I. Y.; Ling, X. Y. Surface-Enhanced Raman Scattering (SERS) Taster: A Machine-Learning-Driven Multireceptor Platform for Multiplex Profiling of Wine Flavors. *Nano Lett.* **2021**, *21* (6), 2642–2649. https://doi.org/10.1021/acs.nanolett.1c00416.

(272) Cheung, W.; Shadi, I. T.; Xu, Y.; Goodacre, R. Quantitative Analysis of the Banned Food Dye Sudan-1 Using Surface Enhanced Raman Scattering with Multivariate Chemometrics. *J. Phys. Chem. C* **2010**, *114* (16), 7285–7290. https://doi.org/10.1021/jp908892n.

(273) Alharbi, O.; Xu, Y.; Goodacre, R. Simultaneous Multiplexed Quantification of Caffeine and Its Major Metabolites Theobromine and Paraxanthine Using Surface-Enhanced Raman Scattering. *Anal Bioanal Chem* **2015**, *407* (27), 8253–8261. https://doi.org/10.1007/s00216-015-9004-8.

(274) Alharbi, O.; Xu, Y.; Goodacre, R. Simultaneous Multiplexed Quantification of Nicotine and Its Metabolites Using Surface Enhanced Raman Scattering. *Analyst* **2014**, *139*.

(275) Oldfield, G.; Ung, T.; Mulvaney, P. Au@SnO2 Core–Shell Nanocapacitors. *Advanced Materials* **2000**, *12* (20), 1519–1522. https://doi.org/10.1002/1521-4095(200010)12:20<1519::AID-ADMA1519>3.0.CO;2-W.

(276) Bai, Z.; Chen, R.; Si, P.; Huang, Y.; Sun, H.; Kim, D.-H. Fluorescent pH Sensor Based on Ag@SiO2 Core–Shell Nanoparticle. *ACS Appl. Mater. Interfaces* **2013**, *5* (12), 5856–5860. https://doi.org/10.1021/am401528w.

(277) Stöber, W.; Fink, A.; Bohn, E. Controlled Growth of Monodisperse Silica Spheres in the Micron Size Range. *Journal of Colloid and Interface Science* **1968**, *26* (1), 62–69. https://doi.org/10.1016/0021-9797(68)90272-5.

(278) Benck, J. D.; Pinaud, B. A.; Gorlin, Y.; Jaramillo, T. F. Substrate Selection for Fundamental Studies of Electrocatalysts and Photoelectrodes: Inert Potential Windows in Acidic, Neutral, and Basic Electrolyte. *PLoS ONE* **2014**, *9* (10), e107942. https://doi.org/10.1371/journal.pone.0107942.

(279) Villa, J. E. L.; Poppi, R. J. A Portable SERS Method for the Determination of Uric Acid Using a Paper-Based Substrate and Multivariate Curve Resolution. *Analyst* **2016**, *141* (6), 1966–1972. https://doi.org/10.1039/C5AN02398J.

(280) Shmaefsky, B. R. Artificial Urine for Laboratory Testing. *The American Biology Teacher* **1990**, *52* (3), 170–172. https://doi.org/10.2307/4449071.

(281) Guhmann, M.; Preis, M.; Gerber, F.; Pöllinger, N.; Breitkreutz, J.; Weitschies, W. Development of Oral Taste Masked Diclofenac Formulations Using a Taste Sensing System. *International Journal of Pharmaceutics* **2012**, *438* (1), 81–90. https://doi.org/10.1016/j.ijpharm.2012.08.047.

(282) Owen, T. *Fundamentals of Modern UV-Visible Spectroscopy: A Primer*; 2000.

(283) Heath, D. J. *UV-Vis-NIR Spectroscopy for Nanomaterials Research*; John Wiley & Sons Ltd: Chichester, UK, 2021.

(284) Zhou, W.; Wang, Z. L. *Scanning Microscopy for Nanotechnology: Techniques and Applications*; Springer Science & Business Media, 2007.

(285) Williams, D. B.; Carter, C. B. *Transmission Electron Microscopy*; Springer US: Boston, MA, 2009. https://doi.org/10.1007/978-0-387-76501-3.

(286) Hofmann, S. *Auger- and X-Ray Photoelectron Spectroscopy in Materials Science: A User-Oriented Guide*; Springer Series in Surface Sciences; Springer: Berlin, Heidelberg, 2013; Vol. 49. https://doi.org/10.1007/978-3-642-27381-0.

(287) Fairley, N.; Fernandez, V.; Richard-Plouet, M.; Guillot-Deudon, C.; Walton, J.; Smith, E.; Flahaut, D.; Greiner, M.; Biesinger, M.; Tougaard, S.; Morgan, D.; Baltrusaitis, J. Systematic and Collaborative Approach to Problem Solving Using X-Ray Photoelectron Spectroscopy. *Applied*

Surface Science Advances **2021**, *5*, 100112. https://doi.org/10.1016/j.apsadv.2021.100112.

(288) Eilers, P. H. C. A Perfect Smoother. *Anal. Chem.* **2003**, *75* (14), 3631–3636. https://doi.org/10.1021/ac034173t.

(289) Haynes, W. M. *CRC Handbook of Chemistry and Physics, 95th Edition*, 95th ed.; CRC Press: Hoboken, 2014.

(290) McKinney, W. Data Structures for Statistical Computing in Python; Austin, Texas, 2010; pp 56–61. https://doi.org/10.25080/Majora-92bf1922-00a.

(291) van der Walt, S.; Colbert, S. C.; Varoquaux, G. The NumPy Array: A Structure for Efficient Numerical Computation. *Computing in Science Engineering* **2011**, *13* (2), 22–30. https://doi.org/10.1109/MCSE.2011.37.

(292) Pedregosa, F.; Varoquaux, G.; Gramfort, A.; Michel, V.; Thirion, B.; Grisel, O.; Blondel, M.; Prettenhofer, P.; Weiss, R.; Dubourg, V.; Vanderplas, J.; Passos, A.; Cournapeau, D.; Brucher, M.; Perrot, M.; Duchesnay, É. Scikit-Learn: Machine Learning in Python. *Journal of Machine Learning Research* **2011**, *12* (85), 2825–2830.

(293) Hunter, J. D. Matplotlib: A 2D Graphics Environment. *Computing in Science Engineering* **2007**, *9* (3), 90–95. https://doi.org/10.1109/MCSE.2007.55.

(294) Ott, R. L.; Longnecker, M. T. *An Introduction to Statistical Methods and Data Analysis*; Cengage Learning, 2008.

(295) James, G.; Witten, D.; Hastie, T.; Tibshirani, R. *An Introduction to Statistical Learning*; Springer Texts in Statistics; Springer New York: New York, NY, 2013; Vol. 103. https://doi.org/10.1007/978-1-4614-7138-7.

(296) Raschka, S. *Python Machine Learning: Unlock Deeper Insights into Machine Learning with This Vital Guide to Cutting-Edge Predictive Analytics*; Community experience distilled; Packt Publishing open source: Birmingham Mumbai, 2016.

(297) Mahoney, E.; Kun, J.; Smieja, M.; Fang, Q. Review—Point-of-Care Urinalysis with Emerging Sensing and Imaging Technologies. *J. Electrochem. Soc.* **2020**, *167* (3), 037518. https://doi.org/10.1149/2.0182003JES.

(298) Yu, K.-H.; Luo, S.-F.; Tsai, W.-P.; Huang, Y.-Y. Intermittent Elevation of Serum Urate and 24-Hour Urinary Uric Acid Excretion. *Rheumatology* **2004**, *43* (12), 1541–1545. https://doi.org/10.1093/rheumatology/keh379.

(299) Goldenberg, R. L.; McClure, E. M. Maternal, Fetal and Neonatal Mortality: Lessons Learned from Historical Changes in High Income Countries and Their Potential Application to Low-Income Countries. *Matern Health Neonatol Perinatol* **2015**, *1*. https://doi.org/10.1186/s40748-014-0004-z.

(300) Buhimschi, C. S.; Norwitz, E. R.; Funai, E.; Richman, S.; Guller, S.; Lockwood, C. J.; Buhimschi, I. A. Urinary Angiogenic Factors Cluster Hypertensive Disorders and Identify Women with Severe Preeclampsia. *Am J Obstet Gynecol* **2005**, *192* (3), 734–741. https://doi.org/10.1016/j.ajog.2004.12.052.

(301) Erden, P. E.; Kılıç, E. A Review of Enzymatic Uric Acid Biosensors Based on Amperometric Detection. *Talanta* **2013**, *107*, 312–323. https://doi.org/10.1016/j.talanta.2013.01.043.

(302) Saatkamp, C. J.; de Almeida, M. L.; Bispo, J. A. M.; Pinheiro, A. L. B.; Fernandes, A. B.; Silveira, L. Quantifying Creatinine and Urea in Human Urine through Raman Spectroscopy Aiming at Diagnosis of Kidney Disease. *J. Biomed. Opt* **2016**, *21* (3), 037001. https://doi.org/10.1117/1.JBO.21.3.037001.

(303) Junge, W.; Wilke, B.; Halabi, A.; Klein, G. Determination of Reference Intervals for Serum Creatinine, Creatinine Excretion and Creatinine Clearance with an Enzymatic and a Modified Jaffé Method. *Clinica Chimica Acta* **2004**, *344* (1), 137–148. https://doi.org/10.1016/j.cccn.2004.02.007.

(304) Jaffe, M. Ueber Den Niederschlag, Welchen Pikrinsäure in Normalem Harn Erzeugt Und Über Eine Neue Reaction Des Kreatinins. **1886**, *10* (5), 391–400. https://doi.org/10.1515/bchm1.1886.10.5.391.

(305) Taussky, H. H.; Brahen, L. Creatinine and Creatine in Urine and Serum* *Based on the Methods of Bonsnes and Taussky (1), Taussky and Kurzmann (2), and Taussky (3). In *Standard Methods of Clinical Chemistry*; Seligson, D., Ed.; Elsevier, 1961; Vol. 3, pp 99–113. https://doi.org/10.1016/B978-1-4831-9684-8.50015-6.

(306) E, L.; R, G.; L, B.; Jp, P.; A, B.; F, T. Rapid and Direct Determination of Creatinine in Urine Using Capillary Zone Electrophoresis. *Clin Chim Acta* **2009**, *409* (1–2), 52–55. https://doi.org/10.1016/j.cca.2009.08.015.

(307) Zuo, Y.; Wang, C.; Zhou, J.; Sachdeva, A.; Ruelos, V. C. Simultaneous Determination of Creatinine and Uric Acid in Human Urine by High-Performance Liquid Chromatography. *Anal Sci* **2008**, *24* (12), 1589–1592. https://doi.org/10.2116/analsci.24.1589.

(308) Weber, J. A.; van Zanten, A. P. Interferences in Current Methods for Measurements of Creatinine. *Clinical Chemistry* **1991**, *37* (5), 695–700. https://doi.org/10.1093/clinchem/37.5.695.

(309) Li, X.; Fang, X.; Yu, Z.; Sheng, G.; Wu, M.; Fu, J.; Chen, H. Direct Quantification of Creatinine in Human Urine by Using Isotope Dilution Extractive Electrospray Ionization Tandem Mass Spectrometry. *Analytica Chimica Acta* **2012**, *748*, 53–57. https://doi.org/10.1016/j.aca.2012.08.040.

(310) Umar, A. A.; Salleh, M. M.; Bakar, N. A. Detection of Creatinine on Triangular Silver Nanoplates Surface Using Surface-Enhanced Raman Scattering Sensor. *IJBNN* **2017**, *3* (4), 335. https://doi.org/10.1504/IJBNN.2017.10006374.

(311) Gangopadhyay, D.; Sharma, P.; Nandi, R.; Das, M.; Ghosh, S.; Singh, R. K. In Vitro Concentration Dependent Detection of Creatinine: A Surface Enhanced Raman Scattering and Fluorescence Study. *RSC Adv.* **2016**, *6* (113), 112562–112567. https://doi.org/10.1039/C6RA22886K.

(312) Gil Rosa, B.; Akingbade, O. E.; Guo, X.; Gonzalez-Macia, L.; Crone, M. A.; Cameron, L. P.; Freemont, P.; Choy, K.-L.; Güder, F.; Yeatman, E.; Sharp, D. J.; Li, B. Multiplexed Immunosensors for Point-of-Care Diagnostic Applications. *Biosensors and Bioelectronics* **2022**, *203*, 114050. https://doi.org/10.1016/j.bios.2022.114050.

(313) Paramelle, D.; Sadovoy, A.; Gorelik, S.; Free, P.; Hobley, J.; Fernig, D. G. A Rapid Method to Estimate the Concentration of Citrate Capped Silver Nanoparticles from UV-Visible Light Spectra. *Analyst* **2014**, *139* (19), 4855. https://doi.org/10.1039/C4AN00978A.

(314) Kodati, V. R.; Tu, A. T.; Turumin, J. L. Raman Spectroscopic Identification of Uric-Acid-Type Kidney Stone. *Appl Spectrosc* **1990**, *44* (7), 1134–1136. https://doi.org/10.1366/0003702904086470.

(315) Zhu, S.; Li, H.; Niu, W.; Xu, G. Simultaneous Electrochemical Determination of Uric Acid, Dopamine, and Ascorbic Acid at Single-Walled Carbon Nanohorn Modified Glassy Carbon Electrode. *Biosensors and Bioelectronics* **2009**, *25* (4), 940–943. https://doi.org/10.1016/j.bios.2009.08.022.

(316) Ali, A. H.; Foss, C. A. Electrochemically Induced Shifts in the Plasmon Resonance Bands of Nanoscopic Gold Particles Adsorbed on Transparent Electrodes. *J. Electrochem. Soc.* **1999**, *146* (2), 628–636. https://doi.org/10.1149/1.1391654.

(317) Karn-orachai, K.; Ngamaroonchote, A. Role of Polyelectrolyte Multilayers over Gold Film for Selective Creatinine Detection Using Raman Spectroscopy. *Applied Surface Science* **2021**, *546*, 149092. https://doi.org/10.1016/j.apsusc.2021.149092.

(318) Vikram, K.; Mishra, S.; Srivastava, S. K.; Singh, R. K. Low Temperature Raman and DFT Study of Creatinine. *Journal of Molecular Structure* **2012**, *1012*, 141–150. https://doi.org/10.1016/j.molstruc.2011.11.018.

(319) Varshney, A.; Rehan, M.; Subbarao, N.; Rabbani, G.; Khan, R. H. Elimination of Endogenous Toxin, Creatinine from Blood Plasma Depends on Albumin Conformation: Site Specific Uremic Toxicity & Impaired Drug Binding. *PLoS ONE* **2011**, *6* (2), e17230. https://doi.org/10.1371/journal.pone.0017230.

(320) Dai, K.; Huang, R.; Jiang, R.; Ke, H.-X.; Li, F.; Jin, S.; Wu, D.-Y.; Tian, Z.-Q. Adsorption and Reduction Reactions of Anthraquinone Derivatives on Gold Electrodes Studied with Electrochemical Surface-Enhanced Raman Spectroscopy. *Journal of Raman Spectroscopy* **2012**, *43* (10), 1367–1373. https://doi.org/10.1002/jrs.4083.

(321) Gonzalez-Gallardo, C. L.; Morales-Hernández, J.; Álvarez-Contreras, L.; Arjona, N.; Guerra-Balcázar, M. Electrochemical Detection of Creatinine on Cu/Carbon Paper Electrodes Obtained by Physical Vapor Deposition. *J Appl Electrochem* **2024**, *54* (1), 115–126. https://doi.org/10.1007/s10800-023-01943-7.

(322) Viswanath, K. B.; Devasenathipathy, R.; Wang, S.; Vasantha, V. S. A New Route for the Enzymeless Trace Level Detection of Creatinine Based on Reduced Graphene Oxide/Silver Nanocomposite Biosensor. *Electroanalysis* **2017**, *29* (2), 559–565. https://doi.org/10.1002/elan.201600425.

(323) Jones, T. Fabrication of Nanostructured Electrodes for Electrochemical Surface-Enhanced Raman Spectroscopy (E-SERS): A Review. *Materials Science and Technology* **2023**, 1–15. https://doi.org/10.1080/02670836.2023.2197729.

(324) Grillet, N.; Manchon, D.; Cottancin, E.; Bertorelle, F.; Bonnet, C.; Broyer, M.; Lermé, J.; Pellarin, M. Photo-Oxidation of Individual Silver

Nanoparticles: A Real-Time Tracking of Optical and Morphological Changes. *J. Phys. Chem. C* **2013**, *117* (5), 2274–2282. https://doi.org/10.1021/jp311502h.

(325) McShan, D.; Ray, P. C.; Yu, H. Molecular Toxicity Mechanism of Nanosilver. *J Food Drug Anal* **2014**, *22* (1), 116–127. https://doi.org/10.1016/j.jfda.2014.01.010.

(326) Bell, S. E. J.; Sirimuthu, N. M. S. Quantitative Surface-Enhanced Raman Spectroscopy. *Chem. Soc. Rev.* **2008**, *37* (5), 1012–1024. https://doi.org/10.1039/B705965P.

(327) Lorén, A.; Engelbrektsson, J.; Eliasson, C.; Josefson, M.; Abrahamsson, J.; Johansson, M.; Abrahamsson, K. Internal Standard in Surface-Enhanced Raman Spectroscopy. *Anal. Chem.* **2004**, *76* (24), 7391–7395. https://doi.org/10.1021/ac0491298.

(328) Zhang, D.; Xie, Y.; Deb, S. K.; Davison, V. J.; Ben-Amotz, D. Isotope Edited Internal Standard Method for Quantitative Surface-Enhanced Raman Spectroscopy. *Anal Chem* **2005**, *77* (11), 3563–3569. https://doi.org/10.1021/ac050338h.

(329) Crespo, J. R. Electrochemical-SERS Analysis of R6G Using a Microcontroller Based Portable Potentiostat, 2017. https://run.unl.pt/handle/10362/53149?locale=en (accessed 2022-01-10).

(330) Jensen, L.; Schatz, G. C. Resonance Raman Scattering of Rhodamine 6G as Calculated Using Time-Dependent Density Functional Theory. *J. Phys. Chem. A* **2006**, *110* (18), 5973–5977. https://doi.org/10.1021/jp0610867.

(331) Masitas, R. A.; Khachian, I. V.; Bill, B. L.; Zamborini, F. P. Effect of Surface Charge and Electrode Material on the Size-Dependent Oxidation of Surface-Attached Metal Nanoparticles. *Langmuir* **2014**, *30* (43), 13075–13084. https://doi.org/10.1021/la5029614.

(332) Scarpettini, A. F.; Bragas, A. V. Coverage and Aggregation of Gold Nanoparticles on Silanized Glasses. *Langmuir* **2010**, *26* (20), 15948–15953. https://doi.org/10.1021/la102937b.

(333) Klug, J.; Pérez, L. A.; Coronado, E. A.; Lacconi, G. I. Chemical and Electrochemical Oxidation of Silicon Surfaces Functionalized with APTES: The Role of Surface Roughness in the AuNPs Anchoring Kinetics. *J. Phys. Chem. C* **2013**, *117* (21), 11317–11327. https://doi.org/10.1021/jp212613f.

(334) Zienkiewicz-Strzałka, M.; Deryło-Marczewska, A.; Kozakevych, R. B. Silica Nanocomposites Based on Silver Nanoparticles-Functionalization and pH Effect. *Appl Nanosci* **2018**, *8* (7), 1649–1668. https://doi.org/10.1007/s13204-018-0837-2.

(335) Witt, J.; Mandler, D.; Wittstock, G. Nanoparticle-Imprinted Matrices as Sensing Layers for Size-Selective Recognition of Silver Nanoparticles. *ChemElectroChem* **2016**, *3* (12), 2116–2124. https://doi.org/10.1002/celc.201600321.

(336) Swartz, M. E.; Krull, I. S. *Handbook of Analytical Validation*; CRC Press, 2012.

(337) Lu, Y.; Wu, C.; You, R.; Wu, Y.; Shen, H.; Zhu, L.; Feng, S. Superhydrophobic Silver Film as a SERS Substrate for the Detection of

Uric Acid and Creatinine. *Biomed. Opt. Express, BOE* **2018**, *9* (10), 4988–4997. https://doi.org/10.1364/BOE.9.004988.

(338) Lu, D.; Cai, R.; Liao, Y.; You, R.; Lu, Y. Two-Dimensional Glass/p-ATP/Ag NPs as Multifunctional SERS Substrates for Label-Free Quantification of Uric Acid in Sweat. *Spectrochimica Acta Part A: Molecular and Biomolecular Spectroscopy* **2023**, *296*, 122631. https://doi.org/10.1016/j.saa.2023.122631.

(339) Alula, M. T.; Lemmens, P.; Bo, L.; Wulferding, D.; Yang, J.; Spende, H. Preparation of Silver Nanoparticles Coated ZnO/Fe3O4 Composites Using Chemical Reduction Method for Sensitive Detection of Uric Acid via Surface-Enhanced Raman Spectroscopy. *Analytica Chimica Acta* **2019**, *1073*, 62–71. https://doi.org/10.1016/j.aca.2019.04.061.

(340) Ansah, I. B.; Lee, W.-C.; Mun, C.; Rha, J.-J.; Jung, H. S.; Kang, M.; Park, S.-G.; Kim, D.-H. In Situ Electrochemical Surface Modification of Au Electrodes for Simultaneous Label-Free SERS Detection of Ascorbic Acid, Dopamine and Uric Acid. *Sensors and Actuators B: Chemical* **2022**, *353*, 131196. https://doi.org/10.1016/j.snb.2021.131196.

(341) Wang, Y.; Chen, J.; Wu, Y.; Chen, Y.; Pan, J.; Lei, J.; Chen, Y.; Sun, L.; Feng, S.; Chen, R. Surface-Enhanced Raman Spectroscopy of Creatinine in Silver Colloid. In *Tenth International Conference on Photonics and Imaging in Biology and Medicine (PIBM 2011)*; SPIE, 2012; Vol. 8329, pp 142–148. https://doi.org/10.1117/12.918990.

(342) Zhang, H.; Li, G.; Li, S.; Xu, L.; Tian, Y.; Jiao, A.; Liu, X.; Chen, F.; Chen, M. Boron Nitride/Gold Nanocomposites for Crystal Violet and Creatinine Detection by Surface-Enhanced Raman Spectroscopy. *Applied Surface Science* **2018**, *457*, 684–694. https://doi.org/10.1016/j.apsusc.2018.06.295.

(343) Chamuah, N.; Saikia, A.; Joseph, A. M.; Nath, P. Blu-Ray DVD as SERS Substrate for Reliable Detection of Albumin, Creatinine and Urea in Urine. *Sensors and Actuators B: Chemical* **2019**, *285*, 108–115. https://doi.org/10.1016/j.snb.2019.01.031.

(344) Li, M.; Du, Y.; Zhao, F.; Zeng, J.; Mohan, C.; Shih, W.-C. Reagent- and Separation-Free Measurements of Urine Creatinine Concentration Using Stamping Surface Enhanced Raman Scattering (S-SERS). *Biomed Opt Express* **2015**, *6* (3), 849–858. https://doi.org/10.1364/BOE.6.000849.

(345) Azimi, S.; Docoslis, A. LESS Is More: Achieving Sensitive Protein Detection by Combining Electric Field Effects and Surface-Enhanced Raman Scattering. *Sensors and Actuators B: Chemical* **2023**, *393*, 134250. https://doi.org/10.1016/j.snb.2023.134250.

(346) Krämer, J.; Kang, R.; Grimm, L. M.; De Cola, L.; Picchetti, P.; Biedermann, F. Molecular Probes, Chemosensors, and Nanosensors for Optical Detection of Biorelevant Molecules and Ions in Aqueous Media and Biofluids. *Chem. Rev.* **2022**, acs.chemrev.1c00746. https://doi.org/10.1021/acs.chemrev.1c00746.

(347) Cooman, T.; Ott, C. E.; Arroyo, L. E. Evaluation and Classification of Fentanyl-Related Compounds Using EC-SERS and Machine Learning. *Journal of Forensic Sciences* **2023**, *68* (5), 1520–1526. https://doi.org/10.1111/1556-4029.15285.

(348) Grys, D.-B.; de Nijs, B.; Huang, J.; Scherman, O. A.; Baumberg, J. J. SERSbot: Revealing the Details of SERS Multianalyte Sensing Using Full Automation. *ACS Sens.* **2021**, *6* (12), 4507–4514. https://doi.org/10.1021/acssensors.1c02116.

(349) Goodfellow, I.; Bengio, Y.; Courville, A. *Deep Learning*; Adaptive computation and machine learning; The MIT Press: Cambridge, Massachusetts, 2016.

(350) *sklearn.neural_network.MLPRegressor — scikit-learn 0.23.1 documentation*. https://scikit-learn.org/stable/modules/generated/sklearn.neural_network.MLPRegressor.html (accessed 2020-07-23).

(351) Mockus, J. Application of Bayesian Approach to Numerical Methods of Global and Stochastic Optimization. *J Glob Optim* **1994**, *4* (4), 347–365. https://doi.org/10.1007/BF01099263.

(352) Snoek, J.; Larochelle, H.; Adams, R. P. Practical Bayesian Optimization of Machine Learning Algorithms. In *Advances in Neural Information Processing Systems 25*; Pereira, F., Burges, C. J. C., Bottou, L., Weinberger, K. Q., Eds.; Curran Associates, Inc., 2012; pp 2951–2959.

(353) Putnam, D. F. *Composition and Concentrative Properties of Human Urine*; NASA, 1971.

(354) Sarigul, N.; Korkmaz, F.; Kurultak, İ. A New Artificial Urine Protocol to Better Imitate Human Urine. *Sci Rep* **2019**, *9*, 20159. https://doi.org/10.1038/s41598-019-56693-4.

(355) Zhang, Z.; Beck, M. W.; Winkler, D. A.; Huang, B.; Sibanda, W.; Goyal, H. Opening the Black Box of Neural Networks: Methods for Interpreting Neural Network Models in Clinical Applications. *Ann Transl Med* **2018**, *6* (11).

(356) Narla, A.; Kuprel, B.; Sarin, K.; Novoa, R.; Ko, J. Automated Classification of Skin Lesions: From Pixels to Practice. *Journal of Investigative Dermatology* **2018**, *138* (10), 2108–2110. https://doi.org/10.1016/j.jid.2018.06.175.

(357) Esteva, A.; Kuprel, B.; Novoa, R. A.; Ko, J.; Swetter, S. M.; Blau, H. M.; Thrun, S. Dermatologist-Level Classification of Skin Cancer with Deep Neural Networks. *Nature* **2017**, *542* (7639), 115–118. https://doi.org/10.1038/nature21056.

(358) Goodfellow, I. J.; Shlens, J.; Szegedy, C. Explaining and Harnessing Adversarial Examples. *arXiv:1412.6572 [cs, stat]* **2015**.

(359) Su, J.; Vargas, D. V.; Sakurai, K. One Pixel Attack for Fooling Deep Neural Networks. *IEEE Transactions on Evolutionary Computation* **2019**, *23* (5), 828–841. https://doi.org/10.1109/TEVC.2019.2890858.

(360) Ogunlade, B.; Tadesse, L. F.; Li, H.; Vu, N.; Banaei, N.; Barczak, A. K.; Saleh, Amr. A. E.; Prakash, M.; Dionne, J. A. Predicting Tuberculosis Drug Resistance with Machine Learning-Assisted Raman Spectroscopy. *ArXiv* **2023**, arXiv:2306.05653v1.

(361) Leordean, C.; Canpean, V.; Astilean, S. Surface-Enhanced Raman Scattering (SERS) Analysis of Urea Trace in Urine, Fingerprint, and Tear Samples. *Spectroscopy Letters* **2012**, *45* (8), 550–555. https://doi.org/10.1080/00387010.2011.649439.

(362) Bouatra, S.; Aziat, F.; Mandal, R.; Guo, A. C.; Wilson, M. R.; Knox, C.; Bjorndahl, T. C.; Krishnamurthy, R.; Saleem, F.; Liu, P.; Dame, Z. T.; Poelzer, J.; Huynh, J.; Yallou, F. S.; Psychogios, N.; Dong, E.; Bogumil, R.; Roehring, C.; Wishart, D. S. The Human Urine Metabolome. *PLoS ONE* **2013**, *8* (9), e73076. https://doi.org/10.1371/journal.pone.0073076.

(363) Glass, D.; Quesada-Cabrera, R.; Bardey, S.; Promdet, P.; Sapienza, R.; Keller, V.; Maier, S. A.; Caps, V.; Parkin, I. P.; Cortés, E. Probing the Role of Atomic Defects in Photocatalytic Systems through Photoinduced Enhanced Raman Scattering. *ACS Energy Lett.* **2021**, *6* (12), 4273–4281. https://doi.org/10.1021/acsenergylett.1c01772.

(364) Ben-Jaber, S.; Glass, D.; Brick, T.; Maier, S. A.; Parkin, I. P.; Cortés, E.; Peveler, W. J.; Quesada-Cabrera, R. Photo-Induced Enhanced Raman Spectroscopy as a Probe for Photocatalytic Surfaces. *Philosophical Transactions of the Royal Society A: Mathematical, Physical and Engineering Sciences* **2023**, *381* (2259), 20220343. https://doi.org/10.1098/rsta.2022.0343.

(365) Das, S.; Jayaraman, V. SnO2: A Comprehensive Review on Structures and Gas Sensors. *Progress in Materials Science* **2014**, *66*, 112–255. https://doi.org/10.1016/j.pmatsci.2014.06.003.

(366) Davison, G.; Yin, Y.; Jones, T.; Parkin, I. P.; Peveler, W. J.; Lee, T.-C. Multi-Mode Enhanced Raman Scattering Spectroscopy Using Aggregation-Free Hybrid Metal/Metal-Oxide Nanoparticles with Intrinsic Oxygen Vacancies. *J. Mater. Chem. C* **2023**, *11* (9), 3334–3341. https://doi.org/10.1039/D2TC05069B.

(367) Seh, Z. W.; Liu, S.; Low, M.; Zhang, S.-Y.; Liu, Z.; Mlayah, A.; Han, M.-Y. Janus Au-TiO2 Photocatalysts with Strong Localization of Plasmonic Near-Fields for Efficient Visible-Light Hydrogen Generation. *Advanced Materials* **2012**, *24* (17), 2310–2314. https://doi.org/10.1002/adma.201104241.

(368) Fernández-Vidal, J.; Gómez-Marín, A. M.; Jones, L. A. H.; Yen, C.-H.; Veal, T. D.; Dhanak, V. R.; Hu, C.-C.; Hardwick, L. J. Long-Life and pH-Stable SnO2-Coated Au Nanoparticles for SHINERS. *J. Phys. Chem. C* **2022**, *126* (29), 12074–12081. https://doi.org/10.1021/acs.jpcc.2c02432.

(369) Li, X.; Lenhart, J. J.; Walker, H. W. Aggregation Kinetics and Dissolution of Coated Silver Nanoparticles. *Langmuir* **2012**, *28* (2), 1095–1104. https://doi.org/10.1021/la202328n.

(370) Gonçalves, L. M.; Batchelor-McAuley, C.; Barros, A. A.; Compton, R. G. Electrochemical Oxidation of Adenine: A Mixed Adsorption and Diffusion Response on an Edge-Plane Pyrolytic Graphite Electrode. *J. Phys. Chem. C* **2010**, *114* (33), 14213–14219. https://doi.org/10.1021/jp1046672.

(371) Mazzara, F.; Patella, B.; Aiello, G.; O'Riordan, A.; Torino, C.; Vilasi, A.; Inguanta, R. Electrochemical Detection of Uric Acid and Ascorbic Acid Using R-GO/NPs Based Sensors. *Electrochimica Acta* **2021**, *388*, 138652. https://doi.org/10.1016/j.electacta.2021.138652.

(372) McNay, G.; Eustace, D.; Smith, W. E.; Faulds, K.; Graham, D. Surface-Enhanced Raman Scattering (SERS) and Surface-Enhanced

Resonance Raman Scattering (SERRS): A Review of Applications. *Appl Spectrosc* **2011**, *65* (8), 825–837. https://doi.org/10.1366/11-06365.

(373) Schultz, Z. Not Too Hot: The Importance of Optimizing Laser Power for Surface-Enhanced Raman Spectroscopy (SERS) Measurements. *Spectroscopy* **2021**, *36* (8), 18–20.

(374) Jørgensen, J. T.; Norregaard, K.; Tian, P.; Bendix, P. M.; Kjaer, A.; Oddershede, L. B. Single Particle and PET-Based Platform for Identifying Optimal Plasmonic Nano-Heaters for Photothermal Cancer Therapy. *Sci Rep* **2016**, *6*, 30076. https://doi.org/10.1038/srep30076.

(375) Baffou, G.; Bordacchini, I.; Baldi, A.; Quidant, R. Simple Experimental Procedures to Distinguish Photothermal from Hot-Carrier Processes in Plasmonics. *Light: Science & Applications* **2020**, *9* (1), 108. https://doi.org/10.1038/s41377-020-00345-0.

(376) Mukherjee, S.; Libisch, F.; Large, N.; Neumann, O.; Brown, L. V.; Cheng, J.; Lassiter, J. B.; Carter, E. A.; Nordlander, P.; Halas, N. J. Hot Electrons Do the Impossible: Plasmon-Induced Dissociation of H2 on Au. *Nano Lett.* **2013**, *13* (1), 240–247. https://doi.org/10.1021/nl303940z.

(377) Lee, J.; Mubeen, S.; Ji, X.; Stucky, G. D.; Moskovits, M. Plasmonic Photoanodes for Solar Water Splitting with Visible Light. *Nano Lett.* **2012**, *12* (9), 5014–5019. https://doi.org/10.1021/nl302796f.

(378) Ingram, D. B.; Linic, S. Water Splitting on Composite Plasmonic-Metal/Semiconductor Photoelectrodes: Evidence for Selective Plasmon-Induced Formation of Charge Carriers near the Semiconductor Surface. *J. Am. Chem. Soc.* **2011**, *133* (14), 5202–5205. https://doi.org/10.1021/ja200086g.

(379) Gomes Silva, C.; Juárez, R.; Marino, T.; Molinari, R.; García, H. Influence of Excitation Wavelength (UV or Visible Light) on the Photocatalytic Activity of Titania Containing Gold Nanoparticles for the Generation of Hydrogen or Oxygen from Water. *J. Am. Chem. Soc.* **2011**, *133* (3), 595–602. https://doi.org/10.1021/ja1086358.

(380) Moskovits, M. The Case for Plasmon-Derived Hot Carrier Devices. *Nature Nanotechnology* **2015**, *10* (1), 6–8. https://doi.org/10.1038/nnano.2014.280.

(381) Ueno, K.; Oshikiri, T.; Shi, X.; Zhong, Y.; Misawa, H. Plasmon-Induced Artificial Photosynthesis. *Interface Focus* **2015**, *5* (3), 20140082. https://doi.org/10.1098/rsfs.2014.0082.

(382) Mubeen, S.; Lee, J.; Singh, N.; Krämer, S.; Stucky, G. D.; Moskovits, M. An Autonomous Photosynthetic Device in Which All Charge Carriers Derive from Surface Plasmons. *Nature Nanotechnology* **2013**, *8* (4), 247–251. https://doi.org/10.1038/nnano.2013.18.

(383) Clavero, C. Plasmon-Induced Hot-Electron Generation at Nanoparticle/Metal-Oxide Interfaces for Photovoltaic and Photocatalytic Devices. *Nature Photon* **2014**, *8* (2), 95–103. https://doi.org/10.1038/nphoton.2013.238.

(384) Zhang, J.; Guan, M.; Lischner, J.; Meng, S.; Prezhdo, O. V. Coexistence of Different Charge-Transfer Mechanisms in the Hot-Carrier Dynamics of Hybrid Plasmonic Nanomaterials. *Nano Lett.* **2019**, *19* (5), 3187–3193. https://doi.org/10.1021/acs.nanolett.9b00647.

(385) Ben-Shahar, Y.; Philbin, J. P.; Scotognella, F.; Ganzer, L.; Cerullo, G.; Rabani, E.; Banin, U. Charge Carrier Dynamics in Photocatalytic Hybrid Semiconductor–Metal Nanorods: Crossover from Auger Recombination to Charge Transfer. *Nano Lett.* **2018**, *18* (8), 5211–5216. https://doi.org/10.1021/acs.nanolett.8b02169.

(386) Yang, J.-L.; Wang, H.-J.; Zhang, H.; Tian, Z.-Q.; Li, J.-F. Probing Hot Electron Behaviors by Surface-Enhanced Raman Spectroscopy. *Cell Reports Physical Science* **2020**, *1* (9), 100184. https://doi.org/10.1016/j.xcrp.2020.100184.

(387) Zhang, Q.; Zhou, Y.; Fu, X.; Villarreal, E.; Sun, L.; Zou, S.; Wang, H. Photothermal Effect, Local Field Dependence, and Charge Carrier Relaying Species in Plasmon-Driven Photocatalysis: A Case Study of Aerobic Nitrothiophenol Coupling Reaction. *J. Phys. Chem. C* **2019**, *123* (43), 26695–26704. https://doi.org/10.1021/acs.jpcc.9b08181.

(388) Liu, G.; Li, Z.; Shi, J.; Sun, K.; Ji, Y.; Wang, Z.; Qiu, Y.; Liu, Y.; Wang, Z.; Hu, P. Black Reduced Porous SnO2 Nanosheets for CO2 Electroreduction with High Formate Selectivity and Low Overpotential. *Applied Catalysis B: Environmental* **2020**, *260*, 118134. https://doi.org/10.1016/j.apcatb.2019.118134.

(389) Dong, W.; Xu, J.; Wang, C.; Lu, Y.; Liu, X.; Wang, X.; Yuan, X.; Wang, Z.; Lin, T.; Sui, M.; Chen, I.-W.; Huang, F. A Robust and Conductive Black Tin Oxide Nanostructure Makes Efficient Lithium-Ion Batteries Possible. *Advanced Materials* **2017**, *29* (24), 1700136. https://doi.org/10.1002/adma.201700136.

(390) Yang, Y.; Wang, Y.; Yin, S. Oxygen Vacancies Confined in SnO2 Nanoparticles for Desirable Electronic Structure and Enhanced Visible Light Photocatalytic Activity. *Applied Surface Science* **2017**, *420*, 399–406. https://doi.org/10.1016/j.apsusc.2017.05.176.

(391) Liu, Q.; Zhan, H.; Huang, X.; Song, Y.; He, S.; Li, X.; Wang, C.; Xie, Z. High Visible Light Photocatalytic Activity of SnO2-x Nanocrystals with Rich Oxygen Vacancy. *European Journal of Inorganic Chemistry* **2021**, *2021* (42), 4370–4376. https://doi.org/10.1002/ejic.202100617.

(392) Thiyagarajan, K.; Sivakumar, K. Oxygen Vacancy-Induced Room Temperature Ferromagnetism in Graphene–SnO2 Nanocomposites. *J Mater Sci* **2017**, *52* (13), 8084–8096. https://doi.org/10.1007/s10853-017-1016-7.

(393) Idriss, H. On the Wrong Assignment of the XPS O1s Signal at 531–532 eV Attributed to Oxygen Vacancies in Photo- and Electro-Catalysts for Water Splitting and Other Materials Applications. *Surface Science* **2021**, *712*, 121894. https://doi.org/10.1016/j.susc.2021.121894.

(394) Morgan, D. J. Photoelectron Spectroscopy of Ceria: Reduction, Quantification and the Myth of the Vacancy Peak in XPS Analysis. *Surface and Interface Analysis* **2023**, *55* (11), 845–850. https://doi.org/10.1002/sia.7254.

(395) Frankcombe, T. J.; Liu, Y. Interpretation of Oxygen 1s X-Ray Photoelectron Spectroscopy of ZnO. *Chem. Mater.* **2023**, *35* (14), 5468–5474. https://doi.org/10.1021/acs.chemmater.3c00801.

(396) Lombardi, J. R.; Birke, R. L. A Unified Approach to Surface-Enhanced Raman Spectroscopy. *J. Phys. Chem. C* **2008**, *112* (14), 5605–5617. https://doi.org/10.1021/jp800167v.

(397) Zhou, L.; Zhou, J.; Lai, W.; Yang, X.; Meng, J.; Su, L.; Gu, C.; Jiang, T.; Pun, E. Y. B.; Shao, L.; Petti, L.; Sun, X. W.; Jia, Z.; Li, Q.; Han, J.; Mormile, P. Irreversible Accumulated SERS Behavior of the Molecule-Linked Silver and Silver-Doped Titanium Dioxide Hybrid System. *Nat Commun* **2020**, *11* (1), 1785. https://doi.org/10.1038/s41467-020-15484-6.

(398) Lombardi, J. R. The Theory of Surface-Enhanced Raman Scattering on Semiconductor Nanoparticles; toward the Optimization of SERS Sensors. *Faraday Discuss.* **2017**, *205* (0), 105–120. https://doi.org/10.1039/C7FD00138J.

(399) Chenal, C.; Birke, R. L.; Lombardi, J. R. Determination of the Degree of Charge-Transfer Contributions to Surface-Enhanced Raman Spectroscopy. *ChemPhysChem* **2008**, *9* (11), 1617–1623. https://doi.org/10.1002/cphc.200800221.

(400) Sheng, S.; Ren, Y.; Yang, S.; Wang, Q.; Sheng, P.; Zhang, X.; Liu, Y. Remarkable SERS Detection by Hybrid Cu2O/Ag Nanospheres. *ACS Omega* **2020**, *5* (28), 17703–17714. https://doi.org/10.1021/acsomega.0c02301.

(401) Li, R.; Lv, H.; Zhang, X.; Liu, P.; Chen, L.; Cheng, J.; Zhao, B. Vibrational Spectroscopy and Density Functional Theory Study of 4-Mercaptobenzoic Acid. *Spectrochimica Acta Part A: Molecular and Biomolecular Spectroscopy* **2015**, *148*, 369–374. https://doi.org/10.1016/j.saa.2015.03.132.

(402) Liu, L. Z.; Wu, X. L.; Gao, F.; Shen, J. C.; Li, T. H.; Chu, P. K. Determination of Surface Oxygen Vacancy Position in SnO2 Nanocrystals by Raman Spectroscopy. *Solid State Communications* **2011**, *151* (11), 811–814. https://doi.org/10.1016/j.ssc.2011.03.029.

(403) Liu, L. Z.; Li, T. H.; Wu, X. L.; Shen, J. C.; Chu, P. K. Identification of Oxygen Vacancy Types from Raman Spectra of SnO2 Nanocrystals. *Journal of Raman Spectroscopy* **2012**, *43* (10), 1423–1426. https://doi.org/10.1002/jrs.4078.

(404) Bao, H.; Motobayashi, K.; Zhang, H.; Cai, W.; Ikeda, K. In-Situ Surface-Enhanced Raman Spectroscopy Reveals a Mars–van Krevelen-Type Gas Sensing Mechanism in Au@SnO2 Nanoparticle-Based Chemiresistors. *J. Phys. Chem. Lett.* **2023**, *14* (17), 4113–4118. https://doi.org/10.1021/acs.jpclett.3c00562.

(405) Sahu, B. K.; Das, A. Significance of In-Plane Oxygen Vacancy Rich Non-Stoichiometric Layer towards Unusual High Dielectric Constant in Nano-Structured SnO2. *Physica E: Low-dimensional Systems and Nanostructures* **2018**, *103*, 60–65. https://doi.org/10.1016/j.physe.2018.05.016.

(406) Maiti, A.; Rodriguez, J. A.; Law, M.; Kung, P.; McKinney, J. R.; Yang, P. SnO2 Nanoribbons as NO2 Sensors: Insights from First Principles Calculations. *Nano Lett.* **2003**, *3* (8), 1025–1028. https://doi.org/10.1021/nl034235v.

(407) Ducéré, J.-M.; Hemeryck, A.; Estève, A.; Rouhani, M. D.; Landa, G.; Ménini, P.; Tropis, C.; Maisonnat, A.; Fau, P.; Chaudret, B. A Computational Chemist Approach to Gas Sensors: Modeling the Response of SnO2 to CO, O2, and H2O Gases. *Journal of Computational Chemistry* **2012**, *33* (3), 247–258. https://doi.org/10.1002/jcc.21959.

(408) Xiong, Y.; Lin, Y.; Wang, X.; Zhao, Y.; Tian, J. Defect Engineering on SnO2 Nanomaterials for Enhanced Gas Sensing Performances. *Advanced Powder Materials* **2022**, *1* (3), 100033. https://doi.org/10.1016/j.apmate.2022.02.001.

(409) Ou, G.; Xu, Y.; Wen, B.; Lin, R.; Ge, B.; Tang, Y.; Liang, Y.; Yang, C.; Huang, K.; Zu, D.; Yu, R.; Chen, W.; Li, J.; Wu, H.; Liu, L.-M.; Li, Y. Tuning Defects in Oxides at Room Temperature by Lithium Reduction. *Nat Commun* **2018**, *9* (1), 1302. https://doi.org/10.1038/s41467-018-03765-0.

(410) Zeng, Q.; Cui, Y.; Zhu, L.; Yao, Y. Increasing Oxygen Vacancies at Room Temperature in SnO2 for Enhancing Ethanol Gas Sensing. *Materials Science in Semiconductor Processing* **2020**, *111*, 104962. https://doi.org/10.1016/j.mssp.2020.104962.

(411) Zhu, H.; Wang, C.; He, Y.; Pu, Y.; Li, P.; He, L.; Huang, X.; Tang, W.; Tang, H. Oxygen Vacancies Engineering in Electrocatalysts Nitrogen Reduction Reaction. *Frontiers in Chemistry* **2022**, *10*.

(412) Brown, A. M.; Sheldon, M. T.; Atwater, H. A. Electrochemical Tuning of the Dielectric Function of Au Nanoparticles. *ACS Photonics* **2015**, *2* (4), 459–464. https://doi.org/10.1021/ph500358q.

(413) Giorgetti, R.; Marcotulli, D.; Tagliabracci, A.; Schifano, F. Effects of Ketamine on Psychomotor, Sensory and Cognitive Functions Relevant for Driving Ability. *Forensic Science International* **2015**, *252*, 127–142. https://doi.org/10.1016/j.forsciint.2015.04.024.

(414) Edinoff, A. N.; Sall, S.; Koontz, C. B.; Williams, A. K.; Drumgo, D.; Mouhaffel, A.; Cornett, E. M.; Murnane, K. S.; Kaye, A. D. Ketamine Evolving Clinical Roles and Potential Effects with Cognitive, Motor and Driving Ability. *Neurology International* **2023**, *15* (1), 352–361. https://doi.org/10.3390/neurolint15010023.

(415) Arango, E.; Toriello, A.; Rosario, Z.; Cooper, G. Increasing Prevalence of Ketamine in Drivers in New York City Including the Identification of 2-Fluoro-Deschloroketamine. *Journal of Analytical Toxicology* **2021**, *45* (8), 799–806. https://doi.org/10.1093/jat/bkab057.

(416) Tang, M. H. Y.; Ching, C. K.; Poon, S.; Chan, S. S. S.; Ng, W. Y.; Lam, M.; Wong, C. K.; Pao, R.; Lau, A.; Mak, T. W. L. Evaluation of Three Rapid Oral Fluid Test Devices on the Screening of Multiple Drugs of Abuse Including Ketamine. *Forensic Science International* **2018**, *286*, 113–120. https://doi.org/10.1016/j.forsciint.2018.03.004.

(417) Cheng, W.-C.; Ng, K.-M.; Chan, K.-K.; Mok, V. K.-K.; Cheung, B. K.-L. Roadside Detection of Impairment under the Influence of Ketamine—Evaluation of Ketamine Impairment Symptoms with Reference to Its Concentration in Oral Fluid and Urine. *Forensic Science International* **2007**, *170* (1), 51–58. https://doi.org/10.1016/j.forsciint.2006.09.001.

Appendix

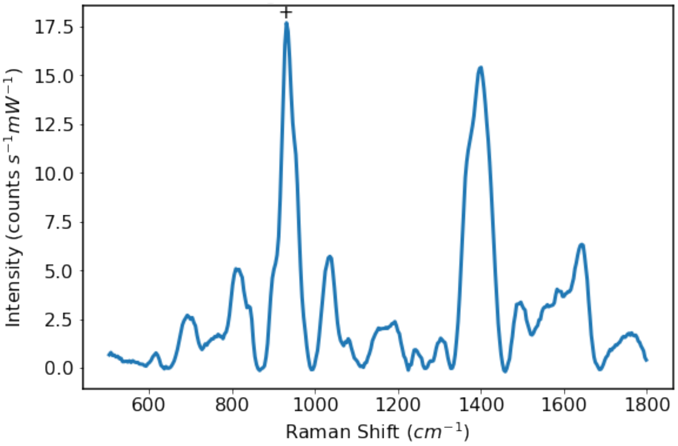

Appendix Figure A.1: SERS spectra of deionised water on an Ag NP/FTO electrode. The characteristic citrate peak is indicated with a +.

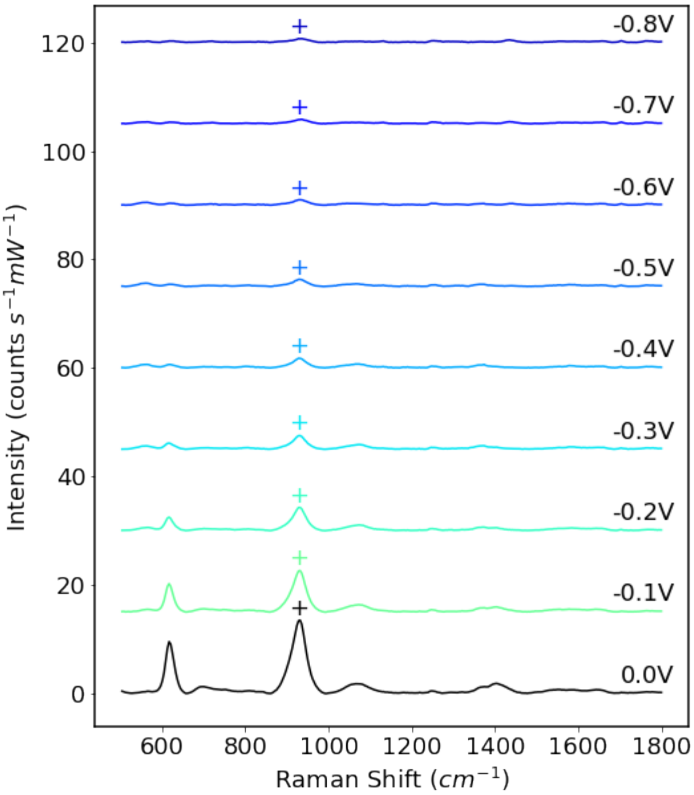

Appendix Figure A.2: E-SERS spectra of 0.1 M NaF$_{(aq)}$. The applied potential was stepped from 0 to -0.8V in 100 mV increments. The characteristic citrate peak is indicated with a +. (RE: Ag/AgCl; WE: Ag NPs on FTO; CE: platinum plate).

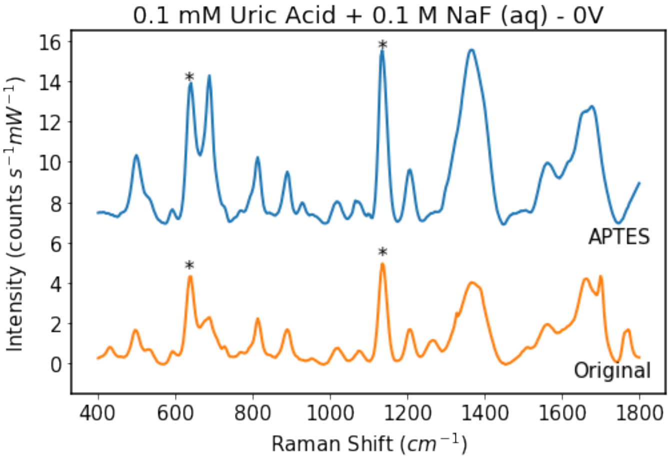

*Appendix Figure A.3: Comparison of E-SERS spectra recorded at 0V in a 0.1 mM UA solution with Ag NP FTO coated electrodes with (blue) and without (orange) APTES coating to improve adhesion. The characteristic UA peaks are indicated with a *. (RE: Ag/AgCl; WE: Ag NPs on FTO; CE: platinum plate).*

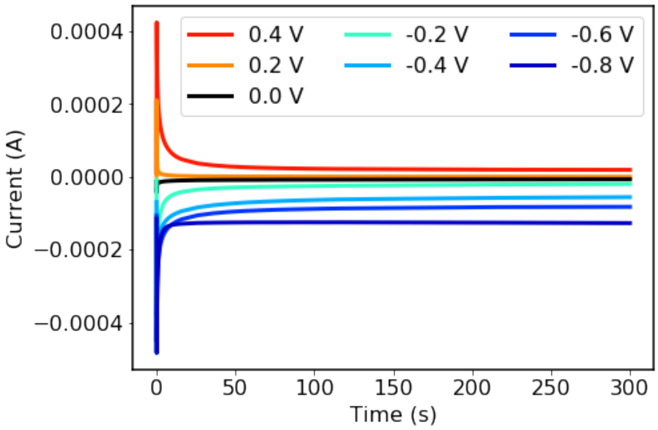

Appendix Figure A.4: Representative chronoamperometry plots for each applied potential in a typical E-SERS scan. (RE: Ag/AgCl; WE: Ag NPs on FTO; CE: platinum plate; supporting electrolyte: 0.1 M NaF).

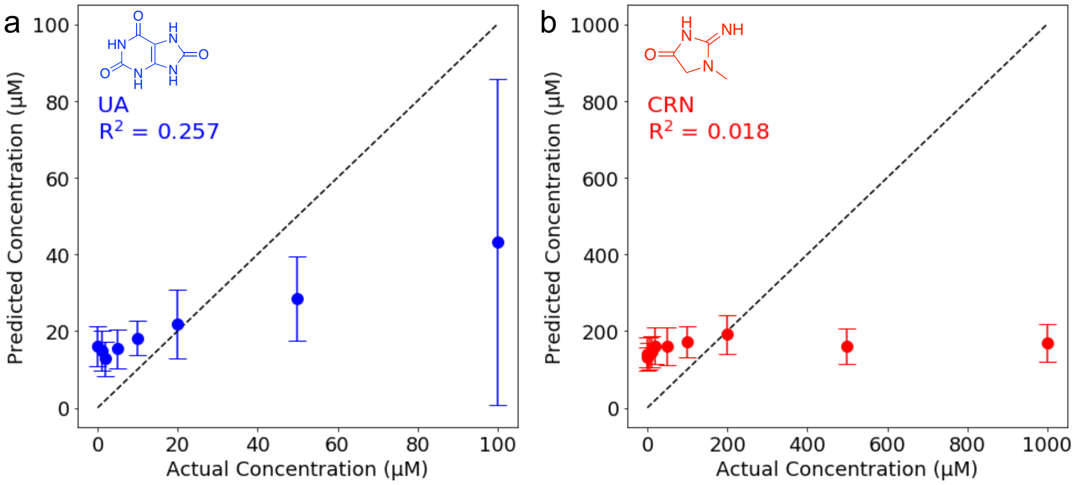

Appendix Figure A.5: A comparison of the actual concentrations and the concentrations predicted by the linear regression models based on the characteristic peaks at the optimal potentials (1138 cm^{-1} at -0.8V for UA and 684 cm^{-1} at 0.4V for CRN) for the test dataset for (a) UA and (b) CRN. The dotted y=x line represents perfect agreement between the actual and predicted concentrations.

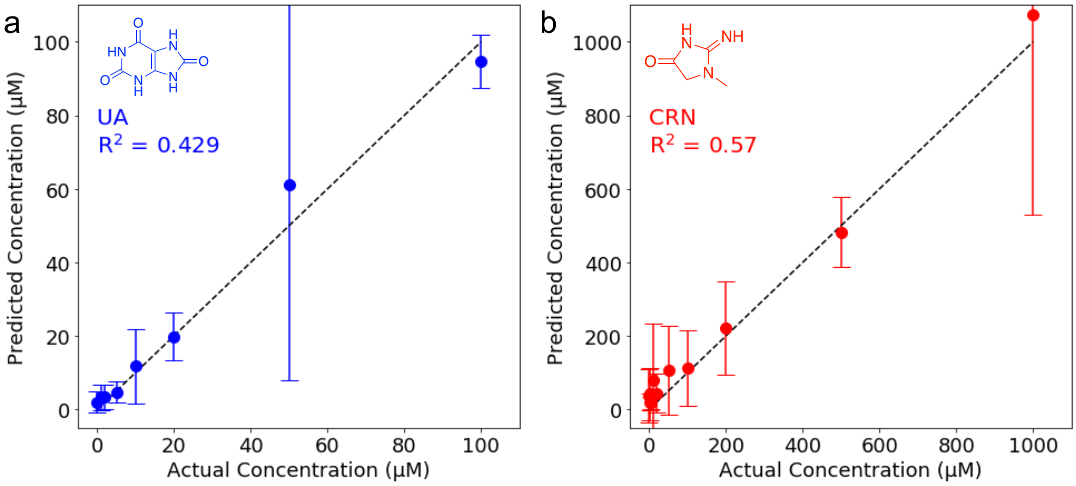

Appendix Figure A.6: A comparison of the actual concentrations and the predicted concentrations for a *two*-step *PLSR-MLP model trained and tested using only the spectra recorded at 0V for (a) UA and (b) CRN. The dotted y=x line represents perfect agreement*

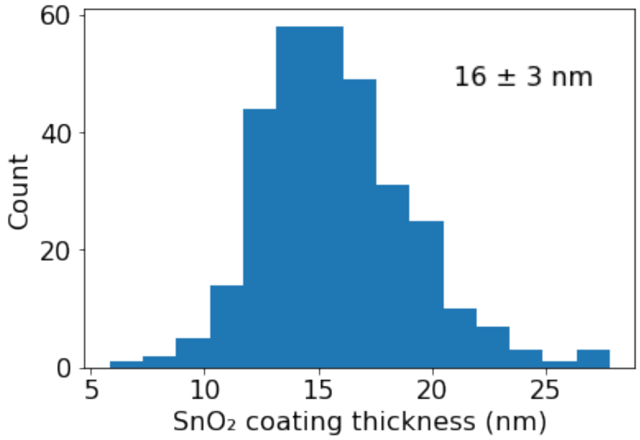

Appendix Figure A.7: SnO_2 coating thickness distribution of the standard double-coated Ag@SnO_2 substrate. The coating thickness of 312 particles was measured from TEM images using ImageJ.

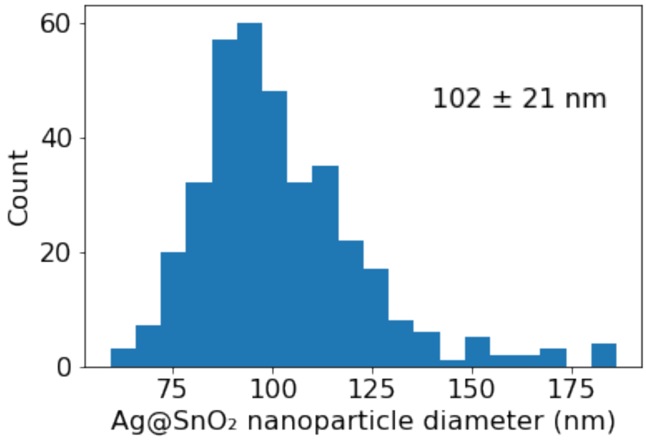

Appendix Figure A.8: Size distribution of the standard double-coated Ag@SnO_2 substrate. The coating thickness of 365 particles was measured from TEM images using ImageJ.

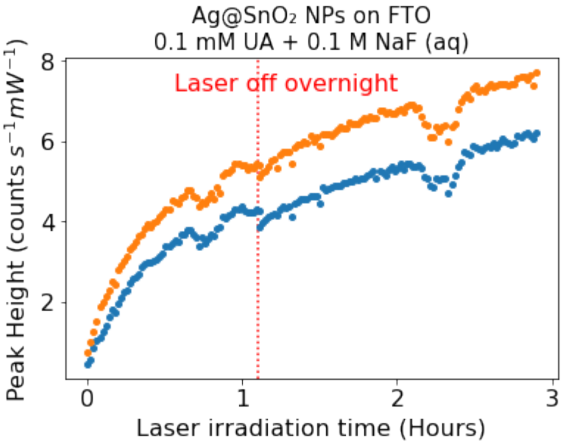

Appendix Figure A.9: The characteristic UA peak heights plotted against time for a 0.1 mM uric acid + 0.1 M NaF solution recorded with a single-coated Ag@SnO$_2$ substrate. The dotted red line indicates when the laser was turned off and the substrate was left in solution overnight.

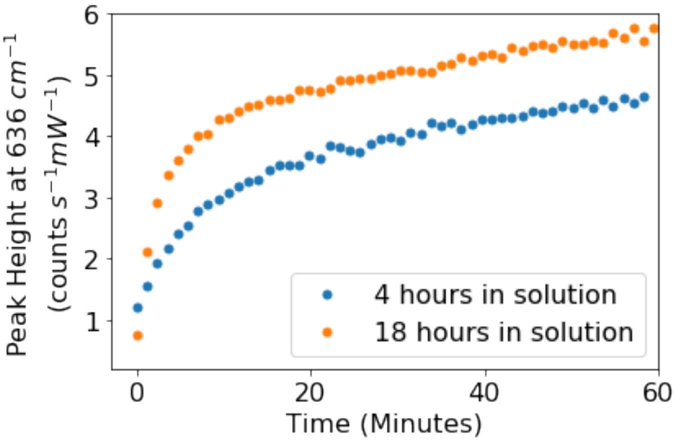

Appendix Figure A.10: The height of the characteristic UA peak at 636 cm^{-1} plotted against time for a 0.1 mM uric acid solution for a Ag@SnO$_2$ substrate which had been submerged in the solution for 4 hours (blue) and 18 hours (orange).

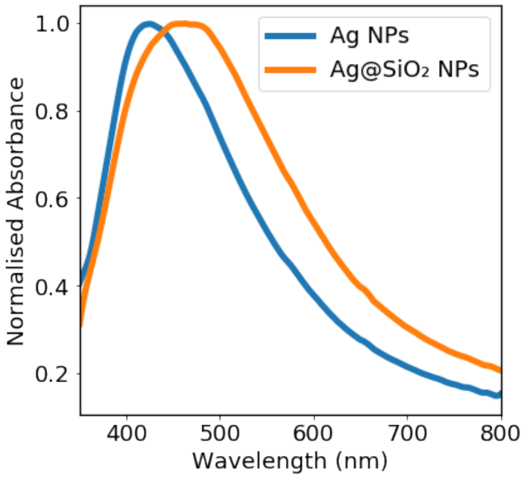

Appendix Figure A.11: UV-vis spectra of Ag NPs (blue) and Ag@SiO$_2$ NPs (orange) plotted with normalised absorbance.

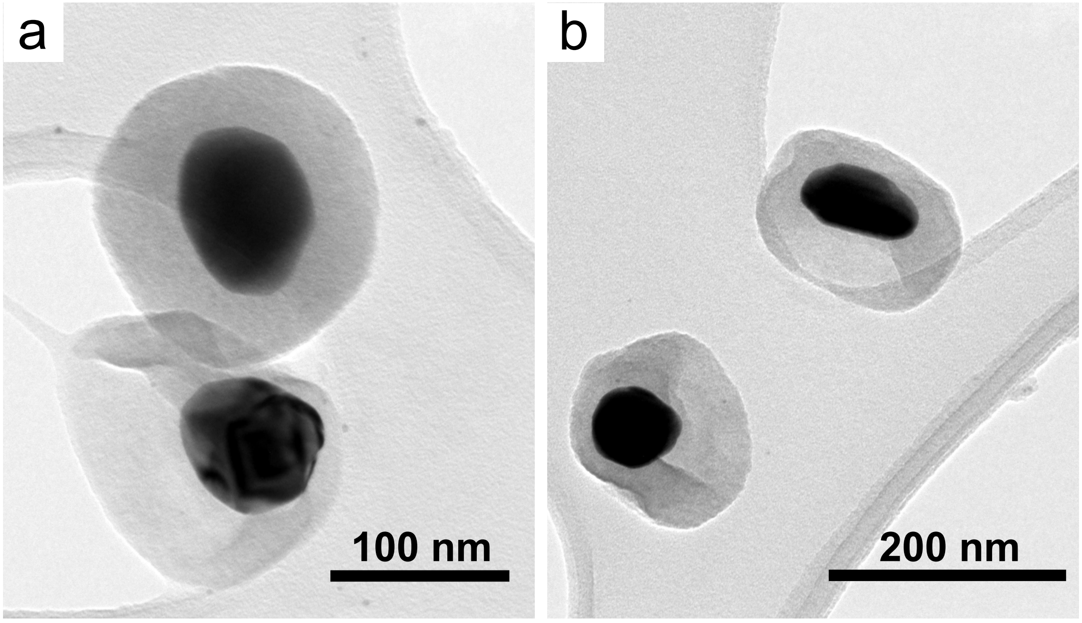

Appendix Figure A.12: TEM images of as-synthesised silicon dioxide coated silver nanoparticles (Ag@SiO$_2$ NPs).

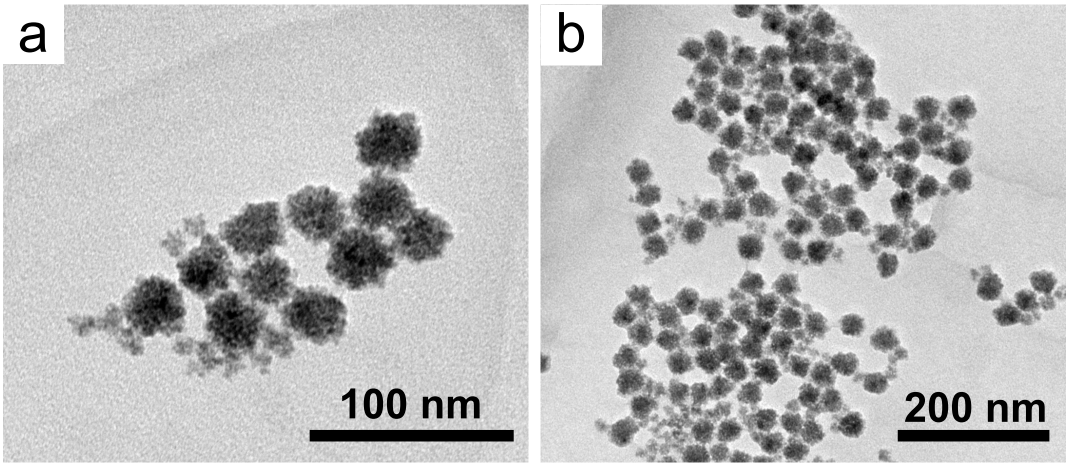

Appendix Figure A.13: TEM images of as-synthesised tin dioxide nanoparticles (SnO_2 NPs).

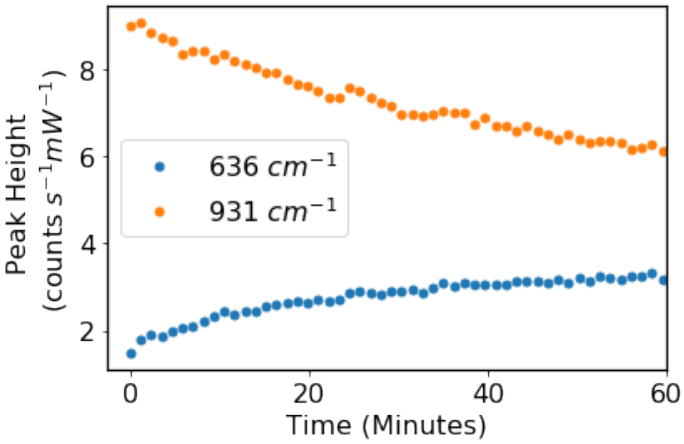

Appendix Figure A.14: Comparison of the height of the uric acid peak at 636 cm^{-1} and the citrate peak at 931 cm^{-1} over irradiation time for a Ag NP substrate in a 0.1 mM UA solution.

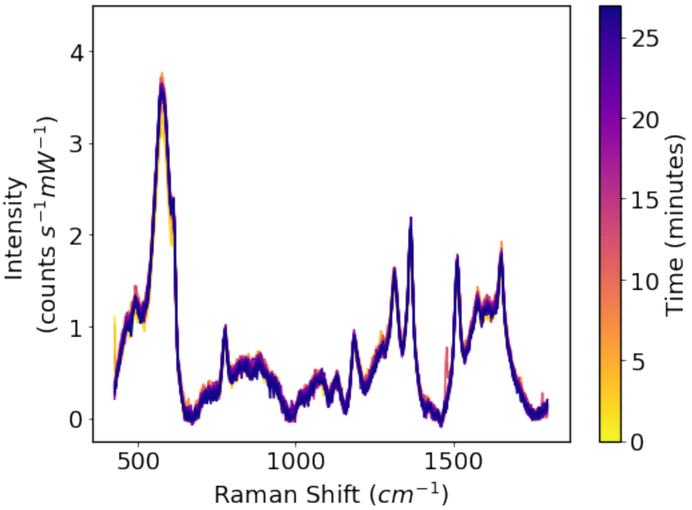

Appendix Figure A.15: Successive SERS spectra of an aqueous 10 μM R6G solution recorded over 25 minutes using a solution containing colloidal Ag@SnO$_2$ NPs. The colour of the spectra indicates the irradiation time with the initial spectra plotted in yellow and the final spectra plotted in blue.

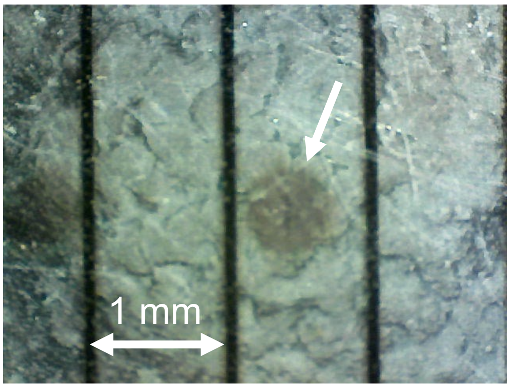

Appendix Figure A.16: Optical image of the "dark spot" which appears on the Ag@SnO$_2$ film at the SERS measurement site after sustained laser irradiation. The black lines are spaced 1 mm apart and the "dark spot" is indicated with a white arrow. Image taken by Xiangyu Wang.

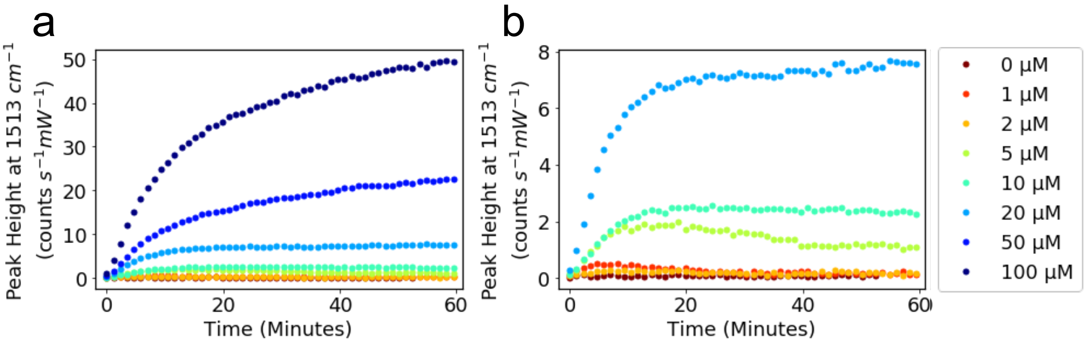

Appendix Figure A.17: The height of the characteristic ketamine peak at 1513 cm^{-1} plotted against time for a Ag@SnO$_2$ substrate irradiated for 60 minutes in a solution containing between 0 - 100 μM ketamine. (b) A zoomed-in section showing the 0 μM to 20 μM ketamine solutions.

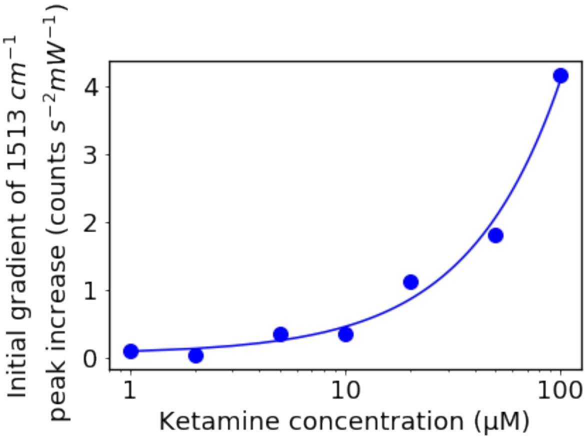

Appendix Figure A.18: The initial gradient of the 1513 cm^{-1} peak height increase plotted against ketamine concentration. A linear relationship is fitted between concentration and gradient for concentrations from 1 μM to 100 μM.

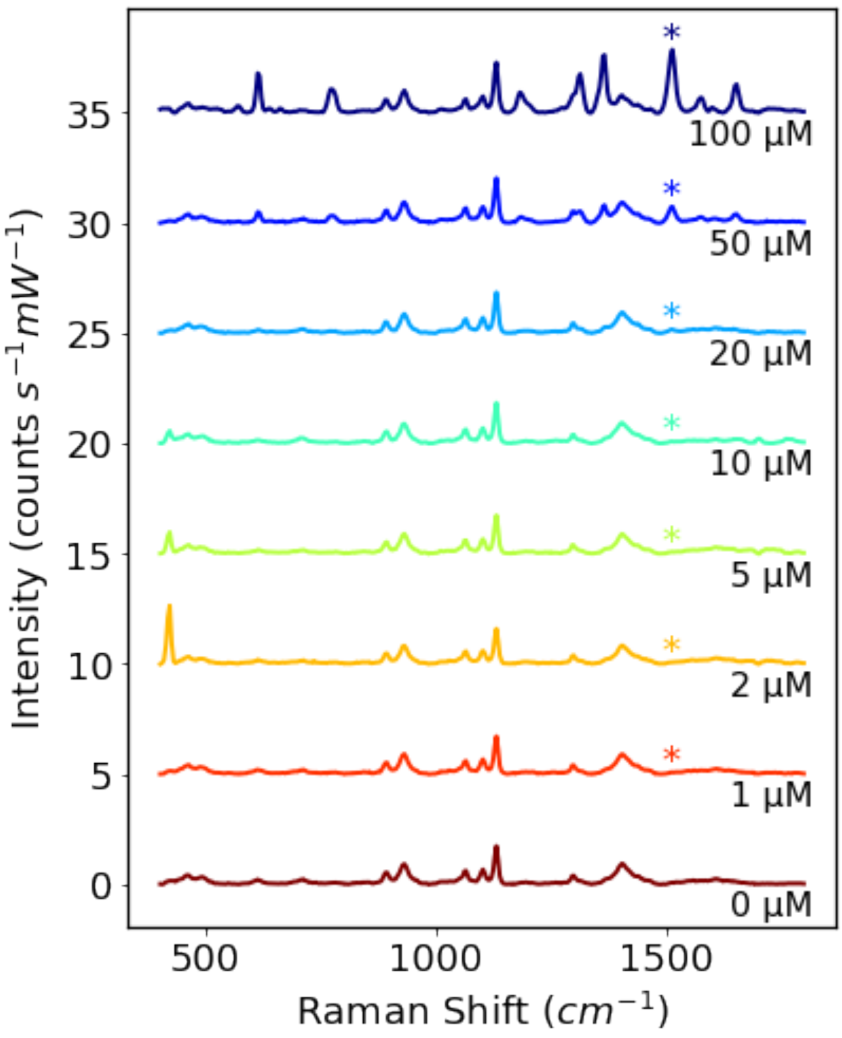

*Appendix Figure A.19: (a) SERS spectra of ketamine solutions with concentrations ranging from 0 µM to 100 µM recorded with Ag NP substrates by Alice Cozens. The characteristic ketamine peak is indicated with a *.*

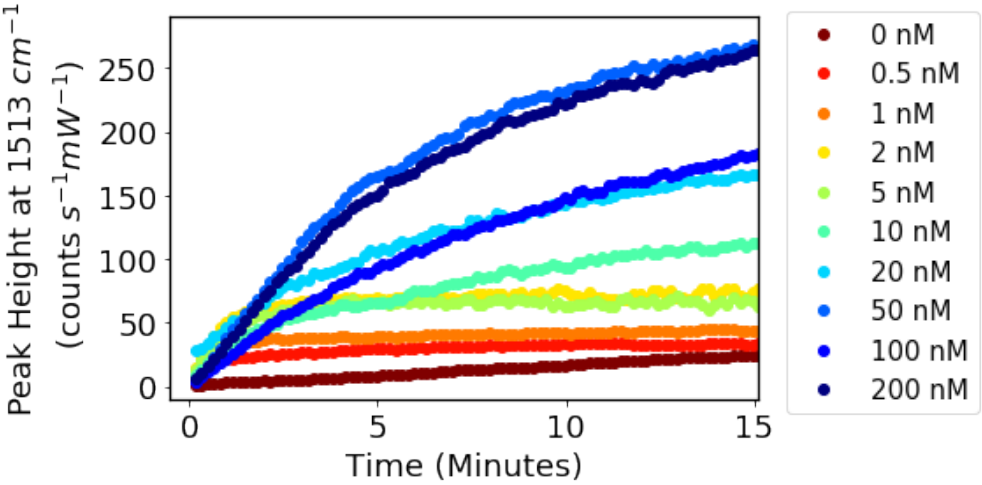

Appendix Figure A.20: The mean height of the characteristic ketamine peak at 1513 cm^{-1} plotted against time for three positions on a Ag@SnO$_2$ substrate irradiated for 15 minutes at the improved measurement position. The solutions contained synthetic saliva and between 0 - 200 nM ketamine.